

EXPLORING THE POTENTIAL OF 20S PROTEASOME MODULATION AS A NOVEL THERAPEUTIC
STRATEGY FOR THE TREATMENT OF NEURODEGENERATIVE DISEASES AND CANCERS

By

Allison Stephanie Vanecek

A DISSERTATION

Submitted to
Michigan State University
in partial fulfillment of the requirements
for the degree of

Chemistry – Doctor of Philosophy

2024

ABSTRACT

The accumulation of intrinsically disordered proteins (IDPs) and the associated disruption of cellular proteostasis is implicated in the progression of a number of neurodegenerative diseases and cancers. Due to the highly disordered nature of IDPs, they are considered “undruggable” targets because of their lack of typical drug binding pockets. The work in this dissertation focuses on the exploration of an alternative approach to pharmacologically regulate these “undruggable” proteins through proteasome-mediated degradation. The 20S proteasome is a large protein degradation complex responsible for maintaining low cellular levels of IDPs. Our approach uses small molecule enhancers of proteolytic activity of the 20S proteasome to enhance the degradation of IDPs, thereby preventing their accumulation and associated toxicity.

To demonstrate the potential use of small molecule 20S activation as a novel therapeutic approach for the treatment of neurodegenerative diseases, we studied the effects of a 20S proteasome activator toward an IDP target associated with the progression of amyotrophic lateral sclerosis (ALS). Recently, 30 to 60 percent of familial ALS cases have been linked to a gene mutation that results in the production of five highly disordered dipeptide repeat (DPR) proteins. The accumulation and aggregation of DPRs have shown to disrupt cellular proteostasis, leading to uncontrolled protein levels, resulting in neuron death and further disease progression. In a recent collaborative study, we have demonstrated that 20S proteasome activator, TCH-165, enhances the degradation of DPR proteins. The enhanced degradation of DPR proteins led to the restoration of cellular proteostasis and provided protection against DPR induced neurotoxicity in ALS disease models.

We then aimed to explore the potential use of small molecule 20S activation as a novel therapeutic strategy for cancer treatment. The overexpression of the highly disordered transcription factor, c-MYC, has been found in more than 70 percent of all human cancers. Dysregulation of c-MYC protein levels and its accumulation has shown to induce its oncogenic transcriptional activity, resulting in the transcription of a number of genes that promote tumor growth and cancer cell proliferation. In a recent study, we demonstrated the ability of TCH-165 to reduce cellular c-MYC protein levels. The enhanced degradation of c-MYC prevented its oncogenic effects, inhibiting cancer cell proliferation and reducing tumor growth *in vivo*.

To further explore this therapeutic strategy, a novel class of 20S proteasome activators was identified and synthetically modified to generate a series of analogues. Through investigation of the biological activities of this new class of 20S proteasome activators, a new component of the therapeutic mechanism was discovered. These findings provide evidence that activation of the 20S proteasome can be tuned to selectively target IDPs based on their amino acid sequence. This suggests the exciting possibility that a small molecule 20S proteasome activator could be designed to selectively target a specific IDP for a more targeted disease treatment. In all, this work suggests that small molecule activation of the 20S proteasome may offer a potential novel therapeutic strategy for the treatment of neurodegenerative diseases and cancers in which intrinsically disordered protein accumulation plays a significant role in disease progression.

ACKNOWLEDGEMENTS

I am so grateful to the amazing people that have made my time in graduate school such a wonderful experience. While my passion for research may have led me to my pursuit of a degree at MSU, it is through the mentoring, support, and friendship of those who became a part of my journey that made this dream a reality. I thank you all from the bottom of my heart.

I would first like to thank my advisor, Dr. Tepe. I cannot thank you enough for allowing me to be a part of your lab and research program. The opportunity to conduct research in such an exciting new field has been an amazing, though sometimes frustrating experience. Yet your support, excitement for our research, and the ability to know when I needed help even when I had not asked, always helped me to persevere in pursuit of my goals. I am also so grateful for your support to pursue the new, sometimes unconventional, ideas I was excited to try. Your encouragement of me to trust my scientific intuition has helped me to become the confident scientist I am today. Lastly, thank you for assembling such an amazing, kind, fun, supportive and brilliant group of people with whom I have had the great pleasure of working with over the past few years.

To all of the members of the Tepe lab, current and past, you have become a second family to me, and I would not have made it through this journey without you. Sophie, I am so grateful that you have been by my side for every step of this journey. From the start of our very first year, you have been a best friend, a creative mind to brainstorm new ideas with, and a great supporter. To Charles, your kindness, words of encouragement, and joyful disposition always light up the lab. Thank you for making even the challenging days in lab so enjoyable. To Katarina, Grace and Taylor, thank you for all of your help and guidance when I joined the lab, for always checking in to hear how my research was going, and the many trips to Sparty's for coffee. Thank you to Kyra and Dare for your collaboration on exciting projects underway in the lab and for being such supportive teammates. Thank you to Shannon, Christi, Konika, Daniel, Evan, Bahar, Sydney and Miracle for your support, great conversation, and friendship. I am so blessed to have had the privilege of working with you all and I cannot wait to see what great things the future has in store for all of you.

I would also like to thank a number of others at MSU and other collaborators for their support along the way. To my committee, Dr. Huang, Dr. Wulff, and Dr. Borhan, thank you for your feedback, ideas, and guidance along the way regarding my research, seminar, and classes. Thank you to Dr. Parent and Dr. Subramanian at the RTSF Cryo-EM Facility at MSU for their guidance and suggestions for my structural biology studies. Dr. Subramanian, thank you for teaching me so many awesome electron microscopy techniques and spending many hours at the microscope with me collecting images. Thank you to Dr. Odom and Dr. Hou for your collaboration on the exciting ruthenium complex studies. Also, thank you to many members of the pharmacology department for their collaboration on various studies throughout the years. Thank you to Dr. Kalb and Dr. Mojsilovic-Petrovic at Northwestern Medicine for their guidance and collaboration on the ALS studies. We were able to obtain quite promising results together and this project was one of my favorites to work on. I would also like to thank all of the members and faculty advisors of MSU's Women in Chemistry (WiC) group for helping to make our fun department events and workshops possible. I have thoroughly enjoyed these events through the years and working with you all to plan them.

To my family, I truly cannot express how much your unending support, love, and encouragement means to me. Thank you for being my biggest cheerleaders, encouraging me to believe in myself, and always being there for me. I would not be where I am today without you. I also would like to thank my family pets back home for always putting a smile on my face and lifting my spirits. Thank you to Maggie, Teresa, Fred, Meagan, Katie, Maggie, Hannah, and all of my friends for being such an amazing support system through the ups and downs of grad school. I always appreciate our coffee dates, game nights, shopping trips, and gym nights. Lastly, to my loved ones no longer with us, thank you for always believing in me and instilling in me the strength and drive to pursue my dreams. I love you all.

TABLE OF CONTENTS

CHAPTER ONE Restoration of Proteostasis Through Modulation of the Ubiquitin Proteasome System Offers Novel Strategy for the Treatment of Neurodegenerative Diseases and Cancers... 1	
1.1 Introduction..... 2	2
1.2 The Ubiquitin Proteasome System..... 5	5
1.3 Dysregulation of IDPs and Imbalanced Proteostasis in Disease 10	10
1.4 Pharmacological Targeting of IDPs in Disease 15	15
1.5 Small Molecule Activation of the 20S Proteasome 17	17
1.6 Conclusion 20	20
REFERENCES 22	22
PART I 20S Proteasome Activation as a Novel Therapeutic for Neurodegenerative Diseases ... 31	
CHAPTER TWO Exploring the Potential of Small Molecule Activation of the 20S Proteasome as a Novel Therapeutic for the Treatment of Amyotrophic Lateral Sclerosis 32	
2.1 Introduction..... 33	33
2.2 Results and Discussion 36	36
2.3 Conclusion 78	78
2.4 Experimental 79	79
REFERENCES 84	84
APPENDIX 92	92
CHAPTER THREE Discovery of a Novel Class of Small Molecule 20S Proteasome Activators Allows for the Exploration of Selective Targeting of Intrinsically Disordered Proteins 102	
3.1 Introduction..... 103	103
3.2 Results and Discussion 107	107
3.3 Conclusion 137	137
3.4 Experimental 138	138
REFERENCES 150	150
APPENDIX 155	155
PART II 20S Proteasome Modulation as a Novel Therapeutic for Cancers 186	
CHAPTER FOUR Identification of a Novel Class of Ruthenium Quinoline Complexes as a Potential Cancer Therapeutic..... 187	
4.1 Introduction..... 188	188
4.2 Results and Discussion 191	191
4.3 Conclusion 200	200
4.4 Experimental 200	200
REFERENCES 203	203
APPENDIX 206	206

CHAPTER FIVE Exploring the Potential of 20S Proteasome Activation as a Novel Cancer Therapeutic Strategy.....	209
5.1 Introduction.....	210
5.2 Results and Discussion	214
5.3 Conclusion	221
5.4 Experimental	221
REFERENCES	224
APPENDIX	228

CHAPTER ONE

Restoration of Proteostasis Through Modulation of the Ubiquitin Proteasome System Offers
Novel Strategy for the Treatment of Neurodegenerative Diseases and Cancers

1.1 Introduction

1.1.1 The Proteostasis Network

Protein homeostasis, or proteostasis, is achieved by maintaining a balance of protein synthesis, folding, and proteolytic degradation through strict regulation of the machineries responsible for these processes.¹ This extensive network of molecular chaperones, proteolytic systems and their regulators are highly interconnected allowing for crosstalk between the systems to coordinate a number of functions necessary to maintain proper protein abundance and a balanced proteome. If an imbalance is detected, the network works together to correct abnormalities to restore proteostasis and ensure proper cellular function. The network is responsible for regulating a wide range of functions including protein synthesis through the regulation of translation, protein folding and transport through the regulation of molecular chaperones, and protein degradation via cellular proteolytic machineries.^{1,2}

Proteins are synthesized by ribosomes in a process known as translation, in which an amino acid sequence encoded by an mRNA strand is synthesized into a polypeptide chain. Translation is tightly regulated to control protein abundance in the cell.³ Once the polypeptide chain is synthesized, for most proteins, it is essential that it is folded into a specific 3D conformation to perform its biological function. Molecular chaperones are proteins that help accomplish this by binding to newly translated or misfolded proteins to aid in their folding or assembly.^{3,4} Furthermore, molecular chaperones prevent aggregation of proteins by promoting folding of proteins in a partially unfolded or misfolded state.³ Another important function performed by molecular chaperones is to transport proteins from their synthesis site in the cytosol to specific cellular compartments in order for the protein to perform its specific function.³ Finally, once a protein has completed its function or is damaged, it is then degraded by the cell's proteolytic machineries. The ubiquitin proteasome system (UPS) and the autophagy-lysosome system are two proteolytic systems in place to degrade these damaged or redundant proteins.^{1,5} Protein degradation allows the cell's amino acid pool to be replenished and prevents the accumulation of proteins which has shown to induce their aggregation leading to proteotoxicity. Due to the crosstalk between the systems of the proteostasis network, it is able to adapt in response to a number of stressors, such as mutations and oxidative stress, to preserve

proteostasis.^{6,7} However, decline in the efficiency of the proteostasis network has been implicated in disease pathogenesis and will be discussed later in this chapter.^{2,8,9}

1.1.2 Intrinsically Disordered Proteins and Their Functions

Despite the long-standing belief that proteins must be folded into a specific, well-defined 3D conformation to perform their biological function, this is not true for all proteins. Cellular proteins are now known to lie on a continuum of protein disorder, ranging from proteins with a highly ordered quaternary structure, to proteins that lack any defined tertiary structure at all.¹⁰ Proteins that consist of mostly disordered regions are referred to as intrinsically disordered proteins (IDPs), however, proteins exist that lie in the midst of this continuum, containing both structured regions and intrinsically disordered regions (IDRs).¹¹ Since the formation of hydrophobic interactions has shown to be the driving force behind protein folding, IDPs and IDRs have shown to be depleted of order-promoting residues (i.e. Trp, Cys, Tyr, Ile, Phe, Val, Asn, and Leu), many of which are quite hydrophobic, and enriched in disorder-promoting residues (i.e. Arg, Pro, Gln, Gly, Glu, Ser, Ala, and Lys), often containing repeats of amino acids.^{12,13} In addition to the low hydrophobic amino acid content of IDPs, many have a high net charge under physiological pH.¹³ These sequence characteristics result in a highly dynamic protein, where parts of an IDP can be disordered or temporarily gain order at any given time. This high conformational flexibility and structural plasticity of IDPs and IDRs allows them to interact with multiple different binding partners to perform a wide variety of unique functions which would be difficult for ordered proteins.¹³

Intrinsically disordered proteins play a central role in the regulation of cellular signaling pathways through transient binding events with multiple binding partners. Often intrinsically disordered proteins undergo transitions to more ordered states or fold into stable secondary or tertiary structures upon binding to their targets, however, this is not always the case.¹⁴ It has been shown that about one-third of protein chaperones are disordered in nature.¹¹ Since IDPs and IDRs can adapt their structures according to different binding partners, they have shown to efficiently bind misfolded proteins, burying their hydrophobic residues and preventing their toxic aggregation.¹¹ A number of IDPs have also shown to aid in the assembly of macromolecular

complexes, such as the ribosome. In these cases, the IDP interacts with multiple binding partners simultaneously to promote the formation of higher-order protein complexes.^{11,15}

Additionally, it has been found that over 90 percent of transcription factors are IDPs or contain IDRs.¹⁴ A transcription factor is a protein that regulates the transcription of genes by promoting the process of RNA synthesis from DNA. The RNA sequences are then translated into proteins that perform specific functions throughout the cell. Transcription factors often contain a structured DNA binding domain and a disordered domain that recruits transcriptional activation or repression components.¹⁴ The transcription factor, c-MYC, is an example of an intrinsically disordered transcription factor that is responsible for the regulation of many genes involved in cell growth and proliferation.¹⁶ c-MYC activates transcription through binding its disordered binding partner MYC Associated Factor X (MAX) to form a heterodimer, which then binds a DNA target sequence to initiate transcription of almost 15 percent of all genes.^{16–18}

1.1.3 Regulation of Intrinsically Disordered Proteins

Due to their promiscuity and ability to bind numerous binding partners, IDP abundance must be tightly regulated to avoid aberrant signaling. Regulation of IDPs is accomplished through a number of mechanisms from protein synthesis to protein degradation. Multiple mechanisms at the transcriptional and translational level are in place to maintain low levels of cellular IDPs and typically for short periods of time.¹⁹ Studies have shown that the mRNA transcripts that encode IDPs tend to have higher mRNA decay rates compared to structured proteins.²⁰ These short mRNA half-lives allow for rapid changes of protein concentration depending on environmental conditions or when signaling inputs change.²¹

Furthermore, the protein half-life of a majority of IDPs have been observed to be shorter than that of most structured proteins.¹⁹ This decreased half-life has been linked to IDPs increased susceptibility to proteolytic degradation by the UPS.^{22,23} However, while IDPs are rapidly degraded by the UPS, mechanisms are in place to protect IDPs from UPS degradation if an IDP is needed in high concentrations or for long periods of time to perform a specific function. A class of proteins known as nanny proteins have shown to stabilize IDPs by binding to the IDRs that facilitate their degradation.²⁴ Through formation of this stable protein complex, the IDP gains a level of order and degradation of the IDP is prevented. Another method of IDP regulation is

through their post-translational modifications, such as phosphorylation. Phosphorylation of IDPs have shown to change the net charge of an IDP, thereby modulating the binding affinity of interactions with binding partners.²⁵ Again, influencing whether an IDP is in a bound or unbound state significantly affects its vulnerability toward proteolytic degradation.

1.2 The Ubiquitin Proteasome System

1.2.1 Structural Features of the Proteasome

The UPS is one of two major proteolytic degradation systems of the proteostasis network. The UPS is responsible for the degradation of proteins spanning a wide degree of protein structure, ranging from highly structured proteins to IDPs which lack a defined tertiary structure. The UPS is made up of the active 26S proteasome, which is primarily responsible for the degradation of structured proteins through a ubiquitin-dependent degradation,^{26,27} and the 20S proteasome which is thought to be a less active/latent isoform. The 20S proteasome has shown to target IDPs for degradation in a ubiquitin-independent manner.^{26,28-30}

The 20S core particle is a threonine protease comprised of four stacked heteroheptameric rings arranged in an $\alpha_7\beta_7\beta_7\alpha_7$ fashion (Figure 1.1A).³¹ Each of the β -rings contains three unique proteolytically active β -subunits (i.e. proteolytic sites), for a total of six proteolytic sites per 20S core particle. Each of these proteolytic sites exhibit different substrate preferences due to the varying substrate binding pockets of each active site.³² These substrate binding pockets among the proteolytic sites vary since they are formed by interactions between the proteolytic subunit and the neighboring β -subunit.³³ The active site specificity is as follows: the chymotrypsin-like site (CT-L; β_5 subunit) preferentially cleaves after large hydrophobic amino acid residues, the trypsin-like site (T-L; β_2 subunit) preferentially cleaves after basic amino acids, and the caspase-like (Casp-L; β_1 subunit) preferentially cleaves after acidic amino residues.^{34,35} Each of these proteolytic sites contains an active threonine residue that binds substrate proteins, followed by subsequential hydrolytic cleavage of the peptide bond and degradation of the substrate.³⁶ The combined proteolytic activities of these proteolytic sites with varying substrate specificities allows for the effective degradation of a wide range of proteins with varying amino acid composition.

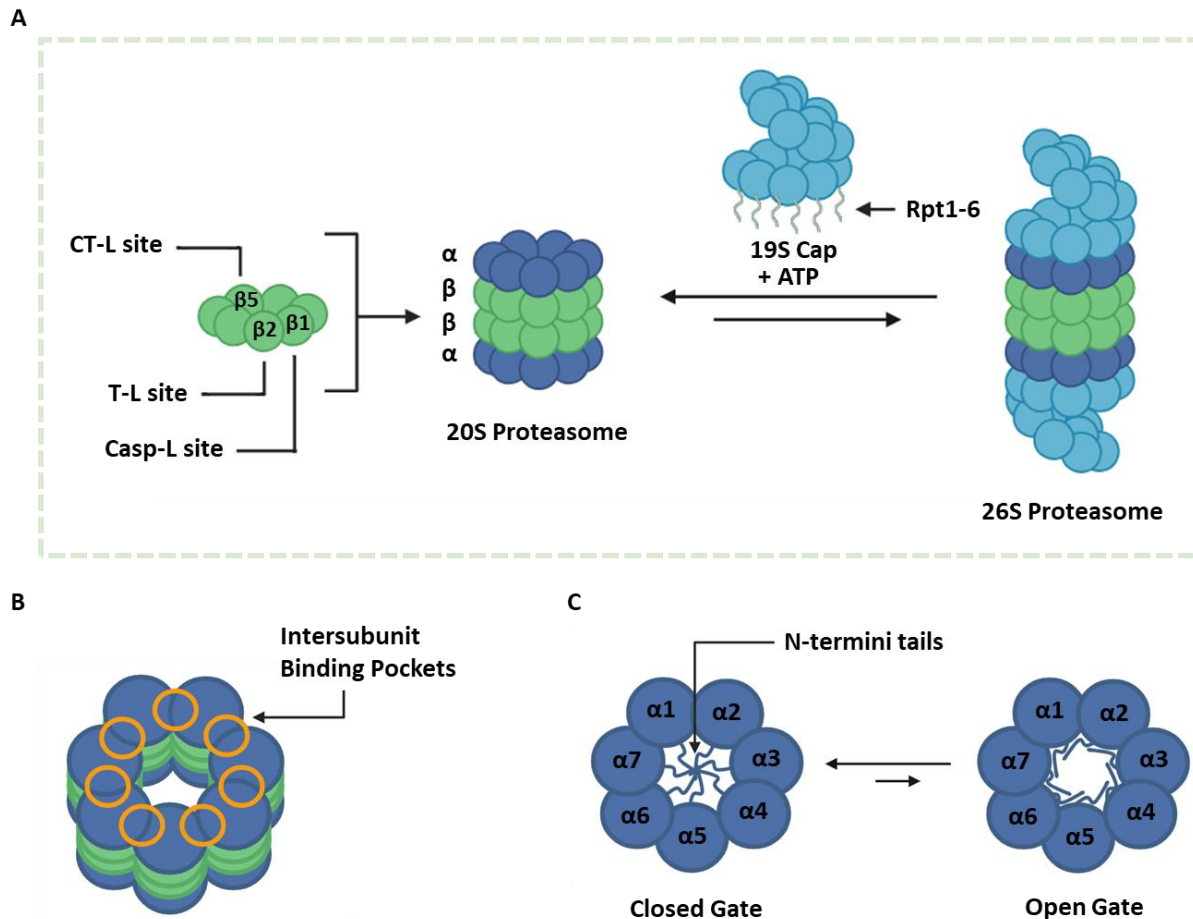


Figure 1.1 Structural components of the ubiquitin proteasome system (UPS). (A) Low activity/latent 20S isoform of the proteasome with the three unique catalytic sites of the β -rings identified (chymotrypsin-like; CT-L ($\beta 5$), trypsin-like; T-L ($\beta 2$), and caspase-like; Casp-L ($\beta 1$)). The 20S proteasome is in a dynamic equilibrium with the fully assembled, active 26S isoform of the proteasome. Formation of the 26S proteasome requires an ATP-dependent docking of the 19S regulatory cap. (B) Docking of the 19S cap occurs through the binding of the Rpt1-6 tails at the base of the 19S cap into the intersubunit pockets on the α -ring of the 20S proteasome. (C) N-termini tails of the α -subunits occlude access to the proteolytic core in the closed conformation of the 20S proteasome (left). The closed conformation is in equilibrium with an open gate conformation (right) in which the N-termini tails are displaced from their obstructive position over the proteolytic core.

The two outer α -rings of the 20S core particle act as gate keepers to the inner proteolytic core.^{31,36,37} The amino termini (N-termini) tails of the α -subunits form a “gate” over the 13-Å central pore of the 20S core particle to occlude access to the proteolytic sites; this conformation is referred to as a closed gate conformation (Figure 1.1C, left).³⁷ The N-termini tails contain a highly conserved tyrosine-aspartate-arginine (YDR) motif which form salt bridges with the

neighboring tails to block access to the central pore.^{32,37} The $\alpha 3$ N-termini tail has shown to be the critical anchor for stabilizing this closed gate conformation, as its deletion has shown to significantly destabilize the closed gate conformation allowing increased substrate access to the proteolytic core.^{37,38} The 20S core particle is found primarily in a closed gate conformation, however, it is in equilibrium with an open gate conformation in which the N-termini tails undergo conformational fluctuations being transiently displaced from their obstructive position over the pore (Figure 1.1C, right).^{39,40}

To induce gate opening of the 20S core particle a regulatory “cap” protein can associate with the 20S core particle to form various activated isoforms of the proteasome.³² The 26S proteasome is one of these activated isoforms that is formed when the 20S proteasome associates with one or two 19S regulatory caps (Figure 1.1A).⁴¹ The 19S cap binds to the 20S core particle using the C-termini tails of six ATPase subunits (Rpt1-6) at the base of the 19S cap.⁴² These Rpt tails are inserted into the intersubunit pockets on the α -ring and bind using a conserved motif (Figure 1.1B). It is interesting to note, that while the combination of Rpt tails of the 19S cap bind to induce an open gate conformation, Rpt-5 is the only peptide tail that has shown to be able to induce an open gate conformation individually.³² Characterization of this motif has been extensively studied revealing a hydrophobic-tyrosine-any residue (HbYX) motif is used for binding.⁴¹ A recent study has further defined the sequence selectivity of this motif, identifying a tyrosine or phenylalanine-tyrosine (Y-F/Y) sequence as the conserved motif.⁴³ Upon binding of the 19S cap using this motif, an ATP-dependent conformational change of the α -ring is induced and opens the gate to the proteolytic core.^{41,42} In addition to the 19S cap, the human 20S proteasome can be activated by two other families of protein cap activators, the 11S (i.e. PA28 α,β,γ ; also known as REG α,β,γ) and PA200.³² These two families of proteasome activator caps differ from the 19S cap, in that their binding does not require ATP and they are unable to aid in the unfolding of protein substrates.³²

1.2.2 Ubiquitin-Dependent Proteasomal Degradation

The 26S proteasome is primarily responsible for the degradation of structured proteins through a ubiquitin-dependent degradation.^{26,27} When a protein has become damaged, misfolded, or redundant, the protein must be degraded to replenish amino acid stores in the

body and avoid the toxic accumulation of proteins. However, for recognition of a protein as a substrate of the 26S proteasome, the protein must be ubiquitinated. Ubiquitin is a small protein that undergoes a set of reactions to be conjugated to other ubiquitin molecules to form a poly-ubiquitin chain. This poly-ubiquitin chain serves as a tag for 26S proteasome recognition, allowing the 26S proteasome to selectively identify and degrade these unneeded proteins.⁴⁴

The attachment of the poly-ubiquitin chain relies on a three-step process involving three different enzymes (E1, E2 and E3 ligases) as shown in Figure 1.2. The ubiquitination process begins with the activation of ubiquitin by an E1 ubiquitin activating enzyme through an ATP-dependent process.⁴⁵ In this reaction a cysteine active site residue of the E1 enzyme reacts with the C-terminal carboxyl group of the ubiquitin molecule to form a thioester bond. Once the ubiquitin molecule is bound to the E1 enzyme, the ubiquitin molecule is transferred to the cysteine active site of the E2 ubiquitin-conjugating enzyme forming a new thioester bond with the E2 enzyme.⁴⁵ Lastly, an E3 ubiquitin ligase binds to both the E2-ubiquitin complex and the protein substrate to be ubiquitinated. The ubiquitin is then transferred to the substrate protein forming an amide bond between the C-terminal end of the ubiquitin molecule and a lysine residue, or on rare occasions other nucleophilic amino acid residues, on the substrate protein.⁴⁵⁻⁴⁷ To form a poly-ubiquitin chain, this set of reactions is repeated to add additional ubiquitin molecules. However, in these successive reactions the ubiquitin molecule is added to a Lysine-48 (i.e. K48) of the previously conjugated ubiquitin molecule for proteins destined for degradation by the UPS.^{45,46} Typically, a poly-ubiquitin tag of four ubiquitin molecules is sufficient for recognition by the 26S proteasome.⁴⁸ Ubiquitination of one of the other seven lysine residues of ubiquitin often designates other fates. For example, ubiquitin linkages on Lysine-63 (i.e. K63) often signals degradation through the autophagy pathway.⁴⁶

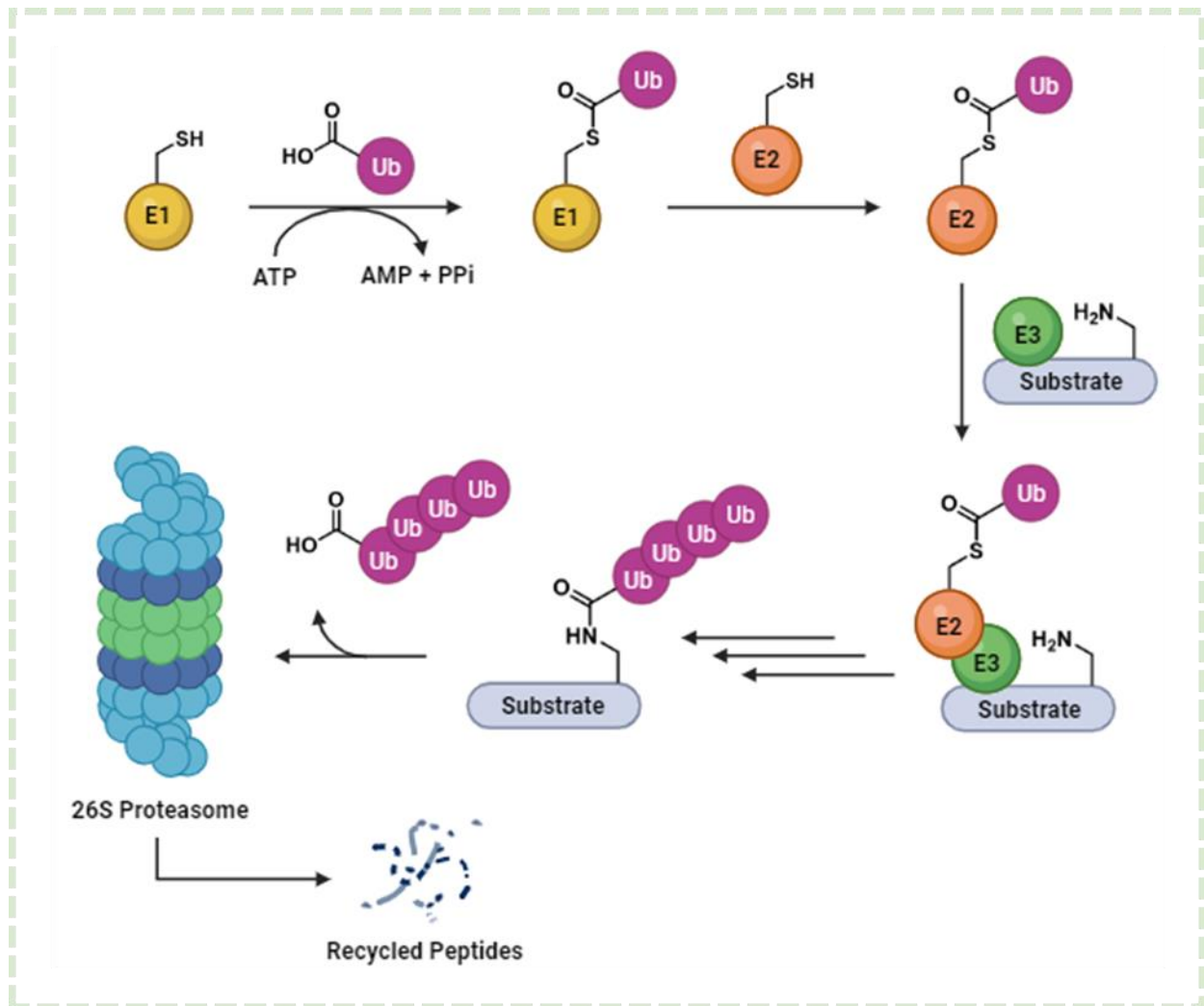


Figure 1.2 Schematic of the ubiquitin-dependent degradation of a protein. A poly-ubiquitin chain is first attached to the target protein through a three-step process using the E1, E2 and E3 enzymes. The ubiquitinated protein is then recognized as a protein substrate for the 26S proteasome by ubiquitin receptors on the 19S cap. Additional subunits on the 19S cap then deubiquitinate, unfold and translocate the protein into the proteolytic core for degradation.

After the poly-ubiquitin chain has been added, ubiquitin receptors on the 19S cap (i.e. Rpn1, Rpn10, and Rpn13) of the proteasome bind the ubiquitylated protein substrate.^{32,44} Through an ATP-dependent process, the protein substrate is then unfolded and translocated into the proteolytic core of the 20S core particle. As the protein is translocated, the Rpn11 subunit, which is a deubiquitinase (DUB) enzyme, removes the poly-ubiquitin chain from the substrate protein to allow it to be recycled and used in another degradation event.^{32,49} Once the substrate

protein reaches the proteolytic sites of the core, the peptide bonds of the substrate protein are hydrolytically cleaved producing small peptide fragments to be recycled by the cell.

1.2.3 20S Proteasome-Mediated Ubiquitin-Independent Degradation

In the absence of 19S caps, the 20S proteasome lacks the ability to recognize poly-ubiquitin chains or unfold protein substrates for degradation. As a result, the 20S proteasome is unable to degrade structured proteins no longer needed by the cell. However, the 20S proteasome is known to be a critical regulator of cellular IDP levels. The degradation of IDPs does not require protein unfolding and occurs in a ubiquitin-independent manner through the 20S proteasome.^{26,28-30} Although, it is important to note that IDPs can also be ubiquitinated and degraded in a ubiquitin-dependent manner through the 26S proteasome.⁴⁵

Additionally, without binding of the 19S cap to induce gate opening, the 20S proteasome is primarily found in a closed gate conformation. In this closed gate conformation, the N-termini tails of the α -subunits block access to the proteolytic core preventing substrate entry.³⁷ However, the 20S proteasome is known to be in equilibrium with an open gate conformation in which the N-termini tails undergo conformational fluctuations that result in displacement of the N-termini tails and gained access to the core.^{39,40} However, because this equilibrium favors a closed conformation, the 20S proteasome has often been considered a latent isoform of the proteasome. Despite the low basal activity of the 20S proteasome, the intermittent presence of open gate 20S proteasomes is sufficient to maintain low levels of IDPs to preserve proteostasis in a healthy cell. Furthermore, direct interactions of IDP substrates with the α 3 subunit of the 20S proteasome's α -ring has shown to induce a conformational change resulting in gate-opening and substrate degradation.⁵⁰ In combination, the ubiquitin-dependent and ubiquitin-independent degradation pathways work harmoniously to maintain healthy levels of two different pools of proteins to preserve cellular proteostasis.

1.3 Dysregulation of IDPs and Imbalanced Proteostasis in Disease

As previously discussed, cellular IDP levels are tightly regulated to control their abundance. This regulation occurs at the transcriptional and translational level, as well as through interactions with binding partners to gain stability and protection from protein degradation.^{19,24,25} The IDPs which are no longer needed are then degraded by the 20S

proteasome to prevent their accumulation. While the low basal activity of the 20S proteasome is sufficient to maintain proteostasis and low IDP levels in a healthy cell, the dysregulation and accumulation of IDPs has been associated with the progression of numerous diseases.⁵¹⁻⁵⁴ This accumulation of IDPs has shown to occur through a variety of mechanisms including, dysregulation of the UPS, mutations, gene amplification, or other cellular dysregulations.⁵⁵

Under typical circumstances crosstalk between the systems of the proteostasis network allow it to adapt in response to a number of stressors, such as mutations and oxidative stress, to preserve proteostasis.^{6,7} However, with age, the efficiency of the proteostasis network declines and has been identified as a major contributor to age-related cellular dysfunction and degenerative diseases.^{2,8,9} Once efficiency has been compromised, damaged, misfolded, and redundant proteins can accumulate causing an imbalance in proteostasis.

1.3.1 Imbalanced Proteostasis in Neurodegenerative Diseases

Disruption of proteostasis and the accumulation of IDPs has been implicated in the progression of a number of neurodegenerative diseases including Parkinson's disease (i.e. α -synuclein), Alzheimer's disease (i.e. tau and amyloid- β), Huntington's disease (i.e. polyQ), and amyotrophic lateral sclerosis (ALS).⁵¹⁻⁵⁴ In these diseases, the accumulation of aggregation-prone proteins has shown to impair the function of components of the proteostasis network resulting in the toxic accumulation of protein aggregates.^{32,56} In context of the work to be discussed in this dissertation, the role of IDP accumulation in the progression of ALS will be discussed in greater detail.

ALS is a fatal neurodegenerative disease characterized by muscle atrophy and the progressive loss in the ability to initiate and control muscle movement, leading to paralysis and ultimately death. Studies have shown that five distinct proteins with high levels of disorder are major drivers of disease progression. These proteins include the superoxide dismutase 1 (SOD1) enzyme, a TAR-DNA binding protein-43 (TDP-43), an RNA-binding protein FUS, actin-binding profilin-1 (PFN1), a cofilin-binding protein C9orf72, and a family of dipeptide repeat (DPR) proteins generated as a result of its intronic hexanucleotide expansions.⁵⁷

The SOD1 protein is predicted to be almost 45 percent disordered using Predictor of Natural Disordered Regions (PONDR) algorithms. Mutations of the *SOD1* gene have been found

in approximately 20 percent of familial ALS cases.⁵⁷ Of the more than 170 SOD1 mutants identified, the mutations result in a varied conformation which exposes a short region of its N-terminal, with many increasing the disorder of SOD1.⁵⁷ This exposed region has shown to cause endoplasmic reticulum (ER) stress and is aggregation-prone due to the exposure of hydrophobic regions.^{58,59} This increased aggregation propensity of IDPs has shown to result in the accumulation of protein aggregates that cause significant cellular toxicity. Mutants of TDP-43, FUS and PFN1 have similar origins in which a point mutation results in an altered protein conformation, affecting its interaction with various cellular components, causing nefarious signaling.⁵⁷

In the previously discussed cases, a point mutation within the coding region of the *SOD1*, *TDP-43*, *FUS* and *PFN1* genes resulted in a structural modification to the endogenous protein in which the gene encodes, producing a mutant protein with altered behavior and interactome of proteins. This is a common mechanism by which mutant IDPs associated with disease pathology are produced. Contrary to these cases, the dipeptide repeat (DPR) proteins that arise from a mutation in the *C9ORF72* gene have a more obscure origin. The DPRs are generated from a hexanucleotide repeat expansion (HRE) of sequence 5' GGGGCC 3' located in a non-coding intron flanked by exons 1a and 1b in the *C9ORF72* gene.^{60,61} The HREs are transcribed into long stretches of mRNA which adopt a stable hairpin secondary structure, allowing for the initiation of repeat-associated non-ATG (RAN) translation.^{62,63} Through this unconventional RAN translation the sense and antisense mRNA strands undergo translation in the absence of a start codon producing, depending on the reading frame, five unique DPR proteins; poly-GA, poly-GP, poly-GR, poly-PR, and poly-PA.^{62,64-67} In other words, the DPR proteins are synthesized based on a portion of the RNA sequence that is not typically used to produce a protein. Therefore, the DPR proteins are not an endogenous protein that has been mutated, but a completely new protein species introduced into the cell. This new species of proteins are known to be highly disordered, aggregation-prone, and highly toxic to neurons.^{56,68}

The mechanism of disease progression is convoluted for these diseases, but the decline in the proteostasis network and dysregulation of the ubiquitin-proteasome system (UPS) has been identified as a major contributing factor.⁶⁹⁻⁷² Evidence suggests that the accumulation of

aggregation-prone IDPs results in the formation of soluble oligomeric IDP aggregates that can allosterically inhibit the 26S and 20S proteasomes.⁷³ This impairment of 20S proteasome function decreases IDP degradation resulting in a self-reinforcing feedback loop leading to further accumulation of toxic aggregates, and ultimately the death of neurons.⁷³ This cascade associated with disease progression is depicted in Figure 1.3.

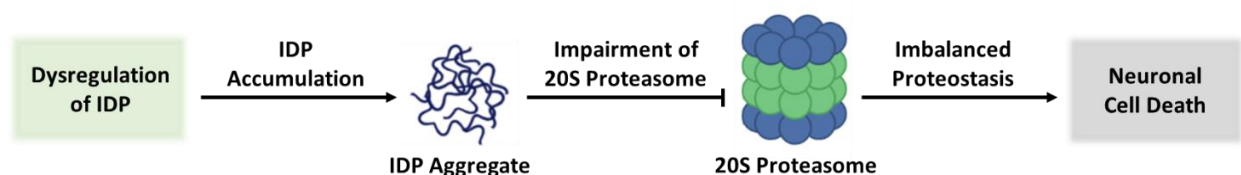


Figure 1.3 Schematic illustrating the cascade of disease progression that has been outlined implicating impairment of 20S proteasome function by the accumulation of IDP aggregates as a driver of neurodegenerative diseases.

While evidence suggests an allosteric mechanism of proteasome impairment, the mechanism by which IDP aggregates inhibit the proteasome has yet to be fully elucidated. Recently, a mechanistic model was proposed suggesting that IDP oligomers bind to the outer sides of the 20S core particle resulting in a conformational change.⁷³ It is proposed that this conformational change allosterically stabilizes the closed gate conformation of the 20S proteasome, restricting access of substrates to the proteolytic chamber for degradation.⁷³ Another recent study suggests that poly-GA DPR proteins entangle proteasomes into large ribbon-like aggregates, trapping them in a state of stalled degradation.⁷⁴ In the work discussed in Chapter 2, my efforts to elucidate the mechanism by which the poly-GR and poly-PR DPR proteins impair proteasome function will be discussed.

1.3.2 Imbalanced Proteostasis in Cancer

Decline in proteostasis and the accumulation of IDPs has also been implicated in the progression of a number of cancers.^{75,76} Extensive alterations in protein expression drive malignant transformation of cancer cells.⁷⁷ As cells transform to cancer cells, there are significant upregulations of many proteins, such as those that regulate cell survival and proliferation, cell migration, and metastasis.⁷⁷ This altered proteostasis and abnormally high levels of certain proteins found in cancer cells places a high burden on the UPS and other proteostasis

machinery.⁷⁸ This is to ensure limited resources in the cell, such as amino acids for protein synthesis, are maintained while maintaining cancer cell growth and survival.

In context of this work, the dysregulation of the transcription factor, c-MYC, and its role in oncogenesis will be discussed. Due to the strong growth-promoting and cell proliferative activities of c-MYC it is typically tightly regulated by the cell.¹⁶ Degradation of c-MYC protein through ubiquitin-dependent degradation by the UPS has shown to be the most prominent mechanism by which proper c-MYC protein levels are maintained.^{79,80} However, its ubiquitin-dependent degradation has shown to rely on a number of post-translational modifications to render it more susceptible to degradation by the UPS. For example, phosphorylation of certain amino acid residues has shown to be required for E3 ligase recognition of c-MYC and subsequent attachment of the poly-ubiquitin chain.^{79,81} Nonetheless, in a healthy cell this nuanced process allows proper c-MYC protein levels to be maintained in order to prevent uncontrolled cell proliferation as well as other c-MYC-mediated functions.

Dysregulation of c-MYC protein levels have shown to result from gene mutations of the MYC gene, such as gene amplification.⁸² Additionally, factors that impact c-MYC protein stability can result in an increase in c-MYC protein levels. For example, mutations of E3 ligases known to be responsible for the ubiquitination of c-MYC protein have been found in a number of cancers.^{79,83} These mutations inactivate their ability to ubiquitinate c-MYC protein, thereby preventing its ubiquitin-dependent degradation by the 26S proteasome.⁸³ Furthermore, alteration of cell signaling pathways are known to impact c-MYC protein stability through alteration of its post-translational modifications, such as its phosphorylation state for E3 ligase recognition.^{79,84,85} This dysregulation of c-MYC protein levels and its accumulation can induce its oncogenic transcriptional activity, resulting in the transcription of a number of genes that promote tumor growth and cancer cell proliferation.^{82,86} In fact, overexpression of c-MYC has been found in more than 70 percent of all human cancers, with a high prevalence in hematological cancers, such as acute lymphoblastic leukemia and multiple myeloma.^{87,88}

1.4 Pharmacological Targeting of IDPs in Disease

1.4.1 Drugging “Undruggable” Targets

Due to the noxious activities induced by their accumulation, IDPs are a highly sought after drug target. However, due to their disorder and lack of typical drug binding pockets they have evaded pharmacological targeting and been termed “undruggable” targets. Recent strategies designed to indirectly target IDPs have begun to show some success toward drugging these targets, and a few of them will be discussed here.

One of these approaches is through the use of small molecules or antibodies to prevent protein-protein interactions that result in toxic signaling. As previously discussed, the accumulation of amyloid- β aggregates has been implicated in the progression of Alzheimer’s disease.⁵² Recently, two monoclonal antibodies (i.e. Lecanemab and Aducanumab) have been FDA approved for the treatment of Alzheimer’s disease.⁸⁹ The monoclonal antibodies target soluble protofibril aggregates of amyloid- β to reduce its further fibrilization, resulting in significant reduction of amyloid plaques.⁹⁰ This reduction of aggregated amyloid plaques has shown to slow clinical decline in early Alzheimer's disease patients.⁹⁰ Similar disruption of protein-protein interactions as a treatment from c-MYC driven cancers has been explored using small molecules.^{91–93} The small molecules aim to interrupt the c-MYC-MAX heterodimerization necessary for its transcriptional activation to reduce c-MYC-promoted gene transcription and its oncogenic signaling.⁹²

Antisense oligonucleotides (ASOs) are also being explored for the treatment of diseases associated with toxic protein accumulation, however, instead of targeting the protein, the mRNA sequence that encodes the protein is targeted using this strategy.^{94,95} ASOs are small single-stranded DNA oligomers that bind a target mRNA sequence.⁹⁵ Depending on the design of the ASO, gene expression is modulated through several distinct mechanisms. For example, some ASOs work through degrading the target mRNA. Once the RNA-DNA complex forms, it recruits the enzyme RNase H to cleave the target mRNA.⁹⁵ By degrading the gene target, the gene will not be translated into a protein, and over time levels of the protein product is reduced. Another strategy uses an ASO to target the mRNA sequence around the start codon to block binding of ribosomal subunits to suppress translation of the target mRNA.⁹⁵ Excitingly, a number of ASO

therapies for ALS are currently under investigation with ASOs that target *SOD1*, *C9orf72*, and *FUS* genes in clinical trials.⁹⁴ In 2023, the FDA approved the ASO Tofersen for the treatment of SOD1-associated ALS cases. ASOs have also been explored to reduce *MYC* translation, with promising studies showing ASO treatment decreases *MYC* mRNA and protein levels, reducing cancer cell proliferation.⁹⁶

Lastly, targeted protein degradation utilizing proteolysis-targeting chimera (PROTAC) molecules are under investigation for reducing IDP levels. PROTACs are a class of heterobifunctional small molecules that consist of two ligands joined by a linker.⁹⁷ One ligand binds a protein to target for degradation, and the other ligand binds an E3 ubiquitin ligase. The simultaneous binding of the target protein and E3 ligase induces the ubiquitination of the target protein and its subsequent ubiquitin-dependent degradation by the UPS.⁹⁷ Development of a PROTAC to target toxic TDP-43 aggregates implicated in the progression of certain forms of ALS is being studied to assess its therapeutic potential. In a recent study, a PROTAC targeting TDP-43 aggregates has shown to effectively induce their ubiquitination and degradation by the UPS.⁹⁸ This translated to a decrease in TDP-43 oligomers in a cellular model and reduced their associated toxicity.⁹⁸ This targeted protein degradation strategy has been employed against c-MYC in an attempt to reduce its anticancer effects. In a recent study, a PROTAC was designed to bind the c-MYC-MAX heterodimer to enhance its degradation, which resulted in inhibition of cancer cell proliferation.⁹⁹

These possible therapeutic strategies offer great hope for the treatment of these devastating diseases. However, additional work is required to further explore these approaches as most are still under development and not yet approved for clinical use. Nonetheless, these studies have validated the idea of targeting IDPs to reduce their accumulation as a potential treatment for these proteotoxic diseases. In the work described in this dissertation, our efforts to develop a unique therapeutic approach to reduce IDP accumulation through a novel mechanism, and its potential use for the treatment of IDP-driven diseases will be discussed.

1.5 Small Molecule Activation of the 20S Proteasome

1.5.1 Pharmacological Regulation of IDPs Through Enhanced Degradation

Due to the highly disordered nature of IDPs, they have been identified as 20S proteasome substrates. Therefore, to pharmacologically regulate these “undruggable” proteins we hypothesize an alternative approach through enhancement of their 20S proteasome-mediated degradation. Small molecule activation of the 20S proteasome is an emerging strategy able to prevent the accumulation of IDPs and the toxicity associated with IDP accumulation.^{100–107} While the 20S proteasome is typically found in a low activity, closed gate conformation, small molecule 20S activators increase the rate of proteolytic activity of the 20S proteasome. This increase in activity has shown to result in enhanced 20S proteasome-mediated degradation of IDPs, thereby preventing their accumulation and associated toxicities.^{100,108}

Exploration of the mechanism by which small molecule 20S activators work have been investigated using the Tepe lab’s first identified 20S activator, TCH-165.¹⁰⁰ The small molecule TCH-165 has shown to potently enhance the rate of proteolytic activity of the 20S proteasome with an effective concentration to obtain a two-fold rate enhancement of 20S activity, EC_{200} , of 1.3 μ M.¹⁰⁰ This increased rate of proteolytic activity has shown to enhance the 20S proteasome-mediated degradation of a number of IDPs associated with disease both in purified protein assays and in cell culture (e.g. α -synuclein, tau441, c-Fos), and is well tolerated *in vivo*.^{100,108} Utilizing atomic force microscopy it was shown that TCH-165 induces an open gate conformation of the 20S proteasome (Figure 1.4B),¹⁰⁰ suggesting that enhanced proteolytic activity is the result of the induction of an open gate conformation.

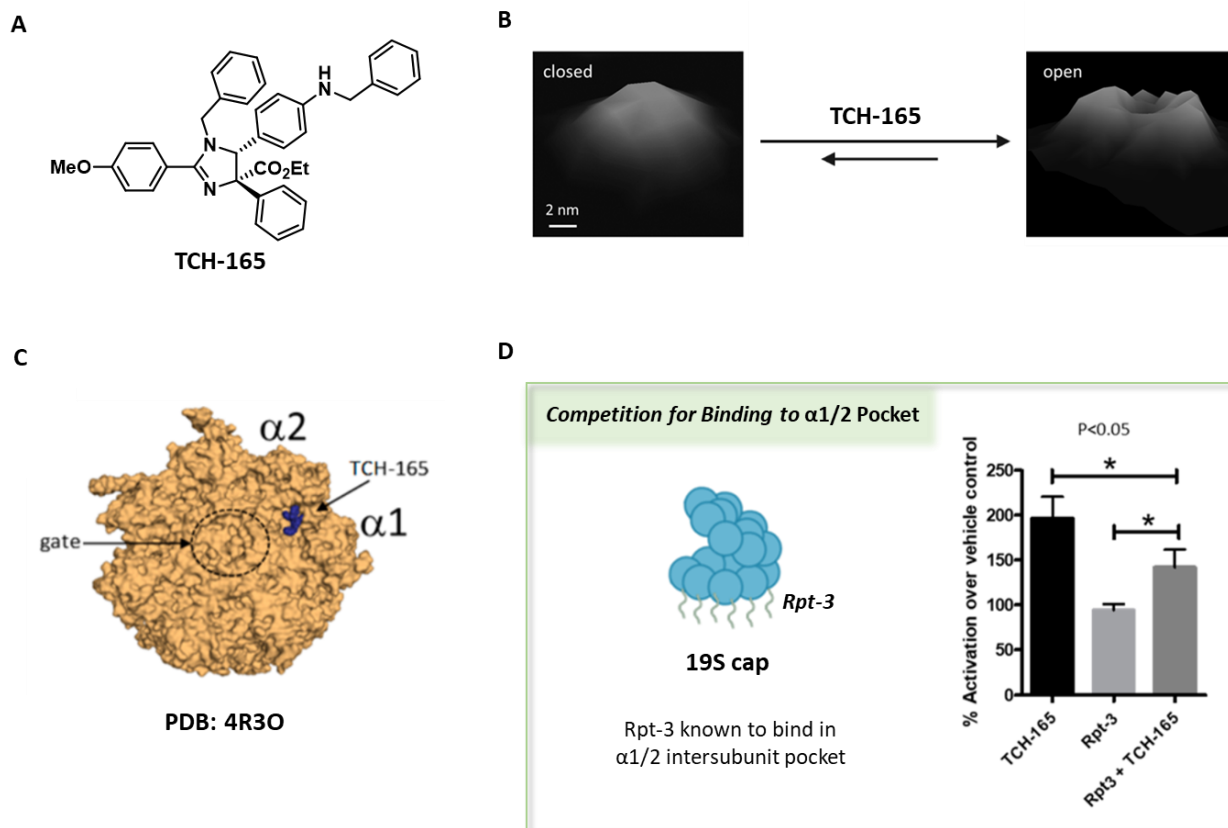


Figure 1.4 Previously published mechanistic data for 20S proteasome activator, TCH-165. (A) Structure of TCH-165. (B) Atomic force microscopy images show TCH-165 induces an open gate conformation of the 20S proteasome, significantly increasing the number of open gate 20S proteasomes. (C) TCH-165 is predicted to bind in the $\alpha 1/2$ intersubunit pocket of the 20S proteasome (top-view; PDB ID: 4R30). (D) The Rpt-3 tail (2 μM) reduces the ability of TCH-165 (1 μM) to enhance proteolysis of a protein substrate. Figure is adapted from Njomen et al.¹⁰⁰

The induction of this open gate conformation is analogous to how the endogenous protein regulatory caps, such as the 19S, activate the 20S proteasome. To bind to the 20S proteasome, the 19S cap binds into the intersubunit pockets between the α -subunits using an HbYX tail motif.⁴¹ Upon docking of the 19S cap, an ATP-dependent conformational change occurs opening the gate to the proteolytic core and allowing for increased substrate access to the proteolytic sites.^{41,42} While the binding site of TCH-165 and other small molecule 20S proteasome activators has yet to be elucidated, molecular docking studies have predicted that TCH-165 binds in the $\alpha 1/2$ intersubunit pocket of the α -ring of the 20S proteasome (Figure 1.4C).¹⁰⁰ Therefore, it is hypothesized that the small molecules mimic binding of the 19S cap to induce an open gate conformation of the 20S proteasome and enhance proteolytic activity.

Additional support for this docking model was obtained through a competition experiment between TCH-165 and the Rpt-3 tail of the 19S cap that is known to dock into the α 1/2 intersubunit pocket (Figure 1.4D). Results of this experiment showed that treatment of purified 20S proteasome with TCH-165 resulted in almost a 200 percent increase in 20S proteasome activity compared to the vehicle control, while treatment with Rpt-3 had no effect on activity.¹⁰⁰ However, treatment of 20S proteasome with both TCH-165 and Rpt-3, significantly reduced the ability of TCH-165 to enhance 20S proteasome activity. These results suggest that TCH-165 and Rpt-3 of the 19S cap compete for binding. However, whether this is through competitive or non-competitive binding cannot be determined from this assay. While a number of studies support the idea that TCH-165 binds into the α 1/2 intersubunit pocket of the α -ring, the binding site of a small molecule 20S proteasome activator has yet to be elucidated. Efforts to solve a ligand-bound 20S proteasome structure using cryogenic electron microscopy (cryo-EM) will be discussed in Chapter 2. Furthermore, continued exploration of this therapeutic strategy is underway to identify additional 20S proteasome activator scaffolds, identify novel therapeutic applications, and further investigate the mechanism of this exciting strategy. In all, this therapeutic strategy shows great promise for the treatment of diseases in which IDP accumulation is implicated in its pathogenesis.

1.5.2 20S Proteasome Activation as a Novel Therapeutic Strategy for the Treatment of Neurodegenerative Diseases and Cancers

The work in this dissertation will assess the therapeutic potential of this strategy for the treatment of neurodegenerative diseases (Part One) and cancers (Part Two). As the goal is to rescue cells from death in neurodegenerative diseases and kill cells in cancer treatment, this seems quite counterintuitive. However, if you consider the implications of reducing the amount of a specific IDP in each disease, thereby decreasing its function, it suggests the strategy may be efficacious for the treatment of both diseases.

While the mechanism of perturbed proteostasis differs between neurodegenerative diseases and cancers, each class of disease has shown to critically burden the proteostasis network. In the case of neurodegenerative diseases, the accumulation of aggregation-prone IDPs results in the formation of soluble oligomeric IDP aggregates that impair UPS function. This

impairment of proteasome function decreases IDP degradation resulting in a self-reinforcing feedback loop leading to further accumulation of toxic aggregates, and ultimately the death of neurons.⁷³ In cancer, the accumulation of IDPs, such as transcription factors, induce its oncogenic transcriptional activity, resulting in the transcription of a number of genes that promote tumor growth and cancer cell proliferation.^{82,86} While the IDPs that accumulate in cancer have not shown to aggregate or inhibit the proteasome through a direct binding interaction, as observed in neurodegenerative diseases, imbalanced proteostasis is still observed. Instead, their accumulation induces aberrant transcriptional activity resulting in the production of abnormally high levels of proteins that regulate cell survival and proliferation, cell migration, and metastasis.⁷⁷ This altered protein abundance in the cell places a high burden on the UPS and other proteostasis machinery.

Since IDP accumulation is at the heart of disease pathogenesis for both classes of disease, I hypothesize that enhanced degradation of these noxious IDPs through small molecule activation of the 20S proteasome may offer a novel therapeutic treatment for neurodegenerative diseases and cancers. By enhancing the 20S proteasome-mediated degradation of IDPs associated with the progression of neurodegenerative diseases, like the DPR proteins, I anticipate their decreased accumulation will reduce or prevent their ability to impair UPS function and alleviate the associated toxicities. Through enhanced 20S proteasome-mediated degradation of IDPs associated with the progression of cancer, like c-MYC, I hypothesize its reduced accumulation could prevent its promotion of cancer cell proliferation and tumor growth.

1.6 Conclusion

Disruption of proteostasis and the accumulation of IDPs has been implicated in the progression of a number of neurodegenerative diseases and cancers. The restoration of proteostasis to regain normal cellular functions is imperative to intercept the progression of these diseases. Small molecule activation of the 20S proteasome is an emerging strategy able to prevent the accumulation of IDPs and the toxicity associated with IDP accumulation.^{100–107} Therefore, this approach offers great promise for restoring proteostasis in proteotoxic diseases, and suggests it has great potential as a novel therapeutic strategy. This dissertation focuses on further exploration of this therapeutic strategy and work done to identify additional 20S

proteasome activators, investigate the therapeutic mechanism, and identify novel therapeutic applications.

In Chapter 2, I will discuss my work to identify novel therapeutic applications of this strategy, as well as my investigations into the binding site of 20S proteasome activators. In Chapter 3, my identification of a new 20S proteasome activator scaffold and the design, synthesis and biological activity of novel analogues synthesized will be discussed. Exploration of this scaffold also led to insightful studies into the mechanism of small molecule 20S proteasome activation that will be discussed in this chapter. In Chapters 4 and 5, the potential of modulating 20S proteasome activity as a novel therapeutic strategy for cancers will be assessed. Specifically, in Chapter 5, the ability of TCH-165 to reduce cellular c-MYC protein levels and reduce oncogenic signaling events caused by its overexpression and accumulation will be examined.

REFERENCES

- (1) Jayaraj, G. G.; Hipp, M. S.; Hartl, F. U. Functional Modules of the Proteostasis Network. *Cold Spring Harbor Perspectives in Biology* **2020**, *12* (1), a033951.
- (2) Klaipts, C. L.; Jayaraj, G. G.; Hartl, F. U. Pathways of Cellular Proteostasis in Aging and Disease. *The Journal of Cell Biology* **2018**, *217* (1), 51–63.
- (3) Hipp, M. S.; Kasturi, P.; Hartl, F. U. The Proteostasis Network and Its Decline in Ageing. *Nature Reviews Molecular Cell Biology* **2019**, *20* (7), 421–435.
- (4) Kim, Y. E.; Hipp, M. S.; Bracher, A.; Hayer-Hartl, M.; Hartl, F. U. Molecular Chaperone Functions in Protein Folding and Proteostasis. *Annual Review of Biochemistry* **2013**, *82*, 323–355.
- (5) Dikic, I. Proteasomal and Autophagic Degradation Systems. *Annual Review of Biochemistry* **2017**, *86* (1), 193–224.
- (6) Gidalevitz, T.; Ben-Zvi, A.; Ho, K. H.; Brignull, H. R.; Morimoto, R. I. Progressive Disruption of Cellular Protein Folding in Models of Polyglutamine Diseases. *Science* **2006**, *311* (5766), 1471–1474.
- (7) Sies, H.; Berndt, C.; Jones, D. P. Oxidative Stress. *Annual Review of Biochemistry* **2017**, *86* (1), 715–748.
- (8) Taylor, R. C.; Dillin, A. Aging as an Event of Proteostasis Collapse. *Cold Spring Harbor Perspectives in Biology* **2011**, *3* (5), 1–17.
- (9) Labbadia, J.; Morimoto, R. I. The Biology of Proteostasis in Aging and Disease. *Annual Review of Biochemistry* **2015**, *84*, 435–464.
- (10) Dunker, A. K.; Lawson, J. D.; Brown, C. J.; Williams, R. M.; Romero, P.; Oh, J. S.; Oldfield, C. J.; Campen, A. M.; Ratliff, C. M.; Hipps, K. W.; Ausio, J.; Nissen, M. S.; Reeves, R.; Kang, C.; Kissinger, C. R.; Bailey, R. W.; Griswold, M. D.; Chiu, W.; Garner, E. C.; Obradovic, Z. Intrinsically Disordered Protein. *Journal of Molecular Graphics and Modelling* **2001**, *19* (1), 26–59.
- (11) Trivedi, R.; Nagarajaram, H. A. Intrinsically Disordered Proteins: An Overview. *International Journal of Molecular Sciences* **2022**, *23* (22), 14050.
- (12) Jorda, J.; Xue, B.; Uversky, V. N.; Kajava, A. V. Protein Tandem Repeats - the More Perfect, the Less Structured. *The FEBS Journal* **2010**, *277* (12), 2673–2682.
- (13) Uversky, V. N. Intrinsically Disordered Proteins and Their “Mysterious” (Meta)Physics. *Frontiers in Physics* **2019**, *7*, 1–18.
- (14) Bondos, S. E.; Dunker, A. K.; Uversky, V. N. Intrinsically Disordered Proteins Play Diverse Roles in Cell Signaling. *Cell Communication and Signaling* **2022**, *20* (1), 20.
- (15) Wright, P. E.; Dyson, H. J. Intrinsically Disordered Proteins in Cellular Signaling and Regulation. *Nature Reviews Molecular Cell Biology* **2015**, *16* (1), 18–29.

- (16) Kumar, S. K.; Rajkumar, V.; Kyle, R. A.; van Duin, M.; Sonneveld, P.; Mateos, M.-V.; Gay, F.; Anderson, K. C. Multiple Myeloma. *Nature Reviews Disease Primers* **2017**, *3* (1), 1–20.
- (17) Carroll, P. A.; Freie, B. W.; Mathsyaraja, H.; Eisenman, R. N. The MYC Transcription Factor Network: Balancing Metabolism, Proliferation and Oncogenesis. *Frontiers of Medicine* **2018**, *12* (4), 412–425.
- (18) Fisher, F.; Crouch, D. H.; Jayaraman, P. S.; Clark, W.; Gillespie, D. A.; Goding, C. R. Transcription Activation by Myc and Max: Flanking Sequences Target Activation to a Subset of CACGTG Motifs in Vivo. *The EMBO Journal* **1993**, *12* (13), 5075–5082.
- (19) Babu, M. M.; van der Lee, R.; de Groot, N. S.; Gsponer, J. Intrinsically Disordered Proteins: Regulation and Disease. *Current Opinion in Structural Biology* **2011**, *21* (3), 432–440.
- (20) Edwards, Y. J.; Lobley, A. E.; Pentony, M. M.; Jones, D. T. Insights into the Regulation of Intrinsically Disordered Proteins in the Human Proteome by Analyzing Sequence and Gene Expression Data. *Genome Biology* **2009**, *10* (5), R50.
- (21) Pérez-Ortín, J. E.; Alepuz, P. M.; Moreno, J. Genomics and Gene Transcription Kinetics in Yeast. *Trends in Genetics* **2007**, *23* (5), 250–257.
- (22) Tompa, P.; Prilusky, J.; Silman, I.; Sussman, J. L. Structural Disorder Serves as a Weak Signal for Intracellular Protein Degradation. *Proteins* **2008**, *71* (2), 903–909.
- (23) Asher, G.; Reuven, N.; Shaul, Y. 20S Proteasomes and Protein Degradation “by Default.” *BioEssays* **2006**, *28* (8), 844–849.
- (24) Tsvetkov, P.; Reuven, N.; Shaul, Y. The Nanny Model for IDPs. *Nature Chemical Biology* **2009**, *5* (11), 778–781.
- (25) Borg, M.; Mittag, T.; Pawson, T.; Tyers, M.; Forman-Kay, J. D.; Chan, H. S. Polyelectrostatic Interactions of Disordered Ligands Suggest a Physical Basis for Ultrasensitivity. *Proceedings of the National Academy of Sciences* **2007**, *104* (23), 9650–9655.
- (26) Ben-Nissan, G.; Sharon, M. Regulating the 20S Proteasome Ubiquitin-Independent Degradation Pathway. *Biomolecules* **2014**, *4* (3), 862–884.
- (27) Erales, J.; Coffino, P. Ubiquitin-Independent Proteasomal Degradation. *Biochimica et Biophysica Acta* **2014**, *1843* (1), 216–221.
- (28) Höhn, T. J. A.; Grune, T. The Proteasome and the Degradation of Oxidized Proteins: Part III—Redox Regulation of the Proteasomal System. *Redox Biology* **2014**, *2*, 388–394.
- (29) Jung, T.; Höhn, A.; Grune, T. The Proteasome and the Degradation of Oxidized Proteins: Part II – Protein Oxidation and Proteasomal Degradation. *Redox Biology* **2014**, *2*, 99–104.
- (30) Tanaka, K.; Mizushima, T.; Saeki, Y. The Proteasome: Molecular Machinery and Pathophysiological Roles. *Biological Chemistry* **2012**, *393* (4), 217–234.
- (31) Groll, M.; Ditzel, L.; Lowe, J.; Stock, D.; Bochtler, M.; Bartunik, H. D. Structure of 20S Proteasome from Yeast at 2.4Å Resolution. *Nature* **1997**, *386* (6624), 463–471.

- (32) Thibaudeau, T. A.; Smith, D. M. A Practical Review of Proteasome Pharmacology. *Pharmacological Reviews* **2019**, *71* (2), 170–197.
- (33) Borissenko, L.; Groll, M. 20S Proteasome and Its Inhibitors: Crystallographic Knowledge for Drug Development. *Chemical Reviews* **2007**, *107* (3), 687–717.
- (34) Arendt, C. S.; Hochstrasser, M. Identification of the Yeast 20S Proteasome Catalytic Centers and Subunit Interactions Required for Active-Site Formation. *Proceedings of the National Academy of Sciences of the United States of America* **1997**, *94* (14), 7156.
- (35) Voges, D.; Zwickl, P.; Baumeister, W. The 26S Proteasome: A Molecular Machine Designed for Controlled Proteolysis. *Annual Review of Biochemistry* **1999**, *68* (1), 1015–1068.
- (36) Finley, D.; Chen, X.; Walters, K. J. Gates, Channels, and Switches: Elements of the Proteasome Machine. *Trends in Biochemical Sciences* **2016**, *41* (1), 77–93.
- (37) Groll, M.; Bajorek, M.; Köhler, A.; Moroder, L.; Rubin, D. M.; Huber, R.; Glickman, M. H.; Finley, D. A Gated Channel into the Proteasome Core Particle. *Nature Structural Biology* **2000**, *7* (11), 1062–1067.
- (38) Köhler, A.; Cascio, P.; Leggett, D. S.; Woo, K. M.; Goldberg, A. L.; Finley, D. The Axial Channel of the Proteasome Core Particle Is Gated by the Rpt2 ATPase and Controls Both Substrate Entry and Product Release. *Molecular Cell* **2001**, *7* (6), 1143–1152.
- (39) Religa, T. L.; Sprangers, R.; Kay, L. E. Dynamic Regulation of Archaeal Proteasome Gate Opening As Studied by TROSY NMR. *Science* **2010**, *328* (5974), 98–102.
- (40) Ruschak, A. M.; Kay, L. E. Proteasome Allostery as a Population Shift between Interchanging Conformers. *Proceedings of the National Academy of Sciences* **2012**, *109* (50), E3454–E3462.
- (41) Smith, D. M.; Chang, S.-C.; Park, S.; Finley, D.; Cheng, Y.; Goldberg, A. Docking of the Proteasomal ATPases' C-Termini in the 20S Proteasomes Alpha Ring Opens the Gate for Substrate Entry. *Molecular Cell* **2007**, *27* (5), 731–744.
- (42) Rabl, J.; Smith, D. M.; Yu, Y.; Chang, S.-C.; Goldberg, A. L.; Cheng, Y. Mechanism of Gate Opening in the 20S Proteasome by the Proteasomal ATPases. *Molecular Cell* **2008**, *30* (3), 360–368.
- (43) Opoku-Nsiah, K. A.; de la Pena, A. H.; Williams, S. K.; Chopra, N.; Sali, A.; Lander, G. C.; Gestwicki, J. E. The YΦ Motif Defines the Structure-Activity Relationships of Human 20S Proteasome Activators. *Nature Communications* **2022**, *13* (1), 1226.
- (44) Grice, G. L.; Nathan, J. A. The Recognition of Ubiquitinated Proteins by the Proteasome. *Cellular and Molecular Life Sciences* **2016**, *73*, 3497–3506.
- (45) Ciechanover, A.; Schwartz, A. L. The Ubiquitin-Proteasome Pathway: The Complexity and Myriad Functions of Proteins Death. *Proceedings of the National Academy of Sciences of the United States of America* **1998**, *95* (6), 2727–2730.
- (46) Kwon, Y. T.; Ciechanover, A. The Ubiquitin Code in the Ubiquitin-Proteasome System and Autophagy. *Trends in Biochemical Sciences* **2017**, *42* (11), 873–886.

- (47) Wang, X.; Herr, R. A.; Hansen, T. H. Ubiquitination of Substrates by Esterification. *Traffic* **2012**, *13* (1), 19–24.
- (48) Thrower, J. S.; Hoffman, L.; Rechsteiner, M.; Pickart, C. M. Recognition of the Polyubiquitin Proteolytic Signal. *The EMBO Journal* **2000**, *19* (1), 94–102.
- (49) de Poot, S. A. H.; Tian, G.; Finley, D. Meddling with Fate: The Proteasomal Deubiquitinating Enzymes. *Journal of Molecular Biology* **2017**, *429* (22), 3525–3545.
- (50) Biran, A.; Myers, N.; Adler, J.; Broennimann, K.; Reuven, N.; Shaul, Y. A 20S Proteasome Receptor for Degradation of Intrinsically Disordered Proteins. *bioRxiv* **2017**, 210898.
- (51) Vilchez, D.; Saez, I.; Dillin, A. The Role of Protein Clearance Mechanisms in Organismal Ageing and Age-Related Diseases. *Nature Communications* **2014**, *5* (5659), 1–13.
- (52) Selkoe, D. J. Alzheimer's Disease. *Cold Spring Harbor Perspectives in Biology* **2011**, *3* (7), 1–16.
- (53) Bosco, D. A.; LaVoie, M. J.; Petsko, G. A.; Ringe, D. Proteostasis and Movement Disorders: Parkinson's Disease and Amyotrophic Lateral Sclerosis. *Cold Spring Harbor Perspectives in Biology* **2011**, *3* (10), 1–24.
- (54) Finkbeiner, S. Huntington's Disease. *Cold Spring Harbor Perspectives in Biology* **2011**, *3* (6), 1–23.
- (55) Uversky, V. N. Wrecked Regulation of Intrinsically Disordered Proteins in Diseases: Pathogenicity of Deregulated Regulators. *Frontiers in Molecular Biosciences* **2014**, *1* (6), 1–24.
- (56) Gupta, R.; Lan, M.; Mojsilovic-Petrovic, J.; Choi, W. H.; Safren, N.; Barmada, S.; Lee, M. J.; Kalb, R. The Proline/Arginine Dipeptide from Hexanucleotide Repeat Expanded C9ORF72 Inhibits the Proteasome. *eNeuro* **2017**, *4* (1), 1–18.
- (57) Santamaria, N.; Alhothali, M.; Alfonso, M. H.; Breydo, L.; Uversky, V. N. Intrinsic Disorder in Proteins Involved in Amyotrophic Lateral Sclerosis. *Cellular and Molecular Life Sciences* **2017**, *74* (7), 1297–1318.
- (58) Hayashi, Y.; Homma, K.; Ichijo, H. SOD1 in Neurotoxicity and Its Controversial Roles in SOD1 Mutation-Negative ALS. *Advances in Biological Regulation* **2016**, *60*, 95–104.
- (59) Münch, C.; Bertolotti, A. Exposure of Hydrophobic Surfaces Initiates Aggregation of Diverse ALS-Causing Superoxide Dismutase-1 Mutants. *Journal of Molecular Biology* **2010**, *399* (3), 512–525.
- (60) DeJesus-Hernandez, M.; Mackenzie, I.; Boeve, B.; Boxer, A.; Baker, M.; Rutherford, N.; Nicholson, A.; Finch, N.; Flynn Gilmer, H.; Adamson, J.; Kouri, N.; Wojtas, A.; Sengdy, P.; Hsiung, G.-Y.; Karydas, A.; Seeley, W.; Josephs, K.; Coppola, G.; Geschwind, D.; Wszolek, Z.; Feldman, H.; Knopman, D.; Petersen, R.; Miller, B.; Dickson, D.; Boylan, K.; Graff-Radford, N.; Rademakers, R. Expanded GGGGCC Hexanucleotide Repeat in Non-Coding Region of C9ORF72 Causes Chromosome 9p-Linked Frontotemporal Dementia and Amyotrophic Lateral Sclerosis. *Neuron* **2011**, *72* (2), 245–256.

- (61) Renton, A. E.; Majounie, E.; Waite, A.; Simón-Sánchez, J.; Rollinson, S.; Gibbs, J. R.; Schymick, J. C.; Laaksovirta, H.; van Swieten, J. C.; Myllykangas, L.; Kalimo, H.; Paetau, A.; Abramzon, Y.; Remes, A. M.; Kaganovich, A.; Scholz, S. W.; Duckworth, J.; Ding, J.; Harmer, D. W.; Hernandez, D. G.; Johnson, J. O.; Mok, K.; Ryten, M.; Trabzuni, D.; Guerreiro, R. J.; Orrell, R. W.; Neal, J.; Murray, A.; Pearson, J.; Jansen, I. E.; Sondervan, D.; Seelaar, H.; Blake, D.; Young, K.; Halliwell, N.; Callister, J. B.; Toulson, G.; Richardson, A.; Gerhard, A.; Snowden, J.; Mann, D.; Neary, D.; Nalls, M. A.; Peuralinna, T.; Jansson, L.; Isoviita, V.-M.; Kaivorinne, A.-L.; Hölttä-Vuori, M.; Ikonen, E.; Sulkava, R.; Benatar, M.; Wu, J.; Chiò, A.; Restagno, G.; Borghero, G.; Sabatelli, M.; ITALSGEN Consortium; Heckerman, D.; Rogaeva, E.; Zinman, L.; Rothstein, J. D.; Sendtner, M.; Drepper, C.; Eichler, E. E.; Alkan, C.; Abdullaev, Z.; Pack, S. D.; Dutra, A.; Pak, E.; Hardy, J.; Singleton, A.; Williams, N. M.; Heutink, P.; Pickering-Brown, S.; Morris, H. R.; Tienari, P. J.; Traynor, B. J. A Hexanucleotide Repeat Expansion in C9ORF72 Is the Cause of Chromosome 9p21-Linked ALS-FTD. *Neuron* **2011**, *72* (2), 257–268.
- (62) Ash, P. E. A.; Bieniek, K. F.; Gendron, T. F.; Caulfield, T.; Lin, W.-L.; DeJesus-Hernandez, M.; van Blitterswijk, M. M.; Jansen-West, K.; Paul, J. W.; Rademakers, R.; Boylan, K. B.; Dickson, D. W.; Petrucelli, L. Unconventional Translation of C9ORF72 GGGGCC Expansion Generates Insoluble Polypeptides Specific to C9FTD/ALS. *Neuron* **2013**, *77* (4), 639–646.
- (63) Zu, T.; Gibbens, B.; Doty, N. S.; Gomes-Pereira, M.; Huguet, A.; Stone, M. D.; Margolis, J.; Peterson, M.; Markowski, T. W.; Ingram, M. A. C.; Nan, Z.; Forster, C.; Low, W. C.; Schoser, B.; Somia, N. V.; Clark, H. B.; Schmechel, S.; Bitterman, P. B.; Gourdon, G.; Swanson, M. S.; Moseley, M.; Ranum, L. P. W. Non-ATG-Initiated Translation Directed by Microsatellite Expansions. *Proceedings of the National Academy of Sciences of the United States of America* **2011**, *108* (1), 260–265.
- (64) Mori, K.; Weng, S.-M.; Arzberger, T.; May, S.; Rentzsch, K.; Kremmer, E.; Schmid, B.; Kretschmar, H. A.; Cruts, M.; Broeckhoven, C. V.; Haass, C.; Edbauer, D. The C9orf72 GGGGCC Repeat Is Translated into Aggregating Dipeptide-Repeat Proteins in FTLD/ALS. *Science* **2013**, *339* (6125), 1335–1338.
- (65) Zu, T.; Liu, Y.; Bañez-Coronel, M.; Reid, T.; Pletnikova, O.; Lewis, J.; Miller, T. M.; Harms, M. B.; Falchook, A. E.; Subramony, S. H.; Ostrow, L. W.; Rothstein, J. D.; Troncoso, J. C.; Ranum, L. P. W. RAN Proteins and RNA Foci from Antisense Transcripts in C9ORF72 ALS and Frontotemporal Dementia. *Proceedings of the National Academy of Sciences of the United States of America* **2013**, *110* (51), E4968-4977.
- (66) Gendron, T. F.; Bieniek, K. F.; Zhang, Y.-J.; Jansen-West, K.; Ash, P. E. A.; Caulfield, T.; Daugherty, L.; Dunmore, J. H.; Castanedes-Casey, M.; Chew, J.; Cosio, D. M.; van Blitterswijk, M.; Lee, W. C.; Rademakers, R.; Boylan, K. B.; Dickson, D. W.; Petrucelli, L. Antisense Transcripts of the Expanded C9ORF72 Hexanucleotide Repeat Form Nuclear RNA Foci and Undergo Repeat-Associated Non-ATG Translation in C9FTD/ALS. *Acta Neuropathologica* **2013**, *126* (6), 829–844.

- (67) Mori, K.; Arzberger, T.; Grässer, F. A.; Gijssels, I.; May, S.; Rentzsch, K.; Weng, S.-M.; Schludi, M. H.; van der Zee, J.; Cruts, M.; Van Broeckhoven, C.; Kremmer, E.; Kretzschmar, H. A.; Haass, C.; Edbauer, D. Bidirectional Transcripts of the Expanded C9orf72 Hexanucleotide Repeat Are Translated into Aggregating Dipeptide Repeat Proteins. *Acta Neuropathologica* **2013**, *126* (6), 881–893.
- (68) Yamakawa, M.; Ito, D.; Honda, T.; Kubo, K.; Noda, M.; Nakajima, K.; Suzuki, N. Characterization of the Dipeptide Repeat Protein in the Molecular Pathogenesis of C9FTD/ALS. *Human Molecular Genetics* **2015**, *24* (6), 1630–1645.
- (69) Brettschneider, J.; Del Tredici, K.; Lee, V. M.-Y.; Trojanowski, J. Q. Spreading of Pathology in Neurodegenerative Diseases: A Focus on Human Studies. *Nature Reviews Neuroscience* **2015**, *16* (2), 109–120.
- (70) Rubinsztein, D. C. The Roles of Intracellular Protein-Degradation Pathways in Neurodegeneration. *Nature* **2006**, *443* (7113), 780–786.
- (71) Selkoe, D. J. Folding Proteins in Fatal Ways. *Nature* **2003**, *426* (6968), 900–904.
- (72) Ciechanover, A.; Brundin, P. The Ubiquitin Proteasome System in Neurodegenerative Diseases: Sometimes the Chicken, Sometimes the Egg. *Neuron* **2003**, *40* (2), 427–446.
- (73) Thibautaud, T. A.; Anderson, R. T.; Smith, D. M. A Common Mechanism of Proteasome Impairment by Neurodegenerative Disease-Associated Oligomers. *Nature Communications* **2018**, *9* (1), 1–14.
- (74) Guo, Q.; Lehmer, C.; Martínez-Sánchez, A.; Rudack, T.; Beck, F.; Hartmann, H.; Pérez-Berlanga, M.; Frottin, F.; Hipp, M. S.; Hartl, F. U.; Edbauer, D.; Baumeister, W.; Fernández-Busnadiego, R. In Situ Structure of Neuronal C9orf72 Poly-GA Aggregates Reveals Proteasome Recruitment. *Cell* **2018**, *172* (4), 696–705.
- (75) Santofimia-Castaño, P.; Rizzuti, B.; Xia, Y.; Abian, O.; Peng, L.; Velázquez-Campoy, A.; Neira, J. L.; Iovanna, J. Targeting Intrinsically Disordered Proteins Involved in Cancer. *Cellular and Molecular Life Sciences* **2020**, *77* (9), 1695–1707.
- (76) Dang, C. V.; Reddy, E. P.; Shokat, K. M.; Soucek, L. Drugging the “undruggable” Cancer Targets. *Nature Reviews Cancer* **2017**, *17* (8), 502–508.
- (77) Pessoa, J.; Martins, M.; Casimiro, S.; Pérez-Plasencia, C.; Shoshan-Barmatz, V. Editorial: Altered Expression of Proteins in Cancer: Function and Potential Therapeutic Targets. *Frontiers in Oncology* **2022**, *12*, 1–6.
- (78) Tsvetkov, P.; Adler, J.; Myers, N.; Biran, A.; Reuven, N.; Shaul, Y. Oncogenic Addiction to High 26S Proteasome Level. *Cell Death & Disease* **2018**, *9* (7), 1–14.
- (79) Farrell, A. S.; Sears, R. C. MYC Degradation. *Cold Spring Harbor Perspectives in Medicine* **2014**, *4* (3), 1–15.
- (80) Thomas, L. R.; Tansey, W. P. Proteolytic Control of the Oncoprotein Transcription Factor Myc. In *Advances in Cancer Research*; Klein, G., Ed.; Academic Press, 2011; Vol. 110, pp 77–106.

- (81) Vervoorts, J.; Lüscher-Firzlaff, J.; Lüscher, B. The Ins and Outs of MYC Regulation by Posttranslational Mechanisms. *Journal of Biological Chemistry* **2006**, *281* (46), 34725–34729.
- (82) Kalkat, M.; De Melo, J.; Hickman, K. A.; Lourenco, C.; Redel, C.; Resetca, D.; Tamachi, A.; Tu, W. B.; Penn, L. Z. MYC Deregulation in Primary Human Cancers. *Genes* **2017**, *8* (6), 151.
- (83) O’Neil, J.; Grim, J.; Strack, P.; Rao, S.; Tibbitts, D.; Winter, C.; Hardwick, J.; Welcker, M.; Meijerink, J. P.; Pieters, R.; Draetta, G.; Sears, R.; Clurman, B. E.; Look, A. T. FBW7 Mutations in Leukemic Cells Mediate NOTCH Pathway Activation and Resistance to γ -Secretase Inhibitors. *Journal of Experimental Medicine* **2007**, *204* (8), 1813–1824.
- (84) Bahram, F.; von der Lehr, N.; Cetinkaya, C.; Larsson, L. G. C-Myc Hot Spot Mutations in Lymphomas Result in Inefficient Ubiquitination and Decreased Proteasome-Mediated Turnover. *Blood* **2000**, *95* (6), 2104–2110.
- (85) Gregory, M. A.; Hann, S. R. C-Myc Proteolysis by the Ubiquitin-Proteasome Pathway: Stabilization of c-Myc in Burkitt’s Lymphoma Cells. *Molecular and Cellular Biology* **2000**, *20* (7), 2423–2435.
- (86) Miller, D. M.; Thomas, S. D.; Islam, A.; Muench, D.; Sedoris, K. C-Myc and Cancer Metabolism. *Clinical Cancer Research* **2012**, *18* (20), 5546–5553.
- (87) Schick, M.; Habringer, S.; Nilsson, J. A.; Keller, U. Pathogenesis and Therapeutic Targeting of Aberrant MYC Expression in Haematological Cancers. *British Journal of Haematology* **2017**, *179* (5), 724–738.
- (88) Dang, C. V. MYC on the Path to Cancer. *Cell* **2012**, *149* (1), 22–35.
- (89) Shi, M.; Chu, F.; Zhu, F.; Zhu, J. Impact of Anti-Amyloid- β Monoclonal Antibodies on the Pathology and Clinical Profile of Alzheimer’s Disease: A Focus on Aducanumab and Lecanemab. *Frontiers in Aging Neuroscience* **2022**, *14*, 1–11.
- (90) McDade, E.; Cummings, J. L.; Dhadda, S.; Swanson, C. J.; Reyderman, L.; Kanekiyo, M.; Koyama, A.; Irizarry, M.; Kramer, L. D.; Bateman, R. J. Lecanemab in Patients with Early Alzheimer’s Disease: Detailed Results on Biomarker, Cognitive, and Clinical Effects from the Randomized and Open-Label Extension of the Phase 2 Proof-of-Concept Study. *Alzheimer’s Research & Therapy* **2022**, *14*, 191.
- (91) Llombart, V.; Mansour, M. R. Therapeutic Targeting of “Undruggable” MYC. *eBioMedicine* **2022**, *75*, 1–17.
- (92) Castell, A.; Yan, Q.; Fawkner, K.; Hydbring, P.; Zhang, F.; Verschut, V.; Franco, M.; Zakaria, S. M.; Bazzar, W.; Goodwin, J.; Zinzalla, G.; Larsson, L.-G. A Selective High Affinity MYC-Binding Compound Inhibits MYC:MAX Interaction and MYC-Dependent Tumor Cell Proliferation. *Scientific Reports* **2018**, *8* (1), 1–17.
- (93) Choi, S. H.; Mahankali, M.; Lee, S. J.; Hull, M.; Petrassi, H. M.; Chatterjee, A. K.; Schultz, P. G.; Jones, K. A.; Shen, W. Targeted Disruption of Myc–Max Oncoprotein Complex by a Small Molecule. *ACS Chemical Biology* **2017**, *12* (11), 2715–2719.

- (94) Boros, B. D.; Schoch, K. M.; Kreple, C. J.; Miller, T. M. Antisense Oligonucleotides for the Study and Treatment of ALS. *Neurotherapeutics* **2022**, *19* (4), 1145–1158.
- (95) Rinaldi, C.; Wood, M. J. A. Antisense Oligonucleotides: The next Frontier for Treatment of Neurological Disorders. *Nature Reviews Neurology* **2018**, *14* (1), 9–21.
- (96) Gill, T.; Wang, H.; Bandaru, R.; Lawlor, M.; Lu, C.; Nieman, L. T.; Tao, J.; Zhang, Y.; Anderson, D. G.; Ting, D. T.; Chen, X.; Bradner, J. E.; Ott, C. J. Selective Targeting of MYC mRNA by Stabilized Antisense Oligonucleotides. *Oncogene* **2021**, *40* (47), 6527–6539.
- (97) Békés, M.; Langley, D. R.; Crews, C. M. PROTAC Targeted Protein Degraders: The Past Is Prologue. *Nature Reviews Drug Discovery* **2022**, *21* (3), 181–200.
- (98) Tseng, Y.-L.; Lu, P.-C.; Lee, C.-C.; He, R.-Y.; Huang, Y.-A.; Tseng, Y.-C.; Cheng, T.-J. R.; Huang, J. J.-T.; Fang, J.-M. Degradation of Neurodegenerative Disease-Associated TDP-43 Aggregates and Oligomers via a Proteolysis-Targeting Chimera. *Journal of Biomedical Science* **2023**, *30* (1), 27.
- (99) Li, X.; Zhang, Z.; Gao, F.; Ma, Y.; Wei, D.; Lu, Z.; Chen, S.; Wang, M.; Wang, Y.; Xu, K.; Wang, R.; Xu, F.; Chen, J.-Y.; Zhu, C.; Li, Z.; Yu, H.; Guan, X. C-Myc-Targeting PROTAC Based on a TNA-DNA Bivalent Binder for Combination Therapy of Triple-Negative Breast Cancer. *Journal of the American Chemical Society* **2023**, *145* (16), 9334–9342.
- (100) Njomen, E.; Osmulski, P. A.; Jones, C. L.; Gaczynska, M.; Tepe, J. J. Small Molecule Modulation of Proteasome Assembly. *Biochemistry* **2018**, *57* (28), 4214–4224.
- (101) Jones, C.; Njomen, E.; Sjogren, B.; Dexheimer, T.; Tepe, J. Small Molecule Enhancement of 20S Proteasome Activity Targets Intrinsically Disordered Proteins. *ACS Chemical Biology* **2017**, *12* (9), 2240–2247.
- (102) Staerz, S. D.; Jones, C. L.; Tepe, J. J. Design, Synthesis, and Biological Evaluation of Potent 20S Proteasome Activators for the Potential Treatment of α -Synucleinopathies. *Journal of Medicinal Chemistry* **2022**, *65* (9), 6631–6642.
- (103) Fiolek, T. J.; Keel, K. L.; Tepe, J. J. Fluspirilene Analogs Activate the 20S Proteasome and Overcome Proteasome Impairment by Intrinsically Disordered Protein Oligomers. *ACS Chemical Neuroscience* **2021**, *12* (8), 1438–1448.
- (104) Fiolek, T. J.; Magyar, C. L.; Wall, T. J.; Davies, S. B.; Campbell, M. V.; Savich, C. J.; Tepe, J. J.; Mosey, R. A. Dihydroquinazolines Enhance 20S Proteasome Activity and Induce Degradation of α -Synuclein, an Intrinsically Disordered Protein Associated with Neurodegeneration. *Bioorganic & Medicinal Chemistry Letters* **2021**, *36*, 127821.
- (105) Huang, L.; Ho, P.; Chen, C.-H. Activation and Inhibition of the Proteasome by Betulinic Acid and Its Derivatives. *FEBS Letters* **2007**, *581* (25), 4955–4959.
- (106) Trader, D. J.; Simanski, S.; Dickson, P.; Kodadek, T. Establishment of a Suite of Assays That Support the Discovery of Proteasome Stimulators. *Biochimica et Biophysica Acta* **2017**, *1861* (4), 892–899.

- (107) Coleman, R. A.; Trader, D. J. Development and Application of a Sensitive Peptide Reporter to Discover 20S Proteasome Stimulators. *ACS Combinatorial Science* **2018**, *20* (5), 269–276.
- (108) Njomen, E.; Vanecek, A.; Lansdell, T. A.; Yang, Y.-T.; Schall, P. Z.; Harris, C. M.; Bernard, M. P.; Isaac, D.; Alkharabsheh, O.; Al-Janadi, A.; Giletto, M. B.; Ellsworth, E.; Taylor, C.; Tang, T.; Lau, S.; Bailie, M.; Bernard, J. J.; Yuzbasiyan-Gurkan, V.; Tepe, J. J. Small Molecule 20S Proteasome Enhancer Regulates MYC Protein Stability and Exhibits Antitumor Activity in Multiple Myeloma. *Biomedicines* **2022**, *10* (5), 938.

PART I

20S Proteasome Activation as a Novel Therapeutic for Neurodegenerative Diseases

CHAPTER TWO

Exploring the Potential of Small Molecule Activation of the 20S Proteasome as a Novel Therapeutic for the Treatment of Amyotrophic Lateral Sclerosis

Part of this chapter is reprinted with permission from **Vanecek, A. S.**; Mojsilovic-Petrovic, J.; Kalb, R. G.; Tepe, J. J. Enhanced Degradation of Mutant *C9ORF72*-Derived Toxic Dipeptide Repeat Proteins by 20S Proteasome Activation Results in Restoration of Proteostasis and Neuroprotection. *ACS Chemical Neuroscience* **2023**, *14* (8), 1439-1448. Copyright [2023] American Chemical Society. <https://doi.org/10.1021/acscemneuro.2c00732>.

2.1 Introduction

2.1.1 Background

ALS and FTD are neurodegenerative diseases that exist on a clinical spectrum displaying both shared and unique features.¹ ALS is characterized by the progressive degeneration of upper and lower motor neurons leading to weakness of limb and bulbar muscles.² FTD is characterized by the progressive degeneration of neurons within the cerebral frontal and anterior temporal lobes leading to progressive deterioration in behavior, language, and personality.¹ A HRE of sequence 5' GGGGCC 3' in an intron flanked by exons 1a and 1b in the *C9ORF72* gene is the most common cause of familial ALS and FTD.^{3,4} Mutations in the *C9ORF72* gene ("C9 mutations") are responsible for 30-60 percent of familial ALS cases and approximately 12 percent of familial FTD cases.³⁻⁵ While the HRE is found in healthy individuals with up to 8 repeats, the number of repeats found in ALS or FTD patients is increased to a few hundred or even thousands.⁶ The molecular pathophysiology driven by the C9 mutation is complex and generally believed to involve three processes: (1) loss of function of the normal C9 protein, (2) an RNA mediated toxic gain-of-function, presumably due to sequestration of RNA binding proteins to an imperfect RNA hairpin structure, and (3) the generation of DPR proteins by repeat-associated non-ATG (RAN) translation.⁷⁻¹¹ Through this unconventional RAN translation, the sense and antisense HRE bearing mRNA strands undergo translation in the absence of a start codon producing, depending on the reading frame, five unique DPR proteins: poly-GA, poly-GP, poly-GR, poly-PR, and poly-PA.^{10,12-15} Arginine containing DPR proteins (e.g., GR_x and PR_x, where x indicates the number of repeats) have been shown to be toxic in a variety of model systems.¹⁶⁻²⁰

Intrinsically disordered proteins (IDPs) make up a class of proteins that lack a defined tertiary structure, allowing for multiple low affinity binding events.^{21,22} DPR proteins were hypothesized to be intrinsically disordered due to an enrichment of disorder-promoting amino acids (G, A, P and R).²³ Additionally, their disorder was anticipated due to their composition of tandem repeats of two amino acids, with the idea that the amount of disorder decreases with disruption of the consecutive repeats.²³ Circular dichroism spectroscopy^{24,25} interrogations of poly-arginine DPR proteins reveal a random coil or turn secondary structure, consistent with the idea that they are IDPs. Additional studies have shown that DPR proteins can undergo liquid-

liquid phase separation (LLPS), a process known to be mediated by intrinsically disordered, low complexity sequence domains (LCDs),²⁵⁻²⁷ The LCDs and tendency of the arginine-rich DPR proteins to undergo LLPS also results in a large interactome of proteins, including a number of RNA-binding proteins and other proteins with LCDs.²⁸ Substantial evidence supports the notion that alterations in the behavior of LLPS condensates underlies the pathogenesis of ALS and FTD.^{28,29}

The ubiquitin-proteasome system (UPS) is the main degradation pathway for IDPs.³⁰⁻³³ The UPS is made up of the active 26S proteasome isoform which is primarily responsible for the degradation of ubiquitinated substrates.³³ However, a less active/latent isoform, the 20S proteasome, can target IDPs directly for degradation independent of ubiquitination.^{30,34} The low basal activity of the 20S proteasome is sufficient to maintain low levels of IDPs in healthy cells, however, dysregulation of the UPS by mutations,³⁵ gene amplification,³⁶ or other cellular dysregulations³⁷ can lead to the accumulation and subsequent aggregation of IDPs. Furthermore, soluble oligomeric IDPs can allosterically inhibit the 20S proteasome, resulting in a self-reinforcing feedback loop leading to further accumulation of toxic aggregates.³⁸ It has been shown that DPR proteins may follow this trend, as recent work shows that poly-PR DPR proteins directly inhibit the 26S proteasome, resulting in a broad buildup of ubiquitinated protein substrates.¹⁶

To protect against the accumulation of these disordered DPR proteins and avoid dysregulation of the UPS, I hypothesized that the enhancement of the proteolytic activity of the 20S proteasome could promote degradation of DPR proteins and prevent impairment of proteasome function. Small molecule activation of the 20S proteasome is an emerging strategy to prevent the accumulation of IDPs and the toxicity associated with IDP accumulation.³⁹⁻⁴⁶ TCH-165 is a potent small molecule activator of the 20S proteasome that can enhance degradation of IDPs both in purified protein assays and in cell culture (e.g. α -synuclein, tau441, c-Fos), and is well tolerated *in vivo*.^{39,47} In this chapter, my work focuses on testing of the hypothesis that TCH-165 could enhance the degradation of DPR proteins in both purified protein assays and in neurons, the latter alleviating their toxic effects on cortical neurons (schematic of hypothesis in Figure 2.1). Herein, evidence that TCH-165 enhances the degradation of DPR proteins and prevents

impairment of proteasome function in purified protein assays is provided. Furthermore, the 20S enhancer restores proteostasis and provides neuroprotection from DPR protein toxicity in cortical neuron culture. Later in the chapter, the mechanism by which the DPR proteins impair proteasome function and how TCH-165 protects against this impairment will be investigated. Lastly, the progress toward elucidating the binding site of a 20S proteasome activator using cryogenic electron microscopy (cryo-EM) will be discussed.

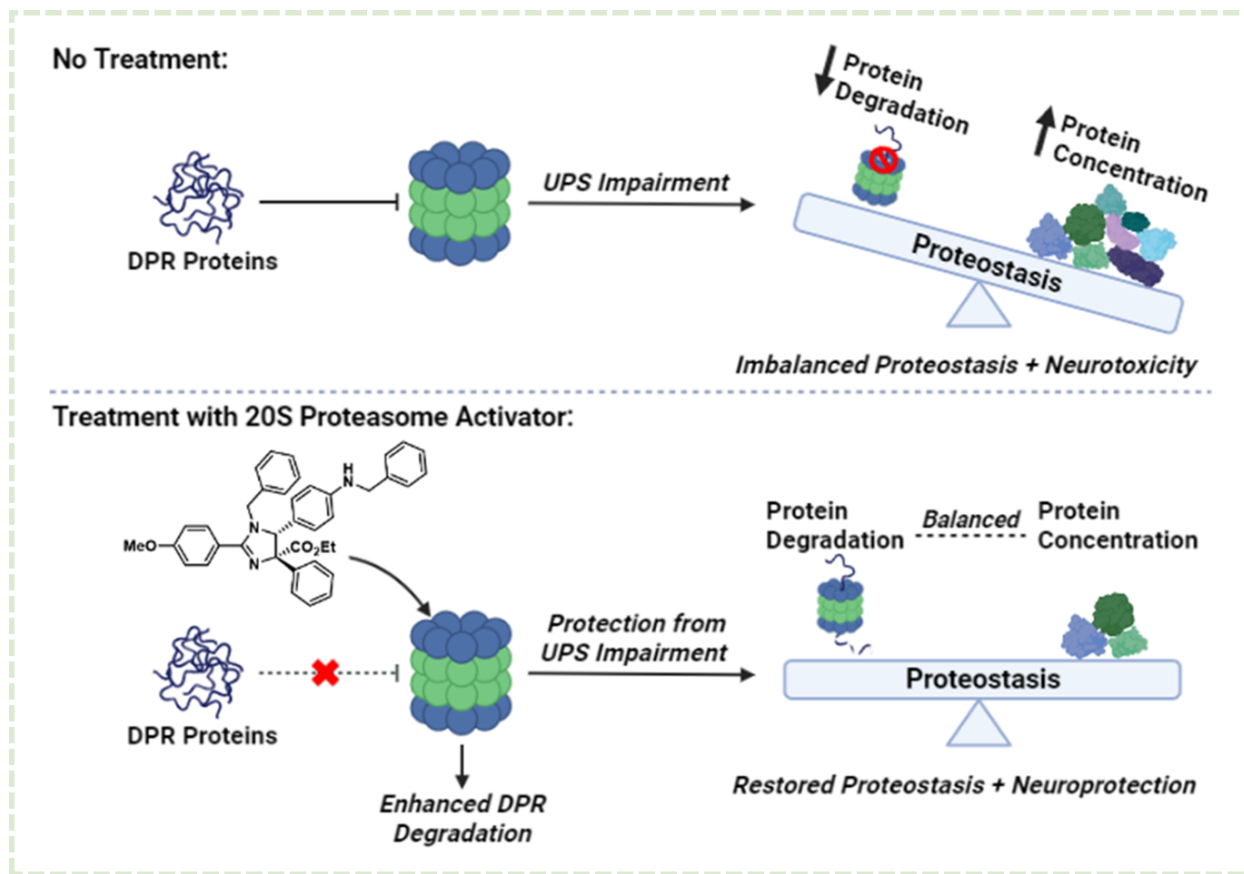


Figure 2.1 Schematic of the hypothesis that small molecule 20S proteasome activators can enhance the 20S proteasome-mediated degradation of DPR proteins, thereby preventing the UPS impairment evoked by their accumulation. Ultimately, it is anticipated these effects would restore proteostasis in the cell and provide protection from DPR-induced neurotoxicity.

2.2 Results and Discussion

The UPS is responsible for ubiquitin-dependent and ubiquitin-independent protein degradation.^{30,34} The 20S proteasome is a threonine protease that targets IDPs for degradation, and is comprised of four heptameric rings ($\alpha_7\beta_7\beta_7\alpha_7$), two β -rings containing three unique proteolytic sites, and two α -rings that act as gates allowing or restricting access to the proteolytic core.⁴⁸ To degrade ubiquitylated substrates, 19S regulatory caps bind to intersubunit pockets between the α -subunits forming the 26S proteasome, and results in a conformational change that opens the gate allowing for substrate entry into the proteolytic chamber.^{49,50} Without binding of the 19S regulatory cap, the 20S proteasome is typically found in a closed gate conformation, thus restricting access to the three catalytic sites and resulting in a low activity/latent isoform of the proteasome.^{30,34} The small molecule, TCH-165, induces an open gate conformation of the 20S proteasome in the absence of the 19S regulatory cap, resulting in increased 20S proteolytic activity and enhanced degradation of highly disordered proteins.³⁹ Since DPR proteins are believed to be highly disordered,²⁴⁻²⁷ we asked whether TCH-165 enhancement of 20S proteasome activity could prevent the toxic accumulation and aggregation of DPR proteins. Herein we demonstrate that the 20S proteasome enhancer, TCH-165, prevents DPR protein accumulation, UPS impairment and DPR protein induced neurotoxicity.

2.2.1 TCH-165 Enhances 20S-Mediated Degradation of Poly-GR and Poly-PR DPR Proteins

To determine whether the DPR proteins are a substrate for the 20S proteasome and explore whether TCH-165 can enhance their degradation, a small poly-GR DPR protein probe conjugated to the fluorophore, 7-amino-4-methylcoumarin (AMC), Suc-GR-GR-GR-AMC (i.e. Suc-GR₃-AMC), was used. Proteolytic cleavage of the poly-GR DPR protein probe results in the release of AMC. Proteolytic activity and probe degradation was then quantified by measuring the free AMC released from the fluorogenic substrate as done with traditional proteasome substrate probes (i.e. Suc-LLVY-AMC).⁵¹ Activation of the 20S proteasome with 20S proteasome enhancer, TCH-165, resulted in an 8.3-fold enhancement in the rate of degradation of the DPR protein probe as compared to the vehicle (untreated 20S proteasome), with an effective concentration to obtain a two-fold rate enhancement, EC₂₀₀, of 1.4 μ M (Figure 2.2). The previously reported³⁹

negative control of the imidazoline scaffold, TCH-23, was also included in the assay and was unable to enhance the rate of degradation of the poly-GR DPR protein probe.

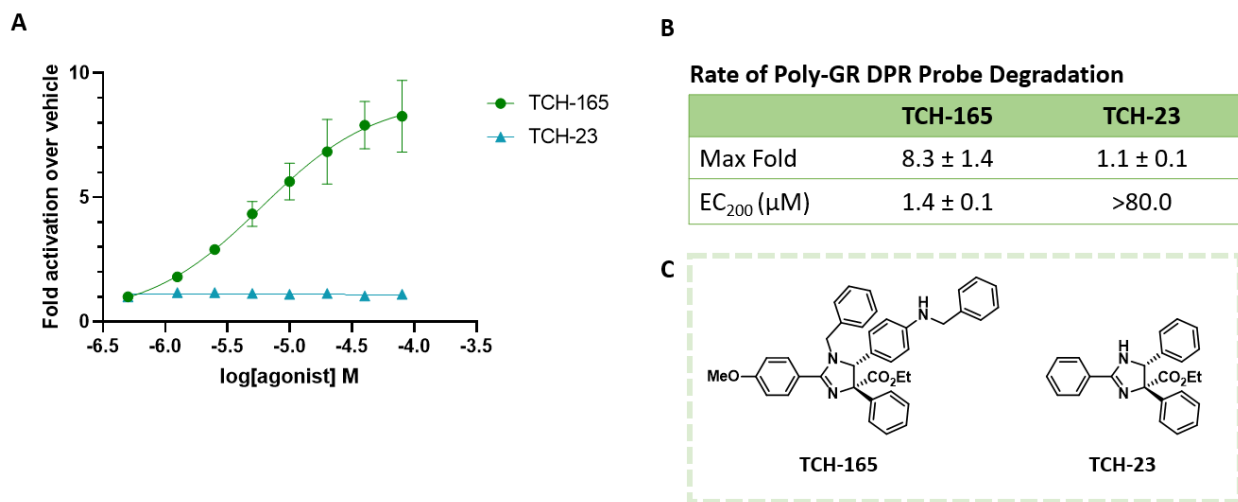


Figure 2.2 TCH-165 enhances degradation of fluorogenic poly-GR DPR protein probe. (A) Dose-response curve of TCH-165 and TCH-23 (inactive control) for 20S proteasome-mediated proteolysis of fluorogenic poly-GR DPR protein probe (Suc-GR₃-AMC) with 20S proteasome pretreated with TCH-165 or TCH-23. (B) Maximum fold enhancement over vehicle (untreated 20S proteasome) and the effective concentration to obtain a two-fold rate enhancement, EC₂₀₀, values were calculated (n=3); error bars denote standard deviation. (C) Structures of TCH-165 and previously published³⁹ inactive control TCH-23 (unable to enhance 20S proteasome activity up to >80.0 μM).

These data indicate that the poly-arginine DPR proteins are substrates for the 20S proteasome and that 20S activation can enhance their rate of degradation. Next, I aimed to determine whether TCH-165 could enhance the rate of degradation of poly-arginine DPR proteins of a more disease-relevant length. To explore this, a digestion of purified HA-tagged DPR proteins of 40 amino acid length was conducted (HA-GR₂₀ or HA-PR₂₀). In this assay, pretreated purified human 20S proteasome was incubated with the poly-GR or poly-PR DPR protein for 30 minutes or 8 hours, respectively. As shown in Figure 2.3, TCH-165 significantly enhances 20S proteasome-mediated degradation of the HA-GR₂₀ DPR protein in a dose dependent manner, with only 5 percent HA-GR₂₀ (95 percent reduction) remaining using 10 μM TCH-165 treatment compared to the basal degradation of the vehicle control (untreated 20S proteasome) following the 30-minute incubation. Conversely, inhibition of the 20S proteasome with bortezomib (BTZ) completely blocked the degradation of HA-GR₂₀ (all replicates can be found in Figure 2.18 of the Appendix).

Similarly, only 37 percent HA-PR₂₀ (63 percent reduction) remained following incubation of TCH-165 (10 μ M) with purified 20S proteasome for 8 hours compared to the basal degradation of the vehicle treated 20S proteasome control (Figure 2.3D; all replicates can be found in Figure 2.19 of the Appendix). I hypothesize that the greater amount of HA-PR₂₀ remaining and the longer incubation time necessary to degrade the poly-PR substrate could be due to the rigidity the proline residues provide to the DPR protein, in contrast to the flexibility the glycine residues impart on the poly-GR DPR proteins. These data indicate that both the poly-arginine DPR proteins (HA-GR₂₀ and HA-PR₂₀) are substrates of the 20S proteasome and that 20S activation with TCH-165 can effectively enhance HA-GR₂₀ degradation by three-fold (using 3 μ M TCH-165) and HA-PR₂₀ degradation by two-fold (using 5 μ M TCH-165).

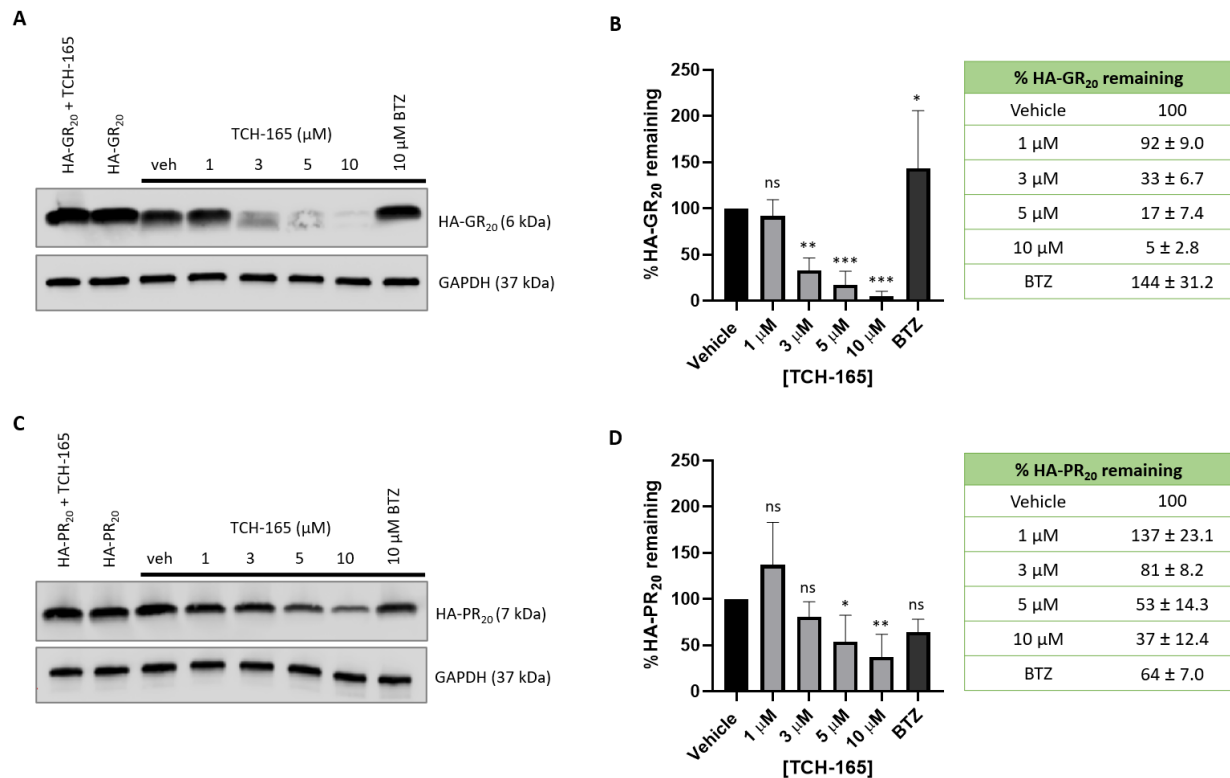


Figure 2.3 TCH-165 enhances 20S proteasome-mediated degradation of purified HA-GR₂₀ and HA-PR₂₀. (A) Representative western blot of HA-GR₂₀ digestion (30 minutes) with the 20S proteasome following pretreatment with TCH-165 (1, 3, 5, 10 μM) or proteasome inhibitor bortezomib (BTZ, 10 μM). Immunoblot probed with anti-HA-tag and anti-GAPDH antibodies. (B) Quantification of HA-GR₂₀ digestion western blots (n=4); one-way ANOVA (ns, not significant, *p ≤ 0.05; **p ≤ 0.01; ***p ≤ 0.001; ****p ≤ 0.0001). (C) Representative western blot of HA-PR₂₀ digestion (8 hours) with the 20S proteasome following pretreatment with TCH-165 (1, 3, 5, 10 μM) or proteasome inhibitor bortezomib (BTZ, 10 μM). Immunoblot probed with anti-HA-tag and anti-GAPDH antibodies. (D) Quantification of HA-PR₂₀ digestion western blots (n=4); one-way ANOVA (ns, not significant, *p ≤ 0.05; **p ≤ 0.01; ***p ≤ 0.001; ****p ≤ 0.0001).

2.2.2 TCH-165 Protects Against 20S Proteasome Impairment by Arginine-rich DPR Proteins

A number of neurodegenerative diseases have been characterized by an accumulation of aggregation-prone IDPs, resulting in dysregulated proteasome function.^{52–54} This loss in proteostasis is a major contributing factor to the pathogenesis of neurodegeneration.^{55–58} Although it has been shown that IDP aggregates directly inhibit both the 26S and 20S proteasomes, the mechanism by which IDP aggregates inhibit the proteasome has yet to be fully elucidated. Recently, a mechanistic model was proposed suggesting that IDP oligomers bind to the outer sides of the 20S core particle resulting in a conformational change that allosterically

stabilizes the closed gate conformation of the proteasome, restricting access of substrates to the proteolytic chamber for degradation.³⁸ Another recent study suggests that poly-GA DPR proteins entangle proteasomes into large ribbon-like aggregates, trapping them in a state of stalled degradation.⁵⁹ Since DPR proteins have shown to inhibit the UPS in cell culture,^{16,17,60} I aimed to explore whether these inhibitory effects result from direct interaction of the DPR proteins on the 20S core particle, potentially through a similar mechanism to the model recently proposed.³⁸ Furthermore, if the DPR proteins also inhibit the proteasome by allosterically stabilizing the closed gate conformation, as proposed for other IDPs,³⁸ small molecule 20S gate-regulators, like TCH-165, could potentially protect against proteasome impairment by the DPR proteins.

I first investigated whether the DPR proteins directly impair function of the 20S proteasome by assaying the chymotryptic-like activity of the proteasome using a small substrate probe conjugated to the fluorophore, 7-amino-4-methylcoumarin, (Suc-LLVY-AMC). I asked whether the DPR proteins above (HA-GR₂₀ or HA-PR₂₀) impaired the proteolytic activity and if so, whether TCH-165 impacted this phenomenon. To explore this, purified human 20S proteasome was pretreated with varying concentrations of TCH-165, followed by incubation with DPR proteins HA-GR₂₀ or HA-PR₂₀. Proteolytic activity was then quantified by measuring the release of AMC from the fluorogenic substrate (Suc-LLVY-AMC).⁵¹ The results show that in the presence of both DPR proteins (HA-GR₂₀ or HA-PR₂₀), 20S proteasome function is impaired, with 20S proteasome activity reduced to 66 percent in the presence of HA-GR₂₀ (Figure 2.4A) and 54 percent in the presence of HA-PR₂₀ (Figure 2.4B).

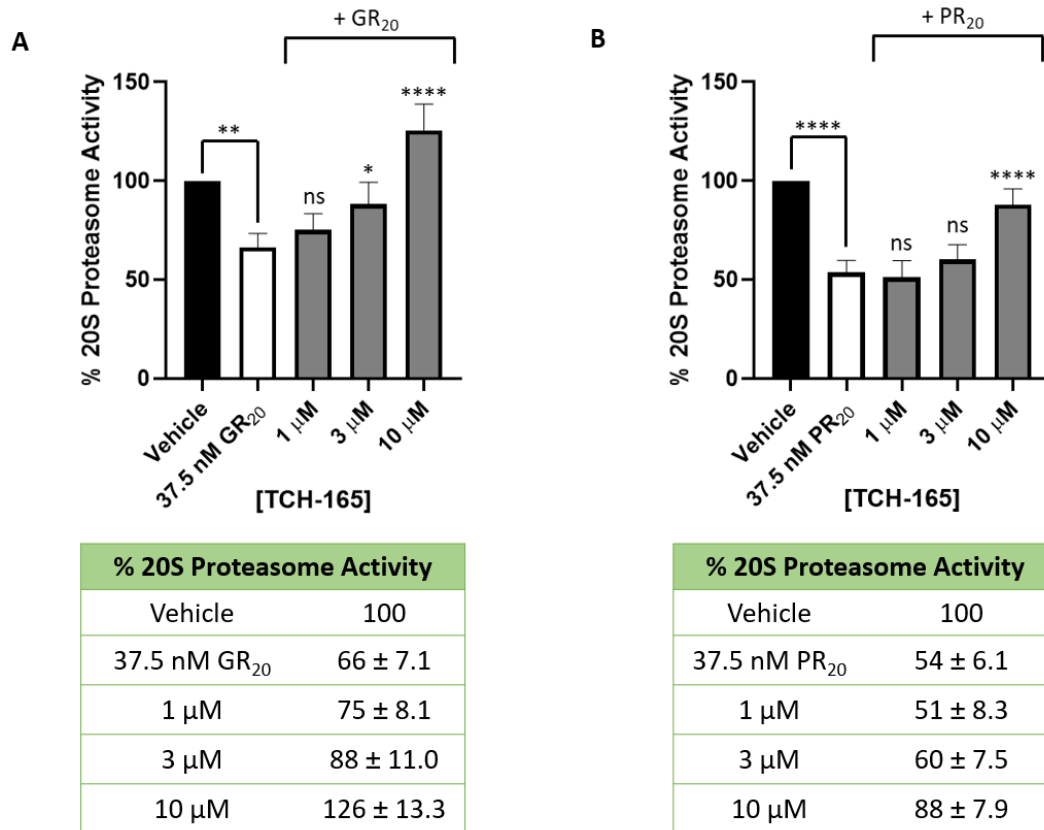


Figure 2.4 TCH-165 protects against 20S proteasome impairment by DPR proteins HA-GR₂₀ and HA-PR₂₀. (A) Dose-response of TCH-165 for 20S proteasome-mediated proteolysis of fluorogenic substrate probe Suc-LLVY-AMC with 20S proteasome pretreated with TCH-165, followed by incubation with HA-GR₂₀. (B) Dose-response of TCH-165 for 20S proteasome-mediated proteolysis of fluorogenic substrate probe Suc-LLVY-AMC with 20S proteasome pretreated with TCH-165, followed by incubation with HA-PR₂₀ (n=3); one-way ANOVA (ns, not significant, *p ≤ 0.05; **p ≤ 0.01; ***p ≤ 0.001; ****p ≤ 0.0001).

Remarkably, 20S activation with TCH-165 was able to protect against proteasome impairment evoked by the DPR proteins in a dose dependent manner (Figure 2.4). In the case of both DPR proteins, TCH-165 was able to significantly prevent 20S proteasome impairment at concentrations of ≥3 μM for HA-GR₂₀ and ≥10 μM for HA-PR₂₀. In agreement with the DPR protein digestion results, a higher concentration of TCH-165 was needed to protect against proteasome impairment by the poly-PR DPR proteins. This may be due to a greater amount of HA-PR₂₀ remaining following the incubation time, compared to the poly-GR DPR protein. The inactive control, TCH-23, was unable to protect against DPR protein impairment of 20S proteasome function evoked by the poly-PR DPR proteins (Figure 2.20B of the Appendix). In the case of the

poly-GR DPR proteins, a modest protection from 20S proteasome impairment was observed (23% increase in 20S proteasome activity; Figure 2.20A of the Appendix), but this protection is significantly lower compared to the ability of TCH-165 (63% increase in 20S proteasome activity) to prevent 20S proteasome impairment by the poly-GR DPR proteins. The inability of TCH-23 to enhance 20S proteolysis (Figure 2.2), but weakly protect against poly-GR induced 20S impairment (Fig. 2.20A of the Appendix), may be indicative of an interruption of efficient poly-GR-20S binding.

I then asked whether TCH-165 could recover 20S proteasome activity when 20S proteasome was first treated with DPR proteins, followed by addition of the small molecule. Gratifyingly, TCH-165 was able to overcome 20S proteasome impairment by poly-GR DPR proteins, resulting in a 60 percent recovery of 20S proteasome function (Figure 2.5A). However, when 20S proteasome was treated with poly-PR DPR proteins, followed by TCH-165, no recovery of 20S proteasome function was observed during the time of the experiment (Figure 2.5B). This could be anticipated, as a higher dose of TCH-165 was needed to significantly prevent 20S proteasome impairment induced by the poly-PR DPR proteins when compared to the poly-GR DPR proteins. The varying effects of TCH-165 observed here may also result from differences in binding affinities of the DPR proteins to the 20S proteasome. Furthermore, addition of the inactive control, TCH-23, following incubation of the 20S proteasome with DPR proteins, resulted in no significant recovery of 20S proteasome function in the case of either DPR protein (Figures 2.21A and 2.21B of the Appendix).

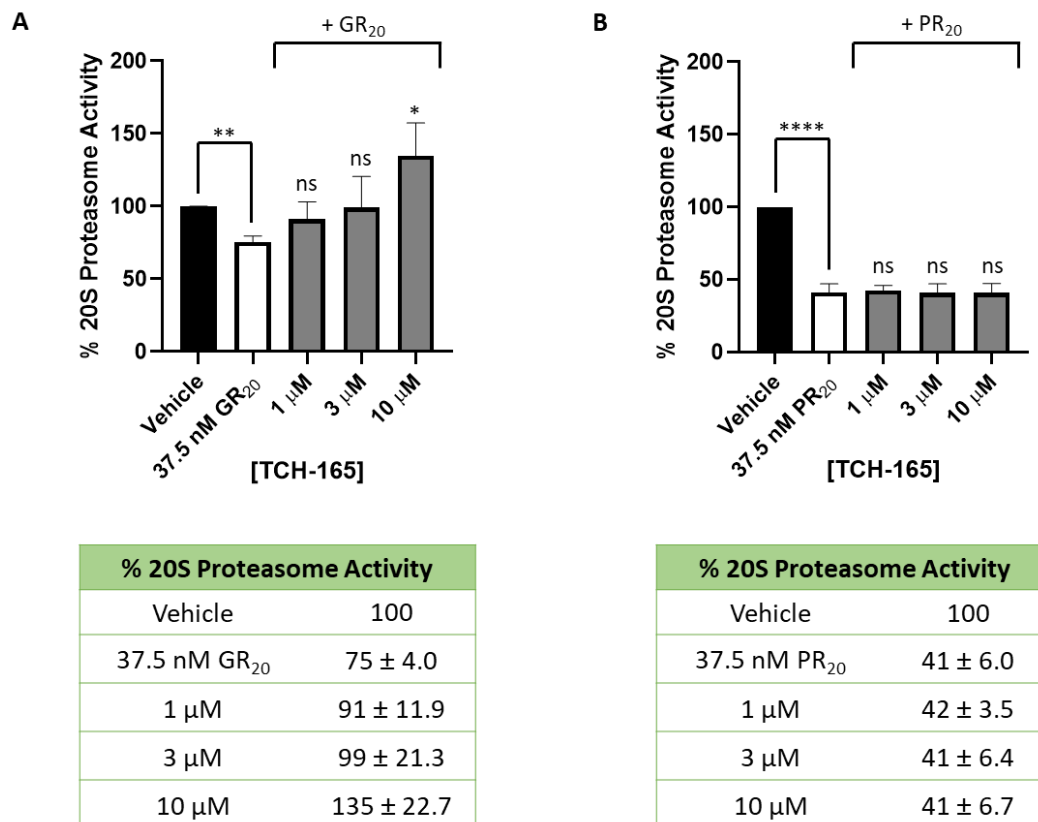


Figure 2.5 TCH-165 overcomes 20S proteasome impairment by HA-GR₂₀. (A) Dose-response of TCH-165 for 20S proteasome-mediated proteolysis of fluorogenic substrate probe Suc-LLVY-AMC with 20S proteasome incubated with HA-GR₂₀ followed by treatment with TCH-165. (B) Dose-response of TCH-165 for 20S proteasome-mediated proteolysis of fluorogenic substrate probe Suc-LLVY-AMC with 20S proteasome incubated with HA-PR₂₀ followed by treatment with TCH-165. (n=3); one-way ANOVA (ns, not significant, *p ≤ 0.05; **p ≤ 0.01; ***p ≤ 0.001; ****p ≤ 0.0001).

These data support the idea that TCH-165 protects against and overcomes 20S proteasome impairment by stabilizing an open gate conformation of the 20S proteasome in the presence of the DPR proteins, allowing substrates to access the proteolytic core for degradation. However, the untreated proteasomes treated only with the DPR proteins, have been stabilized in a closed gate conformation, resulting in restricted access to the proteolytic core and lowered proteasome activity. These results, in combination with the fact that TCH-165 enhances the degradation of DPR proteins, suggest that by preventing the accumulation of DPR proteins, the proteasomes are protected from impairment of proteasome function by DPR proteins.

2.2.3 TCH-165 Prevents the Accumulation of DPR Proteins and Restores Proteostasis in Cortical Neuron Culture

It has previously been shown that DPR proteins inhibit the UPS in cell culture.^{16,17,60} Additional work has shown that increasing protein degradation through the use of a DUB inhibitor,¹⁶ HSP90 inhibitor,⁶¹ or activation of the proteasome through cAMP/protein kinase A-dependent phosphorylation of proteasome subunit PSMD11⁶² counters the toxic effects of the DPR proteins. This suggests impairment of UPS function contributes to DPR protein toxicity. With our finding that both the poly-GR and poly-PR DPR proteins inhibit the 20S proteasome directly, we asked if direct activation of the 20S proteasome with TCH-165 could prevent the accumulation of DPR proteins in cell culture and protect against proteasome impairment.

To investigate this, our collaborators at Northwestern Medicine, Dr. Robert Kalb and Dr. Jelena Mojsilovic-Petrovic, expressed a GFP-tagged DPR protein (i.e. GFP-GR₅₀, GFP-PR₅₀, GFP-GA₅₀) in rat cortical neurons followed by subsequent treatment with TCH-165 (5 μ M) for 48 hours. I then analyzed the DPR protein levels in the neuron lysate with an immunoblot probed with an anti-GFP antibody. Compared to the untreated control, TCH-165 reduced GFP-GR₅₀ DPR protein levels with only 62 percent remaining compared to the untreated control neurons (Figure 2.6). TCH-165 also reduced the amount of another DPR protein not featured in this chapter, GFP-GA₅₀, with only 62 percent remaining compared to the untreated control neurons. Due to solubility issues and the extreme aggregation propensity of the poly-GA DPR proteins, *in vitro* studies utilizing this protein require further optimization. As this manuscript was the first demonstration of utilizing a 20S proteasome activator toward DPR proteins, we decided to focus on exploring the cellular efficacy of TCH-165 toward DPR proteins in which we could obtain *in vitro* support for direct enhancement of DPR protein degradation and protection from proteasome impairment. Therefore, the poly-GA DPR proteins were not included in the remainder of the studies. However, further exploration of the efficacy of TCH-165 toward the poly-GA DPR proteins is warranted, as the poly-GA DPR proteins are known to be highly prevalent in ALS patients and highly prone to aggregation.¹⁷

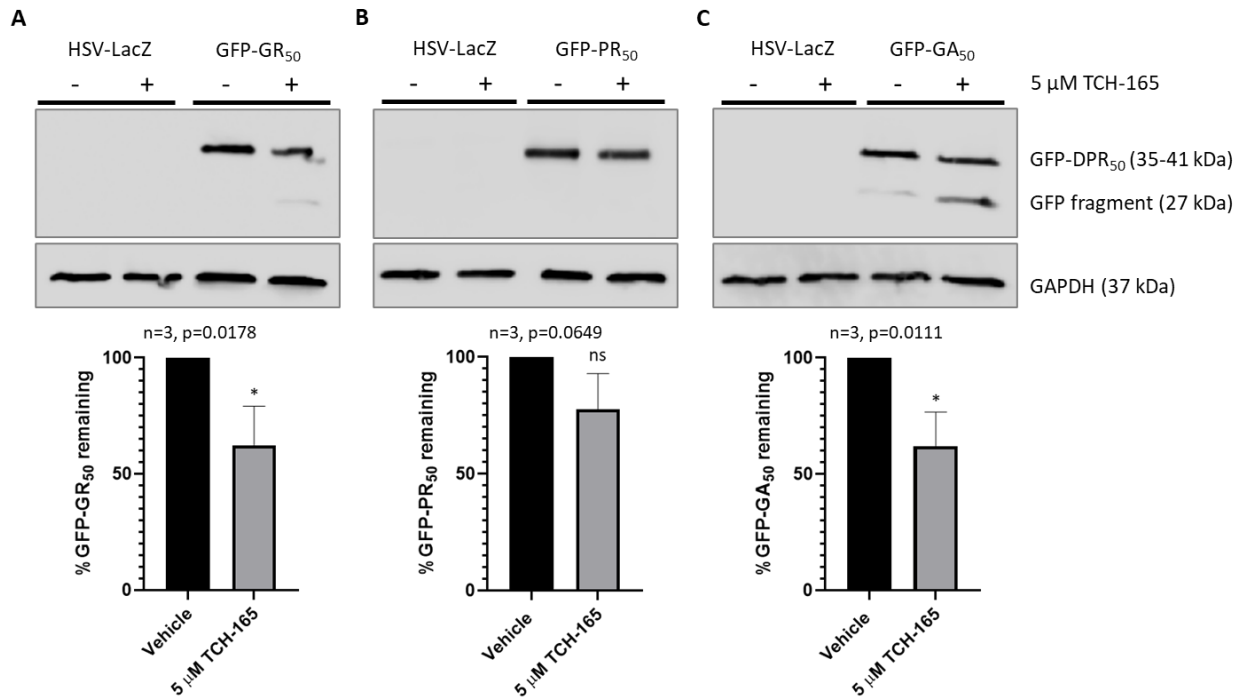


Figure 2.6 TCH-165 reduces the accumulation of GFP-GR₅₀ and GFP-GA₅₀ in rat cortical neurons. Representative western blot and quantification of the amount of GFP-GR₅₀ (A), GFP-PR₅₀ (B), and GFP-GA₅₀ (C) levels in rat cortical neurons following treatment with TCH-165 (5 μM) for 48 hours. Immunoblot probed with anti-GFP and anti-GAPDH antibodies. All data was collected in triplicate (n=3); one-way ANOVA (ns, not significant, *p ≤ 0.05; **p ≤ 0.01; ***p ≤ 0.001; ****p ≤ 0.0001).

While a small decrease in GFP-PR₅₀ protein levels was observed with TCH-165 treatment in these initial neuron experiments, this decrease was not statistically significant (p=0.0649). Therefore, a time course study was designed with an increased TCH-165 concentration to examine multiple time points, to determine whether TCH-165 would be efficacious against GFP-PR₅₀ at any point throughout the 48-hour experiment. This ultimately led to more impactful studies than anticipated. Rather than selecting one of the time points of the experiment to demonstrate the efficacy of TCH-165 to reduce DPR protein levels at a single time point, these experiments demonstrated that TCH-165 is able to reduce protein accumulation over time. Furthermore, a method to evaluate cellular proteostasis in the neurons was incorporated into the experiment providing additional insight.

In the time course experiment, rat cortical neurons were infected with an HSV-GFP-GR₅₀ or HSV-GFP-PR₅₀ vector to induce expression of the DPR proteins. The neurons were subsequently treated with TCH-165 (10 μM) or vehicle control for 12, 24, and 48 hours.

Overexpression of GFP-GR₅₀ resulted in the accumulation of GFP-GR₅₀ (268 percent GFP-GR₅₀ accumulation at 48 hours following infection) and TCH-165 was able to reduce the accumulation of GFP-GR₅₀ (Figure 2.7A and 2.7B; 154 percent accumulation 48 hours following infection). Next, we looked at the abundance of total ubiquitinated protein levels as a general reporter of UPS function. If UPS function is impaired, proteostasis in the cell would be upset and a buildup of ubiquitinated proteins would be evident. To ensure that expression of the DPR proteins resulted in UPS impairment in our system, a control experiment had been conducted prior to the current experiment. The results showed an increase in total ubiquitinated proteins upon expression of GFP-GR₅₀ compared to neurons expressing a control LacZ vector without DPR expression (Figure 2.22 of the Appendix). Therefore, in this time course experiment, the ability of TCH-165 to decrease this buildup of ubiquitinated proteins was investigated.

In the vehicle control treated neurons, we observed that the increase in GFP-GR₅₀ concentration over 48 hours corresponded with an increase in the amount of total ubiquitinated proteins (Figure 2.7A and 2.7B; 219 percent accumulation 48 hours following infection). Remarkably, the reduced accumulation of GFP-GR₅₀ in the TCH-165 treated neurons (Figure 2.7B, left graph) prevented this buildup of total ubiquitinated proteins (Figure 2.7B, right graph; 99 percent 48 hours following infection); all replicates can be found in Figure 2.23 of the Appendix. These observations suggest that TCH-165 can protect against impairment of UPS function and restore overall proteostasis in the cell in the presence of the poly-GR DPR proteins.

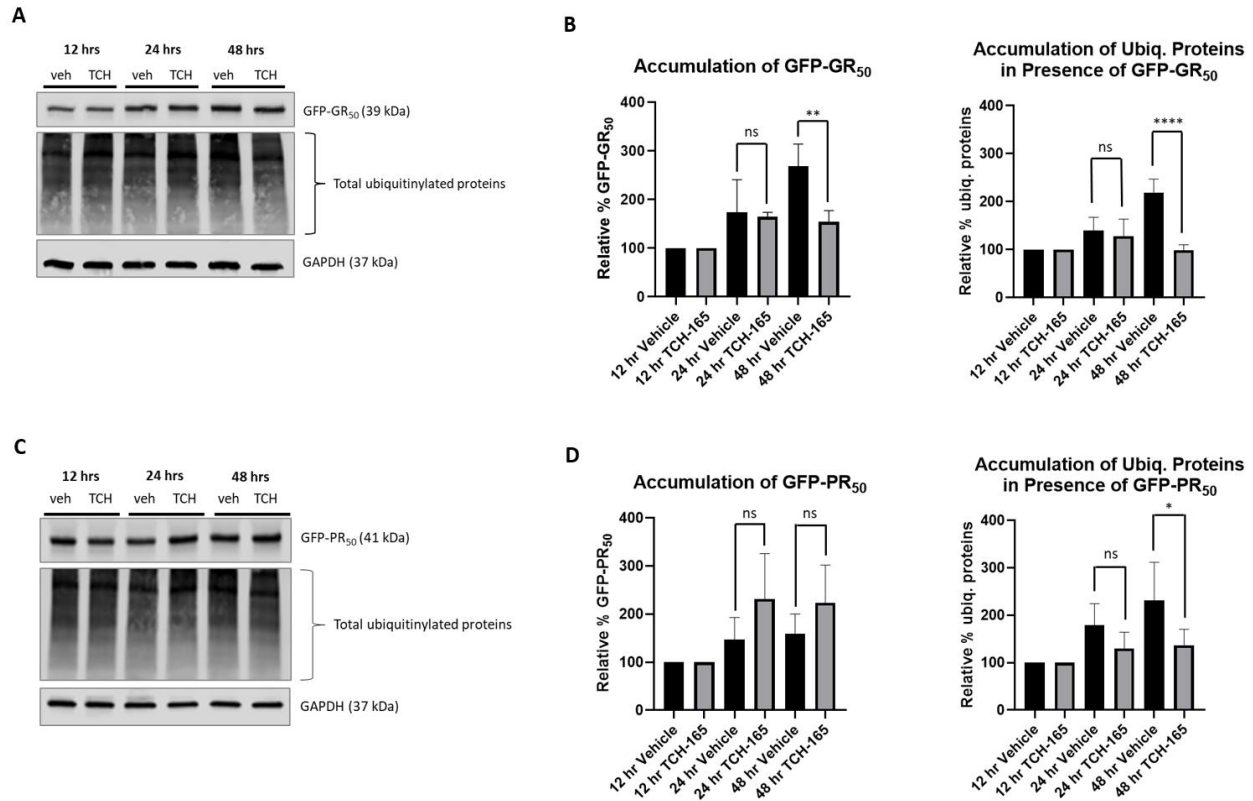


Figure 2.7 TCH-165 reduces the accumulation of GFP-GR₅₀ and prevents proteasome impairment in rat cortical neurons. (A) Representative western blot of the amount of GFP-GR₅₀ and total ubiquitinated protein levels in rat cortical neurons following treatment with TCH-165 (10 μ M) over 48 hours. Immunoblot probed with anti-poly-GR, anti-total ubiquitin, and anti-GAPDH antibodies. (B) Quantification of GFP-GR₅₀ and total ubiquitinated (ubiq.) protein western blots (n=3); one-way ANOVA (ns, not significant, *p \leq 0.05; **p \leq 0.01; ***p \leq 0.001; ****p \leq 0.0001). (C) Representative western blot of the amount of GFP-PR₅₀ and total ubiquitinated protein levels in rat cortical neurons following treatment with TCH-165 (10 μ M) over 48 hours. Immunoblot probed with anti-poly-PR, anti-total ubiquitin, and anti-GAPDH antibodies. (D) Quantification of GFP-PR₅₀ and total ubiquitinated (ubiq.) protein western blots (n=3); one-way ANOVA (ns, not significant, *p \leq 0.05; **p \leq 0.01; ***p \leq 0.001; ****p \leq 0.0001).

As we observed with the cortical neurons expressing GFP-GR₅₀, when cortical neurons were infected with the HSV-GFP-PR₅₀ vector, an accumulation of GFP-PR₅₀ occurred over the course of 48 hours in the vehicle control treated neurons (Figure 2.7C and 2.7D); all replicates shown in Figure 2.24 of the Appendix. Additionally, this accumulation of the poly-PR DPR proteins correlated with an increase in total ubiquitinated protein levels (Figure 2.7D, right graph; 231 percent 48 hours following infection), indicating UPS function is impaired and a loss of cellular proteostasis. Consistent with our *in vitro* data, treatment of the neurons with TCH-165 did not

reduce the accumulation of GFP-PR₅₀ (Figure 2.7D, left graph) as we observed with the poly-GR substrate, within the time frame of the experiment. However, treatment with TCH-165 did prevent the buildup of total ubiquitinated proteins (Figure 2.7D, right graph; 137 percent 48 hours following infection), suggesting TCH-165 is able to provide protection from UPS impairment and preserve cellular proteostasis in the presence of GFP-PR₅₀ without significant reduction in their accumulation.

Our data suggests that TCH-165 is able to protect against impairment of proteasome function by DPR proteins. I propose the mechanism of this protection from 20S proteasome impairment in neurons is likely to occur through one of the following mechanisms: (1) activation of the 20S proteasome results in the degradation of DPR proteins, thereby preventing their accumulation and reducing their inhibitory effects on the 20S proteasome, (2) binding of TCH-165 to the 20S proteasome stabilizes an open gate conformation of the 20S proteasome disallowing inhibitory DPR protein aggregates from binding, or (3) a combination of the two proposed mechanisms depending on the efficiency of 20S proteasome-mediated DPR protein degradation. This work provides support for all possible mechanisms, and our results suggest the mode of protection from UPS impairment by each DPR protein may depend on the structure of the DPR protein and their relative rates of degradation. With respect to the cellular studies, in the case of the poly-GR DPR proteins, we observed that a reduction in their amount correlated with protection from UPS impairment, suggesting the first mechanism as a main mechanism of protection. In the neuron studies exploring the poly-PR DPR proteins, we found that even when a reduction in their amount was not observed, protection of proteasome function was achieved, suggesting the second mechanism of protection as the main route. Despite the three possible mechanisms, the above results provide support for the use of small molecule 20S proteasome activation to overcome UPS impairment, allowing cellular proteostasis to be restored.

2.2.5 TCH-165 Provides Neuroprotection to Cortical Neurons in the Presence of DPR Proteins

Previous works have implicated UPS impairment in DPR protein toxicity.^{16,60} We aimed to explore whether the protection TCH-165 provides against proteasome impairment would provide protection from the cytotoxic effects of DPR proteins in neuron culture. To investigate this, Dr. Robert Kalb and Dr. Jelena Mojsilovic-Petrovic infected rat spinal cord neurons with an

HSV-GFP (control), HSV-GFP-GR₅₀, or HSV-GFP-PR₅₀ vector to induce expression of the DPR proteins and subsequently treated the neurons with TCH-165 (3 μM) or vehicle (DMSO) for five days. The results showed that expression of GFP-GR₅₀ resulted in a significant decrease in motor neuron survival (53 percent survival) when compared to motor neurons expressing only GFP. However, treatment with TCH-165 resulted in a significant increase in survival (88 percent) in the presence of the poly-GR DPR proteins (Figure 2.8A), whereas treatment of control neurons not expressing a DPR protein with TCH-165 had no effect on motor neuron survival (data shown in Figure 2.25 of the Appendix). Similarly, expression of GFP-PR₅₀ resulted in significant neurotoxicity, with a decrease in motor neuron survival to 43 percent when compared to motor neurons expressing only GFP. Again, treatment with TCH-165 resulted in a significant increase in motor neuron survival (83 percent) in the presence of the poly-PR DPR proteins (Figure 2.8B). Similar results were obtained in cortical neurons expressing GFP-GA₅₀ (data shown in Figure 2.26 of the Appendix). These data suggest that protection of UPS function by TCH-165 protects the neuron from DPR protein induced toxicity.

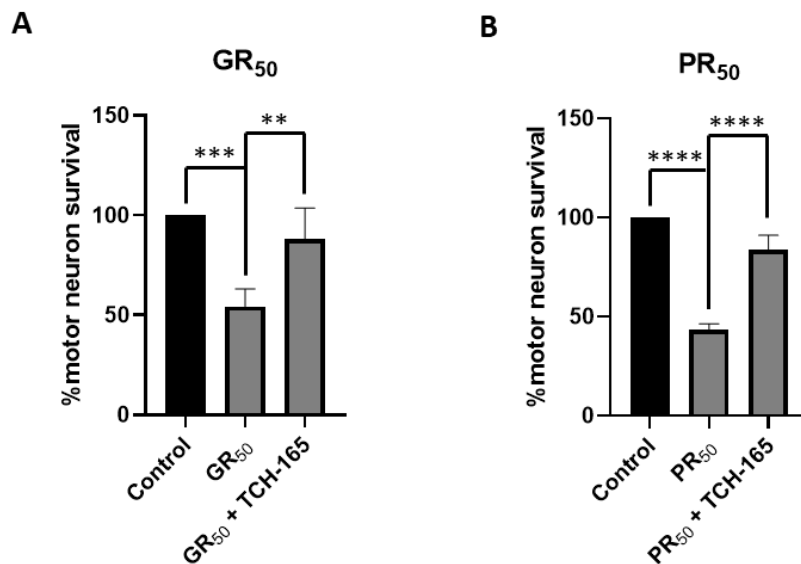


Figure 2.8 TCH-165 provides neuroprotection in the presence of poly-GR and poly-PR DPR proteins in rat spinal cord neurons. (A) Quantification of motor neuron survival following treatment with control (GFP with DMSO), GFP-GR₅₀ (with DMSO), or GFP-GR₅₀ (with 3 μM TCH-165); (n=4); one-way ANOVA (ns, not significant, *p ≤0.05; **p≤0.01; ***p≤0.001; ****p≤0.0001). (B) Quantification of motor neuron survival following treatment with control (GFP with DMSO), GFP-PR₅₀ (with DMSO), or GFP-PR₅₀ (with 3 μM TCH-165); (n=3); one-way ANOVA (ns, not significant, *p ≤0.05; **p≤0.01; ***p≤0.001; ****p≤0.0001).

2.2.4 Deciphering the Mechanism of 20S Proteasome Impairment by DPR Proteins

As previously mentioned, a number of neurodegenerative diseases have been characterized by an accumulation of aggregation-prone IDPs and results in dysregulation of proteasome function.⁵²⁻⁵⁴ This loss in proteostasis is a major contributing factor to the pathogenesis of neurodegeneration.⁵⁵⁻⁵⁸ Although it has been shown that IDP aggregates directly inhibit both the 26S and 20S proteasomes, the mechanism by which IDP aggregates inhibit the proteasome has yet to be fully elucidated. Recently, a mechanistic model was proposed suggesting that IDP oligomers (i.e. amyloid- β and α -synuclein) allosterically inhibit the 20S proteasome by binding to the outer side of the 20S proteasome.³⁸ In this model, it was proposed that IDP oligomers bind to the outer surface between the α -ring and β -ring, resulting in a conformational change that allosterically stabilizes the closed gate conformation of the proteasome and restricts access of substrates to the proteolytic core for degradation.³⁸ There is evidence suggesting that the DPR proteins may interact differently. A recent study showed that poly-GA DPR proteins entangle proteasomes into large ribbon-like aggregates, trapping them in a state of stalled degradation.⁵⁹ To begin deciphering the mechanism of 20S proteasome impairment by the arginine-rich DPR proteins, I aimed to identify where the DPR aggregates bind the 20S proteasome through use of negative staining and electron microscopy. These studies were done in collaboration with Dr. Sundharraman Subramanian and Dr. Kristin Parent at the RTSF Cryo-EM Core Facility at Michigan State University.

Negative staining is a technique used in microscopy in which samples are applied to a small grid consisting of many small squares where the sample is retained. A variety of stains can then be used to enhance the contrast between the background of the grid and the protein sample. In the studies discussed in this chapter, a uranyl acetate stain is used as it strongly scatters electrons and effectively adsorbs to biological material. The stained grids are then visualized using an electron microscope which detects differences in electron density across the grid. It is important to note that high protein concentrations are typically required for this technique to ensure adequate protein particles are deposited on the grid for visualization.

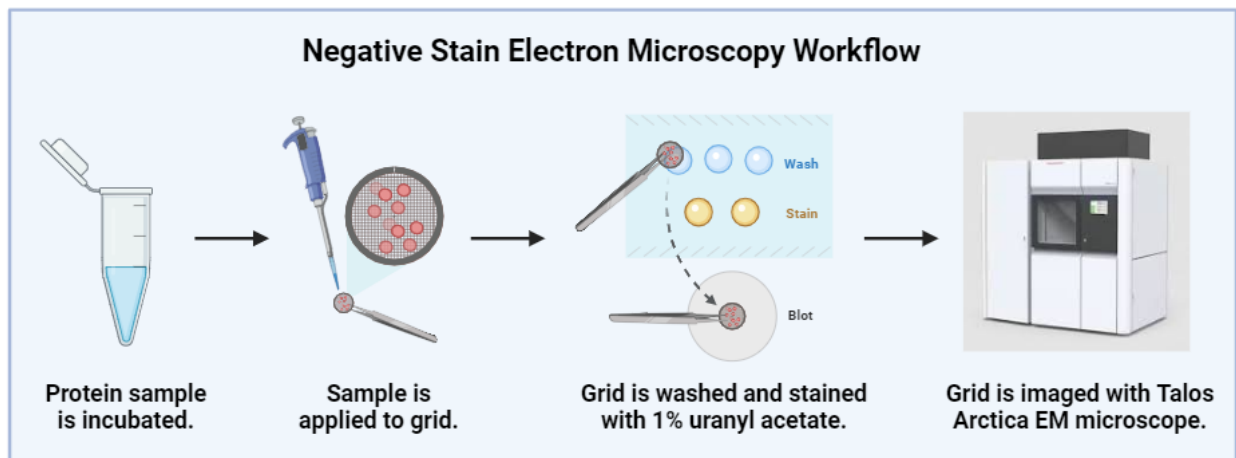


Figure 2.9 General workflow used for negative stain electron microscopy experiments.

For my initial negative stain experiment, the conditions used in the 20S proteasome impairment activity assay discussed above were replicated in an attempt to provide visual evidence for how the 20S proteasome is impaired. In this assay, purified 20S proteasome (70 nM) was pretreated with DMSO or TCH-165 (10 μ M), followed by incubation with HA-PR₂₀ DPR proteins (875 nM; 12.5 to 1 ratio of DPR:20S) for 30 minutes at 37 °C. The samples were then applied to continuous carbon support film Cu grids and stained with 1% uranyl acetate and visualized by electron microscopy. The results showed that in the absence of the HA-PR₂₀ DPR proteins, the 20S proteasomes were found evenly dispersed on the sample grid (Figure 2.10A). However, in the presence of the HA-PR₂₀ DPR proteins, the 20S proteasomes were predominantly found in large aggregates with few free proteasomes (Figure 2.10B). This recruitment of 20S proteasomes is consistent with reports that demonstrate poly-GA DPR proteins entangle proteasomes into large ribbon-like poly-GA aggregates.⁵⁹ Remarkably, when the 20S proteasomes were pretreated with TCH-165 (10 μ M), this recruitment of 20S proteasomes into large aggregates was largely prevented, with much smaller aggregates present and a high number of free 20S proteasomes on the grid (Figure 2.10C). Additionally, the HA-PR₂₀ DPR proteins alone showed only very small spherical aggregates (Figure 2.10D). These results in combination with the activity assay results discussed above (Figure 2.4 and 2.5), suggest that 20S proteasome impairment by the arginine-rich DPR proteins may be the result of recruitment of 20S proteasomes into large DPR protein aggregates.

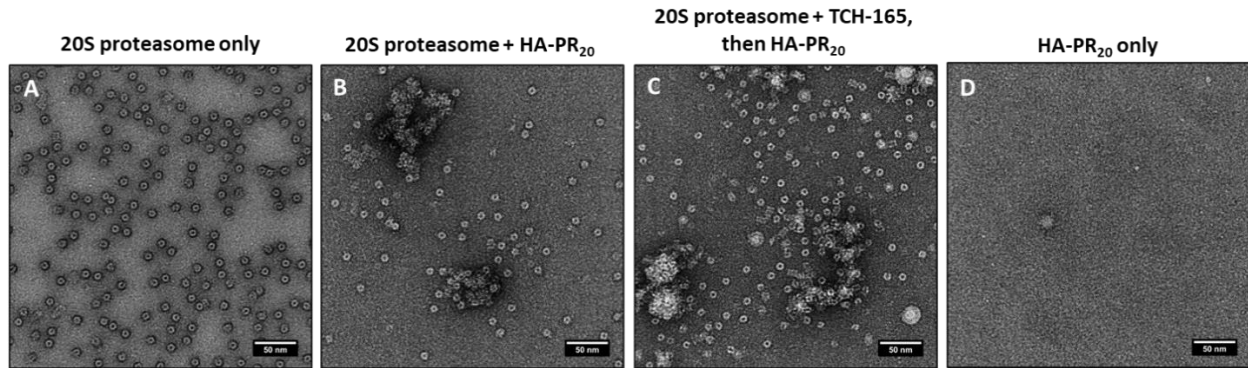


Figure 2.10 Negative stain electron microscopy images. (A) Purified 20S proteasome only. (B) Purified 20S proteasome treated with vehicle (DMSO), followed by incubation with HA-PR₂₀ DPR proteins. (C) Purified 20S proteasome pretreated with TCH-165 (10 μ M), followed by incubation with HA-PR₂₀ DPR proteins. (D) HA-PR₂₀ DPR proteins only.

To explore how the DPR-induced aggregation would change over time, additional time points were included in the next experiment. My hypothesis was that the vehicle (20S + HA-PR₂₀) sample would either maintain or continue to aggregate into these large proteasome/DPR aggregates. However, I anticipated that the TCH-165 treated sample would become less aggregated over time either through enhanced DPR degradation or through an allosteric mechanism which prevents the DPR from binding the 20S proteasomes. While the results of the 30-minute time point were reproducible (Figures 2.11E and 2.11I), the results of the extended time points did not support this hypothesis. After a 2-hour incubation with the HA-PR₂₀ DPR protein, both the vehicle and TCH-165 treated proteasomes were predominantly found in large aggregates (Figures 2.11F and 2.11J). The same results were observed for the 4-hour and 8-hour samples, suggesting that the aggregate formation is irreversible within the time frame of this experiment.

In all, the results suggest that treatment of the 20S proteasomes with TCH-165 slows the aggregation or interaction between the 20S proteasomes and DPR proteins, as evident by the 30-minute time point. However, once the proteasomes have been recruited into these large DPR protein aggregates, TCH-165 is unable to liberate the proteasomes from the aggregates. These results are supported by the activity results discussed above (Figures 2.4 and 2.5). The activity results showed that TCH-165 was able to prevent 20S impairment by the poly-PR DPRs when the 20S proteasome was first pretreated with TCH-165 prior to incubation with HA-PR₂₀. However,

when 20S proteasome was incubated with HA-PR₂₀ prior to treatment with TCH-165, the 20S activator was unable to overcome 20S proteasome impairment by the DPR proteins.

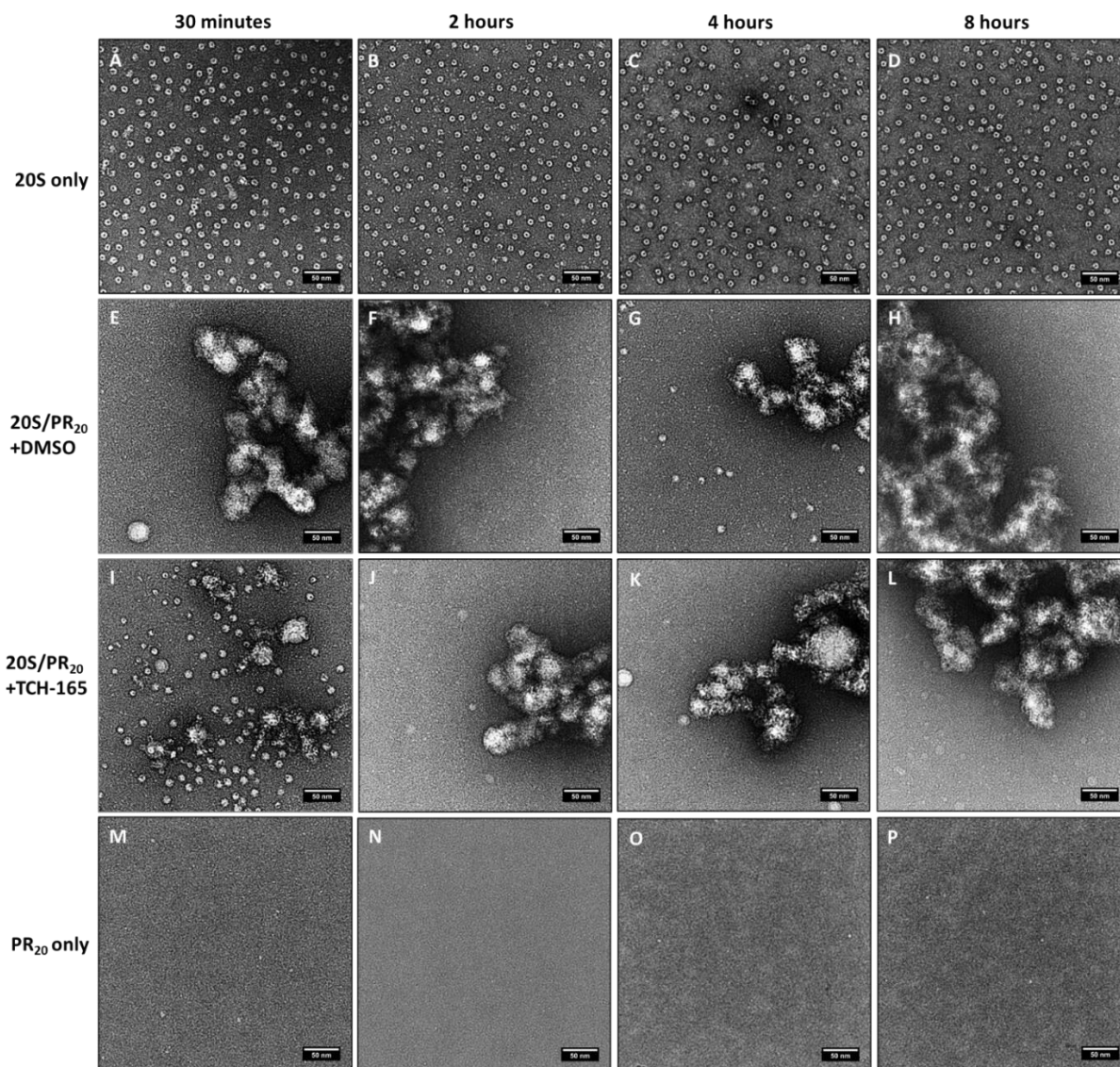


Figure 2.11 Negative stain electron microscopy images. (A-D) Representative images of purified 20S proteasome only with DMSO at various time points. (E-H) Representative images of purified 20S proteasome treated with DMSO, followed by HA-PR₂₀ DPR proteins at various time points. (I-L) Representative images of purified 20S proteasome pretreated with TCH-165 (10 μ M), followed by HA-PR₂₀ DPR proteins at various time points. (M-P) Representative images of purified HA-PR₂₀ DPR proteins only with DMSO at various time points.

While there were clear trends in these negative stain experiments, further optimization of the assay conditions was conducted in an effort to obtain more dramatic differences between the vehicle (20S + HA-PR₂₀) and TCH-165 treated samples. Although differences between the

vehicle and TCH-165 samples were quite evident in the 30-minute time point, each of the samples contained some aggregates and some free proteasomes. Since the negative stain experiment is not a quantitative assay, it is important that any trends are ubiquitous across the entire sample grid. To optimize the negative stain assay conditions, the proteasome activity assay previously discussed was used as it is more cost effective. This was done to ensure assay conditions were ideal to see very large, dramatic differences in 20S proteasome activity between the vehicle and TCH-165 treated samples. If 20S proteasome impairment by the DPR proteins is a result of 20S proteasomes being recruited into large DPR protein aggregates, then decreases in 20S proteasome activity in the activity assay should indicate large aggregate formation.

To begin optimizing, I hypothesized that increasing the amount of HA-PR₂₀ and a longer incubation time of the 20S proteasome and DPR protein could be utilized. This was largely based on the results obtained in the purified HA-PR₂₀ degradation assay in which a DPR:20S ratio of 250:1 and an 8-hour incubation of the 20S proteasome and DPR protein was used. The results of this experiment showed that following the 8-hour incubation with HA-PR₂₀ DPR proteins, TCH-165 treated proteasomes resulted in significant degradation of HA-PR₂₀, with only 37 percent remaining compared to untreated control proteasomes. It is anticipated that with this much of the DPR protein degraded, the DPR's ability to impair the proteasome should be dramatically reduced under these conditions. However, the untreated control proteasome having significantly more DPR protein left undegraded, should result in greater 20S proteasome impairment.

To determine how the increased DPR:20S ratio and longer incubation time would affect proteasome activity, the DPR:20S ratio was increased to 125:1 and three incubation times were tested. Although almost complete proteasome inhibition was observed in the vehicle samples at each of the three incubation times, TCH-165 was unable to prevent proteasome impairment under these conditions (Figure 2.12A). This result was unexpected, as at 8 hours in the *in vitro* HA-PR₂₀ digestion assay, only a small amount of HA-PR₂₀ remained which could impair the proteasome. To determine the cause of the discrepancy in the results of the two assays, the experimental conditions were compared. It was determined that the presence or absence of sodium chloride in the buffer is a possible culprit. In the above *in vitro* activity assays and negative stain experiments discussed thus far, a 38 mM Tris-HCl (pH 7.8) buffer was used. However, in the

digestion assays of both the HA-GR₂₀ and HA-PR₂₀, a 38 mM Tris-HCl, 100 mM NaCl (pH 7.8) buffer was used. Since sodium chloride has shown to lower the activity of the proteasome in *in vitro* fluorogenic peptide degradation assays, I had designed the activity assay without sodium chloride in the buffer to ensure proteasome activity was robust enough to observe inhibition evoked by the DPR proteins. However, the results in Figure 2.12 suggest that sodium chloride may affect DPR-induced proteasome impairment.

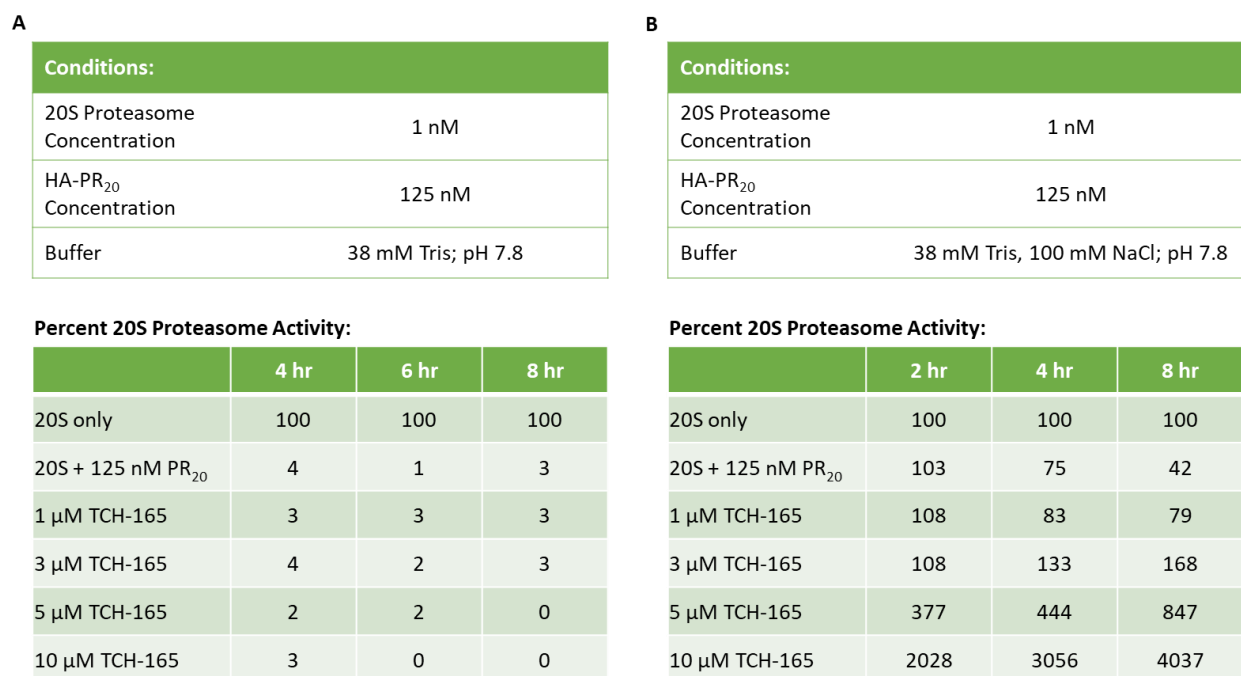


Figure 2.12 TCH-165 provides protection against 20S proteasome impairment by HA-PR₂₀ in the presence of sodium chloride at high DPR to 20S proteasome ratio. 20S proteasome pretreated with DMSO or TCH-165, followed by incubation with HA-PR₂₀ (125 nM; 125:1 DPR to 20S ratio) in 38 mM Tris-HCl buffer (A) or 38 mM Tris-HCl with 100 mM NaCl buffer (B). Proteolytic activity was measured by the degradation of fluorogenic substrate probe Suc-LLVY-AMC.

To test the hypothesis of whether sodium chloride affects DPR protein-induced proteasome impairment, 100 mM sodium chloride was added to the buffer and the above assay was repeated. As in the previous experiment, 20S proteasome was pretreated with DMSO or drug for 15 minutes, followed by incubation with HA-PR₂₀. Comparison of the 4-hour and 8-hour time points in the two experiments in Figure 2.12, shows that addition of sodium chloride into the buffer had a significant effect on DPR-induced proteasome impairment. The vehicle (20S + HA-PR₂₀) sample without sodium chloride in the buffer was almost completely inhibited at the 4, 6 and 8-hour time points. However, in the experiment with sodium chloride present in the buffer,

the vehicle sample was only inhibited by 25 percent at the 4-hour time point and by 58 percent at the 8-hour time point. Furthermore, while TCH-165 was unable to prevent the DPR-induced proteasome impairment in the absence of sodium chloride in the buffer using this high DPR:20S ratio, TCH-165 effectively prevented 20S impairment at both the 4 and 8-hour time points with sodium chloride present in the buffer.

While the mechanism by which sodium chloride effects DPR-induced proteasome impairment cannot be concluded from this assay, it is possible that the sodium chloride affects either the rate, strength, or the morphology of any protein-protein interactions that induce proteasome impairment (i.e. aggregation of HA-PR₂₀ itself, or PR₂₀-20S interactions). Furthermore, the absence or presence of sodium chloride seems to impact the ability of TCH-165 to prevent DPR-induced 20S proteasome impairment. The decreased ability of TCH-165 to prevent 20S impairment in absence of sodium chloride may be due to multiple reasons. For instance, sodium chloride may be necessary for TCH-165 to activate the 20S proteasome effectively, or sodium chloride may be necessary for TCH-165 to interrupt the protein-protein interaction between the 20S proteasome and DPR proteins.

The addition of sodium chloride to the assay buffer resulted in the more efficient prevention of DPR-induced 20S impairment by TCH-165 when the DPR:20S ratio was high (125:1), resulting in large differences in 20S proteasome activity between the vehicle (20S + HA-PR₂₀) and TCH-165 treated samples ($\geq 5 \mu\text{M}$). However, it is important to note that the activity assays used to optimize the negative stain experiment were conducted using only 1 nM 20S proteasome, conversely to the 70 nM used in the negative stain experiments. Therefore, the last step before returning to the electron microscopy imaging was to confirm similar activity results were observed using the higher protein concentrations necessary for imaging.

In the evaluation of the impact of higher protein concentrations on proteasomal impairment, various DPR:20S ratios were tested using 70 nM 20S proteasome (Figure 2.13). While concentration dependent inhibition was observed with increasing concentration of HA-PR₂₀, the large differences between the vehicle and TCH-165 treated samples shown in previous activity assays (using 1 nM 20S proteasome) was not observed. I hypothesized that the skewed drug:20S ratio at the high proteasome concentrations required for the electron microscopy

studies led to the minor differences observed between the activities of the vehicle and TCH-165 treated samples. For the activity assays in which 1 nM 20S proteasome was treated with 10 μ M TCH-165 to significantly prevent proteasome impairment, the drug:20S ratio equates to 10,000:1. However with the 70 nM concentration of 20S proteasome used for the microscopy studies, this ratio is significantly reduced to 143:1 using the same 10 μ M dose. The change in drug:20S ratio may explain why differences were not observed between the vehicle and TCH-165 treated samples using this low TCH-165 dose in the experiment in Figure 2.13. Furthermore, it may provide insight as to why more dramatic differences between the vehicle and TCH-165 treated samples were not observed in the previous negative stain experiments.

20S Proteasome Activity:

	RFU
Vehicle (12.5:1)	5.470
10 μ M TCH-165 (12.5:1)	5.532
Vehicle (25:1)	4.722
10 μ M TCH-165 (25:1)	4.515
Vehicle (50:1)	3.892
10 μ M TCH-165 (50:1)	3.866
Vehicle (100:1)	4.113
10 μ M TCH-165 (100:1)	4.105

Conditions:	
20S proteasome concentration	70 nM
HA-PR ₂₀ concentration	875, 1750, 3500 or 7000 nM
Buffer	38 mM Tris, 100 mM NaCl; pH 7.8

Figure 2.13 High 20S proteasome concentration used for microscopy studies diminishes the ability of a low dose of TCH-165 to provide protection against 20S proteasome impairment by HA-PR₂₀. 20S proteasome (70 nM) was pretreated with DMSO or TCH-165 (10 μ M), followed by incubation with HA-PR₂₀ (875, 1750, 3500, or 7000 nM) in 38 mM Tris-HCl with 100 mM NaCl buffer. 20S proteasome activity was measured using the degradation of fluorogenic substrate probe Suc-LLVY-AMC.

The above findings show that TCH-165 has a greater effect toward preventing DPR-induced proteasome impairment with sodium chloride present in the buffer. Additionally, I hypothesize that a higher drug:20S ratio is required for increased differences between the vehicle and TCH-165 treated samples. Therefore, another negative stain experiment was planned using the conditions listed in Figure 2.14A. To increase the drug:20S ratio in this experiment, the concentration of 20S proteasome was decreased from 70 nM to 40 nM, and TCH-165 was increased to 200 μ M. This allowed for a 5,000:1 drug to proteasome ratio to be achieved, which has shown to allow for large differences in 20S activity between vehicle and TCH-165 treated

samples. In addition, the DMSO concentration was increased to 2% since drug solubility was a concern at this high concentration. Although, if solubility issues did occur, following application of the samples to the grid the grids are washed three times with water, therefore, any insoluble TCH-165 should be removed from the grid during that step.

Prior to imaging the samples prepared for the negative stain experiment, I conducted an activity assay using a small aliquot of the samples to ensure that the new negative stain conditions used in this experiment resulted in differences in 20S proteasome activity. As anticipated, treatment of 20S proteasome alone with TCH-165 resulted in almost a 300 percent increase in 20S proteasome activity compared to 20S proteasome treated with DMSO (Figure 2.14B). Furthermore, incubation of 20S proteasome incubated with DMSO, followed by incubation with HA-PR₂₀ resulted in proteasome impairment, with only 15 percent proteasome activity remaining compared to the 20S proteasome only sample. Gratifyingly, treatment with TCH-165 preserved this proteasome impairment with 104 percent 20S proteasome activity remaining in the presence of HA-PR₂₀. Therefore, it seemed that the negative stain conditions had been optimized to see the desired degree of difference between the samples. However, when the samples were imaged by electron microscopy, this was not observed.

As before, in the 20S proteasome only sample, the 20S proteasomes were found evenly dispersed across the grid (Figure 2.14C1). However, the high concentration of TCH-165 used here was observed to have major solubility issues. While the wash step was predicted to remove any insoluble TCH-165, the drug appeared to precipitate small clusters of the proteins which were not completely washed away (Figure 2.14C2). Since the experiment aims to investigate protein-protein interactions, any component of the experiment that also affects aggregation cannot be included. Lastly, incubation of the 20S proteasome with HA-PR₂₀ and DMSO in the vehicle treated sample did not result in the large aggregates observed in previous negative stain experiments (Figure 2.14C3). The lack of large aggregates was unexpected as the activity results of this exact sample showed only 15 percent proteasome activity remaining compared to the 20S proteasome only sample. This discrepancy could be due to a few reasons, including the formation of such large aggregates that they are precipitated out prior to grid preparation, or the large aggregates do not remain on the grid during the wash step. Another possibility is that addition of sodium

chloride to the buffer modifies the manner in which the HA-PR₂₀ DPR proteins impair 20S proteasome function. Perhaps in the presence of sodium chloride, binding of HA-PR₂₀ is much more localized to individual proteasomes, as has been suggested for α -synuclein and amyloid- β .³⁸ While this observation is not useful in the case of the negative stain experiments, these conditions could be useful for attempting to obtain a cryo-EM structure of an individual 20S proteasome bound to an HA-PR₂₀ aggregate. Structure reconstruction of large amorphous aggregates of DPRs and multiple 20S proteasomes would be extremely difficult to solve, however, localized binding of a small DPR protein aggregate to an individual 20S proteasome may be more easily reconstructed to determine the DPR protein binding site.

A

Negative Stain Experimental Conditions:

	Initial Conditions	Newly Optimized
Buffer	38 mM Tris (pH 7.8)	38 mM Tris, 100 mM NaCl, (pH 7.8)
20S conc.	70 nM	40 nM
PR ₂₀ conc.	875 nM (12.5:1)	5,000 nM (125:1)
TCH-165 conc.	10 μM (143:1 drug:20S)	200 μM (5,000:1 drug:20S)
DMSO	1%	2%

B

20S Activity Data for Imaged Samples:

	% 20S Proteasome Activity
20S only + DMSO	100
20S only + TCH-165 (200 μM)	273*
20S + PR ₂₀ + DMSO	15
20S + PR ₂₀ + TCH-165 (200 μM)	104

*Due to high concentration of 20S, substrate was fully consumed prior to completion of kinetic readings.

C

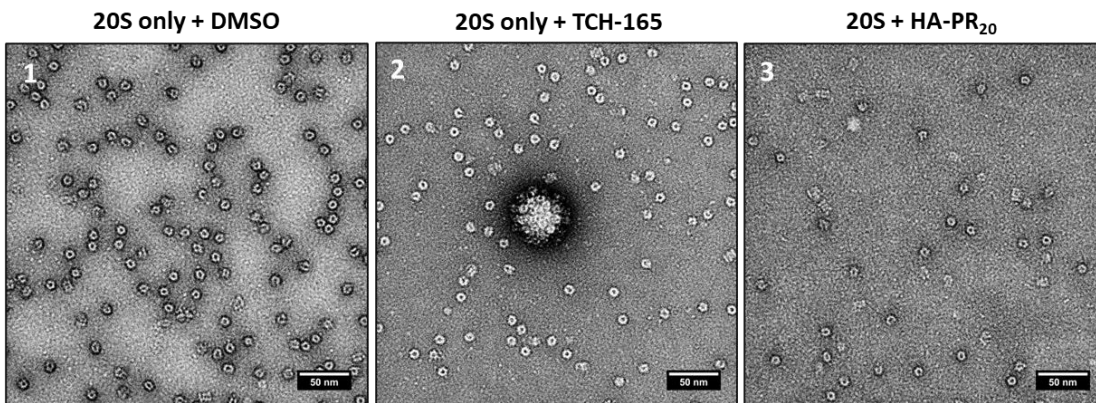


Figure 2.14 Experiment results using the new negative stain conditions. (A) Table of previous and new negative stain conditions. (B) 20S proteasome pretreated with DMSO or TCH-165, followed by incubation with HA-PR₂₀ (125 nM; 125:1 DPR to 20S ratio) in 38 mM Tris-HCl with 100 mM NaCl buffer. Proteolytic activity was measured by the degradation of fluorogenic substrate probe Suc-LLVY-AMC. (C) Negative stain electron microscopy images (1) Image of purified 20S proteasome only treated with DMSO (2) Image of purified 20S proteasome only treated with TCH-165 (200 μM) (3) Image of purified 20S proteasome treated with DMSO, followed by incubation with HA-PR₂₀ DPR proteins.

2.2.5 Future Work

While the newly “optimized” conditions for the negative stain experiment did not produce successful images, they did provide a lot of insight into how to move forward with further mechanistic studies using the negative stain technique. In the case of the earlier experiments when sodium chloride was not included in the buffer, following a 30-minute incubation the vehicle (20S + HA-PR₂₀) sample was found to be in a largely aggregated state, whereas the TCH-165 treated proteasomes were found predominately in a free state. Conversely, when sodium chloride was included in the buffer, the vehicle was found to be almost entirely inhibited, yet in a free state.

The opposing findings raise the question of which buffer provides the most physiological and disease-relevant results. Since the poly-PR DPR proteins are highly positively charged, a recent study discussing the effect of various salts on the aggregation of charged peptides in water may provide insight.⁶³ In this work, the authors studied the effects of sodium, potassium and magnesium salts on the aggregation of a highly charged protein. The results showed that compared to the aggregation of the protein in water, the size and morphology of the protein aggregates varied greatly upon addition of the different ions.⁶³ With this in mind, I am inclined to say that the negative staining results using the buffer without sodium chloride may be the more physiologically relevant results. Although the body contains many sodium ions, it also contains potassium, magnesium, and many other ions that could also affect the aggregation of the poly-PR DPR proteins. Therefore, the removal of all from the buffer may be best for these *in vitro* experiments, since we aim to visualize the effect of HA-PR₂₀ on aggregation of the proteasome and not any erroneous aggregation effects due to salts in the buffer.

While the mechanism of 20S proteasome impairment by poly-PR DPR proteins remains undetermined, I hypothesize that the initial negative staining results (Figures 2.10 and 2.11) may provide the most accurate representation of the proteasome impairment observed in the rat cortical neurons. With respect to the cellular studies, in the case of the poly-GR DPR proteins, we observed that a reduction in their amount correlated with protection from UPS impairment, suggesting the enhanced proteasomal clearance provides the protection. However, in the neuron studies exploring the poly-PR DPR proteins, we found that even when a reduction in their amount

was not observed, protection of proteasome function was achieved, suggesting an allosteric mechanism of protection. As the incubation time for both the cellular PR₅₀ experiment and the early negative stain experiment was rather short to allow for enhanced degradation of the poly-PR DPR proteins, any protection observed by TCH-165 treatment in these experiments is likely the result of an allosteric mechanism.

To further explore whether this allosteric mechanism involves the prevention of proteasome recruitment into large DPR protein aggregates, as observed in the initial negative stain experiments, I propose the following modifications to the experimental conditions should be explored. One possible modification could be to conduct the experiment using a higher drug:20S ratio without sodium chloride in the buffer. However, the altered drug:20S ratio should be achieved by reducing the 20S proteasome concentration, not through increase of the drug concentration, to avoid drug solubility issues. In the initial experiment, 70 nM 20S proteasome was used to ensure adequate proteasome particles would be present on the sample grid. However, through the optimization discussed, the proteasome concentration was reduced to 40 nM and resulted in an adequate amount of proteasome particles on the grid. Preliminary results suggest a proteasome concentration as low as 20 nM may be used in the experiment. Another possible modification could be a slight increase of the DPR:20S ratio, as a higher DPR:20S ratio was never visualized by electron microscopy without sodium chloride in the buffer. Furthermore, additional 20S proteasome activators with increased solubility should be explored.

Despite the unelucidated mechanism of how the DPR proteins impair the 20S proteasome, the above results provide overwhelming evidence that activation of the 20S proteasome by TCH-165 provides protection from proteasome impairment. This ultimately led to protection from DPR-induced neurotoxicity and suggests small molecule 20S proteasome activation is an exciting avenue to explore toward developing a novel therapeutic for the treatment of ALS.

2.2.6 Investigating the Binding Site of Small Molecule 20S Proteasome Activators with Cryo-EM

Utilization of the structural biology techniques discussed in the previous section led to another exciting project with the goal of determining the binding site of a 20S proteasome activator. Mechanistic evidence has shown that TCH-165 induces an open gate conformation of

the 20S proteasome, resulting in enhanced 20S proteolytic activity.³⁹ While molecular docking studies predict that TCH-165 and other small molecules bind into the intersubunit pockets on the α -ring to induce this open gate conformation, the binding site of the ligands remain to be elucidated.^{39,41,42} Discovery of the ligand binding site would have vast impacts on the further development of 20S proteasome activation as a therapeutic strategy, significantly increasing the sophistication of small molecule design and advancing SAR studies of 20S activator scaffolds. Furthermore, if the ligand binding site is determined to be the intersubunit pockets of the α -ring as predicted, the molecular docking model currently being used to predict ligand binding sites and ligand-receptor interactions would be validated. Further discussion of the molecular docking studies being conducted in the Tepe lab will be discussed in Chapter 3.

To determine the binding site of a 20S proteasome activator, we propose cryogenic electron microscopy (cryo-EM) can be utilized. While no structures of a 20S proteasome with a small molecule 20S activator bound have been solved, structures have been reported with bound proteasome inhibitors.⁶⁴⁻⁶⁶ Furthermore, structures of 20S proteasomes bound to their endogenous protein activator caps have been solved.⁶⁷⁻⁶⁹ A recent structure has taken this a step further, replacing the typical tails found on one of these endogenous protein activator caps with a synthetic peptide analogue.⁷⁰ These latter studies have revealed conformational changes associated with gate opening resulting from activation by the endogenous protein activator caps.⁷⁰ In the Tepe lab, we aimed to determine the binding site of a 20S proteasome activator and determine the conformational changes associated with small molecule 20S proteasome activation. The cryo-EM studies discussed in this chapter were conducted in collaboration with Dr. Sundharraman Subramanian and Dr. Kristin Parent at the RTSF Cryo-EM Core Facility at Michigan State University. In the following studies, my focus was on the design of the experiments and method development, while Dr. Subramanian's focus was the data acquisition and data processing.

Cryogenic electron microscopy (cryo-EM) is a structural biology technique used to determine the structure of biological molecules and has been used to determine the structure of many proteins, viruses, and other cellular components. The technique involves the flash-freezing of solutions of proteins or other biological molecules, which are subsequently bombarded with a

beam of electrons to produce microscope images of individual molecules in a variety of 2D orientations. The obtained images are then averaged to reconstruct the 3D structure of the biomolecule, providing important insight into protein functions, how proteins malfunction in disease, and how proteins can be targeted with drugs.

As one would expect, the cryo-EM workflow consists of multiple steps that must be optimized in order to obtain a high-resolution 3D structure of a protein. A high-resolution structure ($\leq 3 \text{ \AA}$) is one in which every atom in the electron density map is resolved to recognition. While a low-resolution structure ($>3 \text{ \AA}$) only shows the basic contours of protein chains and individual atoms cannot be concretely identified. Therefore, a high-resolution structure is the goal of the work in this chapter, as this would allow for the resolution of individual amino acids to determine key binding interactions between the 20S proteasome and small molecule activator ligand. While optimization of the individual parameters will be discussed in detail later in the chapter, the general workflow used for cryo-EM studies is as follows (Figure 2.15).

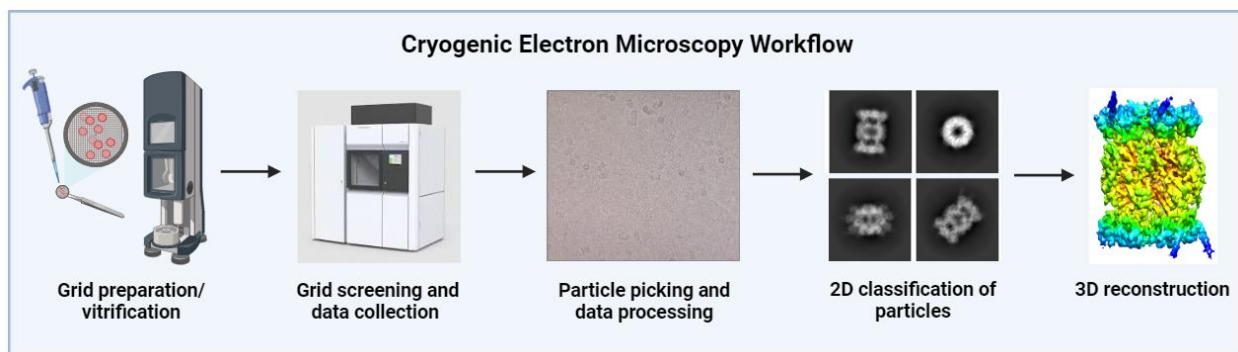


Figure 2.15 General workflow of cryogenic electron microscopy (cryo-EM) experiments.

The EM grids are made of a conductive material, such as copper, and consist of hundreds of small holes in which the sample will be frozen. Prior to sample application, the grids are typically treated with a low-energy glow discharge plasma under reduced pressure in atmospheric air. The ions generated during this process remove any residual organic contaminants and reduce the hydrophobicity of the grids.⁷¹ The increased hydrophilicity of the grids aids in spreading of aqueous solutions on the grid. The sample is then applied to the grid and immediately blotted with filter paper using a semi-automated apparatus (i.e. Vitrobot Mark IV) to create a thin film of protein/buffer on the grid. The grid is then plunged into liquid ethane

by the Vitrobot to form a vitreous layer of ice, freezing the protein sample in an amorphous state within the holes of the grid.⁷¹ The vitrification allows for such rapid freezing of the sample that it prevents the formation of ice crystals that significantly reduce the quality of ice and images collected. The blotting time is often a vital step that must be optimized, as it controls the ice thickness on the grids. If the ice is too thick, electrons may undergo multiple scattering events reducing image quality and decreasing phase contrast of the images.⁷² Since particles are picked during image collection by phase contrast, decreased phase contrast results in a fewer number of particles picked and reduced resolution of the final structure. However, if the ice is too thin, the sample will not remain frozen within the holes of the grid. Once the grids have been prepared, they are then screened for quality. During this screen the ice thickness is examined, the grids are inspected for the presence of ice crystals, and the number of protein particles within the grid squares is assessed. When a high-quality grid is selected, image collection begins and often occurs over the course of multiple days. During image collection, the software picks particles which are sorted into multiple 2D classes based on orientation of the particles.⁷³ Following image collection, classes of 2D orientations are selected to be averaged for 3D reconstruction of the protein to determine its structure.⁷³

2.2.7 Challenges of Solving a Cryo-EM Structure of the 20S Proteasome

While structures of the proteasome have been solved using cryo-EM, a large majority of the structures solved are of archaeal 20S proteasomes, such as the *Thermoplasma acidophilum* 20S proteasome (T20S proteasome).⁷⁴ In fact, archaeal 20S proteasomes have been extensively studied with great success due to the lower complexity of their structure in comparison to eukaryotic 20S proteasomes. The human 20S proteasome is comprised of hetero-heptameric rings of seven different α -subunits and seven β -subunits, resulting in *C2* symmetry.⁷⁵ However, the T20S proteasome is comprised of homo-heptameric rings of just one α -subunit and one β -subunit, resulting in a higher order *D7* symmetry.^{74,75} The greater symmetry of the T20S proteasome allows for a seven-fold increase in internal averaging of the T20S subunits compared to that of the human 20S proteasome.⁷⁵ With an increase in internal averaging, fewer 2D images are required for 3D structure reconstruction. It is worth noting here that I expressed and purified T20S proteasome with the hopes of using it in my own cryo-EM studies. However, I found that

our 20S proteasome activators were unable to effectively enhance activity of the T20S proteasome, suggesting that they may not efficiently bind to the T20S proteasome (data shown in Figure 2.27 of the Appendix).

Due to the lack of symmetry in the human 20S proteasome, a greater number of 2D images with high counts of proteasome particles per image need to be collected for 3D reconstruction. However, a higher number of particles often requires the use of increased protein concentrations, which may be disadvantageous in our studies. As discussed with the negative stain experiments above, a high protein concentration skewed the drug:20S ratio. While a concentration of drug that allows for 20S proteasome activation is not necessarily required to see a bound ligand, surely use of a concentration that did modulate 20S proteasome activity would ensure that the ligand was bound, and an open gate conformation is likely induced. However, with high proteasome concentrations needed for cryo-EM, our 20S proteasome activators would likely be insoluble at the concentrations needed to activate this high concentration of proteasome (as observed in the negative stain experiments previously discussed). Therefore, I hypothesized that keeping the protein concentration low would likely be advantageous for our studies.

Another reason the human 20S proteasome has become a notoriously challenging protein structure to solve with cryo-EM, is due to a preferred orientation issue on the grid. As previously stated, prior to application of the sample to the grid, the grids are glow discharged. Glow discharging of the grids occurs in an apparatus under partial vacuum in atmospheric air to apply a negative charge to the grid. The process renders the surface of the grid hydrophilic and allows more of the aqueous sample to be retained. However, in the case of the human 20S proteasome, this traditional glow discharge process is known to cause a preferred orientation of 20S proteasome particles on the grid. It has been shown that under these conditions, the outer surface of the α -ring of the 20S proteasome preferentially interacts with the grid, resulting in a strong preferred top-view orientation of 20S proteasomes on the grid.^{75,76} This high prevalence of top-view proteasomes can be seen in the 20S proteasome only samples of the negative stain experiments discussed in this chapter. This preferred orientation is extremely unfavorable for cryo-EM studies, as it is essential that the orientation of protein particles on the grid are in highly

randomized orientations. The randomized orientation allows for 2D images to be captured from all angles of individual particles, so that the full 3D structure of the proteasome may be resolved without any “blind spots.” For example, if only top-view (α -ring) orientations of the proteasome were captured in the 2D images, only the 3D structure of the α -ring would be able to be reconstructed successfully. Therefore, unless the preferred orientation issue can be solved, a higher protein concentration will likely need to be used, as this would increase the probability of obtaining 2D images of side-view and other non-top-view orientations of the particles. However, again, unfortunately increasing protein concentration would further decrease the drug:20S ratio and possibly reduce chances of obtaining a high number of ligand-bound 20S proteasomes.

To overcome these known challenges regarding the use of the human 20S proteasome as a cryo-EM substrate, the proteasome concentration, glow discharge process, and grid preparation parameters (i.e. grid type, blot time) required substantial optimization before a high-resolution structure of the 20S proteasome could be obtained. It was essential that a method to obtain a high-resolution 20S proteasome structure be developed before a ligand was introduced, because if the resolution of the proteasome structure is low, any bound ligand would be undetectable. The optimization studies conducted to develop this method will be discussed herein.

2.2.8 Goals for Obtaining a High-Resolution Structure of the 20S Proteasome

Prior to my time in the Tepe lab, an initial attempt was conducted to obtain a cryo-EM structure of TCH-165 bound to the 20S proteasome. This initial study was conducted with a 20S proteasome concentration of 2.5 mg/mL in an attempt to ensure enough proteasome particles would be present on the grid. Additionally, the hope was that this high protein concentration would also allow for a sufficient collection of non-top-view 2D images for reconstruction. The drug was then added to a final concentration of 200 μ M. While this concentration pushed the solubility limits of TCH-165, any insoluble TCH-165 particulate matter could later be filtered out prior to grid preparation. However, following analysis of the data, the resolution of the resulting structure was determined to be between 7-8 Å. Analysis of the 2D images showed a strong preferred orientation issue, with almost all top-view orientations of the 20S proteasome. Due to the low resolution of the structure, it could not be determined whether the small molecule 20S

activator was bound. While further image collection can often be performed to increase the resolution, the data set here was not high enough quality to warrant further image collection.

With the known challenges associated with utilizing the 20S proteasome in cryo-EM studies, and the issues experienced in the Tepe lab's initial cryo-EM experiment, it was clear that the cryo-EM method must be optimized to obtain a high-resolution control 20S proteasome structure prior to addition of a ligand. While addition of the ligand may require additional optimization later on, ensuring our cryo-EM method was optimized first was vital. Then, if no ligand was observed in a high-resolution structure of the 20S proteasome, the reason could be better pinpointed to indicate an issue with ligand binding, such as a low population of ligand-bound proteasomes.

To develop a method for obtaining a high-resolution structure of the 20S proteasome, I outlined the following goals. The first goal is that a high number of proteasome particles must be present within the 2D images. Typically, 2D images of upwards of 40,000-50,000 individual particles must be averaged to reconstruct a good resolution structure. However, to accomplish this goal, another method rather than increased protein concentration was desirable to allow for a suitable drug:20S ratio. The second goal was to obtain a highly randomized orientation of individual proteasome particles on the grid by overcoming the proteasome's preferred orientation issue. Once a method for obtaining a high resolution 20S proteasome structure was determined, the third goal was to incorporate a ligand to achieve a high number of ligand-bound proteasomes. As 3D structures are reconstructed through averaging of the 2D images, if only a small number of proteasomes were bound to the ligand, the electron density of the ligand would be averaged out in the final 3D structure due to a greater number of unbound proteasomes being present within the sample. Therefore, in a quest to solve a structure of a ligand-bound 20S proteasome the aforementioned parameters of the cryo-EM sample preparation and workflow were optimized to achieve these three goals.

2.2.9 Cryo-EM Method Development – Control 20S Proteasome Structure

While an experiment to obtain a high-resolution control 20S proteasome structure was needed for cryo-EM method development, it would also be used as a non-activated 20S proteasome control (DMSO treatment) for comparison against a small molecule activated 20S

proteasome. While our main goal is to determine the binding site of a 20S proteasome activator and determine individual amino acids in which the ligand interacts with, we also aimed to elucidate any conformational changes observed upon treatment with a 20S activator. Since atomic force microscopy studies have shown that TCH-165 induces an open gate conformation of the 20S proteasome,³⁹ we aimed to explore this further and analyze individual subunits of the proteasome that may be responsible for this induction of the open gate conformation. To do this, an unbound, control 20S proteasome structure was needed to compare with a ligand-bound 20S proteasome.

The previous attempt conducted in our lab was performed using the buffer in which the 20S proteasome comes supplied by RnD Systems, as this buffer does not contain glycerol. Glycerol is typically included in proteasome storage buffers as it is a cryoprotectant to ensure protein stability during freeze/thaw cycles. However, it should not be included in the cryo-EM experiments as it is known to negatively impact cryo-EM grid freezing and result in poor ice quality. However, it is important to note that our *in vitro* 20S proteasome activity assays to evaluate a small molecule's ability to enhance 20S proteasome activity are conducted in a 38 mM Tris-HCl, 100 mM NaCl buffer of pH 7.8. Hence, all of our activity assay results and indirect evidence of 20S proteasome binding by the 20S activators were obtained using the Tris buffer. Therefore, the remainder of the cryo-EM experiments discussed in this chapter were conducted using this activity assay buffer. This would allow for direct correlations to be made between any conformational changes observed in a cryo-EM structure and enhancement of 20S proteasome activity by the ligands.

I next aimed to find a technique that could be employed to remedy the proteasome's preferred orientation issue. It has been shown in a couple of studies that coating the grid with a solution of 0.1% poly L-lysine hydrobromide following the traditional glow discharge step places a positive charge on the grid and produces a much more random orientation of proteasome particles on the grid.^{77,78} A similar method uses a modified glow discharge protocol in which glow discharge occurs in the presence of pentylamine.^{70,75} I hypothesized the poly L-lysine coating may also aid in a higher retainment of proteasome particles on the grid, as studies using similar methods to apply a positive charge to the EM grids have been able to achieve high-resolution

structures with lower proteasome concentrations.⁷⁰ Since I aimed to use the lowest proteasome concentration possible to achieve a good drug:20S ratio, in this control study I used a proteasome concentration of 0.5 mg/mL. This concentration would allow for a suitable drug:20S ratio to be achieved in later experiments when a 20S activator ligand was incorporated. With these parameters selected (Figure 2.16A), the 20S proteasome control sample was prepared by incubating purified human 20S proteasome (0.5 mg/mL) with 2% DMSO at 37 °C for 30 minutes.

For this experiment, two types of EM grids were tested: a R1.2/1.3 Quantifoil grid with no support, and a R1.2/1.3 UT Quantifoil grid with an ultra-thin film carbon support. The grids were then prepared using the previously reported protocol for the poly L-lysine grid coating.⁷⁸ In this procedure, an EM grid is glow discharged in the traditional manner to apply a negative charge to the grid. Next, a 0.1% poly L-lysine hydrobromide solution (5 µL) is placed on the EM grid and adsorbed for 90 seconds, washed twice with 5 µL drops of water, and then allowed to dry completely. The sample was then applied to the grid and blotted with a Vitrobot Mark IV for 3.0 or 3.5 seconds to investigate which blot time gave a desirable ice thickness. The grids prepared were then screened to determine which of the grid preparation parameters provided the highest quality grid. Upon screening, a good mix of top-view and side-view proteasome particles was observed, validating the poly L-lysine coating technique had been successful in overcoming the proteasome's preferred orientation issue using our protocol. Additionally, there was a slightly higher number of proteasomes on the grid than previous experiments we had conducted without the poly L-lysine coating, suggesting the coating may have helped retain additional particles. Ultimately, a sample prepared on the R1.2/1.3 Quantifoil grid with a blot time of 3.5 seconds was selected for image collection, as it had the highest quality ice and a sufficient number of proteasome particles present.

Following one day of image collection, a preliminary analysis of the data prompted us to halt image collection. From one day of imaging, 1100 images were collected with a total of 8,000 particles in the collection of 2D images. While this number of particles was somewhat improved from our earlier cryo-EM experiments, ultimately, we aimed to reach at least 40,000-50,000 total particles to obtain a high-resolution structure. If each image continued to average 8 proteasome particles, image collection would likely have to continue for several days to achieve an acceptable

resolution. Therefore, we decided to process the data as is, as the poly L-lysine coating had at least been successful in providing a random orientation of proteasome particles.

To determine what effect the more randomized orientation of particles would have on our structure resolution, the data was processed by Dr. Sundharraman Subramanian at the RTSF Cryo-EM Core Facility at Michigan State University using CryoSPARC software. The general procedure for data processing is outlined here. During image collection setup, an appropriate phase contrast threshold is set to pick particles from the ice. After the particles are selected, they are extracted from the micrographs and any particles with a similar orientation are placed into a particle stack forming a 2D class of particles (Figure 2.16B). The quality of the 2D classes is then assessed. At this stage of analysis, poorly resolved 2D classes are typically eliminated from further downstream 3D analysis. The highly resolved 2D classes are then used as the input for 3D classification to produce an electron density map, and ultimately reconstruct the 3D structure.

To estimate the resolution of the reconstructed structure, the Fourier shell correlation (FSC) is calculated. To calculate the FSC, the dataset is divided randomly into two halves and each half is processed independently to produce two half maps.⁷⁹ The half maps are then correlated against each other to provide the FSC value. As is typical, in our experiments the resolution at which the FSC curve crosses a threshold of 0.143 (blue line of Figure 2.16C) is used to report the resolution of the cryo-EM reconstructions.⁷⁹ As shown in Figure 2.16C, the FSC plot of the electron density maps estimated a 6.03 Å structure with C2 symmetry applied (Figure 2.16D). While this resolution is not below the 3.0 Å goal, for one day of imaging a 6.0 Å structure is quite promising. As in the early cryo-EM experiment with TCH-165, a 7.0-8.0 Å structure was obtained after three days of imaging. While there were still fewer particles per image than desired, the random orientation of particles provided by the poly L-lysine grid coating seemed to have quite a positive effect on the structure resolution. Therefore, the next step was to find a method to further increase proteasome particles present on the grid.

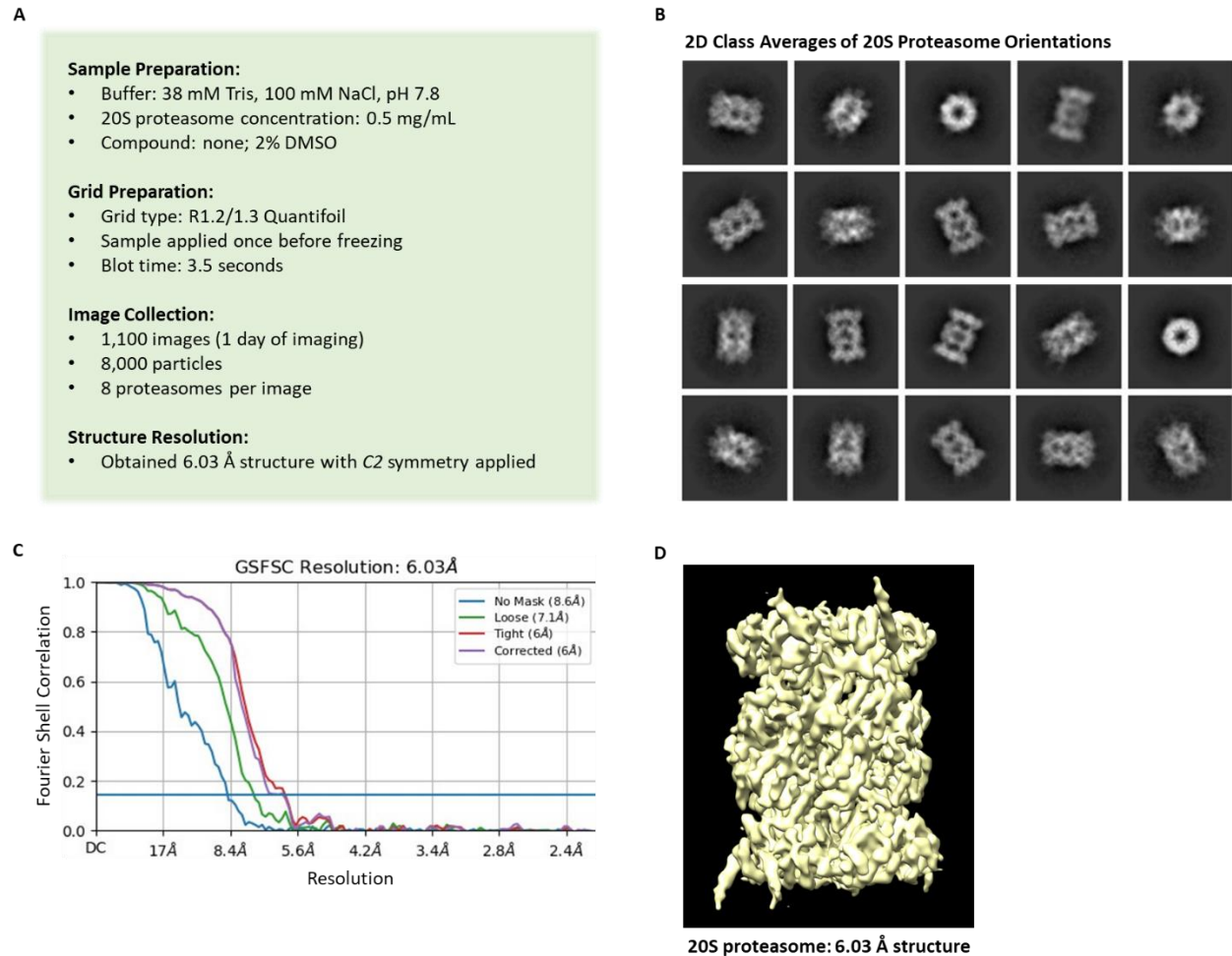


Figure 2.16 Control 20S proteasome cryo-EM experiment. (A) Experimental parameters and summary of dataset. (B) Representative 2D class averages selected for 3D reconstruction. (C) FSC plots of the electron density maps result in 6.03 Å structure. (D) Reconstructed 6.03 Å structure of the 20S proteasome with C2 symmetry applied.

To increase protein particles on the grid, a literature search revealed a technique that has been used to increase the number of particles on the grid without increasing protein concentration of the sample. As done in our previous experiment, typically the protein sample is applied to the EM grid, and then a Vitrobot is used to blot the grid for a selected time to achieve appropriate ice thickness. However, in this new technique, the sample is applied to the grid and manually blotted to near dryness with Whatman filter paper. Then, the sample application and manual blotting process is repeated twice more to increase protein concentration on the grid. Following the third blot, the grid is plunged into liquid ethane by the Vitrobot. This technique was utilized in our next experiment which is outlined below.

2.2.10 Cryo-EM Experiment with 20S Proteasome Treated with 20S Activator Ligand

In the next experiment, I decided to incorporate a 20S proteasome activator ligand. Since the resolution of the structure was 6.03 Å after only one day of imaging, I anticipated the resolution could be improved with additional image collection in the next experiment. Even at the 6.03 Å resolution, the protein side chains were resolved quite well when comparing with published structures of the 20S proteasome. As the cryo-EM experiment with TCH-165 resulted in drug solubility issues, I chose the 20S proteasome activator, SS-4-15 (Figure 2.17A), due to its comparable potency (i.e. $EC_{200} = 1.2 \pm 0.6 \mu\text{M}$) and increased solubility. A concentration of 200 μM SS-4-15 was selected for use in the experiment, as it provided a drug:20S ratio of about 300:1 and had good solubility. Furthermore, this drug:20S ratio has shown to effectively enhance 20S proteasome activity, albeit the activity assay was conducted at a concentration of 1 nM 20S, instead of 670 nM (0.5 mg/mL).

To prepare the cryo-EM sample, 20S proteasome (0.5 mg/mL) was incubated with SS-4-15 (200 μM) at 37 °C for 30 minutes. For grid preparation, grids were again prepared using two grid types: a R1.2/1.3 Quantifoil grid with no support, and a R1.2/1.3 UT Quantifoil grid with an ultra-thin film carbon support, and four different blot times were tested (i.e. 2.5, 3.0, 3.5, and 4.0 seconds). Although these parameters were already tested in the previous control experiment, incorporation of the small molecule ligand could have a substantial impact on how the sample freezes and the ice quality. Contrary to the control experiment, the triple sample application/blot technique was used in which the sample was applied and manually blotted three times, with the final blot performed using a Vitrobot Mark IV, followed by plunging into liquid ethane to freeze the grid.

Following approximately 2.5 days of image collection, 2000 images were collected with a total of 35,000 particles in this collection of images, which was quite close to our goal of 40,000-50,000 particles. Utilizing the triple sample application/blot technique, the number of particles per image increased from about 8 particles per image to approximately 20 proteasome particles per image. The data was again processed by Dr. Sundharraman Subramanian using CryoSPARC software. The same data processing procedure described in the previous experiment was used. Particle picking provided the 2D class averages shown in Figure 2.17B. However, analysis of the

quality of these 2D classes resulted in a very interesting observation. By examining the various 2D class averages, it was estimated that approximately 50 percent of the proteasomes had been denatured or “fallen apart.” As shown in Figure 2.17B, there were approximately 1,600 particles of a side-view with several β -subunits removed from the proteasome’s structure (column 2, row 2 of 2D averages), compared to the approximately 3,600-3,900 particles of side-view classes of fully assembled proteasomes. Additionally, 2D classes of individual α -rings and/or β -rings were quite prevalent among the collected images. As evidence of the proteasome being denatured was not observed in the control experiment, it suggests the denatured proteasomes are induced by addition of the 20S activator, as the same concentration of DMSO and mechanical handling of the sample was used for both experiments. I hypothesized that the high drug concentration used in this experiment may be responsible for this denaturation.

For further downstream 3D analysis, the poorly resolved 2D classes of denatured 20S proteasomes were eliminated. The highly resolved 2D classes were then used for 3D classification to produce electron density maps and reconstruction of the structure (Figure 2.17B). To estimate the resolution of the reconstructed structure, the Fourier shell correlation (FSC) was calculated. As in the previous experiment, the resolution at which the FSC crosses a threshold of 0.143 (blue line of Figure 2.17C) was used to report the resolution of the cryo-EM reconstruction. As shown in Figure 2.17C, the FSC plot of the electron density maps estimated a 3.26 Å structure with the application of C2 symmetry (Figure 2.17D).

To examine the structure for the bound ligand, our reconstructed structure was aligned with a published 20S proteasome structure (PDB ID: 4R3O)⁶⁴ to look for any changes in electron density between the two structures (the overlaid structures are shown in Figure 2.17D). As the published structure has no bound ligands, any additional electron densities in our structure may indicate a bound 20S proteasome activator. However, following the comparison of the two structures, no added electron densities were detected in our reconstructed structure. Since our structure was very well resolved, additional electron density from a ligand should be detectable, therefore it was concluded that no ligand was bound in our structure.

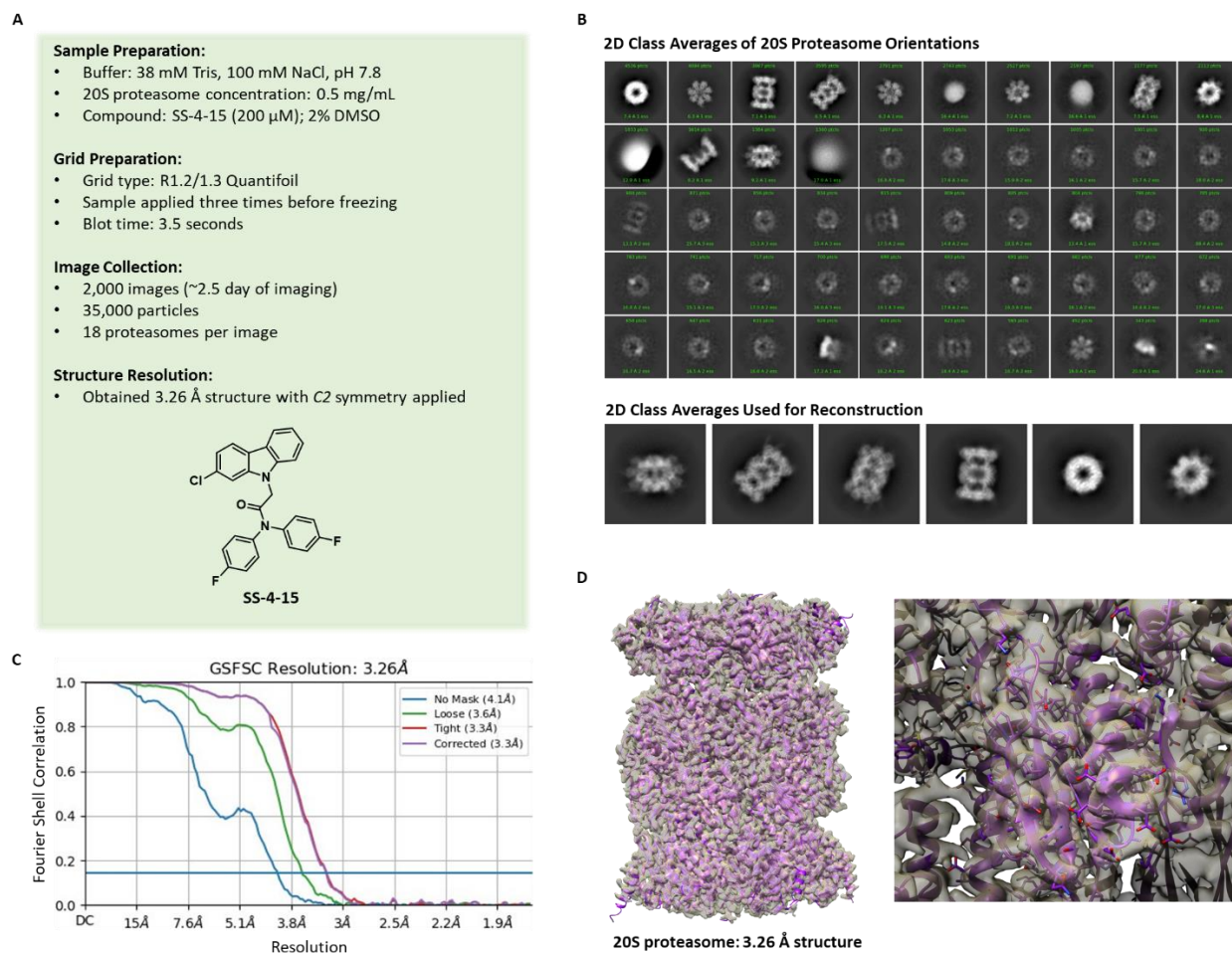


Figure 2.17 Cryo-EM experiment with 20S activator treated 20S Proteasome. (A) Experimental parameters and summary of dataset. (B) Representative 2D class averages and those selected for 3D reconstruction. (C) FSC plots of the electron density maps resulted in a 3.26 \AA structure with C2 symmetry applied. (D) Reconstructed 3.26 \AA structure of the 20S proteasome with C2 symmetry applied (purple; left image) aligned with published 20S proteasome structure (PDB ID: 4R30; gray). Zoomed in view of two overlaid structures to show level of detail resolved in our reconstructed structure (right image).

Due to the small size of the ligand, 447 Daltons in comparison to the 750,000 Dalton proteasome, it may be difficult to locate such a small additional electron density. Therefore, we also analyzed our structure to ascertain whether any conformational changes associated with gate opening had occurred as an additional way to check for ligand binding. This was done by aligning the β -rings of our structure to that of a 20S proteasome in a closed gate conformation (PDB ID: 4R30)⁶⁴ since it has been reported that the β -subunits remain mostly unchanged during gate opening.^{67,68} Comparison of our structure and the closed gate 20S structure revealed very

similar, overlapping electron densities of the N-termini tails which occlude the central pore in a closed gate conformation. We also aligned our structure with a recently published open gated proteasome. The structure of this open gate proteasome, revealed that during gate opening, the N-termini tails of the α -subunits which occlude the gate of the central pore in a closed gate α -ring were displaced from the central pore, and the diameter of the pore increased in width by 3.8 Å compared to a closed gate α -ring.⁷⁰ The electron densities of the displaced N-termini tails of this open gate proteasome did not align with the densities of the N-termini tails in our structure. Therefore, with these two comparisons, we concluded that our reconstructed structure is in a closed gate conformation further supporting the conclusion that no 20S activator ligand was bound in our structure.

After reflecting upon the data, I propose a couple of possible explanations as to why a 20S activator ligand was not observed. The dataset collected resulted in a very curious observation that almost 50 percent of the proteasome particles found in the 2D class averages were denatured in the 20S activator treated sample. As this denaturation was not observed in the control 20S proteasome experiment, this effect was likely induced by drug treatment, as no differences in mechanical handling during sample preparation was conducted. I hypothesized that the high concentration of 20S activator used in this study may have resulted in this denaturation. This could be due to a high number of bound ligands resulting in non-specific binding, or perhaps the high concentration of drug had caused the drug to aggregate which upon binding to the 20S proteasome denatured the protein. Therefore, we hypothesized it is possible that the denatured proteasomes might have once belonged to a population of ligand-bound 20S proteasome particles. However, at some point during sample or grid preparation, the proteasomes were disassembled. While we attempted to analyze the denatured 2D classes for evidence of ligand bound to any of the proteasome pieces, due to their reduced prevalence, the disassembled pieces were not as highly resolved as the fully assembled 2D classes. Ultimately, the resolution of these denatured proteasome pieces was too low to identify whether the ligand was bound in these structures.

Another possible explanation for the ligand not being detected in the structure may be due to a low population of ligand-bound 20S proteasomes in comparison to unbound 20S

proteasomes. Since the 3D structure is reconstructed through averaging of the various 2D classes, if only a small population of the 20S proteasomes have a ligand bound, it is possible that the electron density of the ligand is averaged out in the final 3D structure. This is because the software is unable to sort unbound 20S proteasomes and ligand-bound 20S proteasomes into separate 2D classes, due to the small size of the ligand in comparison to the proteasome. However, there are methods that could be implemented into future cryo-EM studies to allow for unbound proteasomes to be sorted from ligand-bound proteasomes. Further avenues to explore in an attempt to address these issues will be discussed in the future work section below.

2.2.11 Future Work

While further work is required to obtain a ligand-bound 20S proteasome structure, the method we developed and discussed in this chapter has shown to result in the reconstruction of high-resolution 20S proteasome structures in several of our studies. Once a suitable ligand is discovered, the hope is that the ligand can be easily incorporated and used in this method to solve the structure. Work is ongoing in pursuit of solving a ligand-bound 20S proteasome structure by concurrent exploration of the following strategies.

One of the avenues currently being explored is the incorporation of a technique that allows for sorting unbound 20S proteasomes from ligand-bound 20S proteasomes. Immunogold labeling with Au nanoparticles has been widely used in electron microscopy studies to label a sample component.^{80,81} In negative stain studies, proteins have been labeled using an Au nanoparticle-tagged antibody specific to the protein of interest.⁸⁰ Due to the high electron density of the Au nanoparticle, the electron density is easily detectable and appears as a dark spot on the protein in the micrographs. Additional studies have conjugated Au nanoparticles directly to the protein for visualization by electron microscopy.⁸² Application of this strategy to our work could be used to conjugate an Au nanoparticle to a 20S proteasome activator. Following incubation with the 20S proteasome, this would allow for particles with the Au nanoparticle-tagged ligand bound to be sorted from the proteasome particles lacking this obvious added density from the Au nanoparticle. This would allow the 2D class of unbound 20S proteasomes to be eliminated prior to 3D reconstruction to avoid averaging out electron density of the ligand in the final 3D structure.

Another strategy currently being explored is the use of covalent ligands. While attempts to design a covalent 20S proteasome activator have yet to be successful, this is a promising avenue to explore since the off rate of the drug would be eliminated using this approach. In an adjacent study, a photo affinity labeling approach is being explored in collaboration with Dare George. For this approach, a diazirine was incorporated in the structure of a 20S proteasome activator ligand. To prepare the sample, the 20S proteasome is incubated with the ligand to allow for binding to the 20S activator's typical binding site, then UV light is used to covalently attach the ligand in place. This strategy is currently being explored in combination with the previous Au nanoparticle strategy. In this study, an alkyne and the diazirine will both be added onto the 20S proteasome activator ligand. Following photo affinity labeling, the alkyne can undergo a click reaction with an Au nanoparticle conjugated to an azide. This will allow for covalent attachment of the ligand to the 20S proteasome, and also allow for better sorting of the unbound and ligand-bound 20S proteasome populations.

Exploration of these strategies to ensure ligand binding and allow for the sorting of ligand-bound 20S proteasomes from unbound proteasomes provide very exciting avenues to explore. Despite whether these strategies directly lead to solving the structure of a ligand-bound 20S proteasome, the knowledge gained from these approaches will be invaluable, as they could provide insight into why we have been unable to detect a bound ligand in our structures. With this information, the method to solve a 20S proteasome structure can be further fine-tuned.

2.3 Conclusion

The 20S proteasome activator TCH-165 has shown to potently enhance proteolytic activity of the 20S proteasome. Mechanistic studies have provided evidence that this enhanced proteolytic activity is due to induction of an open gate conformation. In this chapter, progress toward solving a cryo-EM structure of a 20S proteasome bound to a small molecule 20S activator was discussed. While further work is required to solve a structure of a ligand-bound 20S proteasome, a method to obtain a high-resolution 20S proteasome structure has been successfully developed. Once a suitable ligand is designed, the method outlined in this chapter can be used to solve a structure to identify the ligand binding site and elucidate the conformational changes associated with gate opening.

Furthermore, 20S proteasome activation by TCH-165 was shown to enhance the degradation of DPR proteins and reduce the accumulation of poly-GR DPR proteins in cortical neuron culture. Additionally, TCH-165 provided protection from proteasome impairment by both poly-GR and poly-PR DPR proteins in purified protein assays and in neurons, allowing global proteostasis to be restored. Finally, these benefits from 20S proteasome activation provided protection from the cytotoxic effects of accumulating DPR proteins in neurons. Preliminary investigation into the mechanism by which DPR proteins impair 20S proteasome function, revealed UPS impairment may result from recruitment of 20S proteasomes into large DPR protein aggregates. Remarkably, treatment with TCH-165 was able to prevent this recruitment of 20S proteasomes in these initial studies. In all, the work in this chapter suggests that small molecule activation of the 20S proteasome may offer a potential novel therapeutic strategy for the treatment of ALS.

2.4 Experimental

2.4.1 Materials and Reagents

Human 20S proteasome and fluorogenic substrate *N*-succinyl-Leu-Leu-Val-Tyr-7-amido-4-methylcoumarin (Suc-LLVY-AMC) were obtained from R&D Systems, Inc. (Minneapolis, MN). Fluorogenic poly-GR DPR protein substrate (Suc-GR₃-AMC), HA-GR₂₀, and HA-PR₂₀ DPR proteins were synthesized by GenScript (Piscataway, NJ). The precast sodium dodecyl sulfate gels, PVDF membrane and blocking grade milk were purchased from Bio-Rad (Hercules, CA). Radiance Plus Western ECL reagent was purchased from Azure Biosystems, Inc. (Dublin, CA). Bicinchoninic acid (BCA) assay kit was from ThermoFisher Scientific. Rabbit monoclonal anti-HA-tag, anti-mouse HRP-linked, and anti-rabbit HRP-linked antibodies were purchased from Cell Signaling Technology (Danvers, MA). The mouse monoclonal anti-total ubiquitin and anti-GAPDH HRP-linked antibodies were purchased from Novus Biologicals (Littleton, CO). The rabbit polyclonal anti-poly-PR antibody was purchased from Sigma-Aldrich.

2.4.2 Methods

20S proteasome-mediated degradation of fluorogenic poly-GR DPR protein substrate. Purified 20S proteasome (final concentration of 1 nM) in assay buffer (38 mM Tris-HCl, 100 mM NaCl, pH 7.8) was added to a black, clear-bottom 96-well plate and incubated with various concentrations

of drug (1.25-80 μM) at 37 °C for 15 minutes. Fluorogenic poly-GR DPR protein substrate (Suc-GR₃-AMC) was added to each well to a final concentration of 20 μM . Fluorescence was measured at 37 °C taking kinetic readings every 5 minutes at 380/460 nm for 1 hour.

20S proteasome-mediated degradation of DPR protein. Purified 20S proteasome (final concentration of 2 nM) in assay buffer (38 mM Tris-HCl, 100 mM NaCl, pH 7.8) was incubated with varying concentrations of drug (final concentrations ranging from 1-10 μM ; 2% DMSO) and incubated at 37 °C for 15 minutes. Purified HA-GR₂₀ or HA-PR₂₀ were added to a final concentration of 0.5 μM and the samples were incubated at 37 °C for 30 minutes and 8 hours, respectively. Following incubation, the samples were boiled at 95 °C with 5X SDS loading buffer, resolved on a 4-20% Tris/glycine gel and transferred to a PVDF membrane that was probed with anti-HA-tag (Cell Signaling; cat# 3724S) or anti-GAPDH-HRP (Novus; cat# NBP2-27103H) antibodies. After washing and application of appropriate secondary antibodies the blots were developed with ECL Western reagent (Radiance Plus, Azure Biosystems; cat# AC2103) and imaged with a chemiluminescent Western blot imager (Azure Biosystems 300Q). Band intensities were acquired using Biorad Image Lab analysis software. Statistical analyses were performed with GraphPad Prism 8.1; One-way ANOVA with a post hoc Sidak test was used for multiple comparisons of group means (ns, not significant, * $p \leq 0.05$; ** $p \leq 0.01$; *** $p \leq 0.001$; **** $p \leq 0.0001$).

Preventing 20S proteasome impairment by DPR protein. Purified 20S proteasome (final concentration of 1 nM) in assay buffer (38 mM Tris-HCl, pH 7.8) was incubated with various concentrations of drug (1, 3, and 10 μM) at 37 °C for 15 minutes (0.25% final DMSO concentration). Lyophilized HA-GR₂₀ or HA-PR₂₀ powder was dissolved in DMSO to a final concentration of 1 mM and aliquots were stored at -80 °C until just before use. Dipeptide repeat protein (HA-GR₂₀ or HA-PR₂₀) was added to a final concentration of 37.5 nM and incubated for 5 minutes on ice or at 37 °C, respectively. After incubation, 100 μL of the reaction mixture was added to three wells of a black, clear-bottom 96-well plate. Fluorogenic proteasome substrate Suc-LLVY-AMC was added to each well to a final concentration of 40 μM . Fluorescence was measured at 37 °C taking kinetic readings every 5 minutes at 380/460 nm for 1 hour. Statistical analyses were performed with GraphPad Prism 8.1; One-way ANOVA with a post hoc Sidak test

was used for multiple comparisons of group means (ns, not significant, * $p \leq 0.05$; ** $p \leq 0.01$; *** $p \leq 0.001$; **** $p \leq 0.0001$).

Overcoming 20S proteasome impairment by DPR protein. Lyophilized HA-GR₂₀ or HA-PR₂₀ powder was dissolved in DMSO to a final concentration of 1 mM and aliquots were stored at -80 °C until just before use. Purified 20S proteasome (final concentration of 1 nM) in assay buffer (38 mM Tris-HCl, pH 7.8) was incubated with DPR protein (HA-GR₂₀ or HA-PR₂₀) (final concentration of 37.5 nM) for 5 minutes on ice or at 37 °C, respectively. Various concentrations of drug (1, 3, and 10 μ M) were added and incubated at room temperature for 15 minutes (0.25% final DMSO concentration). After incubation, 100 μ L of the reaction mixture was added to three wells of a black, clear-bottom 96-well plate. Fluorogenic proteasome substrate Suc-LLVY-AMC was added to each well to a final concentration of 40 μ M. Fluorescence was measured at 37 °C taking kinetic readings every 5 minutes at 380/460 nm for 1 hour. Statistical analyses were performed with GraphPad Prism 8.1; Brown-Forsythe and Welch ANOVA with a post hoc Dunnett's T3 test was used for multiple comparisons of group means (ns, not significant, * $p \leq 0.05$; ** $p \leq 0.01$; *** $p \leq 0.001$; **** $p \leq 0.0001$).

Restoring proteostasis in the presence of DPR proteins in rat cortical neurons. Days *in vitro* cortical neurons cultures were scraped from culture dishes, pelleted in a microcentrifuge tube, and resuspended in chilled lysis buffer (10 mM Tris, 0.5 mM DTT, 5 mM Mg₂ATP, 5 mM MgCl₂, pH 7.8). Pellets were vortexed for 15 seconds and left on ice for 30 minutes. The lysate was clarified by centrifugation at 6000 x g (4 °C) for 20 minutes. Total protein of the lysate was quantified by bicinchoninic acid assay (BCA assay, ThermoFisher Scientific), normalized to 2 mg/mL total protein, and boiled with 5X SDS loading buffer at 95 °C. Lysates (40 μ g) were resolved on a 4-20% Tris/glycine gel and transferred to a PVDF membrane. The membrane was probed with anti-poly-GR (Cleveland lab), anti-poly-PR (Sigma-Aldrich; cat# ABN1354), anti-total ubiquitin (Novus; cat# NB300-130), and anti-GAPDH-HRP (Novus; cat# NBP2-27103H) antibodies. After washing and application of appropriate secondary antibodies the blots were developed with ECL Western reagent (Radiance Plus, Azure Biosystems; cat# AC2103) and imaged with a chemiluminescent Western blot imager (Azure Biosystems 300Q). Band intensities were acquired using Biorad Image Lab analysis software. Statistical analyses were performed with GraphPad

Prism 8.1; One-way ANOVA with a post hoc Sidak test was used for multiple comparisons of group means (ns, not significant, * $p \leq 0.05$; ** $p \leq 0.01$; *** $p \leq 0.001$; **** $p \leq 0.0001$).

Pure neuronal cultures.⁸³

Neuroprotection in the presence of DPR proteins.⁸³

Sample preparation for 20S proteasome impairment negative stain experiments (*initial conditions*). Purified 20S proteasome (70 nM) in assay buffer (50 mM Tris; pH 7.8) was pretreated with 1% DMSO or TCH-165 (final concentration of 10 μ M) for 15 minutes at 37 °C. The HA-PR₂₀ DPR proteins were then added to a final concentration of 875 nM (12.5:1 ratio of DPR:20S) and incubated for 30 mins, 2 hours, 4 hours or 8 hours at 37 °C.

Sample preparation for 20S proteasome impairment negative stain experiments (*later conditions*). Purified 20S proteasome (40 nM) in assay buffer (50 mM Tris, 100 mM NaCl; pH 7.8) was pretreated with 2% DMSO or TCH-165 (final concentration of 200 μ M) for 15 minutes at 37 °C. The HA-PR₂₀ DPR proteins were then added to a final concentration of 5,000 nM (125:1 ratio of DPR:20S) and incubated for 8 hours at 37 °C.

Negative stain electron microscopy sample preparation. Continuous carbon support film grids (Cu 400 mesh carbon coated Formvar grids; Ted Pella) were glow discharged (PELCO easiGlow, 15 mA) for 45 seconds. The sample (4 μ L) was applied to the grid for 45 seconds and then washed three times with water by quickly floating the grid on a water droplet. The sample was then quickly floated on a droplet of 1% aqueous uranyl acetate, followed by floating of the grid on the stain for 12 seconds. The grids were allowed to fully dry and then imaged at the RTSF Cryo-EM Core facility at Michigan State University using a Talos Arctica microscope operated at 200 keV. Micrographs were collected at a nominal magnification of 92000 (1.12 Å/px) with an exposure time of 0.50 seconds and an objective lens defocus setting of 5 μ m underfocus.

Cryo-electron microscopy sample/grid preparation. Purified 20S proteasome (0.5 mg/mL) in buffer (38 mM Tris, NaCl, pH 7.8) was incubated with DMSO or 20S activator (200 μ M) at 37 °C for 30 minutes. Following incubation, the sample was placed on ice. R1.2/1.3 or R1.2/1.3 UT Quantifoil grids were glow discharged for 45 seconds in a PELCO easiGlow glow discharging unit (15 mA) in atmospheric air. Next, 5 μ L of a 0.1% poly L-lysine hydrobromide solution was placed onto the hydrophilized grids and absorbed for 90 seconds, washed twice with 5 μ L drops of water,

and allowed to dry completely. The protein sample (4 μL) was then applied to the grids, and the grids were manually blotted to near dryness with Whatman filter paper inside the Vitrobot Mark IV chamber (4 $^{\circ}\text{C}$, 95% humidity). The sample application and blotting process was then repeated two more times, with the final blot being performed by the Vitrobot Mark IV (with a blot time of 3.5 seconds). The grid was then plunged into liquid ethane and stored under liquid nitrogen.

Cryo-electron microscopy data collection. Cryo-EM data were collected at the RTSF Cryo-EM Core facility at Michigan State University using a Talos Arctica microscope operated at 200 keV. The micrographs were collected at a nominal magnification of 120,000X with a dose rate of 39.57 $\text{e}^{-}/\text{\AA}^2$. Data processing was carried out using CryoSPARC software by Dr. Sundharraman Subramanian. The overall resolution was estimated based on the gold-standard Fourier shell correlation ($\text{FSC}_{0.143}$).

REFERENCES

- (1) Van Langenhove, T.; van der Zee, J.; Van Broeckhoven, C. The Molecular Basis of the Frontotemporal Lobar Degeneration–Amyotrophic Lateral Sclerosis Spectrum. *Annals of Medicine* **2012**, *44* (8), 817–828.
- (2) Rowland, L.; Shneider, N. Amyotrophic Lateral Sclerosis. *The New England Journal of Medicine* **2001**, *344* (22), 1688–1700.
- (3) DeJesus-Hernandez, M.; Mackenzie, I.; Boeve, B.; Boxer, A.; Baker, M.; Rutherford, N.; Nicholson, A.; Finch, N.; Flynn Gilmer, H.; Adamson, J.; Kouri, N.; Wojtas, A.; Sengdy, P.; Hsiung, G.-Y.; Karydas, A.; Seeley, W.; Josephs, K.; Coppola, G.; Geschwind, D.; Wszolek, Z.; Feldman, H.; Knopman, D.; Petersen, R.; Miller, B.; Dickson, D.; Boylan, K.; Graff-Radford, N.; Rademakers, R. Expanded GGGGCC Hexanucleotide Repeat in Non-Coding Region of C9ORF72 Causes Chromosome 9p-Linked Frontotemporal Dementia and Amyotrophic Lateral Sclerosis. *Neuron* **2011**, *72* (2), 245–256.
- (4) Renton, A. E.; Majounie, E.; Waite, A.; Simón-Sánchez, J.; Rollinson, S.; Gibbs, J. R.; Schymick, J. C.; Laaksovirta, H.; van Swieten, J. C.; Myllykangas, L.; Kalimo, H.; Paetau, A.; Abramzon, Y.; Remes, A. M.; Kaganovich, A.; Scholz, S. W.; Duckworth, J.; Ding, J.; Harmer, D. W.; Hernandez, D. G.; Johnson, J. O.; Mok, K.; Ryten, M.; Trabzuni, D.; Guerreiro, R. J.; Orrell, R. W.; Neal, J.; Murray, A.; Pearson, J.; Jansen, I. E.; Sondervan, D.; Seelaar, H.; Blake, D.; Young, K.; Halliwell, N.; Callister, J. B.; Toulson, G.; Richardson, A.; Gerhard, A.; Snowden, J.; Mann, D.; Neary, D.; Nalls, M. A.; Peuralinna, T.; Jansson, L.; Isoviita, V.-M.; Kaivorinne, A.-L.; Hölttä-Vuori, M.; Ikonen, E.; Sulkava, R.; Benatar, M.; Wu, J.; Chiò, A.; Restagno, G.; Borghero, G.; Sabatelli, M.; ITALSGEN Consortium; Heckerman, D.; Rogaeva, E.; Zinman, L.; Rothstein, J. D.; Sendtner, M.; Drepper, C.; Eichler, E. E.; Alkan, C.; Abdullaev, Z.; Pack, S. D.; Dutra, A.; Pak, E.; Hardy, J.; Singleton, A.; Williams, N. M.; Heutink, P.; Pickering-Brown, S.; Morris, H. R.; Tienari, P. J.; Traynor, B. J. A Hexanucleotide Repeat Expansion in C9ORF72 Is the Cause of Chromosome 9p21-Linked ALS-FTD. *Neuron* **2011**, *72* (2), 257–268.
- (5) Talbot, K. Familial versus Sporadic Amyotrophic Lateral Sclerosis—a False Dichotomy? *Brain* **2011**, *134* (12), 3429–3434.
- (6) Rutherford, N. J.; Heckman, M. G.; DeJesus-Hernandez, M.; Baker, M. C.; Soto-Ortolaza, A. I.; Rayaprolu, S.; Stewart, H.; Finger, E.; Volkening, K.; Seeley, W. W.; Hatanpaa, K. J.; Lomen-Hoerth, C.; Kertesz, A.; Bigio, E. H.; Lippa, C.; Knopman, D. S.; Kretschmar, H. A.; Neumann, M.; Caselli, R. J.; White, C. L.; Mackenzie, I. R.; Petersen, R. C.; Strong, M. J.; Miller, B. L.; Boeve, B. F.; Uitti, R. J.; Boylan, K. B.; Wszolek, Z. K.; Graff-Radford, N. R.; Dickson, D. W.; Ross, O. A.; Rademakers, R. Length of Normal Alleles of C9ORF72 GGGGCC Repeat Do Not Influence Disease Phenotype. *Neurobiology of Aging* **2012**, *33* (12), 2950.e5-2950.e7.
- (7) Schmitz, A.; Pinheiro Marques, J.; Oertig, I.; Maharjan, N.; Saxena, S. Emerging Perspectives on Dipeptide Repeat Proteins in C9ORF72 ALS/FTD. *Frontiers in Cellular Neuroscience* **2021**, *15*, 637548.

- (8) Taylor, J. P.; Brown, R.; Cleveland, D. Decoding ALS: From Genes to Mechanism. *Nature* **2016**, *539*, 197–206.
- (9) Jiang, J.; Zhu, Q.; Gendron, T. F.; Saberi, S.; McAlonis-Downes, M.; Seelman, A.; Stauffer, J. E.; Jafar-nejad, P.; Drenner, K.; Schulte, D.; Chun, S.; Sun, S.; Ling, S.-C.; Myers, B.; Engelhardt, J.; Katz, M.; Baughn, M.; Platoshyn, O.; Marsala, M.; Watt, A.; Heyser, C. J.; Ard, M. C.; De Muynck, L.; Daugherty, L. M.; Swing, D. A.; Tessarollo, L.; Jung, C. J.; Delpoux, A.; Utzschneider, D. T.; Hedrick, S. M.; de Jong, P. J.; Edbauer, D.; Van Damme, P.; Petrucelli, L.; Shaw, C. E.; Bennett, C. F.; Da Cruz, S.; Ravits, J.; Rigo, F.; Cleveland, D. W.; Lagier-Tourenne, C. Gain of Toxicity from ALS/FTD-Linked Repeat Expansions in C9ORF72 Is Alleviated by Antisense Oligonucleotides Targeting GGGGCC-Containing RNAs. *Neuron* **2016**, *90* (3), 535–550.
- (10) Ash, P. E. A.; Bieniek, K. F.; Gendron, T. F.; Caulfield, T.; Lin, W.-L.; DeJesus-Hernandez, M.; van Blitterswijk, M. M.; Jansen-West, K.; Paul, J. W.; Rademakers, R.; Boylan, K. B.; Dickson, D. W.; Petrucelli, L. Unconventional Translation of C9ORF72 GGGGCC Expansion Generates Insoluble Polypeptides Specific to C9FTD/ALS. *Neuron* **2013**, *77* (4), 639–646.
- (11) Zu, T.; Gibbens, B.; Doty, N. S.; Gomes-Pereira, M.; Huguette, A.; Stone, M. D.; Margolis, J.; Peterson, M.; Markowski, T. W.; Ingram, M. A. C.; Nan, Z.; Forster, C.; Low, W. C.; Schoser, B.; Somia, N. V.; Clark, H. B.; Schmechel, S.; Bitterman, P. B.; Gourdon, G.; Swanson, M. S.; Moseley, M.; Ranum, L. P. W. Non-ATG-Initiated Translation Directed by Microsatellite Expansions. *Proceedings of the National Academy of Sciences of the United States of America* **2011**, *108* (1), 260–265.
- (12) Mori, K.; Weng, S.-M.; Arzberger, T.; May, S.; Rentzsch, K.; Kremmer, E.; Schmid, B.; Kretzschmar, H. A.; Cruts, M.; Broeckhoven, C. V.; Haass, C.; Edbauer, D. The C9orf72 GGGGCC Repeat Is Translated into Aggregating Dipeptide-Repeat Proteins in FTLD/ALS. *Science* **2013**, *339* (6125), 1335–1338.
- (13) Zu, T.; Liu, Y.; Bañez-Coronel, M.; Reid, T.; Pletnikova, O.; Lewis, J.; Miller, T. M.; Harms, M. B.; Falchook, A. E.; Subramony, S. H.; Ostrow, L. W.; Rothstein, J. D.; Troncoso, J. C.; Ranum, L. P. W. RAN Proteins and RNA Foci from Antisense Transcripts in C9ORF72 ALS and Frontotemporal Dementia. *Proceedings of the National Academy of Sciences of the United States of America* **2013**, *110* (51), E4968-4977.
- (14) Gendron, T. F.; Bieniek, K. F.; Zhang, Y.-J.; Jansen-West, K.; Ash, P. E. A.; Caulfield, T.; Daugherty, L.; Dunmore, J. H.; Castanedes-Casey, M.; Chew, J.; Cosio, D. M.; van Blitterswijk, M.; Lee, W. C.; Rademakers, R.; Boylan, K. B.; Dickson, D. W.; Petrucelli, L. Antisense Transcripts of the Expanded C9ORF72 Hexanucleotide Repeat Form Nuclear RNA Foci and Undergo Repeat-Associated Non-ATG Translation in C9FTD/ALS. *Acta Neuropathologica* **2013**, *126* (6), 829–844.
- (15) Mori, K.; Arzberger, T.; Grässer, F. A.; Gijssels, I.; May, S.; Rentzsch, K.; Weng, S.-M.; Schludi, M. H.; van der Zee, J.; Cruts, M.; Van Broeckhoven, C.; Kremmer, E.; Kretzschmar, H. A.; Haass, C.; Edbauer, D. Bidirectional Transcripts of the Expanded C9orf72 Hexanucleotide Repeat Are Translated into Aggregating Dipeptide Repeat Proteins. *Acta Neuropathologica* **2013**, *126* (6), 881–893.

- (16) Gupta, R.; Lan, M.; Mojsilovic-Petrovic, J.; Choi, W. H.; Safren, N.; Barmada, S.; Lee, M. J.; Kalb, R. The Proline/Arginine Dipeptide from Hexanucleotide Repeat Expanded C9ORF72 Inhibits the Proteasome. *eNeuro* **2017**, *4* (1), 1–18.
- (17) Zhang, Y.-J.; Jansen-West, K.; Xu, Y.-F.; Gendron, T. F.; Bieniek, K. F.; Lin, W.-L.; Sasaguri, H.; Caulfield, T.; Hubbard, J.; Daugherty, L.; Chew, J.; Belzil, V. V.; Prudencio, M.; Stankowski, J. N.; Castanedes-Casey, M.; Whitelaw, E.; Ash, P. E. A.; DeTure, M.; Rademakers, R.; Boylan, K. B.; Dickson, D. W.; Petrucelli, L. Aggregation-Prone C9FTD/ALS Poly(GA) RAN-Translated Proteins Cause Neurotoxicity by Inducing ER Stress. *Acta Neuropathologica* **2014**, *128* (4), 505–524.
- (18) May, S.; Hornburg, D.; Schludi, M. H.; Arzberger, T.; Rentzsch, K.; Schwenk, B. M.; Grässer, F. A.; Mori, K.; Kremmer, E.; Banzhaf-Strathmann, J.; Mann, M.; Meissner, F.; Edbauer, D. C9orf72 FTL/ALS-Associated Gly-Ala Dipeptide Repeat Proteins Cause Neuronal Toxicity and Unc119 Sequestration. *Acta Neuropathologica* **2014**, *128* (4), 485–503.
- (19) Mizielińska, S.; Grönke, S.; Niccoli, T.; Ridler, C. E.; Clayton, E. L.; Devoy, A.; Moens, T.; Norona, F. E.; Woollacott, I. O. C.; Pietrzyk, J.; Cleverley, K.; Nicoll, A. J.; Pickering-Brown, S.; Dols, J.; Cabecinha, M.; Hendrich, O.; Fratta, P.; Fisher, E. M. C.; Partridge, L.; Isaacs, A. M. C9orf72 Repeat Expansions Cause Neurodegeneration in *Drosophila* through Arginine-Rich Proteins. *Science* **2014**, *345* (6201), 1192–1194.
- (20) Wen, X.; Tan, W.; Westergard, T.; Krishnamurthy, K.; Markandiah, S. S.; Shi, Y.; Lin, S.; Shneider, N. A.; Monaghan, J.; Pandey, U. B.; Pasinelli, P.; Ichida, J. K.; Trotti, D. Antisense Proline-Arginine RAN Dipeptides Linked to C9ORF72-ALS/FTD Form Toxic Nuclear Aggregates That Initiate In Vitro and In Vivo Neuronal Death. *Neuron* **2014**, *84* (6), 1213–1225.
- (21) Dunker, A. K.; Lawson, J. D.; Brown, C. J.; Williams, R. M.; Romero, P.; Oh, J. S.; Oldfield, C. J.; Campen, A. M.; Ratliff, C. M.; Hipps, K. W.; Ausio, J.; Nissen, M. S.; Reeves, R.; Kang, C.; Kissinger, C. R.; Bailey, R. W.; Griswold, M. D.; Chiu, W.; Garner, E. C.; Obradovic, Z. Intrinsically Disordered Protein. *Journal of Molecular Graphics and Modelling* **2001**, *19* (1), 26–59.
- (22) DeForte, S.; Uversky, V. N. Order, Disorder, and Everything in Between. *Molecules* **2016**, *21* (8).
- (23) Jorda, J.; Xue, B.; Uversky, V. N.; Kajava, A. V. Protein Tandem Repeats - the More Perfect, the Less Structured. *The FEBS Journal* **2010**, *277* (12), 2673–2682.
- (24) Flores, B. N.; Dulchavsky, M. E.; Krans, A.; Sawaya, M. R.; Paulson, H. L.; Todd, P. K.; Barmada, S. J.; Ivanova, M. I. Distinct C9orf72-Associated Dipeptide Repeat Structures Correlate with Neuronal Toxicity. *PLOS ONE* **2016**, *11* (10), 1–18.

- (25) Boeynaems, S.; Bogaert, E.; Kovacs, D.; Konijnenberg, A.; Timmerman, E.; Volkov, A.; Guharoy, M.; De Decker, M.; Jaspers, T.; Ryan, V. H.; Janke, A. M.; Baatsen, P.; Vercruyse, T.; Kolaitis, R.-M.; Daelemans, D.; Taylor, J. P.; Kedersha, N.; Anderson, P.; Impens, F.; Sobott, F.; Schymkowitz, J.; Rousseau, F.; Fawzi, N. L.; Robberecht, W.; Van Damme, P.; Tompa, P.; Van Den Bosch, L. Phase Separation of C9orf72 Dipeptide Repeats Perturbs Stress Granule Dynamics. *Molecular Cell* **2017**, *65* (6), 1044–1055.
- (26) Molliex, A.; Temirov, J.; Lee, J.; Coughlin, M.; Kanagaraj, A. P.; Kim, H. J.; Mittag, T.; Taylor, J. P. Phase Separation by Low Complexity Domains Promotes Stress Granule Assembly and Drives Pathological Fibrillization. *Cell* **2015**, *163* (1), 123–133.
- (27) Boeynaems, S.; Holehouse, A. S.; Weinhardt, V.; Kovacs, D.; Van Lindt, J.; Larabell, C.; Van Den Bosch, L.; Das, R.; Tompa, P. S.; Pappu, R. V.; Gitler, A. D. Spontaneous Driving Forces Give Rise to Protein–RNA Condensates with Coexisting Phases and Complex Material Properties. *Proceedings of the National Academy of Sciences* **2019**, *116* (16), 7889–7898.
- (28) Lee, K.-H.; Zhang, P.; Kim, H. J.; Mitrea, D.; Sarkar, M.; Freibaum, B.; Cika, J.; Coughlin, M.; Messing, J.; Molliex, A.; Maxwell, B.; Kim, N. C.; Temirov, J.; Moore, J.; Kolaitis, R.-M.; Shaw, T.; Bai, B.; Peng, J.; Kriwacki, R.; Taylor, J. P. C9orf72 Dipeptide Repeats Impair the Assembly, Dynamics and Function of Membrane-Less Organelles. *Cell* **2016**, *167* (3), 774–788.
- (29) Solomon, D. A.; Smikle, R.; Reid, M. J.; Mizielińska, S. Altered Phase Separation and Cellular Impact in C9orf72-Linked ALS/FTD. *Frontiers in Cellular Neuroscience* **2021**, *15*, 1–24.
- (30) Ben-Nissan, G.; Sharon, M. Regulating the 20S Proteasome Ubiquitin-Independent Degradation Pathway. *Biomolecules* **2014**, *4* (3), 862–884.
- (31) Höhn, T. J. A.; Grune, T. The Proteasome and the Degradation of Oxidized Proteins: Part III—Redox Regulation of the Proteasomal System. *Redox Biology* **2014**, *2*, 388–394.
- (32) Jung, T.; Höhn, A.; Grune, T. The Proteasome and the Degradation of Oxidized Proteins: Part II – Protein Oxidation and Proteasomal Degradation. *Redox Biology* **2014**, *2*, 99–104.
- (33) Tanaka, K.; Mizushima, T.; Saeki, Y. The Proteasome: Molecular Machinery and Pathophysiological Roles. *Biological Chemistry* **2012**, *393* (4), 217–234.
- (34) Eraldes, J.; Coffino, P. Ubiquitin-Independent Proteasomal Degradation. *Biochimica et Biophysica Acta* **2014**, *1843* (1), 216–221.
- (35) Lehman, N. L. The Ubiquitin Proteasome System in Neuropathology. *Acta Neuropathologica* **2009**, *118* (3), 329–347.
- (36) Eriksen, J. L.; Przedborski, S.; Petrucelli, L. Gene Dosage and Pathogenesis of Parkinson’s Disease. *Trends in Molecular Medicine* **2005**, *11* (3), 91–96.
- (37) Uversky, V. N. Wrecked Regulation of Intrinsically Disordered Proteins in Diseases: Pathogenicity of Deregulated Regulators. *Frontiers in Molecular Biosciences* **2014**, *1* (6), 1–24.

- (38) Thibaut, T. A.; Anderson, R. T.; Smith, D. M. A Common Mechanism of Proteasome Impairment by Neurodegenerative Disease-Associated Oligomers. *Nature Communications* **2018**, *9* (1), 1–14.
- (39) Njomen, E.; Osmulski, P. A.; Jones, C. L.; Gaczynska, M.; Tepe, J. J. Small Molecule Modulation of Proteasome Assembly. *Biochemistry* **2018**, *57* (28), 4214–4224.
- (40) Jones, C.; Njomen, E.; Sjogren, B.; Dexheimer, T.; Tepe, J. Small Molecule Enhancement of 20S Proteasome Activity Targets Intrinsically Disordered Proteins. *ACS Chemical Biology* **2017**, *12* (9), 2240–2247.
- (41) Staerz, S. D.; Jones, C. L.; Tepe, J. J. Design, Synthesis, and Biological Evaluation of Potent 20S Proteasome Activators for the Potential Treatment of α -Synucleinopathies. *Journal of Medicinal Chemistry* **2022**, *65* (9), 6631–6642.
- (42) Fiolek, T. J.; Keel, K. L.; Tepe, J. J. Fluspirilene Analogs Activate the 20S Proteasome and Overcome Proteasome Impairment by Intrinsically Disordered Protein Oligomers. *ACS Chemical Neuroscience* **2021**, *12* (8), 1438–1448.
- (43) Fiolek, T. J.; Magyar, C. L.; Wall, T. J.; Davies, S. B.; Campbell, M. V.; Savich, C. J.; Tepe, J. J.; Mosey, R. A. Dihydroquinazolines Enhance 20S Proteasome Activity and Induce Degradation of α -Synuclein, an Intrinsically Disordered Protein Associated with Neurodegeneration. *Bioorganic & Medicinal Chemistry Letters* **2021**, *36*, 127821.
- (44) Huang, L.; Ho, P.; Chen, C.-H. Activation and Inhibition of the Proteasome by Betulinic Acid and Its Derivatives. *FEBS Letters* **2007**, *581* (25), 4955–4959.
- (45) Trader, D. J.; Simanski, S.; Dickson, P.; Kodadek, T. Establishment of a Suite of Assays That Support the Discovery of Proteasome Stimulators. *Biochimica et Biophysica Acta* **2017**, *1861* (4), 892–899.
- (46) Coleman, R. A.; Trader, D. J. Development and Application of a Sensitive Peptide Reporter to Discover 20S Proteasome Stimulators. *ACS Combinatorial Science* **2018**, *20* (5), 269–276.
- (47) Njomen, E.; Vanecek, A.; Lansdell, T. A.; Yang, Y.-T.; Schall, P. Z.; Harris, C. M.; Bernard, M. P.; Isaac, D.; Alkharabsheh, O.; Al-Janadi, A.; Giletto, M. B.; Ellsworth, E.; Taylor, C.; Tang, T.; Lau, S.; Bailie, M.; Bernard, J. J.; Yuzbasiyan-Gurkan, V.; Tepe, J. J. Small Molecule 20S Proteasome Enhancer Regulates MYC Protein Stability and Exhibits Antitumor Activity in Multiple Myeloma. *Biomedicines* **2022**, *10* (5), 938.
- (48) Budenholzer, L.; Cheng, C. L.; Li, Y.; Hochstrasser, M. Proteasome Structure and Assembly. *Journal of Molecular Biology* **2017**, *429* (22), 3500–3524.
- (49) Smith, D. M.; Chang, S.-C.; Park, S.; Finley, D.; Cheng, Y.; Goldberg, A. Docking of the Proteasomal ATPases' C-Termini in the 20S Proteasomes Alpha Ring Opens the Gate for Substrate Entry. *Molecular Cell* **2007**, *27* (5), 731–744.
- (50) Rabl, J.; Smith, D. M.; Yu, Y.; Chang, S.-C.; Goldberg, A. L.; Cheng, Y. Mechanism of Gate Opening in the 20S Proteasome by the Proteasomal ATPases. *Molecular Cell* **2008**, *30* (3), 360–368.

- (51) Gaczynska, M.; Osmulski, P. A. Characterization of Noncompetitive Regulators of Proteasome Activity. In *Methods in Enzymology*; Ubiquitin and Protein Degradation, Part A; Academic Press, 2005; Vol. 398, pp 425–438.
- (52) Brettschneider, J.; Del Tredici, K.; Lee, V. M.-Y.; Trojanowski, J. Q. Spreading of Pathology in Neurodegenerative Diseases: A Focus on Human Studies. *Nature Reviews Neuroscience* **2015**, *16* (2), 109–120.
- (53) Rubinsztein, D. C. The Roles of Intracellular Protein-Degradation Pathways in Neurodegeneration. *Nature* **2006**, *443* (7113), 780–786.
- (54) Selkoe, D. J. Folding Proteins in Fatal Ways. *Nature* **2003**, *426* (6968), 900–904.
- (55) Ciechanover, A.; Brundin, P. The Ubiquitin Proteasome System in Neurodegenerative Diseases: Sometimes the Chicken, Sometimes the Egg. *Neuron* **2003**, *40* (2), 427–446.
- (56) Keller, J. N.; Hanni, K. B.; Markesbery, W. R. Impaired Proteasome Function in Alzheimer’s Disease. *Journal of Neurochemistry* **2000**, *75* (1), 436–439.
- (57) McNaught, K. S. P.; Olanow, C. W.; Halliwell, B.; Isacson, O.; Jenner, P. Failure of the Ubiquitin–Proteasome System in Parkinson’s Disease. *Nature Reviews Neuroscience* **2001**, *2* (8), 589–594.
- (58) Ortega, Z.; Díaz-Hernández, M.; Lucas, J. J. Is the Ubiquitin-Proteasome System Impaired in Huntington’s Disease? *Cellular and Molecular Life Sciences* **2007**, *64* (17), 2245–2257.
- (59) Guo, Q.; Lehmer, C.; Martínez-Sánchez, A.; Rudack, T.; Beck, F.; Hartmann, H.; Pérez-Berlanga, M.; Frottin, F.; Hipp, M. S.; Hartl, F. U.; Edbauer, D.; Baumeister, W.; Fernández-Busnadiego, R. In Situ Structure of Neuronal C9orf72 Poly-GA Aggregates Reveals Proteasome Recruitment. *Cell* **2018**, *172* (4), 696–705.
- (60) Yamakawa, M.; Ito, D.; Honda, T.; Kubo, K.; Noda, M.; Nakajima, K.; Suzuki, N. Characterization of the Dipeptide Repeat Protein in the Molecular Pathogenesis of C9FTD/ALS. *Human Molecular Genetics* **2015**, *24* (6), 1630–1645.
- (61) Licata, N. V.; Cristofani, R.; Salomonsson, S.; Wilson, K. M.; Kempthorne, L.; Vaizoglu, D.; D’Agostino, V. G.; Pollini, D.; Loffredo, R.; Pancher, M.; Adami, V.; Bellosta, P.; Ratti, A.; Viero, G.; Quattrone, A.; Isaacs, A. M.; Poletti, A.; Provenzani, A. C9orf72 ALS/FTD Dipeptide Repeat Protein Levels Are Reduced by Small Molecules That Inhibit PKA or Enhance Protein Degradation. *The EMBO Journal* **2022**, *41* (1), 1–23.
- (62) Khosravi, B.; LaClair, K. D.; Riemenschneider, H.; Zhou, Q.; Frottin, F.; Mareljic, N.; Czuppa, M.; Farny, D.; Hartmann, H.; Michaelsen, M.; Arzberger, T.; Hartl, F. U.; Hipp, M. S.; Edbauer, D. Cell-to-Cell Transmission of C9orf72 Poly-(Gly-Ala) Triggers Key Features of ALS/FTD. *The EMBO Journal* **2020**, *39* (8), 1–19.
- (63) Ghosh, S.; T, D.; Baul, U.; Vemparala, S. Aggregation Dynamics of Charged Peptides in Water: Effect of Salt Concentration. *bioRxiv* 1–15.
- (64) Harshbarger, W.; Miller, C.; Diedrich, C.; Sacchettini, J. Crystal Structure of the Human 20S Proteasome in Complex with Carfilzomib. *Structure* **2015**, *23* (2), 418–424.

- (65) Haselbach, D.; Schrader, J.; Lambrecht, F.; Henneberg, F.; Chari, A.; Stark, H. Long-Range Allosteric Regulation of the Human 26S Proteasome by 20S Proteasome-Targeting Cancer Drugs. *Nature Communications* **2017**, *8* (1), 15578.
- (66) Schrader, J.; Henneberg, F.; Mata, R. A.; Tittmann, K.; Schneider, T. R.; Stark, H.; Bourenkov, G.; Chari, A. The Inhibition Mechanism of Human 20S Proteasomes Enables Next-Generation Inhibitor Design. *Science* **2016**, *353* (6299), 594–598.
- (67) Whitby, F. G.; Masters, E. I.; Kramer, L.; Knowlton, J. R.; Yao, Y.; Wang, C. C.; Hill, C. P. Structural Basis for the Activation of 20S Proteasomes by 11S Regulators. *Nature* **2000**, *408* (6808), 115–120.
- (68) Yu, Y.; Smith, D. M.; Kim, H. M.; Rodriguez, V.; Goldberg, A. L.; Cheng, Y. Interactions of PAN's C-Termini with Archaeal 20S Proteasome and Implications for the Eukaryotic Proteasome–ATPase Interactions. *The EMBO Journal* **2010**, *29* (3), 692–702.
- (69) Dong, Y.; Zhang, S.; Wu, Z.; Li, X.; Wang, W. L.; Zhu, Y.; Stoilova-McPhie, S.; Lu, Y.; Finley, D.; Mao, Y. Cryo-EM Structures and Dynamics of Substrate-Engaged Human 26S Proteasome. *Nature* **2019**, *565* (7737), 49–55.
- (70) Opoku-Nsiah, K. A.; de la Pena, A. H.; Williams, S. K.; Chopra, N.; Sali, A.; Lander, G. C.; Gestwicki, J. E. The YΦ Motif Defines the Structure-Activity Relationships of Human 20S Proteasome Activators. *Nature Communications* **2022**, *13* (1), 1226.
- (71) Passmore, L. A.; Russo, C. J. Specimen Preparation for High-Resolution Cryo-EM. *Methods in Enzymology* **2016**, *579*, 51–86.
- (72) Bhella, D. Cryo-Electron Microscopy: An Introduction to the Technique, and Considerations When Working to Establish a National Facility. *Biophysical Reviews* **2019**, *11* (4), 515–519.
- (73) Sigworth, F. J. Principles of Cryo-EM Single-Particle Image Processing. *Microscopy* **2016**, *65* (1), 57–67.
- (74) Chuah, J. J. Y.; Thibaudeau, T. A.; Smith, D. M. Minimal Mechanistic Component of HbYX-Dependent Proteasome Activation That Reverses Impairment by Neurodegenerative-Associated Oligomers. *Communications Biology* **2023**, *6* (1), 1–10.
- (75) Morris, E. P.; da Fonseca, P. C. A. High-Resolution Cryo-EM Proteasome Structures in Drug Development. *Acta Crystallographica Section D* **2017**, *73* (6), 522–533.
- (76) Baumeister, W.; Dahlmann, B.; Hegerl, R.; Kopp, F.; Kuehn, L.; Pfeifer, G. Electron Microscopy and Image Analysis of the Multicatalytic Proteinase. *FEBS letters* **1988**, *241* (1–2), 239–245.
- (77) Ding, Z.; Fu, Z.; Xu, C.; Wang, Y.; Wang, Y.; Li, J.; Kong, L.; Chen, J.; Li, N.; Zhang, R.; Cong, Y. High-Resolution Cryo-EM Structure of the Proteasome in Complex with ADP-AIFx. *Cell Research* **2017**, *27* (3), 373–385.
- (78) Lander, G. C.; Estrin, E.; Matyskiela, M. E.; Bashore, C.; Nogales, E.; Martin, A. Complete Subunit Architecture of the Proteasome Regulatory Particle. *Nature* **2012**, *482* (7384), 186–191.

- (79) Rosenthal, P. B.; Henderson, R. Optimal Determination of Particle Orientation, Absolute Hand, and Contrast Loss in Single-Particle Electron Cryomicroscopy. *Journal of Molecular Biology* **2003**, *333* (4), 721–745.
- (80) Piludu, M.; Medda, L.; Monduzzi, M.; Salis, A. Gold Nanoparticles: A Powerful Tool to Visualize Proteins on Ordered Mesoporous Silica and for the Realization of Theranostic Nanobioconjugates. *International Journal of Molecular Sciences* **2018**, *19* (7), 1991.
- (81) Goldberg, M. W.; Fišerová, J. Immunogold Labeling for Scanning Electron Microscopy. In *High-Resolution Imaging of Cellular Proteins: Methods and Protocols*; Schwartzbach, S. D., Skalli, O., Schikorski, T., Eds.; Methods in Molecular Biology; Springer: New York, NY, 2016; pp 309–325.
- (82) Gregori, L.; Hainfeld, J. F.; Simon, M. N.; Goldgaber, D. Binding of Amyloid β Protein to the 20S Proteasome. *Journal of Biological Chemistry* **1997**, *272* (1), 58–62.
- (83) Vanecek, A. S.; Mojsilovic-Petrovic, J.; Kalb, R. G.; Tepe, J. J. Enhanced Degradation of Mutant C9ORF72-Derived Toxic Dipeptide Repeat Proteins by 20S Proteasome Activation Results in Restoration of Proteostasis and Neuroprotection. *ACS Chemical Neuroscience* **2023**, *14* (8), 1439–1448.

APPENDIX

2.1 *In vitro* Degradation of HA-GR₂₀

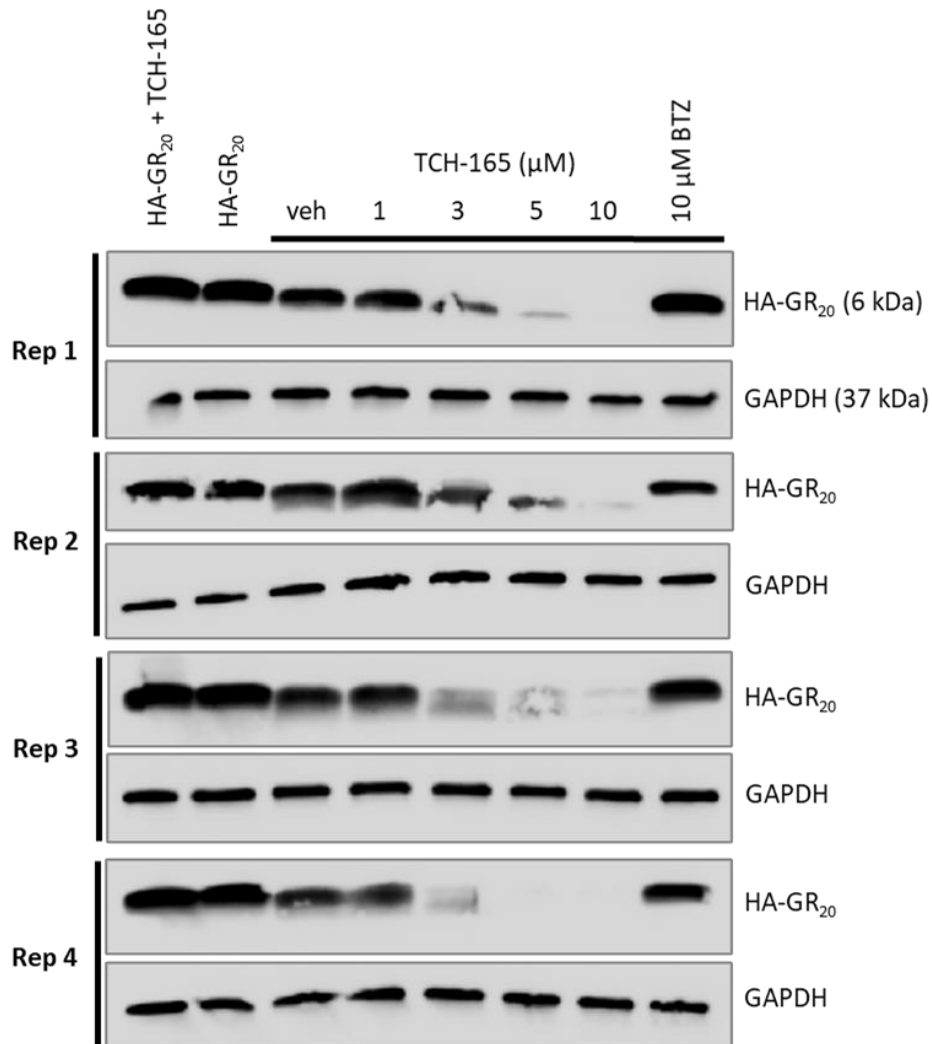


Figure 2.18 20S proteasome-mediated degradation of HA-GR₂₀. Immunoblots (n=4) of HA-GR₂₀ digestion by purified 20S proteasome pretreated with DMSO, TCH-165 (1, 3, 5, 10 μM), or proteasome inhibitor, bortezomib, BTZ (10 μM) for 30 minutes.

2.2 *In vitro* Degradation of HA-PR₂₀

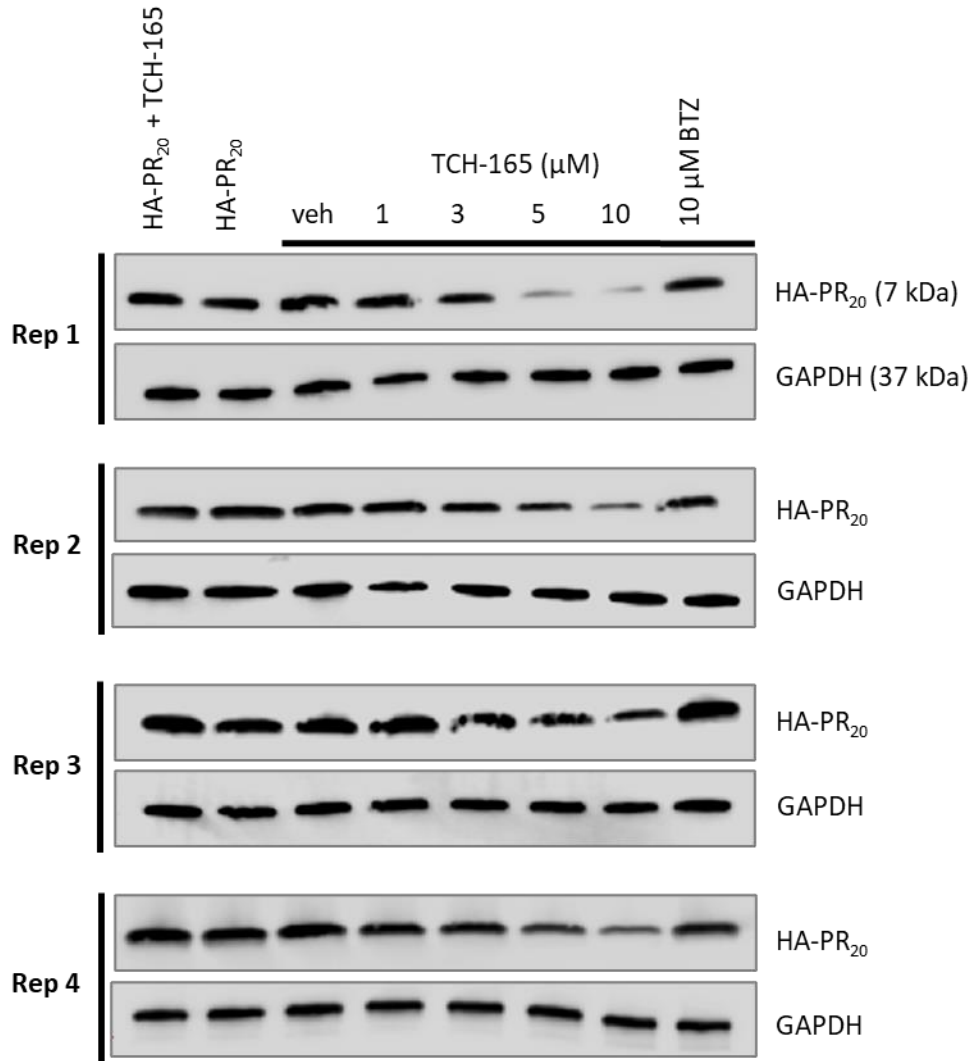


Figure 2.19 20S proteasome-mediated degradation of HA-PR₂₀. Immunoblots (n=4) of HA-PR₂₀ digestion by purified 20S proteasome pretreated with DMSO, TCH-165 (1, 3, 5, 10 μM), or proteasome inhibitor, bortezomib, BTZ (10 μM) for 8 hours.

2.3 Preventing 20S Proteasome Impairment with TCH-23

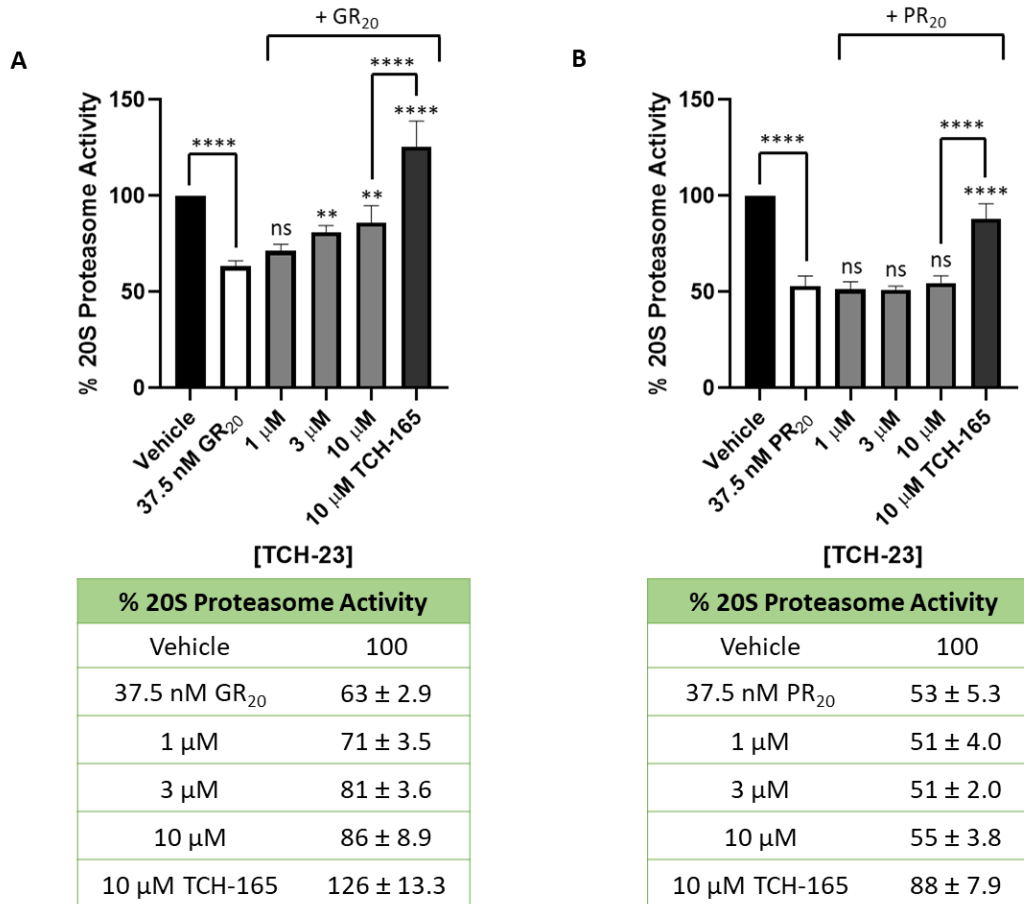


Figure 2.20 Preventing 20S proteasome impairment by HA-GR₂₀ and HA-PR₂₀ with TCH-23. (A) Dose-response of TCH-23 for 20S proteasome-mediated proteolysis of fluorogenic substrate Suc-LLVY-AMC with 20S proteasome pretreated with TCH-23, followed by incubation with HA-GR₂₀. (B) Dose-response of TCH-23 for 20S proteasome-mediated proteolysis of fluorogenic substrate Suc-LLVY-AMC with 20S proteasome pretreated with TCH-23, followed by incubation with HA-PR₂₀ (n=3); one-way ANOVA (ns, not significant, *p ≤ 0.05; **p ≤ 0.01; ***p ≤ 0.001; ****p ≤ 0.0001).

2.4 Overcoming 20S Proteasome Impairment with TCH-23

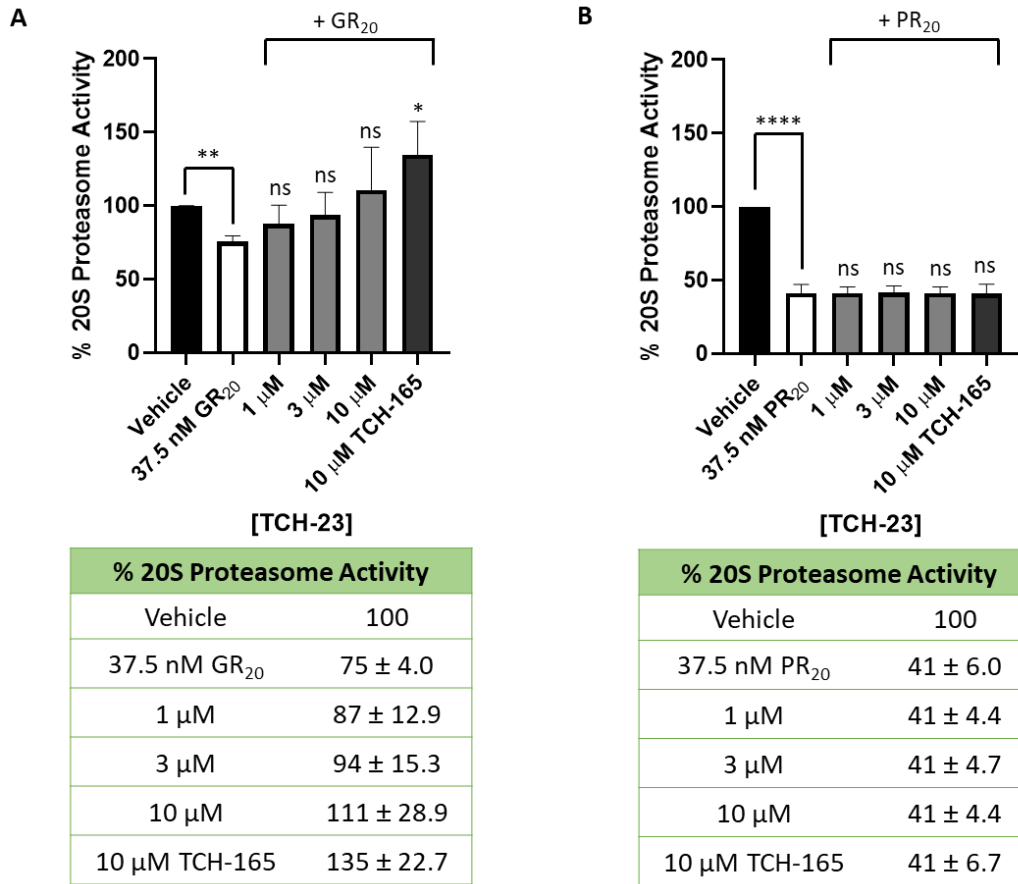


Figure 2.21 Overcoming 20S proteasome impairment by HA-GR₂₀ and HA-PR₂₀ with TCH-23. (A) Dose-response of TCH-23 for 20S proteasome-mediated proteolysis of fluorogenic substrate Suc-LLVY-AMC with 20S proteasome pretreated with TCH-23, followed by incubation with HA-GR₂₀. (B) Dose-response of TCH-23 for 20S proteasome-mediated proteolysis of fluorogenic substrate Suc-LLVY-AMC with 20S proteasome pretreated with TCH-23, followed by incubation with HA-PR₂₀ (n=3); one-way ANOVA (ns, not significant, *p ≤ 0.05; **p ≤ 0.01; ***p ≤ 0.001; ****p ≤ 0.0001).

2.5 UPS Impairment by GFP-GR₅₀ in Rat Cortical Neurons

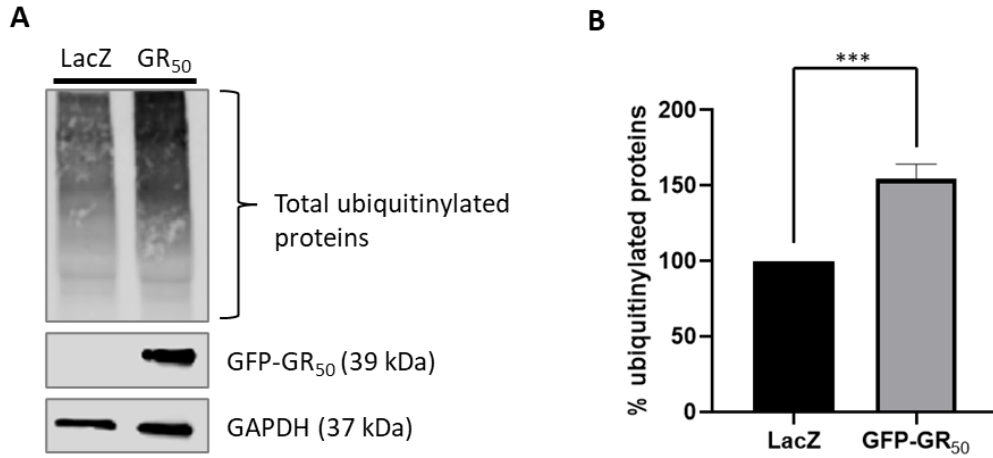
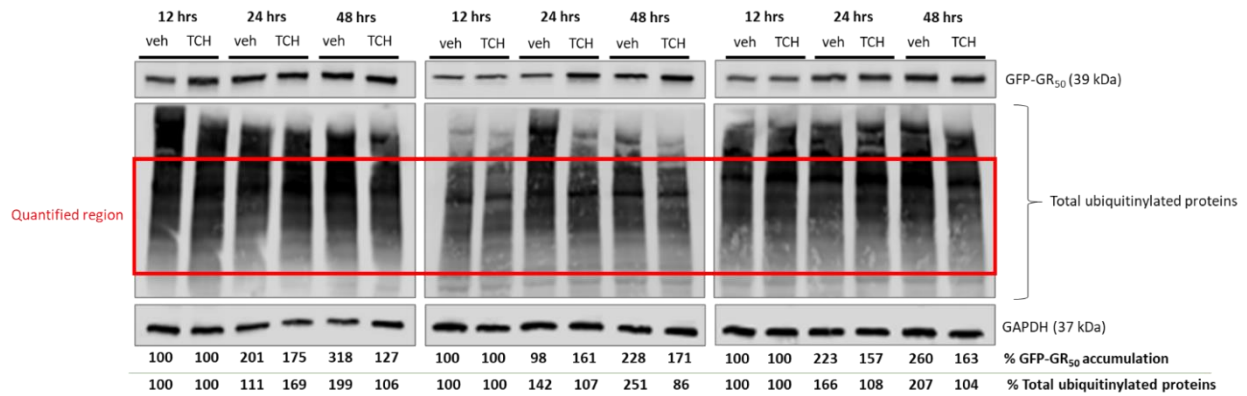


Figure 2.22 UPS function is impaired by GFP-GR₅₀ in rat cortical neurons. (A) Representative western blot of the amount of total ubiquitinated proteins present in rat cortical neurons following expression of GFP-GR₅₀ for 48 hours. Immunoblot probed with anti-poly-GR, anti-total ubiquitin, and anti-GAPDH antibodies. (B) Quantification of total ubiquitinated protein western blots (n=3); student's t test (ns, not significant, *p ≤ 0.05; **p ≤ 0.01; ***p ≤ 0.001; ****p ≤ 0.0001).

2.6 Neuronal GFP-GR₅₀ Time Course Assay

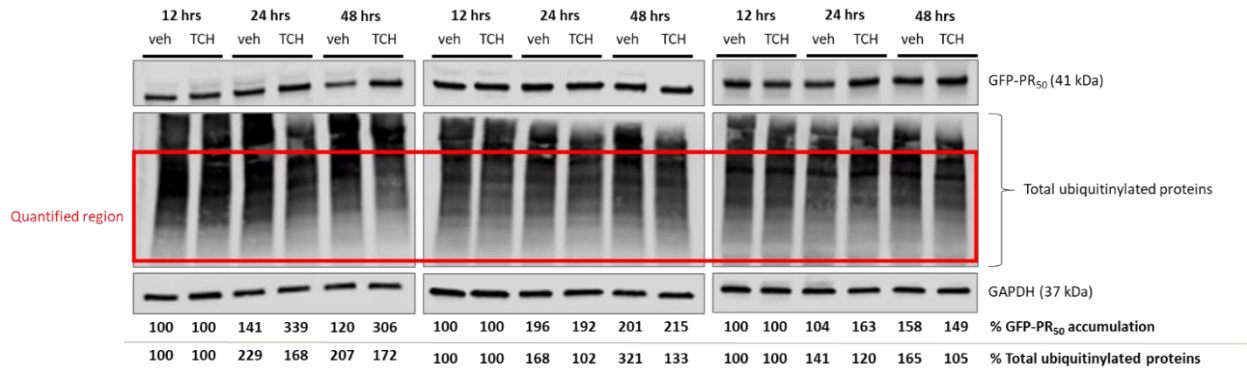


Time Following Infection (hours)	Vehicle (% GFP-GR ₅₀)	10 μM TCH-165 (% GFP-GR ₅₀)	Vehicle (% total ubiq. proteins)	10 μM TCH-165 (% total ubiq. proteins)
12	100	100	100	100
24	174	164	140	128
48	268	154	219	99

n=3

Figure 2.23 Restoring proteostasis in the presence of GFP-GR₅₀. Immunoblots (n=3) of cortical neuron lysate expressing GFP-GR₅₀ DPR protein following treatment with DMSO or TCH-165 (10 μM) for 12, 24, and 48 hours. The red box indicates the quantified region of the blots.

2.7 Neuronal GFP-PR₅₀ Time Course Assay



Time Following Infection (hours)	Vehicle (% GFP-PR ₅₀)	10 μM TCH-165 (% GFP-PR ₅₀)	Vehicle (% total ubiq. proteins)	10 μM TCH-165 (% total ubiq. proteins)
12	100	100	100	100
24	147	231	179	130
48	160	223	231	137

n=3

Figure 2.24 Restoring proteostasis in the presence of GFP-PR₅₀. Immunoblots (n=3) of cortical neuron lysate expressing GFP-PR₅₀ DPR protein following treatment with DMSO or TCH-165 (10 μM) for 12, 24, and 48 hours. The red box indicates the quantified region of the blots.

2.8 Motor Neuron Survival Data for Control Rat Cortical Neurons Treated with TCH-165

Number of Motor Neurons

Control	LacZ	LacZ + TCH-165
43	39	33
43	42	35
41	33	45
39	38	37
40	41	42
37	42	44
41	39	39

n=1
Average motor neuron survival

Figure 2.25 Cytotoxicity data for control neurons treated with TCH-165. Data shows no change in motor neuron survival when control rat spinal cord neurons were infected with a LacZ control vector or treated with TCH-165 (3 μ M).

2.9 Motor Neuron Survival in the Presence of GFP-GA₅₀

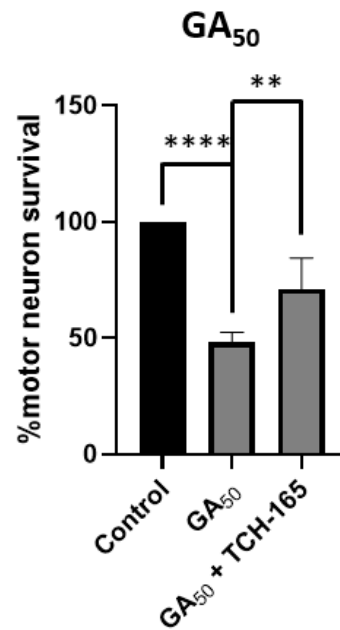


Figure 2.26 TCH-165 provides neuroprotection in the presence of poly-GA DPR proteins in rat spinal cord neurons. (A) Quantification of motor neuron survival following treatment with control (GFP with DMSO), GFP-GA₅₀ (with DMSO), or GFP-GA₅₀ (with 3 μ M TCH-165); (n=4); one-way ANOVA (ns, not significant, *p \leq 0.05; **p \leq 0.01; ***p \leq 0.001; ****p \leq 0.0001).

2.10 T20S Proteasome Activity Assay

T20S Proteasome Activity - RFU

Concentration (μM)	SS-4-20	Chlorpromazine	Astemizole	TCH-165
100	0.082	0.014	0.001	0.016
50	0.051	0.015	0.003	0.015
25	0.038	0.017	0.014	0.015
12.5	0.029	0.016	0.018	0.015
6.25	0.022	0.015	0.018	0.013
3.125	0.020	0.015	0.018	0.015
Vehicle	0.016	0.016	0.016	0.016

Figure 2.27 Purified T20S proteasome (2 nM) was incubated with DMSO or drug (3.125-100 μM) in assay buffer (38 mM Tris-HCl, 100 mM NaCl; pH 7.8) for 15 minutes at 37 °C. Proteolytic activity was measured by the degradation of fluorogenic substrate probe Suc-LLVY-AMC.

CHAPTER THREE

Discovery of a Novel Class of Small Molecule 20S Proteasome Activators Allows for the Exploration of Selective Targeting of Intrinsically Disordered Proteins

3.1 Introduction

3.1.1 Background

The degree of protein structure lies on a wide continuum ranging from proteins with a highly ordered quaternary structure to proteins lacking a defined tertiary structure; the latter are referred to as intrinsically disordered proteins (IDPs).¹ IDPs are important for many cell signaling processes,² however, accumulation has shown to elicit toxic signaling events.^{3,4} A number of neurodegenerative diseases including amyotrophic lateral sclerosis (ALS), Parkinson's disease and Alzheimer's disease have been characterized by an accumulation of aggregation-prone IDPs.⁵⁻⁸ This accumulation has shown to result in an imbalance in cellular proteostasis and the progressive death of neurons, leading to further disease progression.⁹⁻¹¹ Dysregulation of the ubiquitin-proteasome system (UPS) has been implicated as one of the major contributors to this loss of proteostasis.^{10,12-15}

The UPS is made up of the active 26S proteasome which is primarily responsible for the degradation of ubiquitylated substrates,^{16,17} and a less active/latent isoform, the 20S proteasome, which can only target IDPs for degradation.^{16,18-20} The 20S core particle is comprised of four heptameric rings ($\alpha_7\beta_7\beta_7\alpha_7$), with two inner β -rings containing three unique proteolytic sites responsible for chymotrypsin-like (CT-L), trypsin-like (T-L), and caspase-like (Casp-L) activity, and two outer α -rings that act as gate keepers to the inner proteolytic core.²¹⁻²³ The 19S regulatory caps then bind into intersubunit pockets between the α -subunits, forming the 26S proteasome. Upon docking of the 19S caps, an ATP-dependent conformational change occurs opening the gate to the proteolytic core.^{24,25} Without binding of the 19S regulatory cap, the 20S proteasome is often found in a closed gate, latent/low activity conformation, yet capable of maintaining low IDP levels.^{16,17} The low basal activity of the 20S proteasome is sufficient to maintain proper IDP levels in a healthy cell, however, accumulation of IDPs can occur through dysregulation of the UPS, mutations, gene amplification, or other cellular dysregulations.²⁶ Furthermore, the accumulation of these aggregation-prone IDPs has shown to lead to the formation of IDP aggregates, which were recently proposed to impair 20S proteasome-mediated proteolysis, resulting in the additional accumulation of toxic IDP aggregates.²⁷ To combat the

toxic accumulation of IDPs, a new strategy aimed to enhance 20S proteasome activity through small molecule activation has emerged.

Recent advances to understand the mechanism through which activation of the 20S proteasome occurs have shown that some small molecules enhance activity of the 20S proteasome through induction of an active, open gate conformation.²⁸ This has shown to be true in the case of the Tepe lab's first identified 20S proteasome activator, TCH-165. Through the use of atomic force microscopy, TCH-165 was shown to induce an open gate conformation of the 20S proteasome in the absence of the 19S regulatory cap, this ultimately allowing for more efficient substrate entry into the proteolytic core resulting in the increased rate of IDP degradation.²⁸ While TCH-165 has shown to be effective toward a number of IDP targets associated with disease,²⁸⁻³⁰ there is a need to identify additional 20S proteasome activator scaffolds to further validate this strategy as a potential therapeutic approach.

Since small molecule activation of the 20S proteasome is such a new approach, known examples of small molecules capable of enhancing 20S proteasome activity are scarce. The earliest identified examples included detergents, such as sodium dodecyl sulfate (SDS), lipids, fatty acids and a few natural products.³¹⁻³⁶ It has been shown that SDS enhances 20S proteolytic activity at low concentrations (0.02-0.08%) in *in vitro* assays. The mechanism by which SDS induces 20S proteasome activation has not been fully elucidated, but it is believed that SDS induces gate opening through partial denaturation of the 20S proteasome. While SDS-induced 20S proteasome activation is not therapeutically relevant, it remains a useful tool for *in vitro* enzyme activity assays to assess the ability of small molecules to inhibit the proteasome.^{31,32} The natural products betulinic acid, ursolic acid and oleuropein have also shown to enhance 20S proteolytic activity in *in vitro* activity assays, however, none of these compounds were able to enhance the degradation of misfolded proteins *in vitro* or in cells.³⁶⁻³⁸ In general, these molecules do not possess drug-like properties and suffer from a lack of translational activity in physiologically and disease-relevant conditions. As a result, they are not considered to be *bona fide* 20S proteasome activators.

In the search to identify 20S proteasome activators with increased drug-like properties, small molecules which adhere to Lipinski's Rule of Five are under exploration.³⁹ Lipinski's Rule of

Five is a set of guidelines that were formed based on the observation that the majority of small molecule drugs share similar chemical and physical properties. Lipinski suggests that a small molecule drug typically has a molecular weight (MW) less than 500 g/mol, an octanol-water partition coefficient (cLog P) no greater than 5, and no more than 5 hydrogen bond donors and 10 hydrogen bond acceptors.³⁹ These properties have shown to result in small molecules that are able to cross biological membranes to reach the desired target receptors. To obtain more drug-like 20S proteasome activators, several high-throughput screens (HTS) of libraries of FDA-approved drugs have been conducted in an effort to repurpose existing pharmacological drugs for use as 20S proteasome activators.^{37,40} Drug repurposing is a strategic approach that has been explored to accelerate the drug discovery process by identifying a new therapeutic use for an existing drug. This approach has attracted great interest due to the fact that a majority of FDA-approved drugs adhere to Lipinski's rules and have already demonstrated cell and membrane permeability, as well as efficacy toward a biological target.

In 2016, utilizing this strategy of drug repurposing, Trader and Kodadek reported a HTS of the NIH Clinical Collection which is comprised of 726 small molecules.³⁷ From this screen, two new 20S proteasome activators, MK-886 and AM-404, were identified and demonstrated efficacy toward the enhancement of proteasome-mediated turnover of a misfolded protein in cells.³⁷ At this same time, following the discovery of TCH-165 as a 20S proteasome activator and gaining an interest in this new field, the Tepe lab conducted their own HTS of the NIH Clinical Collection and Prestwick libraries.⁴⁰ From this screen, several new 20S proteasome activators were identified including the neuroleptic agents fluspirilene⁴¹ and chlorpromazine,⁴⁰ as well as additional phenothiazine scaffolds (Figure 3.1). Further follow-up structure-activity relationship (SAR) studies on the phenothiazine scaffold have been conducted to synthesize analogues with increased potency for enhancement of 20S proteolytic activity.^{40,42} As chlorpromazine is a repurposed drug, it was necessary to eliminate the scaffold's endogenous neuroleptic activity to avoid toxic off-target effects when utilizing the compound as a 20S proteasome activator. This was accomplished through removal of the dopamine D₂ receptor binding moiety of the ligand, which prevented binding to the D₂ receptor thereby eliminating endogenous neuroleptic activity. An SAR study was also conducted using the newly identified fluspirilene scaffold, resulting in the

identification of novel analogues which prevented the accumulation and oligomerization of α -synuclein, an IDP implicated in the progression of Parkinson's disease.⁴¹

With great importance to the work outlined in this chapter, the antihistamine drug, astemizole, was also identified as a novel 20S proteasome activator in the screen (Figure 3.1). In order to increase its selectivity for activation of the 20S proteasome over its endogenous antihistamine targets, the compound was synthetically modified to abrogate its endogenous antihistamine activity. Herein, the design, synthesis and biological activity of novel analogues based on this benzimidazole scaffold will be discussed. Furthermore, exploration of this scaffold led to insightful studies into the mechanism of small molecule 20S proteasome activation.

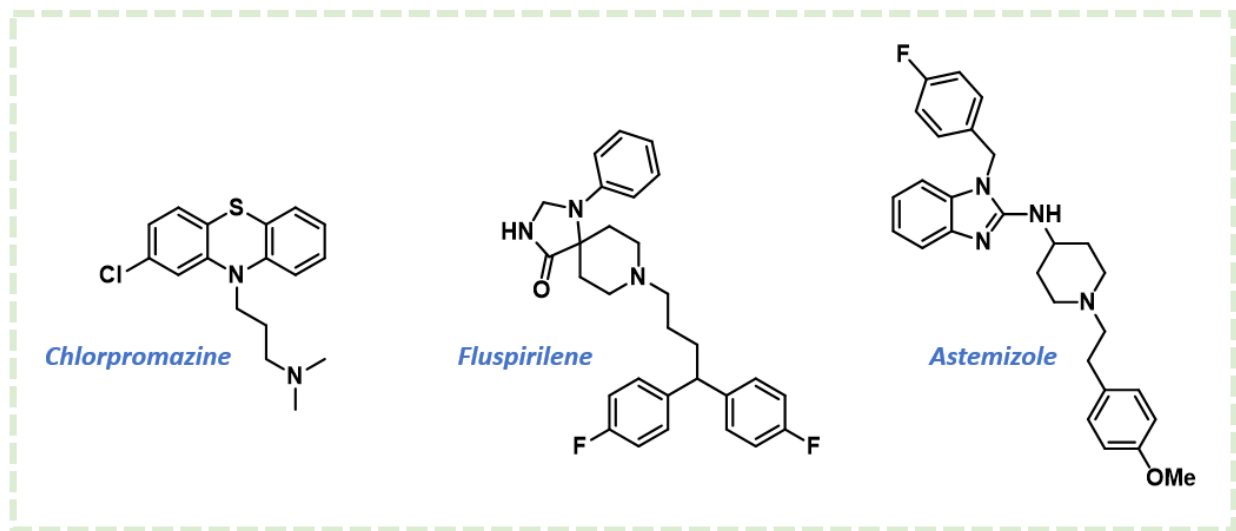


Figure 3.1 Structures of 20S proteasome activators identified in the 2017 HTS of the NIH Clinical Collection and Prestwick libraries conducted by the Tepe lab.⁴⁰

3.2 Results and Discussion

3.2.1 Astemizole Enhances the Rate of Proteolytic Activity of the 20S Proteasome

To confirm the results of the high-throughput screen and validate astemizole as a true hit, the ability of astemizole to enhance proteolytic activity of the 20S proteasome was evaluated using a fluorogenic peptide degradation assay which utilizes short peptide substrates conjugated to the fluorophore 7-amino-4-methylcoumarin (AMC). The three fluorogenic substrate probes (Suc-LLVY-AMC, Boc-LRR-AMC, and Z-LLE-AMC) were used to test for activation of 20S proteasome activity for the combined three proteolytic sites of the 20S proteasome, the chymotrypsin-like (CT-L), trypsin-like (T-L), and caspase-like (Casp-L) sites, respectively. To explore the ability of astemizole to enhance 20S proteasome activity, purified human 20S proteasome was pretreated with varying concentrations of astemizole, followed by addition of the three fluorogenic substrate probes. Proteolytic cleavage of the peptide results in the release of AMC; this fluorescence was measured over time to quantify 20S proteolytic activity. A dose-response curve (Figure 3.2B) was generated demonstrating a dose-dependent increase in the rate of 20S proteasome activity upon treatment with astemizole. From this experiment, it was concluded that astemizole enhances the rate of 20S proteolytic activity with an effective concentration required to increase 20S proteasome activity by 200% (i.e. EC_{200}) of $4.0 \mu\text{M}$ (Figure 3.2C), with a maximum fold enhancement of 7.5-fold over the vehicle at the highest concentration tested (i.e. 750%).

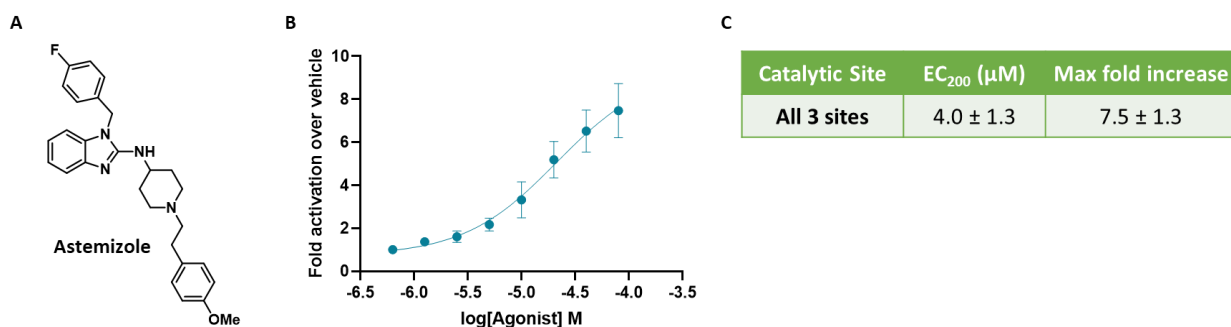


Figure 3.2 Astemizole enhances the rate of 20S-mediated degradation of peptide substrates of the 20S proteasome. (A) Structure of astemizole. (B) Dose-response curve of astemizole for 20S-mediated proteolysis of fluorogenic substrates Suc-LLVY-AMC, Boc-LRR-AMC, and Z-LLE-AMC specific to the 3 proteolytic sites CT-L, T-L, and Casp-L, respectively. (C) EC_{200} and maximum fold activation values for astemizole ($n=3$); error bars denote standard deviation.

3.2.2 Predicting the Binding Site of Astemizole Through Molecular Docking

The endogenous 20S proteasome activator, 19S cap, binds into the intersubunit pockets between the α -subunits using an HbYX tail motif.²⁴ Upon docking of the 19S cap, an ATP-dependent conformational change occurs opening the gate to the proteolytic core and allowing for increased substrate access to the proteolytic sites.^{24,25} As previously discussed, small molecule 20S proteasome activator, TCH-165, has also shown to induce an open gate conformation of the 20S proteasome resulting in an enhanced rate of proteolytic activity.²⁸ While the binding site of TCH-165 and other small molecule 20S proteasome activators has yet to be elucidated, molecular docking studies have predicted that TCH-165 binds in the α 1/2 intersubunit pocket of the α -ring of the 20S proteasome.²⁸ Another 20S proteasome activator identified in the HTS, fluspirilene, is predicted to bind in a different intersubunit pocket, the α 2/3 intersubunit pocket.⁴¹ Therefore, it is hypothesized that the small molecules mimic binding of the 19S cap to induce an open gate conformation of the 20S proteasome and enhance proteolytic activity.

Since astemizole was validated as a novel 20S proteasome activator, I conducted molecular docking studies to predict its binding site and determine if the predicted binding site of this new scaffold would support the above hypothesis. The molecular docking studies were performed using Autodock Vina™ and supported through computational resources and services provided by the Institute for Cyber-Enabled Research at Michigan State University. Unbiased docking studies were performed by docking against the entirety of the human 20S proteasome (PDB ID: 4R3O)⁴³ to determine if ligands preferentially docked in any location. The studies predicted the top nine favored binding modes of the ligand, which were analyzed using PyMOL and BIOVIA Discovery Studio 2020 to determine the predicted ligand-receptor interactions. Upon analysis of the top nine binding modes of astemizole for the 20S proteasome, astemizole was found to preferentially bind to the α 2/3 intersubunit pocket of the 20S proteasome (Figure 3.3A), the same intersubunit pocket in which fluspirilene is predicted to bind.⁴¹ A more detailed analysis of the predicted ligand-receptor interactions within the α 2/3 intersubunit pocket revealed some shared ligand-receptor interactions with those predicted for fluspirilene, such as the interactions with the PHE60 and PHE61 amino acid residues.⁴¹ Additional unique interactions such as pi-anion interactions with GLU63 and a hydrogen bond with SER62 were also predicted to contribute to

ligand binding of astemizole (Figure 3.3B). It is important to note that while additional ligand-receptor interactions were predicted for astemizole and the analogues discussed in this chapter, weaker interactions such as van der Waals interactions were excluded from the 2D ligand-receptor interaction diagrams and discussion for the sake of clarity.

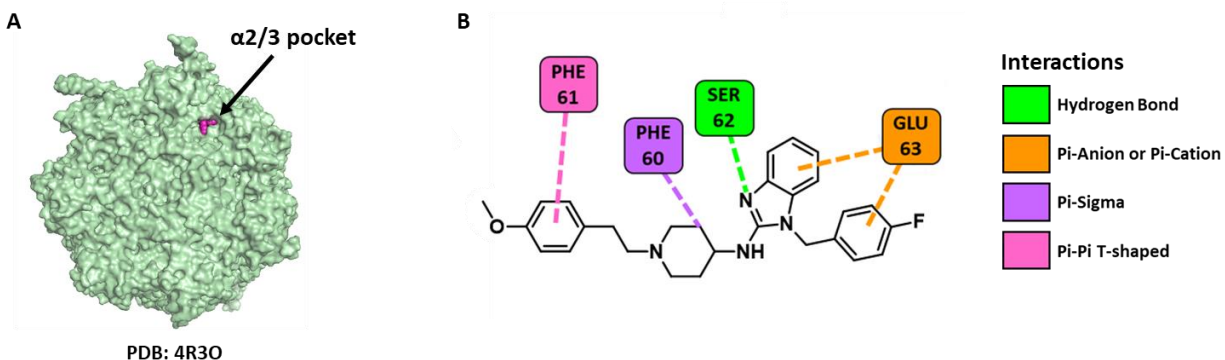


Figure 3.3 Molecular docking predicts astemizole binding site. (A) Astemizole is predicted to bind in the $\alpha 2/3$ intersubunit pocket of the 20S proteasome (top-view; PDB ID: 4R30). (B) Select predicted ligand-receptor interactions between amino acid residues of the $\alpha 2/3$ intersubunit pocket and astemizole.

3.2.3 Goals for the Molecular Docking-Guided Design of Analogues

The docking model for the astemizole scaffold was then used to guide the design and synthesis of a series of analogues utilizing the benzimidazole core of the scaffold. The analogues were designed with the following three goals in mind; (1) eliminate endogenous antihistamine activity of the scaffold, (2) maintain drug-like properties, such as a low MW and cLog P, and (3) maintain or enhance the ability to activate the 20S proteasome. Once an analogue was designed, molecular docking studies were conducted to predict whether the compound would bind into the $\alpha 2/3$ intersubunit pocket and if so, which amino acids within the pocket was the ligand predicted to interact with. Once synthesized, analogues were tested for their ability to enhance activity of the 20S proteasome. This allowed for analysis of which structural motifs of the scaffold were necessary for binding to the 20S proteasome to give the scaffold its ability to enhance 20S proteolytic activity.

The first analogues designed focused on elimination of the endogenous antihistamine activity of the scaffold, which I hypothesized could be accomplished through the removal of the H_1 histamine receptor binding site. Analysis of the H_1 receptor binding pocket in complex with a

number of H₁ receptor-antagonists has identified a salt bridge formed between an aspartate residue of the receptor and the tertiary amine moiety of the ligand as the main stabilizing interaction for ligand-receptor binding.^{44–47} Therefore, it was hypothesized that removing the tertiary amine moiety would interrupt formation of the stabilizing salt bridge and abrogate endogenous antihistamine activity. Furthermore, with removal of the tertiary amine moiety, the aryl methoxy “tail” portion of the scaffold was also removed. This further decreased the molecular weight of the analogues, helping to satisfy the analogue design goal of maintaining drug-like properties.

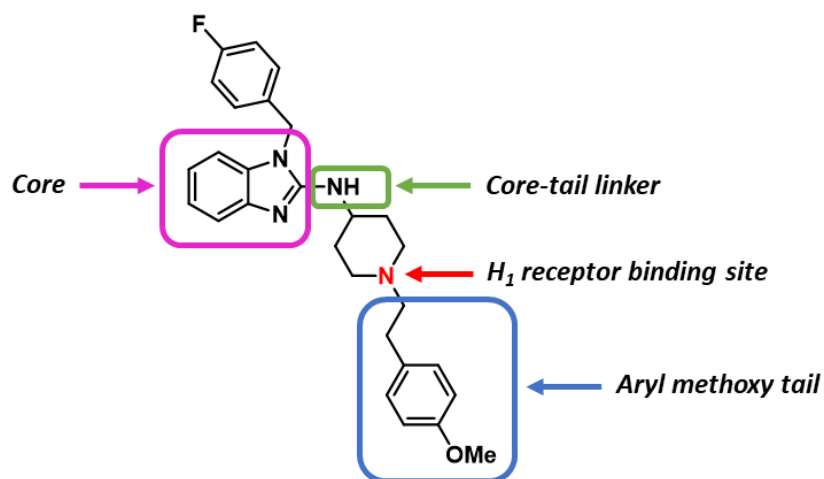
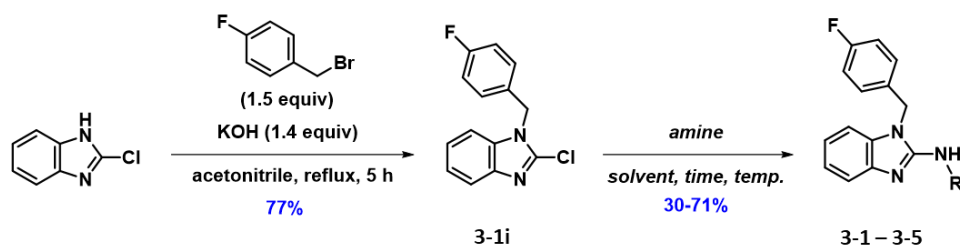


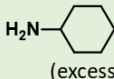
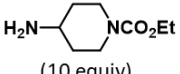
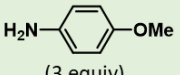
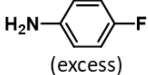
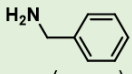
Figure 3.4 Astemizole scaffold with modification points outlined. Removal of the tertiary amine moiety is hypothesized to eliminate endogenous antihistamine activity of the scaffold. Analogues discussed in this chapter were synthesized and tested for biological activity to determine how substitutions of the core, core-tail linker, and aryl methoxy tail portion of the scaffold impacted biological activity.

3.2.4 Synthesis and Biological Testing of Analogues

With this strategy in mind, a series of analogues were synthesized including only a small core portion of astemizole’s structure and removing the tertiary amine moiety responsible for binding to the H₁ receptor. Synthesis of compound **3-1** began with the benzylation of 2-chloro-1*H*-benzimidazole with 4-fluorobenzyl bromide to afford **3-1i**, followed by a neat thermal coupling reaction with cyclohexylamine (Figure 3.5).



Amination Conditions:

Compound	Amine	Solvent	Temp. (°C)	Reaction Time	Yield
3-1	 (excess)	---	110	2 d	42%
3-2i^a	 (10 equiv)	DMA	155	3 d	45%
3-3	 (3 equiv)	EtOH	Reflux	1 d	71%
3-4	 (excess)	---	140	2 d	51%
3-5	 (excess)	---	125	2 d	30%

^a Resulting amination product was deprotected by refluxing in 48% HBr for 3 h to afford compound **3-2** in 83% yield.

Figure 3.5 Synthesis of Compounds **3-1** through **3-5**.

The analogue was then tested for its ability to enhance 20S proteolytic activity using the fluorogenic peptide degradation assay. The results showed compound **3-1** was only able to activate the 20S proteasome 4.1-fold over the vehicle with an EC₂₀₀ value of 28.0 μM (Figure 3.6). This suggested that the piperidine ring and/or the pi system of the aryl methoxy “tail” may be essential for interaction with the 20S proteasome. To explore the necessity of the piperidine ring, compound **3-2** was synthesized. Synthesis began with a thermal coupling reaction of the benzimidazole **3-1i** with ethyl 4-aminopiperidinecarboxylate to ensure selective coupling of the primary amine to give compound **3-2i**, followed by deprotection⁴⁸ of the carbamate with 48% HBr to afford compound **3-2**. Upon biological testing, compound **3-2** was unable to enhance 20S proteolytic activity and was deemed inactive with an EC₂₀₀ value greater than 80.0 μM (Figure

3.6). These results further suggested that the pi system of the aryl methoxy “tail” is necessary for ligand binding to the 20S proteasome.

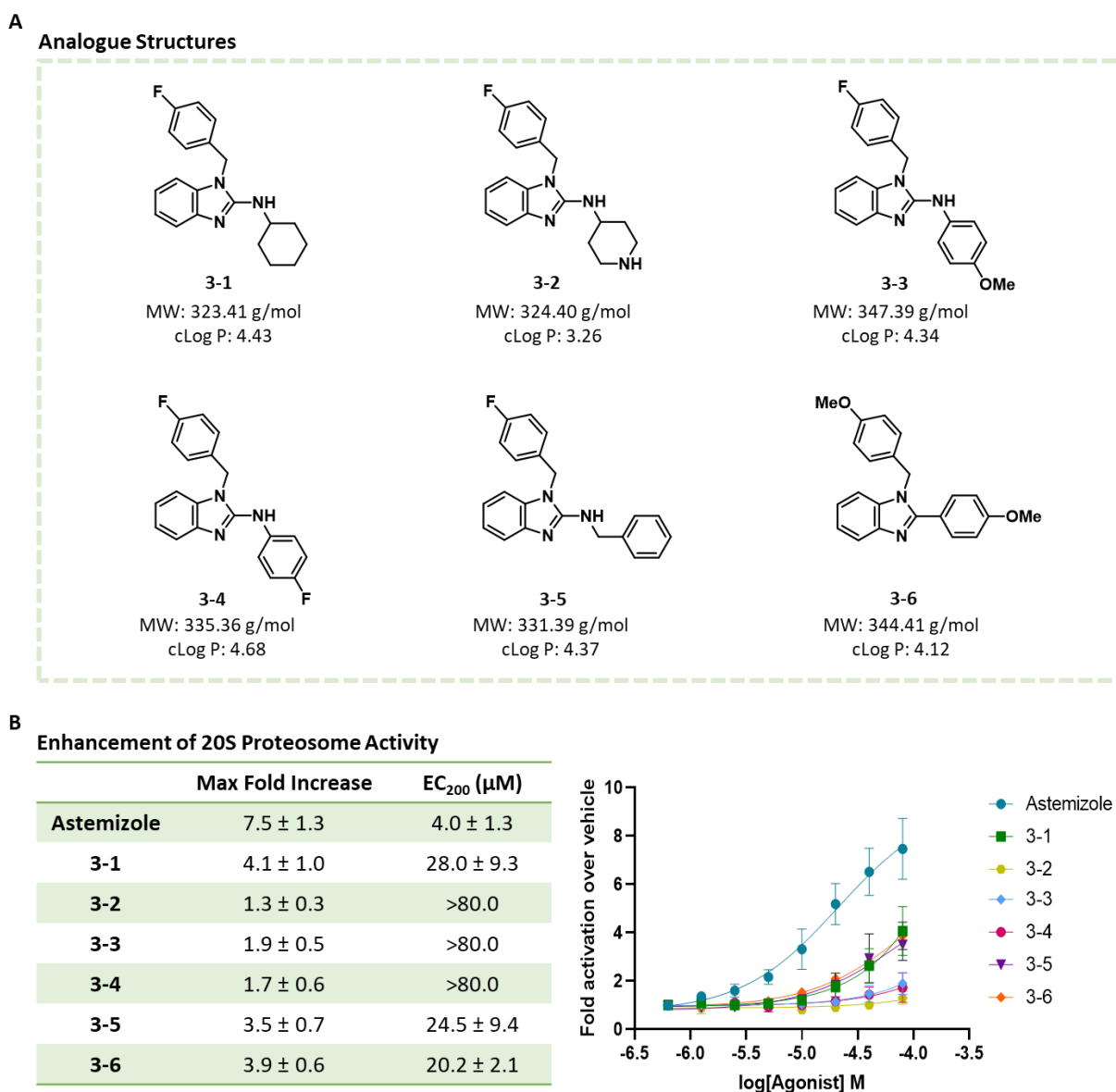


Figure 3.6 Astemizole analogues synthesized and evaluation of their biological activity. (A) Structures of synthesized analogues with molecular weight (MW) and predicted octanol-water partition coefficient (cLog P) for each structure denoted. (B) Dose-response curve of compounds **3-1** through **3-6** for 20S proteasome-mediated proteolysis of fluorogenic substrates Suc-LLVY-AMC, Boc-LRR-AMC and Z-LLE-AMC. The maximum fold increase and EC₂₀₀ values for all analogues are denoted (n=3); error bars denote standard deviation.

To further explore this, the molecular docking of the two analogues was analyzed to evaluate how modification of the scaffold may have affected the predicted ligand-receptor binding interactions. If significant differences between the predicted ligand-receptor binding interactions of the analogues and astemizole are observed, this may help explain their losses in potency and aid in validation of the docking model. While both compounds **3-1** and **3-2** were predicted to bind in the $\alpha 2/3$ intersubunit pocket, there were differences in their predicted ligand-receptor interactions that may help explain their decreases in activity. Similarly to astemizole, compound **3-1** is predicted to have pi-anion interactions with GLU63, a hydrogen bond with SER62, and a pi-sigma interaction with PHE60. However, compound **3-1** was not predicted to form the pi-pi T-shaped interaction with PHE61, which could result in the loss in potency observed by this analogue in comparison to astemizole (Figure 3.7B). Compound **3-2** lost this same interaction with PHE61, but also lost the pi-sigma interaction with PHE60 (Figure 3.7C). The loss of these interactions could have a vast impact on the orientation of the ligand within the binding pocket and may explain its inability to enhance 20S activity compared to compound **3-1** and astemizole. While the docking model is strictly predictive, the activity and predicted ligand-receptor interactions correlated with one another, supporting the docking model.

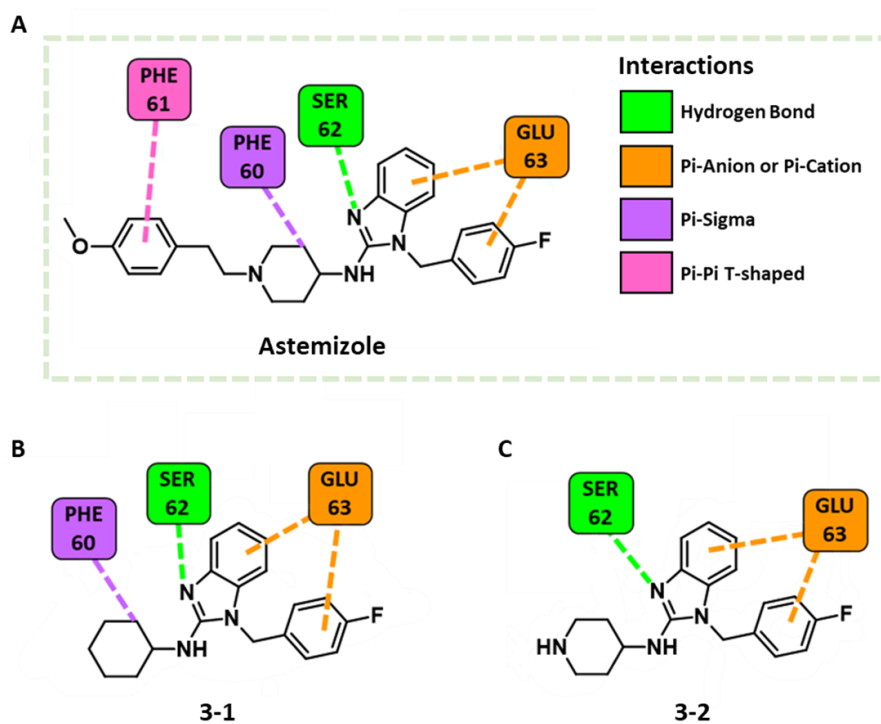
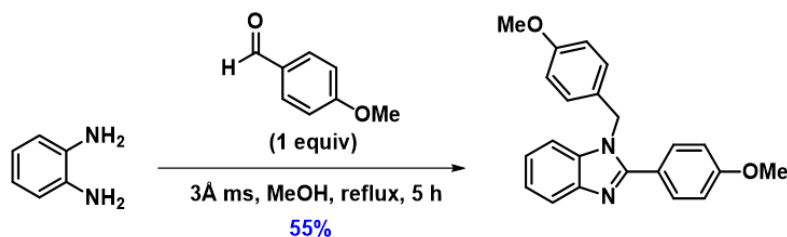


Figure 3.7 Molecular docking predicts analogue binding sites. Select predicted ligand-receptor interactions between amino acids of the $\alpha 2/3$ intersubunit pocket and astemizole (A), compound **3-1** (B) and compound **3-2** (C). Docking studies were performed using the human 20S proteasome (PDB ID: 4R3O) as the macromolecule.

To further explore the necessity of the aryl methoxy moiety of the scaffold, compounds **3-3**, **3-4**, **3-5** and **3-6** were synthesized varying the position of the aryl ring to determine how altering the position of the pi-system would affect the molecule's ability to enhance 20S proteolytic activity. Compounds **3-3**, **3-4** and **3-5** were synthesized using a thermal coupling reaction of the benzimidazole core **3-1i** and a primary amine through either a neat reaction or through use of a high boiling solvent (Figure 3.5). Compound **3-6** was synthesized through a cyclization of *o*-phenylenediamine and an aromatic aldehyde under non-oxidative conditions to afford the benzylated 2-arylbenzimidazole in one step (Scheme 3.1).⁴⁹ Compounds **3-3** through **3-6** were then tested for their ability to enhance activity of the 20S proteasome but were deemed inactive in comparison to astemizole. At the highest concentration tested, the analogues were only able to enhance activity of the 20S proteasome between 1.7 to 3.9-fold over the vehicle with EC₂₀₀ values ranging from 20.2 μM to greater than 80.0 μM (Figure 3.6).

Scheme 3.1: Synthesis of Compound **3-6**.



The molecular docking results of these compounds were then examined to explore whether losses of predicted ligand-receptor interactions in comparison to those predicted for astemizole may be responsible for the decreases in activity. While incorporation of the aryl ring of the aniline is predicted to pick up a pi-pi interaction with PHE60 in the docking results of compounds **3-3** through **3-6**, the compounds are generally oriented slightly different within the binding pocket. This resulted in a decrease in the frequency of predicted interactions with SER62 and GLU63 as predicted for the earlier compounds, and the incorporation of novel ligand-receptor interactions with other amino acids within the pocket. For compound **3-3**, a pi-pi interaction is predicted to occur with PHE60, as well as a pi-cation interaction with ARG91. Compound **3-4** is also predicted to form a pi-pi interaction with PHE60, as well as a pi-cation interaction and hydrogen bond with GLU63. However, these compounds were inactive in the activity assay, suggesting that these predicted interactions alone do not effectively induce an active conformation of the 20S proteasome.

The molecular docking results of compound **3-5** predicted a hydrogen bond with GLU63, pi-pi interactions with PHE60 and TYR66, and an additional pi-sigma interaction with THR80. Compound **3-6** is predicted to also form pi-pi interactions with PHE60 and PHE61, as well as a pi-cation interaction with ARG91 and a hydrogen bond with ILE65. Since compounds **3-5** and **3-6** showed increased biological activity in comparison to compounds **3-3** and **3-4**, it is hypothesized that the increased number or types of ligand-receptor interactions predicted for compounds **3-5** and **3-6** may induce a more favorable conformational change of the 20S proteasome. This could then result in more efficient substrate access to the proteolytic core and may explain the increase in activity compared to the former compounds. In all, incorporation of the aryl ring of the aniline is predicted to result in an additional pi-pi interaction in the case of each of these analogues,

however, likely due to their small size, the orientation of the compounds within the binding pocket is quite variable. Therefore, with the docking predictions and activity results, I hypothesized that the original length and position of the aryl methoxy tail portion of the scaffold was necessary to ensure the compound was in the proper orientation within the binding pocket to give the molecule its activity.

3.2.5 Synthesis and Biological Testing of Acyl Astemizole

The activity data for compounds **3-1** through **3-6** demonstrated that major structural modifications, such as removal of the aryl methoxy tail, resulted in significant decreases in the molecules' ability to enhance 20S proteasome activity. This suggested that an extended scaffold was necessary to form additional ligand-receptor interactions to have a potency for 20S proteasome activity on par with astemizole. To test this hypothesis, an acylated version of astemizole was synthesized. Compound **3-7** (referred to in this chapter as acyl astemizole) was synthesized by coupling compound **3-2** with 4-methoxyphenylacetyl chloride (Figure 3.8A). For the synthesis of this compound, the tertiary amine primarily responsible for stabilizing the interaction with the H₁ histamine receptor binding site was acylated. This was done to remove the basicity of the nitrogen, thereby preventing formation of the stabilizing salt bridge interaction and eliminating the antihistamine activity of the compound. Similar ligand modification has shown previous success in removal of endogenous activity in the design of analogues of another repurposed 20S proteasome activator scaffold previously published by the Tepe lab.⁴⁰ Along with acyl astemizole, additional analogues with this acylated tail and various heterocyclic core and core-tail linkers were designed and synthesized in collaboration with Kyra Dvorak. At this point in the project, Kyra focused on synthesis of the analogues, while I focused on further exploration of the biological activities of the molecules. In these studies, we aimed to explore if the smaller structural modifications found in analogues **3-7** through **3-12** could be incorporated without decreasing the molecule's ability to enhance activity of the 20S proteasome.

Following synthesis, the ability of acyl astemizole to enhance activity of the 20S proteasome was evaluated. A dose-response curve was generated showing an increase in 20S proteasome activity with increasing dose of acyl astemizole. From this experiment, we can conclude that acyl astemizole is able to enhance 20S proteolytic activity 8.3-fold (i.e. 830%) over the vehicle with an EC₂₀₀ value of 4.6 μ M (Figure 3.8B). The potency of this compound was similar to astemizole's, therefore the docking of acyl astemizole was analyzed to explore whether the two compounds shared similar ligand-receptor interactions, perhaps those that had been lost with previous analogues. As shown in Figure 3.8C, acyl astemizole is predicted to form a pi-anion interaction and hydrogen bond with GLU63, similar to how astemizole is predicted to interact with this amino acid residue. Additionally, the pi-sigma interaction with PHE60 and the pi-pi T-shaped interaction with PHE61 were predicted to form, as well as a new pi-cation interaction with ARG91. These docking results in combination with the activity data suggest that reestablishing the interactions with PHE60 and PHE61, potentially in combination with the newly formed interaction with ARG91, resulted in an increase in potency similar to that of astemizole.

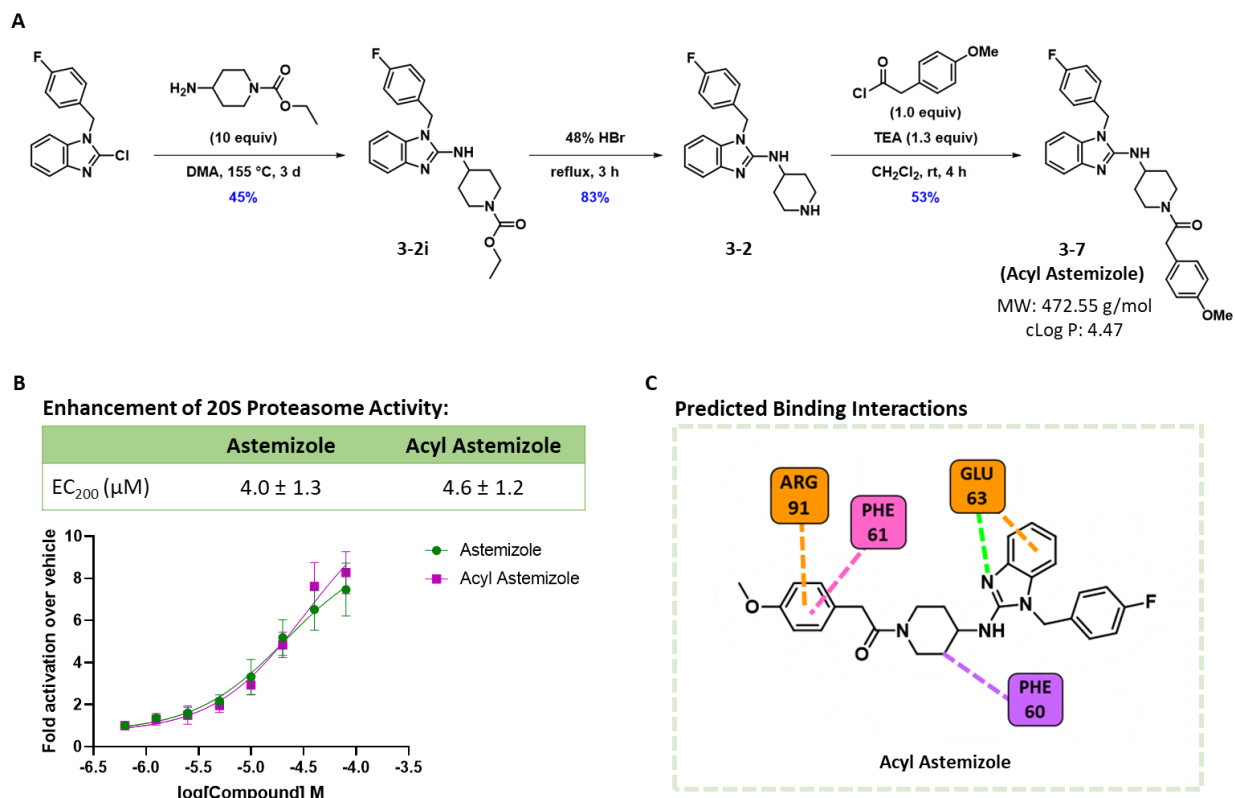


Figure 3.8 Acyl astemizole enhances 20S proteasome-mediated degradation of peptide substrates of the 20S proteasome. (A) Synthesis of acyl astemizole. (B) Dose-response curve of acyl astemizole and astemizole for 20S proteasome-mediated proteolysis of fluorogenic substrates Suc-LLVY-AMC, Boc-LRR-AMC, and Z-LLE-AMC with calculated EC₂₀₀ values. (C) Select predicted ligand-receptor interactions between amino acids of the α 2/3 intersubunit pocket and acyl astemizole. Docking studies were performed using the human 20S proteasome (PDB ID: 4R3O) as the macromolecule.

Compounds **3-8** through **3-12** (synthesized by Kyra Dvorak; Figure 3.9A) were also tested for their ability to enhance 20S proteolytic activity to probe other structural modifications that could be incorporated without losing activity. To further explore whether the aryl ring of the benzimidazole was contributing to important binding interactions, the aryl ring was removed to afford the imidazoline **3-8**. The compound's ability to degrade the fluorogenic substrate probes was then tested. The results showed almost a two-fold loss in potency (i.e. EC₂₀₀) compared to acyl astemizole (Figure 3.9B). We then designed analogue **3-9** to determine how reincorporation of the aryl ring to the imidazoline scaffold at a rotatable position would affect the activity. The activity assay results showed a large decrease in the maximum fold increase compared to acyl astemizole, but almost a two-fold increase in potency, emphasizing the importance of this aryl

ring of the core in the binding pocket (Figure 3.9B). Analysis of the molecular docking results supported the activity data. Compound **3-8** was predicted to form a pi-cation interaction and hydrogen bond with ARG91, a hydrogen bond with TYR66, and a pi-pi interaction with PHE60. Whereas the more active imidazoline **3-9**, in addition to those same ligand-receptor interactions, is also predicted to form a pi-pi interaction with PHE61 and a hydrogen bond with GLU63. The predicted ligand-receptor interactions for compound **3-9**, as well as the EC₂₀₀ values, are quite comparable with acyl astemizole and further support the docking model.

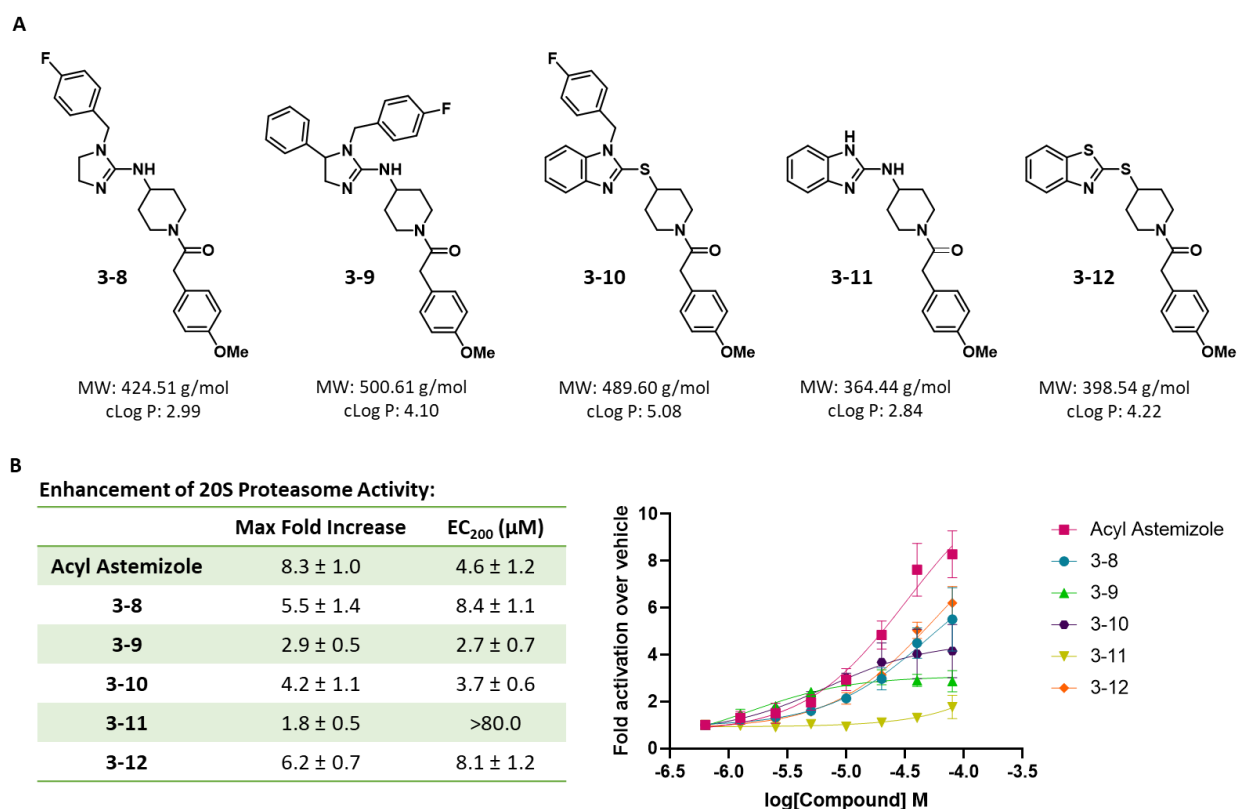


Figure 3.9 Analogues with extended scaffold enhance 20S-mediated degradation of peptide substrates of the 20S proteasome. (A) Structure of analogues synthesized by Kyra Dvorak. (B) Dose-response curve of analogues for 20S proteasome-mediated proteolysis of fluorogenic substrates Suc-LLVY-AMC, Boc-LRR-AMC, and Z-LLE-AMC with calculated max fold increase and EC₂₀₀ values. All data was collected in triplicate (n=3); error bars denote standard deviation.

We then explored whether the amine core-tail linker could be modified without losing activity. The coupling of the acyl astemizole tail to afford 2-amino-benzimidazoles was a difficult transformation to facilitate, requiring harsh thermal coupling conditions to synthesize many of the analogues. Therefore, we aimed to explore whether the incorporation of a sulfur atom at the

2-position of the benzimidazole instead of an amine would maintain biological activity and allow for ease of synthesis. Compound **3-10** was synthesized and its ability to enhance 20S proteasome activity was tested (Figure 3.9). Although the maximum fold increase in activity over the vehicle was decreased, the EC₂₀₀ value was comparable to that of acyl astemizole. Analysis of the molecular docking results revealed very similar predicted ligand-receptor binding interactions between compound **3-10** and acyl astemizole. Compound **3-10** is predicted to form a pi-cation interaction and hydrogen bond with GLU63, a hydrogen bond with SER62, and pi-pi interactions with PHE61, TYR154 and PHE60. Furthermore, PHE60 is predicted to form a pi-sulfur interaction with the sulfur atom at the 2-position of the benzimidazole. In combination, the predicted docking interactions and activity data suggest that replacement of the amine with a sulfur atom is a feasible option for future analogue development.

Lastly, to explore the necessity of the fluorobenzyl group on the benzimidazole core. Acyl astemizole was debenzylated to afford compound **3-11** (Figure 3.9A), which upon activity testing was shown to be unable to enhance 20S proteasome activity. Interestingly, exchange of the 2-amino-benzimidazole core for the 2-sulfur-benzothiazole core (compound **3-12**), resulted in an analogue with moderate activity (EC₂₀₀ = 8.1 μM; Figure 3.9B). As exchange of the amine core-tail linker for the sulfur core-tail linker had no significant effect on the EC₂₀₀ values when comparing the EC₂₀₀ values of acyl astemizole and compound **3-10**, the data suggests that incorporation of the benzothiazole core may be responsible for the increase in activity of **3-12** in comparison to compound **3-11**. The molecular docking results provide some support for this activity data. Compound **3-11** was predicted to form a pi-sigma interaction with GLU63, and hydrogen bonds with SER62 and TYR154. However, the more active analogue **3-12** is predicted to form hydrogen bonds with TYR66 and ARG91 and a pi-pi interaction with PHE60. In addition, PHE61 is predicted to form a pi-sulfur interaction with the sulfur atom of the benzothiazole core, which may help explain the increase in activity between the two analogues. While further analogue development is needed to test this hypothesis, incorporation of the benzothiazole core into future analogues is an exciting avenue to explore further.

In all, several analogues with the extended scaffold (Compounds **3-7** through **3-12**) showed comparable activities to the parent compound astemizole. Furthermore, even with the

extended scaffold, select structural modifications led to losses in activity, suggesting the scaffold is sensitive to further structure-activity relationship (SAR) studies. While analogue development is ongoing, my next goal in the project was to conduct more in-depth biological studies to further explore the utility of this scaffold as a 20S proteasome activator. For these studies, astemizole and acyl astemizole were used as model compounds for the scaffold.

3.2.6 Further Exploration of the Efficacy of the Astemizole Scaffold Toward Various IDP Targets

With the synthesis of acyl astemizole I had accomplished my three main goals of analogue design by removing endogenous antihistamine activity, maintaining drug-like properties (i.e. low molecular weight and cLog P), and maintaining the ability to enhance 20S proteolytic activity. Therefore, using astemizole and acyl astemizole, my next goal of the project was to conduct more in-depth biological studies to explore the efficacy of these newly identified 20S proteasome activators. In the first of these studies, I assessed the ability of astemizole and acyl astemizole to enhance the 20S proteasome-mediated degradation of a disease relevant IDP *in vitro*. The IDP α -synuclein was used in these experiments as it has been implicated in the progression of Parkinson's disease.⁵⁰ Similar to the disease progression cascade outlined for ALS in the previous chapter, the accumulation and aggregation of α -synuclein has shown to impair proteasome function, causing an imbalance in proteostasis and resulting in neurotoxicity.^{51,52} As α -synuclein is a known proteasome substrate, it is hypothesized that enhancing its 20S proteasome-mediated degradation through small molecule activation of the 20S proteasome could prevent its accumulation, thereby decreasing its toxic effects.

In this experiment, purified human 20S proteasome was pretreated with varying concentrations of the 20S proteasome activator, followed by a 2-hour incubation with α -synuclein. Following the two-hour incubation, the digestion products were separated by protein gel electrophoresis and visualized through silver staining of the gel to quantify the amount of α -synuclein remaining (Figure 3.10; all replicates are shown in Figures 3.19 and 3.20 of the Appendix). Astemizole was only able to significantly enhance the 20S proteasome-mediated degradation of α -synuclein at the highest concentration tested (10 μ M), with 51 percent α -synuclein remaining relative to the vehicle. Acyl astemizole was able to enhance the 20S proteasome-mediated degradation in a much more dose-dependent manner. As shown in Figure

In this experiment, purified human 20S proteasome was pretreated with 20S proteasome activator, followed by a 1-hour incubation with tau. Following the incubation, the digestion products were separated by protein gel electrophoresis and visualized using an immunoblot to quantify the amount of tau remaining (Figures 3.11A and 3.11C). Preliminary results show astemizole and acyl astemizole effectively enhanced the 20S proteasome-mediated degradation of tau at the 20 μ M dose compared to the untreated control, with 44 and 32 percent tau remaining, respectively. The positive control TCH-165 (10 μ M) also enhanced the degradation of tau, with only 65 percent tau remaining compared to the vehicle. Conversely, inhibition of the 20S proteasome with bortezomib (BTZ) completely blocked the degradation of tau.

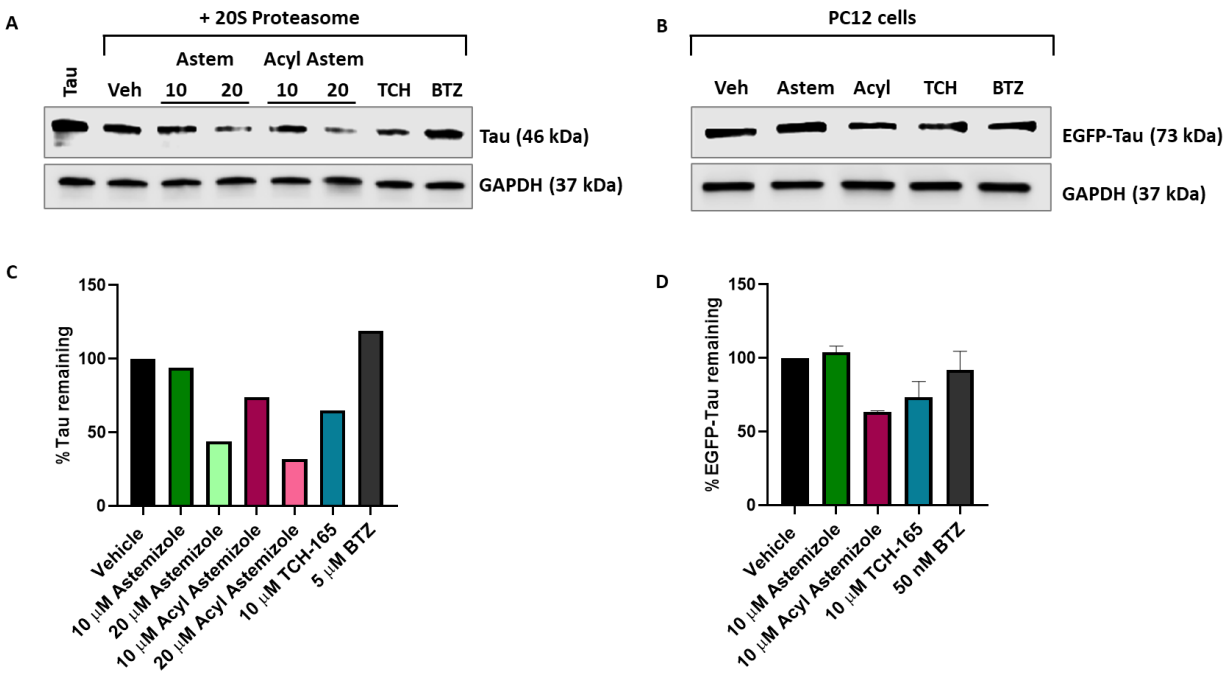


Figure 3.11 Acyl astemizole enhances 20S proteasome-mediated degradation of tau. (A) Immunoblot of *in vitro* tau digestion (1 h) with purified 20S proteasome pretreated with 20S proteasome activator (10 μ M or 20 μ M), or proteasome inhibitor bortezomib (BTZ, 5 μ M). Immunoblot probed with anti-tau and anti-GAPDH antibodies. (C) Quantification of *in vitro* tau digestion immunoblot (n=1). (B) Representative immunoblot of the amount of EGFP-Tau in PC12 cells following an 18-hour treatment with vehicle (DMSO), 20S proteasome activator (10 μ M), or BTZ (50 nM). Immunoblot probed with anti-tau and anti-GAPDH antibodies. (D) Quantification of cellular EGFP-Tau immunoblots (n=2); error bars denote standard deviation.

Since astemizole and acyl astemizole had shown to enhance 20S proteasome-mediated degradation of tau *in vitro*, I next aimed to explore if this effect would translate in a cellular degradation model of tau. In this experiment, PC12 cells were transiently transfected with a plasmid to express an EGFP-tagged tau conjugate protein (pRK5-EGFP-Tau; Addgene plasmid #46904). Following a 48-hour transfection, the transfected cells were treated with vehicle (DMSO), 20S proteasome activator (10 μ M), or BTZ (50 nM) for 18 hours. The cells were then harvested, lysed, and probed for the amount of tau using an immunoblot (Figures 3.11B and 3.11D; all replicates can be found in Figure 3.21 of the Appendix). These preliminary experiments show that astemizole did not reduce cellular tau protein levels. However, acyl astemizole was able to reduce the amount of tau to 64 percent (36 percent reduction) compared to the vehicle control, similar to the positive control TCH-165. The proteasome inhibitor, BTZ, prevented the reduction of tau, suggesting that proteasomal degradation is responsible for the decrease in tau protein levels observed in the assay. While the reason astemizole was unable to reduce tau protein levels in cells cannot be determined from this assay, a number of reasons are possible, including solubility issues in the cell culture media or non-specific binding at the high concentration used. A study conducted to evaluate the cytotoxicity of these compounds in cells provided some support for the non-specific binding of astemizole, demonstrating that astemizole has toxic off-target effects at concentrations above 2.5 μ M, whereas acyl astemizole did not cause any toxicity until approximately 20 μ M (data shown in Figure 3.22 of the Appendix).

3.2.7 Exploring the Efficacy of the Astemizole Scaffold Toward Poly-GR DPR Proteins

To explore the efficacy of astemizole and acyl astemizole toward another IDP target, I aimed to investigate whether the compounds could enhance the degradation of the poly-GR DPR proteins as I have previously shown with 20S proteasome activator, TCH-165.²⁹ In this experiment, the ability of the compounds to enhance 20S proteasome-mediated degradation of the fluorogenic poly-GR DPR protein (Suc-GRGRGR-AMC) was evaluated. As discussed in the previous chapter, proteolytic cleavage of the DPR protein substrate results in release of the AMC fluorophore. The fluorescence is then quantified to measure the amount of the DPR probe degraded. As shown in Figure 3.12, acyl astemizole was able to effectively enhance degradation of the poly-GR DPR protein probe with a concentration of 8.9 μ M necessary to double the rate

of degradation. This effective concentration correlated well with the 4.6 μM potency of acyl astemizole to enhance 20S proteolytic activity. While the compound was less effective toward the poly-GR DPR proteins than the positive control, TCH-165, this was anticipated due to TCH-165 being almost four times more potent for enhancement of 20S proteolytic activity. However, surprisingly, while acyl astemizole and astemizole have nearly identical potencies for enhancing 20S proteolytic activity, astemizole was only able to enhance degradation of the poly-GR DPR protein at very high concentrations. Although astemizole's potency for enhancing 20S proteolytic activity is 4.0 μM , a concentration of 29.8 μM was required to double the rate of the poly-GR DPR protein degradation.

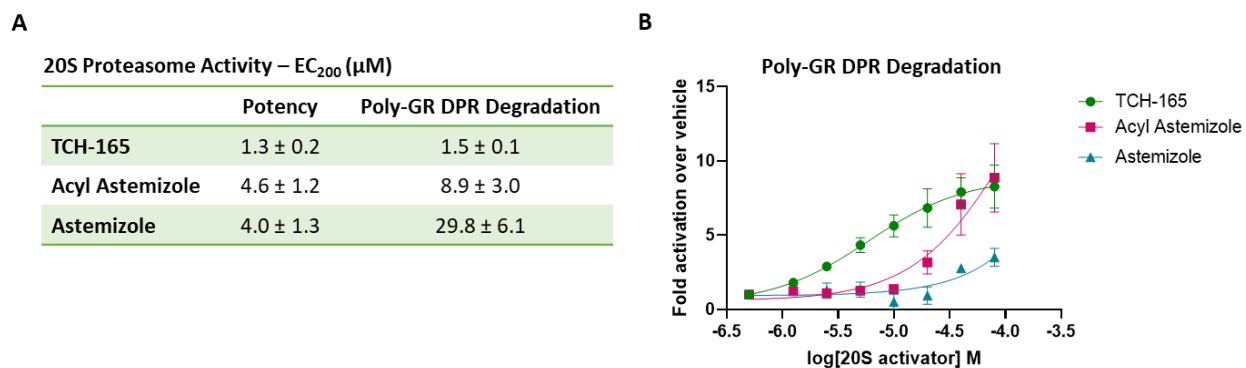


Figure 3.12 20S proteasome activators enhance degradation of poly-GR DPR proteins to a varying degree. (A) Effective concentration to obtain a two-fold rate enhancement, EC₂₀₀ value, for degradation of the poly-GR DPR probe was calculated and compared to the concentration of drug required for a two-fold rate enhancement of 20S proteasome activity (i.e. potency). (B) Dose-response curve of 20S proteasome activators for 20S-mediated proteolysis of fluorogenic poly-GR DPR probe (Suc-GR₃-AMC) with 20S proteasome pretreated with TCH-165, acyl astemizole, or astemizole. All data was collected in triplicate (n=3); error bars denote standard deviation.

All previous mechanistic evidence at the time had suggested that 20S proteasome activators enhance 20S proteasome activity through induction of an open gate conformation of the 20S proteasome.⁵⁵ Therefore, one would anticipate that if astemizole and acyl astemizole both induce an open gate conformation with similar potency, both compounds should be able to effectively and equally enhance the degradation of the poly-GR DPR proteins. However, this was not observed, suggesting that induction of an open gate conformation of the 20S proteasome is not the only requirement for enhancing 20S proteasome-mediated degradation. To begin to

explain these perplexing results, I set out to further explore the mechanism of small molecule activation of the 20S proteasome to elucidate any undiscovered mechanistic components.

3.2.8 Poly-GR DPR Proteins Offer Novel Route to Explore the Therapeutic Mechanism

As previously discussed, the proteasome degrades proteins through the use of three unique proteolytic sites ($\beta 5$, $\beta 2$, and $\beta 1$) responsible for chymotrypsin-like (CT-L), trypsin-like (T-L), and caspase-like (Casp-L) proteolytic activity, respectively²² (Figure 3.13). Each of these proteolytic sites is responsible for cleaving, or hydrolyzing, the peptide bond following a different class of amino acids, due to the shape and environment of the substrate binding pocket within the active site. The CT-L proteolytic site is known to cleave after large hydrophobic amino acid residues (i.e. tyrosine and phenylalanine), the Casp-L site cleaves after acidic amino acid residues (i.e. aspartic acid and glutamic acid), and the T-L site cleaves after basic amino acid residues (i.e. arginine and lysine).²² When all of these proteolytic activities are combined, the proteasome is capable of cleaving after all three classes of amino acids and is able to effectively degrade a wide range of proteins with varying amino acid composition. However, since the poly-arginine DPR proteins are composed of only arginine, a basic amino acid, and one other amino acid (i.e. glycine or proline), an interesting question is raised. Are all three of the proteolytic sites of the 20S proteasome necessary to effectively degrade the poly-arginine DPR proteins, or is proteolytic activity of only the T-L site sufficient to allow for their degradation? If T-L site proteolytic activity on its own is sufficient for the degradation of the poly-arginine DPR proteins, I hypothesized that this could explain the differences in the ability of astemizole and acyl astemizole to enhance degradation of the poly-arginine DPR proteins.

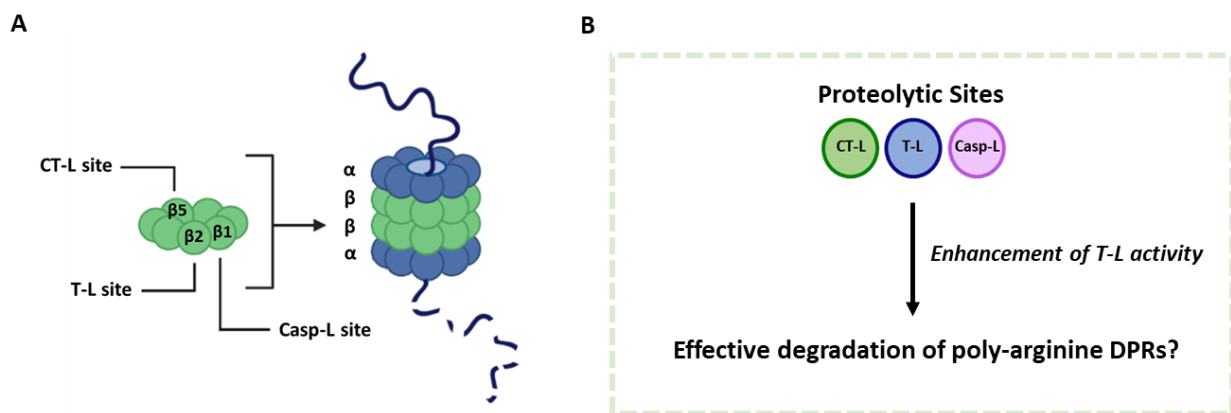


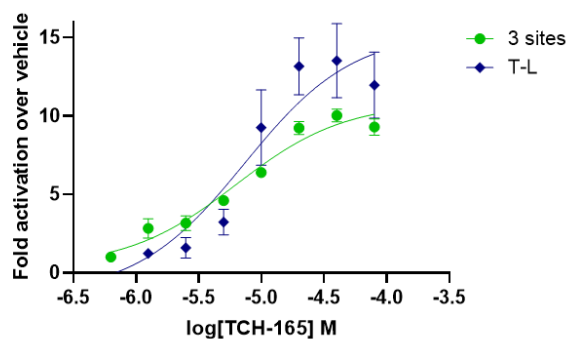
Figure 3.13 (A) The 20S proteasome degrades disordered proteins through use of three unique proteolytic sites ($\beta 5$, $\beta 2$, and $\beta 1$) responsible for chymotrypsin-like (CT-L), trypsin-like (T-L), and caspase-like (Casp-L) proteolytic activity, respectively. Both β -rings contain each of the three sites. (B) Schematic illustrating the hypothesis that poly-arginine DPRs can be effectively degraded by selective enhancement of T-L site proteolytic activity.

To investigate whether astemizole and acyl astemizole activate the T-L proteolytic site of the 20S proteasome differently, the compound's ability to enhance the degradation of a fluorogenic peptide substrate specific for the T-L site (Boc-LRR-AMC) was measured (note: the compound's ability to enhance the degradation of fluorogenic probes specific for the CT-L and Casp-L sites individually can be found in Figures 3.23, 3.24 and 3.25 of the Appendix). The results of the T-L site activity assay demonstrated that acyl astemizole enhanced the rate of T-L site proteolytic activity with a potency, or EC_{200} value, of 9.1 μM (Figure 3.14B). However, astemizole was less effective in enhancing the rate of T-L site proteolytic activity, with an EC_{200} value of 20.1 μM (Figure 3.14C). Since TCH-165 had shown to be the most effective toward the DPR proteins, it was also included in this experiment, resulting in an EC_{200} of 2.0 μM for enhancement of T-L site proteolytic activity (Figure 3.14A). Remarkably, the potencies of each compound for enhancement of T-L site activity correlated very well with each compound's ability to enhance degradation of the poly-GR DPR proteins. This data suggests that the compound's ability to enhance activity of the T-L site is what determines its ability to enhance degradation of the poly-arginine DPR proteins. Furthermore, it provides a possible explanation for astemizole's ineffectiveness toward the poly-GR DPR proteins.

A

20S Proteolytic Activity – TCH-165

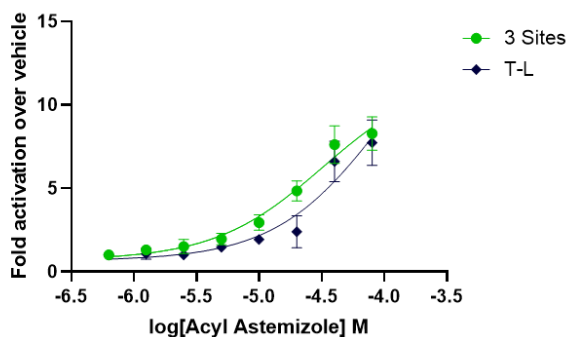
	EC ₂₀₀ (μM)
Potency for 3 sites	1.3 ± 0.2
Potency for T-L site	2.0 ± 0.4
Poly-GR DPR Degradation	1.5 ± 0.1



B

20S Proteolytic Activity – Acyl Astemizole

	EC ₂₀₀ (μM)
Potency for 3 sites	4.6 ± 1.2
Potency for T-L site	9.1 ± 2.0
Poly-GR DPR Degradation	8.9 ± 3.0



C

20S Proteolytic Activity – Astemizole

	EC ₂₀₀ (μM)
Potency for 3 sites	4.0 ± 1.3
Potency for T-L site	20.1 ± 6.8
Poly-GR DPR Degradation	29.8 ± 6.1

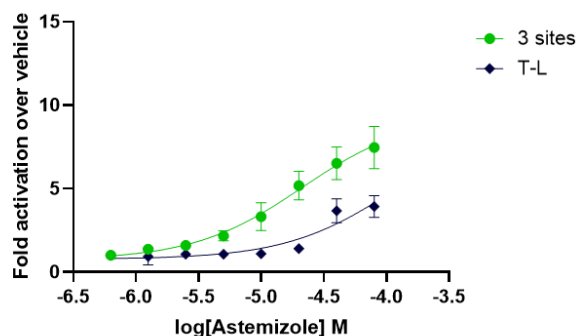


Figure 3.14 The ability of 20S proteasome activator to enhance activity of the T-L site determines its effectiveness toward enhancing DPR degradation. Dose-response curve of TCH-165 (A), acyl astemizole (B) and astemizole (C) for 20S-mediated proteolysis of fluorogenic substrate Boc-LRR-AMC (T-L site); Suc-LLVY-AMC, Boc-LRR-AMC and Z-LLE-AMC (3 sites); or Suc-GR₃-AMC (poly-GR DPR degradation). All data was collected in triplicate (n=3); error bars denote standard deviation.

3.2.9 Enhancing Activity of Select Proteolytic Sites of the 20S Proteasome

As the next step of the project, I aimed to explore whether activation of a 20S proteasome with only T-L site proteolytic activity would result in effective degradation of the poly-arginine DPR proteins. However, in order to accomplish this, several experimental design limitations had to be overcome. One limitation was that a 20S proteasome activator that enhances only the T-L site selectively is not known. Secondly, traditional methods to physically remove the T-L site from the proteasome using a knockout in a cellular system would surely prevent the proteasome from assembling into a fully functioning 20S proteasome. Therefore, I designed a novel method that allowed for selective enhancement of only T-L site activity upon treatment with a range of 20S proteasome activators. This was accomplished through the use of proteasome inhibitors selective for each of the three proteolytic sites. The inhibitors were used to mimic physical removal of the proteolytic site by fully inhibiting proteolytic activity of the site. To conduct these experiments, I proposed the workflow shown in Figure 3.15 could be used to enhance activity of select proteolytic sites, specifically the T-L site in this example. In step one, 20S proteasome would be treated with a covalent proteasome inhibitor selective for the CT-L and Casp-L sites to completely inhibit their activities. In step two, the proteasome with only the T-L site left functional would then be treated with a 20S proteasome activator, which theoretically should allow for activation of the T-L site selectively.

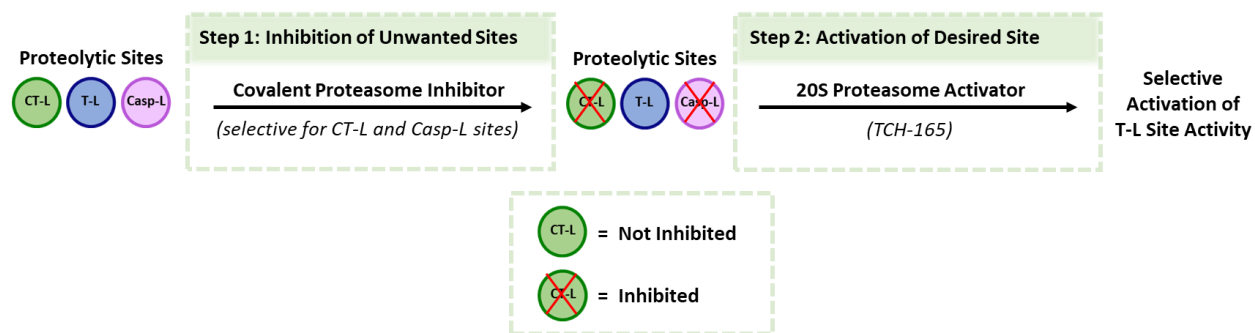


Figure 3.15 Proposed workflow for achieving selective activation of specific proteolytic sites.

To validate this proposed workflow, a number of proof-of-concept studies were conducted to experimentally support that the method would result in enhancement of select proteolytic activities. To test my hypothesis that poly-arginine DPR proteins can be effectively degraded by enhancing activity of only the T-L site of the 20S proteasome, the workflow above needed to be optimized to produce two different “modified” proteasomes. I hypothesized a 20S proteasome with only T-L site proteolytic activity would allow for the effective degradation of the poly-arginine DPR proteins (Figure 3.16A), while a 20S proteasome with only CT-L and Casp-L site activity would result in no degradation of the DPR proteins (Figure 3.16B).

To begin developing the method to produce a 20S proteasome with only T-L site proteolytic activity, an experiment to determine an inhibitor concentration to selectively inhibit the CT-L and Casp-L sites was conducted. The covalent proteasome inhibitor, bortezomib (BTZ), is known to be selective for inhibition of the CT-L and Casp-L sites at low concentrations, therefore a titration of the drug was performed to determine a proper dose. Using three fluorogenic peptide probes specific to each of the three proteolytic sites, the proteolytic activity was evaluated for each of the three sites following treatment with BTZ. The data was used to generate a dose-response curve and showed a decrease in 20S proteasome activity for each of the proteolytic sites with increasing dose of the inhibitor (Figure 3.16C). Gratifyingly, while lower concentrations of BTZ did inhibit the CT-L and Casp-L sites, the T-L site was not inhibited until higher concentrations of the inhibitor. Ultimately, a BTZ dose of 1.25 μM was chosen as the concentration of inhibitor to be used prior to treatment with a 20S proteasome activator. This was due to the fact that at this concentration selective inhibition of the CT-L and Casp-L sites was achieved, while the T-L site remained fully functional.

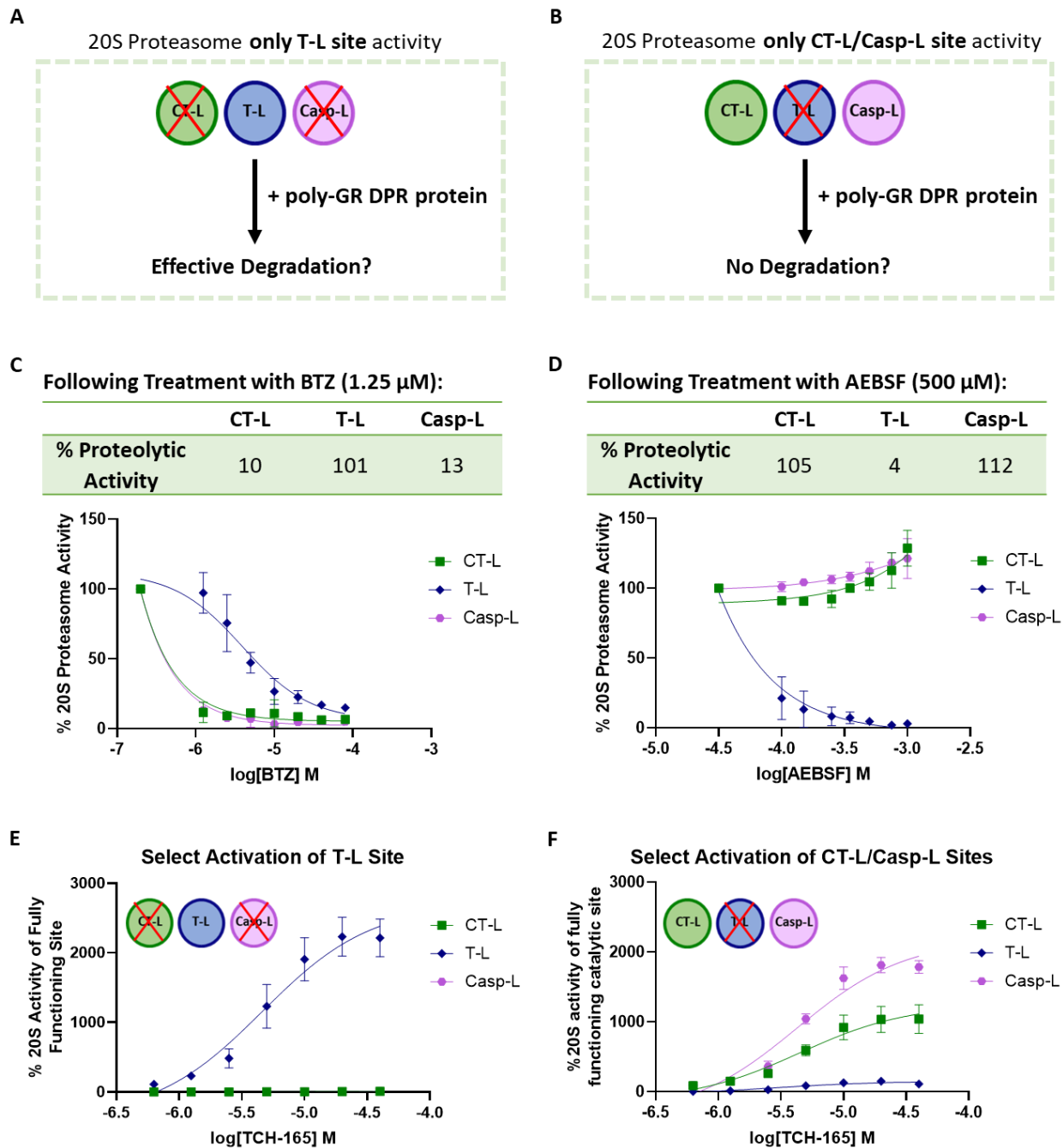


Figure 3.16 Proof-of-concept studies show selective activation of specific proteolytic sites is possible. (A) Depiction of a “modified” proteasome with only T-L site activity; red “X” over a proteolytic site denotes the site is inhibited. (B) Depiction of a “modified” proteasome with only CT-L/Casp-L site activities. (C) Dose-response curve of bortezomib (BTZ) for 20S-mediated proteolysis of fluorogenic substrates Suc-LLVY-AMC, Boc-LRR-AMC, and Z-LLE-AMC specific to the 3 proteolytic sites CT-L, T-L, and Casp-L, respectively. (D) Dose-response curve of 4-(2-aminoethyl) benzenesulfonyl fluoride hydrochloride (AEBSF) for 20S-mediated proteolysis of the three fluorogenic substrates above. (E) Dose-response curve of TCH-165 for the 20S-mediated proteolysis of the three unique fluorogenic substrates with the CT-L and Casp-L sites inhibited

Figure 3.16 (cont'd)

with BTZ prior to addition of 20S activator. (F) Dose-response curve of TCH-165 for the 20S-mediated proteolysis of the three unique fluorogenic substrates with the T-L site inhibited with AEBSF prior to addition of 20S activator. All data was collected in triplicate (n=3); error bars denote the standard deviation.

After determining a BTZ concentration that allowed for selective inhibition of the CT-L and Casp-L sites, the next step was to explore whether subsequential treatment with a 20S proteasome activator would result in selective activation of the uninhibited T-L site. To investigate this, purified 20S proteasome was pretreated with BTZ (1.25 μ M) for 15 minutes to inhibit the CT-L and Casp-L sites, followed by treatment with 20S proteasome activator, TCH-165. The proteolytic activity of each of the three proteolytic sites was then measured and resulted in selective activation of the T-L site with no effect on the inhibited CT-L and Casp-L sites (Figure 3.16E). Similar results were obtained when 20S proteasome was treated with BTZ, followed by treatment with astemizole or acyl astemizole (Figure 3.26 of the Appendix). These results demonstrated that it was possible to selectively inhibit the CT-L and Casp-L proteolytic sites to allow for the selective activation of only the T-L site and completed the method development for producing a “modified” proteasome with only T-L site proteolytic activity.

To develop a method to produce a 20S proteasome with only CT-L and Casp-L site proteolytic activities, an experiment to determine an inhibitor concentration to selectively inhibit the T-L site was conducted. The proteasome inhibitor, 4-(2-aminoethyl)benzenesulfonyl fluoride hydrochloride (AEBSF) is a selective inhibitor of the T-L site at certain concentrations, therefore a titration of the drug was conducted to determine a proper dose. Again, using three fluorogenic peptide probes specific to each of the three proteolytic sites, the proteolytic activity was evaluated for each of the three sites following treatment with AEBSF. The data was used to generate a dose-response curve and showed a dose-dependent decrease in T-L site activity upon increasing concentration of the drug, while the CT-L and Casp-L sites remained uninhibited and fully functional at these concentrations (Figure 3.16D). Ultimately, an AEBSF concentration of 500 μ M was chosen as the concentration of inhibitor to be used prior to treatment with a 20S proteasome activator. This was due to the fact that at this concentration selective inhibition of the T-L site was achieved, while the CT-L and Casp-L sites remained fully functional.

Following selection of an AEBSF concentration that allowed for selective inhibition of the T-L site, the next step was to explore whether subsequential treatment with a 20S proteasome activator would result in selective activation of the uninhibited CT-L and Casp-L sites. To investigate this, purified 20S proteasome was pretreated with AEBSF (500 μ M) for 30 minutes to inhibit the T-L site, followed by treatment with 20S proteasome activator, TCH-165. The proteolytic activity of each of the three proteolytic sites was then measured and resulted in selective activation of the CT-L and Casp-L sites with a negligible effect on the inhibited T-L site (Figure 3.16F). Similar results were obtained when 20S proteasome was treated with AEBSF, followed by treatment with astemizole or acyl astemizole (Figure 3.27 of the Appendix). These results demonstrated that it was possible to selectively inhibit the T-L proteolytic site to allow for the selective activation of only the CT-L and Casp-L sites and completed the method development for producing a “modified” proteasome with only CT-L and Casp-L site proteolytic activities.

3.2.10 Poly-Arginine DPR Proteins are Effectively Degraded by only T-L Site Proteolytic Activity

Following the development of a method to produce the two “modified” proteasomes, they were then used to test the original hypothesis that poly-arginine DPR proteins can be effectively degraded by enhancing activity of only the T-L site of the 20S proteasome. To conduct these experiments, the ability of the compounds to enhance 20S-mediated degradation of the fluorogenic poly-GR DPR protein was evaluated for proteasomes with the following proteolytic activities: (1) all 3 proteolytic sites are functional, (2) only the T-L site is functional, and (3) only the CT-L and Casp-L sites are functional. As shown in Figure 3.17, when only the T-L site is functional, TCH-165, acyl astemizole and astemizole are able to effectively enhance the degradation of the DPR protein to nearly the same extent as when all three proteolytic sites are functional. As observed previously, astemizole had a lesser efficacy toward the degradation of the DPR proteins when compared with TCH-165 and acyl astemizole, which is likely explained by astemizole’s decreased ability to enhance activity of the T-L site. However, when T-L proteolytic activity is inhibited, and only the CT-L and Casp-L sites are functional, no degradation of the poly-arginine DPR protein was observed with any of the three 20S proteasome activators. In all, the data supports the hypothesis that poly-arginine DPR proteins can be effectively degraded by enhancement of only T-L site proteolytic activity of the 20S proteasome.

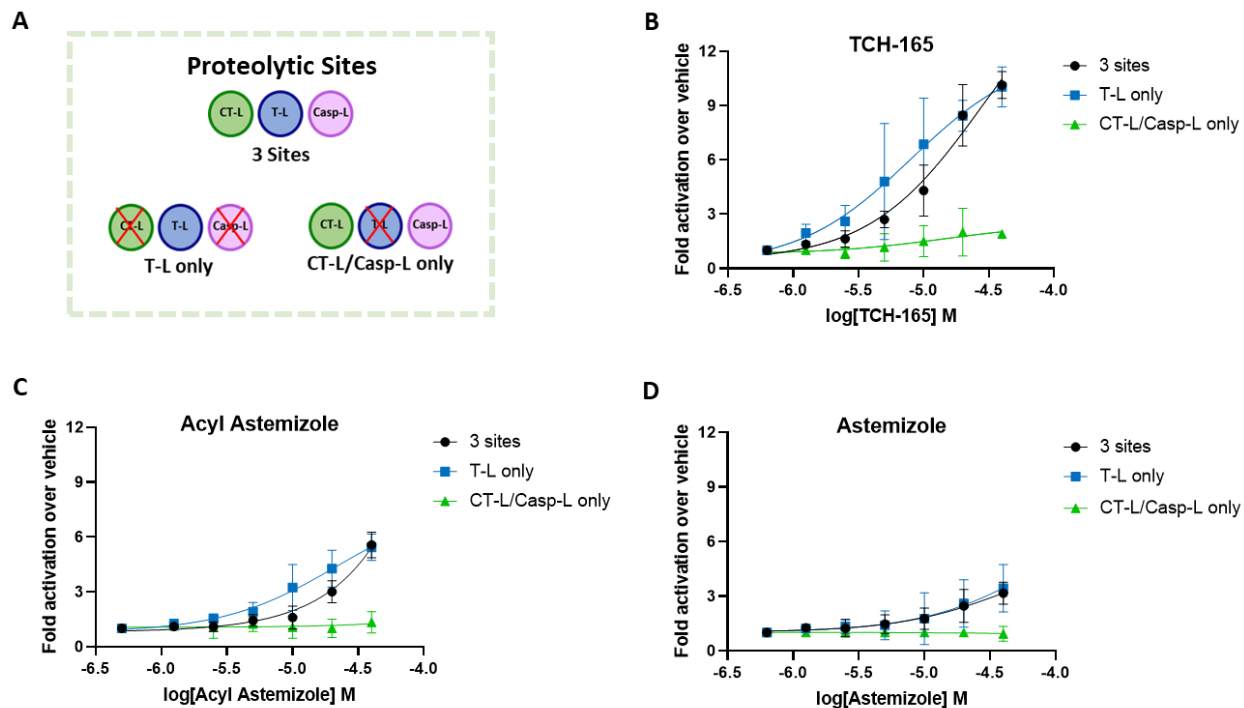


Figure 3.17 Degradation of poly-GR DPR probe (Suc-GR₃-AMC) with all three proteolytic site activities, with only T-L site activity, or with only CT-L and Casp-L site activities. (A) Schematic designating the proteolytic sites involved in each experiment. Red “X” over a proteolytic site denotes the site is inhibited. Dose-response curve of TCH-165 (B), acyl astemizole (C), or astemizole (D) for 20S-mediated proteolysis of fluorogenic substrate Suc-GR₃-AMC. All data was collected in triplicate (n=3); error bars denote standard deviation.

3.2.11 Future Work

The studies described above provided valuable new insight into the mechanism of small molecule activation of the 20S proteasome. The results suggest that in addition to inducing an open gate conformation of the 20S proteasome, small molecule 20S activators induce additional conformational changes that differentially enhance activities of the three unique proteolytic sites. The above data supports the hypothesis that the degradation of IDPs with limited amino acid diversity, such as the poly-arginine DPR proteins, can be enhanced through selective enhancement of T-L site proteolytic activity. This suggests the exciting possibility that a small molecule 20S proteasome activator could be designed to selectively enhance T-L site activity, providing the means to selectively degrade poly-arginine DPR proteins for a more targeted treatment of ALS. However, a second hypothesis can be made for targeting IDPs with a more diverse amino acid composition.

As discussed previously, the three proteolytic sites of the proteasome, the CT-L, T-L and Casp-L sites preferentially cleave after large hydrophobic, basic, and acidic amino acid residues, respectively.²² Therefore, to effectively degrade IDPs that contain a wide variety of amino acids from all three of the main amino acid classes, I hypothesize that each of the three proteolytic site activities of the proteasome are necessary for their effective degradation. To test this hypothesis, I have designed the following assay which is currently in preliminary stages. In part one of the experiment, the selectivity of the proteasome's three proteolytic sites will be investigated. Secondly, the effect on proteolytic cleavage selectivity by 20S proteasome activators which differentially enhance activities of the three proteolytic sites will be evaluated.

In this experiment, the degradation fragment pattern and cleavage sites of a disordered protein substrate will be analyzed using mass spectrometry following digestion with the 20S proteasome. For this assay, a probe (referred to as the RYE probe in this chapter) with one cleavage site for each of the three proteolytic sites was synthesized (GenScript). The remainder of the probe consists of glycine and alanine residues, as none of the three proteolytic sites have selectivity for cleavage after these small aliphatic amino acids. The predicted likelihood of cleavage at the three proposed cleavage sites and all other amino acids of the probe was predicted using NetChop 3.0 software,^{56,57} an algorithm used to predict proteasomal cleavage sites. A representation of the probe is shown in Figure 3.18A; the full probe sequence and cleavage site predictions are shown in Figure 3.28 of the Appendix. With these predicted cleavage sites and the known preference of the proteolytic sites for cleaving after certain amino acids, it is hypothesized that the T-L site will selectively cleave after the arginine (R) residue of the probe, the CT-L site will cleave after the tyrosine (Y), and the Casp-L site will cleave after the glutamic acid (E) residue of the probe.

In part one of the experiment, the selectivity of the proteolytic sites will be evaluated. To do this, select proteolytic sites will be inhibited through use of selective proteasome inhibitors as shown above, followed by the evaluation of the degradation fragments produced. For example, if the Casp-L site is inhibited, cleavage after the acidic amino acid in the probe (i.e. glutamic acid, E) should not occur, thereby altering the degradation fragmentation pattern of the probe produced. To directly mirror the degradation experiments with the poly-arginine DPR proteins,

degradation of the RYE probe will be evaluated by 20S proteasomes with the following proteolytic activities: (1) all 3 proteolytic sites are functional, (2) only the T-L site is functional, and (3) only the CT-L and Casp-L sites are functional. As shown in Figure 3.18A, it is anticipated that if all three proteolytic sites are functional, the probe will be cleaved into four fragments of 10 amino acids (10 aa). However, if the CT-L and Casp-L sites were to be inhibited, with only the T-L site functional, it is predicted that cleavage at the tyrosine (Y) and glutamic acid (E) residues would be prevented, resulting in cleavage at only the T-L cleavage site (arginine, R) which would produce one 10 amino acid fragment and one 30 amino acid fragment (Figure 3.18B). Lastly, if the T-L site is inhibited, and only the CT-L and Casp-L sites are functional, it is predicted that only cleavage at the tyrosine (Y) and glutamic acid (E) residues would occur, producing one 20 amino acid fragment and two 10 amino acid fragments (Figure 3.18C). Completion of this experiment may provide valuable insight into the selectivity of the proteasome's proteolytic sites. Furthermore, it is essential for testing the hypothesis that IDPs with a high amino acid diversity require each of the three proteolytic site activities of the proteasome to be effectively degraded.

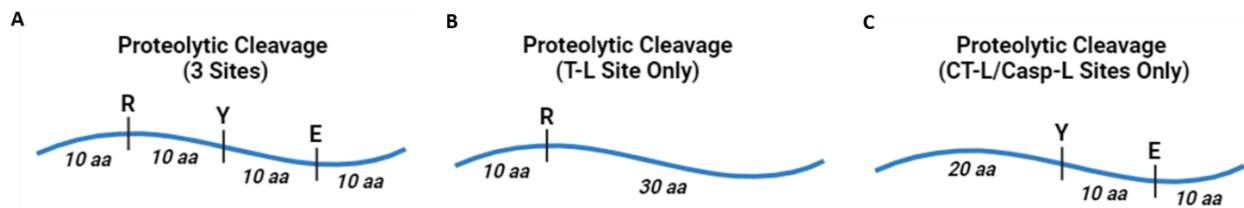


Figure 3.18 The RYE probe may allow the selectivity of the 20S proteasome's three unique proteolytic sites to be investigated. (A) It is hypothesized that if all 3 sites are functional, the probe will be cleaved at the R, Y, and E cleavage sites producing four 10 amino acid (aa) fragments. (B) If only the T-L site is functional, it is predicted the probe will only be cleaved at the R cleavage site producing one 10 aa fragment and one 30 aa fragment. (C) If only the CT-L and Casp-L sites are functional, it is predicted the probe will be cleaved at the Y and E cleavage sites producing one 20 aa fragment and two 10 aa fragments.

In part two of the experiment, the effect different 20S proteasome activators have on proteolytic cleavage selectivity will be evaluated. As discussed previously, 20S proteasome activators differentially activate the three unique proteolytic activities of the 20S proteasome. While TCH-165 activates all 3 sites relatively equal, acyl astemizole favorably activates the CT-L and T-L sites, while astemizole favorably activates only the CT-L site (data shown in Figures 3.23, 3.24 and 3.25 of the Appendix). Therefore, if the proteolytic sites demonstrate strict selectivity in the above assay, it could be hypothesized that these three different 20S proteasome activators could result in different fragmentation patterns due to favored activation of select proteolytic sites. To determine this, 20S proteasome with all three proteolytic sites functional will be treated with the three different small molecule 20S proteasome activators. Following incubation with the RYE probe, the degradation fragments and cleavage sites produced will be analyzed to determine whether the three 20S activators preferentially induce cleavage by the proteolytic sites they favorably activate. The completion of this experiment could provide novel insight into why 20S proteasome activators have shown varying effectiveness toward certain IDPs. Additionally, this information could be useful when choosing a 20S proteasome activator for use against an IDP target. For example, if targeting an IDP composed of a large number of acidic amino acids, a 20S proteasome activator which favorably activates the Casp-L site may be sufficient. However, if the IDP target has a high amino acid diversity, a 20S proteasome activator which activates all three proteolytic sites may be most effective.

3.3 Conclusion

In this chapter, astemizole was identified and validated as a new 20S proteasome activator scaffold. A series of analogues were then designed and synthesized, resulting in the discovery of three small molecules which satisfied the goals of analogue design outlined at the start of the SAR study. Astemizole and acyl astemizole were then used to further study the biological activities of this newly identified 20S proteasome activator scaffold. Both compounds demonstrated effectiveness toward enhancing the 20S proteasome-mediated degradation of α -synuclein and tau *in vitro*. While astemizole showed significant toxicity and was unable to reduce tau protein levels in cell culture, acyl astemizole effectively reduced cellular tau protein levels with minimal cytotoxic effects. Lastly, exploration of the efficacy of astemizole and acyl

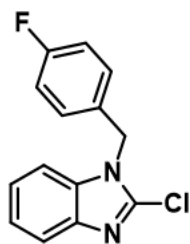
astemizole toward the poly-arginine DPR proteins led to the development of insightful mechanistic studies. The studies suggest that in addition to inducing an open gate conformation of the 20S proteasome, small molecule 20S activators induce additional conformational changes that differentially enhance activities of the three unique proteolytic sites. In the case of the poly-arginine DPR proteins, select enhancement of T-L site proteolytic activity resulted in their effective degradation. This suggests the exciting possibility that a small molecule 20S proteasome activator could be designed to selectively enhance T-L site proteolytic activity, providing the means to selectively degrade poly-arginine DPR proteins for a more targeted treatment of ALS.

3.4 Experimental

3.4.1 Synthetic Methods

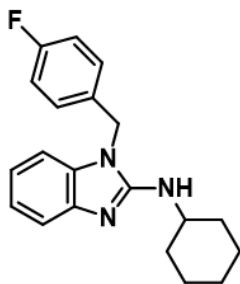
General Information. Reactions were carried out under a nitrogen atmosphere in flame-dried glassware. Magnetic stirring was used for all reactions. Solvents and reagents were purchased from commercial suppliers and used without further purification. Reported yields refer to chromatographically and spectroscopically pure compounds. ^1H and ^{13}C NMR spectra were recorded on a Varian Unity Plus-500 spectrometer. Chemical shifts are reported relative to the residue peaks of the solvent (Acetone- d_6 : 2.09 ppm for ^1H and 205.9 ppm for ^{13}C), (Methanol- d_4 : 3.34 ppm for ^1H and 49.9 ppm for ^{13}C), (CDCl_3 : 7.26 ppm for ^1H and 77.4 ppm for ^{13}C) and (DMSO- d_6 : 2.54 ppm for ^1H and 39.5 ppm for ^{13}C). The following abbreviations are used to denote the multiplicities: s = singlet, d = doublet, dd = doublet of doublets, t = triplet, and m = multiplet. Infrared spectra were recorded on a Jasco Series 6600 FTIR spectrometer. HRMS were obtained at the Mass Spectrometry Facility of Michigan State University with a Micromass Q-ToF Ultima API LC-MS/MS mass spectrometer.

Synthesis and Characterization of Compounds 3-1i through 3-7



2-Chloro-1-(4-fluorobenzyl)-1H-benzimidazole (3-1i) 2-chloro-1H-benzimidazole (13.12 mmol, 2 g), KOH (18.37 mmol, 1.03 g) and dry acetonitrile (80 mL) was heated to reflux and stirred for 1 hour. 4-fluorobenzyl bromide (19.68 mmol, 2.45 mL) was added. The reaction mixture was refluxed with stirring for 6 hours. The reaction mixture was cooled to room temperature, washed with water, and extracted with dichloromethane. The organic layer was evaporated and recrystallized with dichloromethane and hexane to afford **3-1i** (2.6 g, 77%) as a white solid.

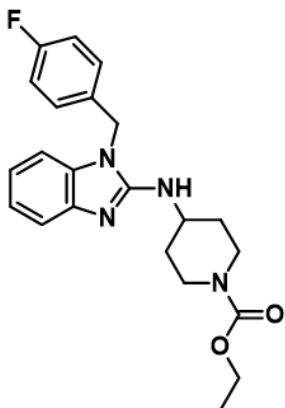
^1H NMR (500 MHz, Acetone- d_6) δ 7.68 –7.59 (m, 1H), 7.58 –7.50 (m, 1H), 7.39 –7.30 (m, 2H), 7.31–7.23 (m, 2H), 7.19 – 7.07 (m, 2H), 5.55 (d, J = 1.1 Hz, 2H). ^{13}C NMR (126 MHz, Methanol- d_4) δ 163.87 (d, J = 245.6 Hz), 142.30, 141.86, 136.22, 132.89 (d, J = 3.1 Hz), 130.14 (d, J = 8.1 Hz), 124.93, 124.39, 119.58, 116.76 (d, J = 22.0 Hz), 111.66, 48.04. IR (neat): 1602, 1506, 1233 cm^{-1} . m/z : [(M+H) $^+$] calcd for ($\text{C}_{14}\text{H}_{11}\text{ClFN}_2^+$) 261.0595; Found 261.0599. mp 70-74 $^\circ\text{C}$.



2-cyclohexylamine-1-(4-fluorobenzyl)-1H-benzimidazole (3-1) 2-chloro-1-(4-fluorobenzyl)-1H-benzimidazole (Compound **3-1i**) (0.38 mmol, 100 mg) was dissolved in cyclohexylamine (26.17 mmol, 3 mL). The reaction mixture was stirred at 110 $^\circ\text{C}$ for 2 days and then washed with a saturated solution of ammonium chloride and extracted with dichloromethane. Crude product

was purified by column chromatography on silica gel (ethyl acetate/hexane; 40:60) to afford compound **3-1** (51.5 mg, 42%) as a yellow solid.

^1H NMR (500 MHz, Methanol- d_4) δ 7.29 (d, J = 7.8 Hz, 1H), 7.10 (dd, J = 8.4, 5.3 Hz, 2H), 7.04 – 6.92 (m, 4H), 6.92 – 6.86 (m, 1H), 5.17 (s, 2H), 3.76 (m, 1H), 2.10 – 2.01 (m, 2H), 1.75 (m, 2H), 1.69 – 1.61 (m, 1H), 1.43 (m, 2H), 1.28 (m, 2H), 1.18 (m, 1H). ^{13}C NMR (126 MHz, Methanol- d_4) δ 162.13 (d, J = 244.4 Hz), 154.07, 141.71, 133.91, 132.43 (d, J = 3.2 Hz), 128.20 (d, J = 8.2 Hz), 120.95, 119.19, 114.99 (d, J = 21.9 Hz), 114.50, 107.50, 51.85, 43.75, 33.02, 25.38, 24.99. IR (neat): 3230, 3036, 2851 cm^{-1} . m/z : $[(\text{M}+\text{H})^+]$ calcd for $(\text{C}_{20}\text{H}_{22}\text{FN}_3)^+$ 324.1876; Found 324.1878. mp 165-168 $^\circ\text{C}$.

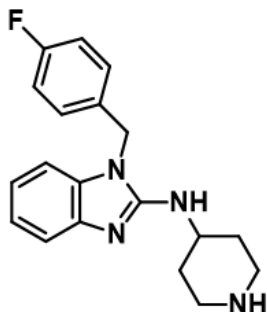


Ethyl 4-((1-(4-fluorobenzyl)-1H-benzimidazole-2-yl) amino) piperidine-1-carboxylate (3-2i)

Compound **3-1i** (0.38 mmol, 100 mg) was dissolved in dimethylacetamide (3 mL), followed by addition of ethyl 4-aminopiperidinecarboxylate (3.8 mmol, 0.65 mL). The reaction mixture was stirred at 155 $^\circ\text{C}$ in a silicone oil bath for 68 hours and then cooled to room temperature. The reaction mixture was then diluted with ethyl acetate and poured into a 50% saturated brine solution and then extracted with dichloromethane. The crude product was purified by column chromatography on silica gel (hexane/ethyl acetate; 10:90) to afford compound **3-2i** (69.5 mg, 45%) as a yellow solid.

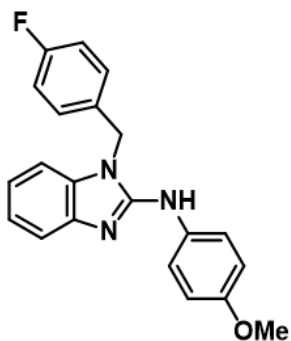
^1H NMR (500 MHz, Methanol- d_4) δ 7.35 – 7.26 (m, 1H), 7.15 – 7.09 (m, 2H), 7.06 – 6.98 (m, 4H), 6.93 (m, 1H), 5.22 (s, 2H), 4.10 (m, 4H), 3.95 (m, 2H), 2.98 (s, 1H), 2.10 – 1.98 (m, 2H), 1.45 (dd, J = 11.9, 4.2 Hz, 2H), 1.24 (m, 3H). ^{13}C NMR (126 MHz, Methanol- d_4) δ 163.56 (d, J = 244.6 Hz),

157.19, 155.18, 142.92, 135.30, 133.76 (d, $J = 2.9$ Hz), 129.59 (d, $J = 8.4$ Hz), 122.50, 120.86, 116.44 (d, $J = 21.7$ Hz), 116.08, 109.13, 62.70, 51.43, 45.24, 44.10, 33.11, 14.96. IR (neat): 3275, 1694, 1220 cm^{-1} . m/z : $[(M+H)^+]$ calcd for $(\text{C}_{22}\text{H}_{26}\text{FNO}_2^+)$ 397.2040; Found 397.2070. mp 120-123 $^{\circ}\text{C}$.



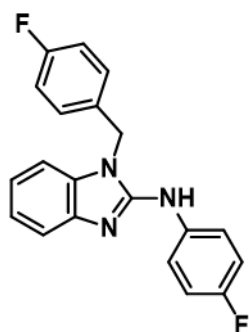
1-(4-fluorobenzyl)-N-(piperidin-4-yl)-1H-benzo[d]imidazol-2-amine (3-2) Compound **3-2i** (0.76 mmol, 300 mg) was dissolved in 48% HBr (10 mL) and heated to reflux and stirred for 3 hours. The reaction mixture was cooled to room temperature and neutralized with solid sodium bicarbonate, washed with water, and then extracted with dichloromethane. The organic layer was evaporated to afford compound **3-2** (204 mg, 83%) as a yellow solid.

^1H NMR (500 MHz, Chloroform- d) δ 7.46 (d, $J = 7.9$ Hz, 1H), 7.12 – 7.04 (m, 3H), 7.02 – 6.93 (m, 4H), 5.03 (s, 2H), 4.23 (s, 1H), 3.98 (s, 1H), 2.98 (m, 2H), 2.68 (m, 3H), 2.09 – 2.02 (m, 2H), 1.33 – 1.25 (m, 2H). ^{13}C NMR (126 MHz, Chloroform- d) δ 162.36 (d, $J = 247.0$ Hz), 153.31, 142.32, 134.47, 131.22 (d, $J = 3.3$ Hz), 128.21 (d, $J = 8.1$ Hz), 121.51, 119.73, 116.39, 116.06 (d, $J = 21.8$ Hz), 107.25, 50.11, 45.14, 44.93, 33.60. IR (neat): 3290, 3245, 1218 cm^{-1} . m/z : $[(M+H)^+]$ calcd for $(\text{C}_{19}\text{H}_{22}\text{FN}_4^+)$ 325.1828; Found 325.1826. mp 120-126 $^{\circ}\text{C}$.



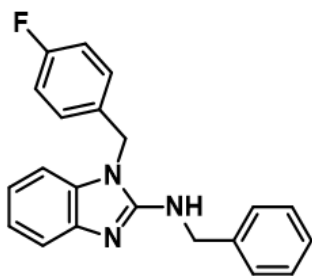
1-(4-fluorobenzyl)-N-(4-methoxyphenyl)-1H-benzo[d]imidazol-2-amine (3-3) Compound **3-1i** (0.38 mmol, 100 mg) and p-anisidine (1.14 mmol, 140 mg) were refluxed in ethanol (9 mL) for 24 hours. The reaction mixture was cooled to room temperature, evaporated, and recrystallized from diethyl ether to afford compound **3-3** (94.4 mg, 71%) as a light purple solid.

^1H NMR (500 MHz, Methanol- d_4) δ 7.44 – 7.41 (m, 3H), 7.41 – 7.39 (m, 2H), 7.34 – 7.31 (m, 2H), 7.20 – 7.08 (m, 5H), 5.57 (s, 2H), 3.87 (s, 3H). ^{13}C NMR (126 MHz, Methanol- d_4) δ 164.04 (d, J = 245.9 Hz), 161.13, 150.82, 132.11, 131.39 (d, J = 3.3 Hz), 130.39, 130.08 (d, J = 8.6 Hz), 128.91, 128.33, 125.68, 125.24, 125.06, 117.00 (d, J = 22.0 Hz), 116.60, 116.28, 113.12, 111.80, 56.14, 46.75. IR (neat): 3176, 1634 cm^{-1} . m/z : $[(\text{M}+\text{H})^+]$ calcd for $(\text{C}_{21}\text{H}_{18}\text{FN}_3\text{O}^+)$ 348.1512; Found 348.1545. mp 231-234 $^\circ\text{C}$.



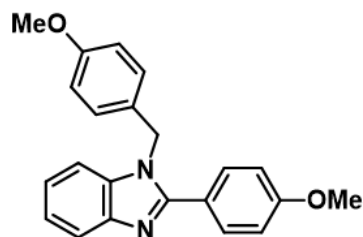
1-(4-fluorobenzyl)-N-(4-fluorophenyl)-1H-benzo[d]imidazol-2-amine (3-4) Compound **3-1i** (0.38 mmol, 100 mg) was dissolved in 4-fluoroaniline (2 mL) and stirred at 140 $^\circ\text{C}$ for 2 days. The reaction mixture was cooled to room temperature and recrystallized from ethyl acetate to afford compound **3-4** (65.9 mg, 51%) as a blue solid.

^1H NMR (500 MHz, Methanol- d_4) δ 7.59 – 7.52 (m, 2H), 7.46 – 7.39 (m, 4H), 7.38 – 7.29 (m, 4H), 7.20 – 7.12 (m, 2H), 5.59 (s, 2H). ^{13}C NMR (126 MHz, Methanol- d_4) δ 164.91 (d, J = 77.7 Hz), 162.95 (d, J = 78.3 Hz), 150.66, 133.02 (d, J = 3.2 Hz), 132.26, 131.48 (d, J = 3.3 Hz), 130.63, 130.26 (d, J = 8.1 Hz), 128.93 (d, J = 9.0 Hz), 126.01, 125.57, 118.39 (d, J = 23.4 Hz), 117.19 (d, J = 22.1 Hz), 113.44, 112.12, 47.06. IR (neat): 3182, 1634 cm^{-1} . m/z : [(M+H) $^+$] calcd for (C₂₀H₁₅F₂N₃ $^+$) 336.1312; Found 336.1320. mp 230-233 $^{\circ}\text{C}$.



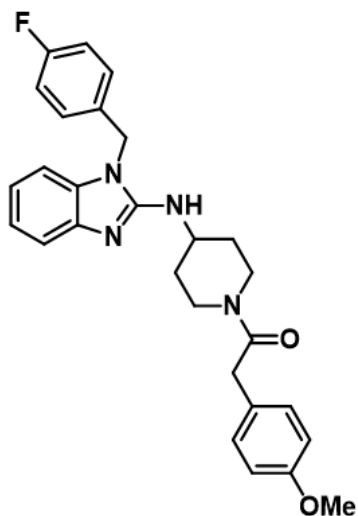
N-benzyl-1-(4-fluorobenzyl)-1H-benzo[d]imidazol-2-amine (3-5) Compound **3-1i** (0.38 mmol, 100 mg) was added to flask, followed by benzylamine (2 mL). The neat reaction mixture was stirred at 125 $^{\circ}\text{C}$ for 2 days. The reaction mixture was cooled to room temperature, and crude product was purified by column chromatography on silica gel (ethyl acetate/hexane) to afford compound **3-5** (38.1 mg, 30%) as a white solid.

^1H NMR (500 MHz, Methanol- d_4) δ 7.32 – 7.24 (m, 5H), 7.22 – 7.18 (m, 1H), 7.15 – 7.11 (m, 2H), 7.07 – 6.94 (m, 5H), 5.24 (s, 2H), 4.65 (s, 2H). ^{13}C NMR (126 MHz, Methanol- d_4) δ 163.60 (d, J = 244.6 Hz), 156.07, 142.90, 140.70, 135.57, 133.73 (d, J = 2.9 Hz), 129.67 (d, J = 8.2 Hz), 129.39, 128.28, 128.07, 122.47, 120.87, 116.43 (d, J = 21.8 Hz), 116.17, 108.98, 47.39, 45.32. IR (neat): 3210, 1620 cm^{-1} . m/z : [(M+H) $^+$] calcd for (C₂₁H₁₈FN₃ $^+$) 332.1563; Found 332.1593. mp 201-206 $^{\circ}\text{C}$.



1-(4-methoxybenzyl)-2-(4-methoxyphenyl)-1H-benzo[d]imidazole (3-6) Methanol (8 mL) was added to 3Å MS (1.4 g), followed by *o*-phenylenediamine (1.85 mmol, 200 mg) and 4-methoxybenzaldehyde (1.85 mmol, 0.22 mL). The reaction mixture was heated to reflux and stirred for 5 hours, and then cooled to room temperature and filtered, followed by evaporation of the organic phase. Crude product was purified by column chromatography on silica gel (ethyl acetate/methanol; 95:5) to give compound **3-6** (229 mg, 55%) as a white solid.

^1H NMR (500 MHz, Chloroform-*d*) δ 8.23 – 7.99 (m, 1H), 7.92 (d, J = 8.0 Hz, 1H), 7.72 – 7.67 (m, 2H), 7.38 – 7.27 (m, 2H), 7.07 (d, J = 8.6 Hz, 2H), 7.04 – 6.99 (m, 2H), 6.93 – 6.88 (m, 2H), 5.42 (s, 2H), 3.87 (s, 3H), 3.81 (s, 3H). ^{13}C NMR (126 MHz, Chloroform-*d*) δ 160.90, 159.10, 154.12, 143.13, 136.09, 130.69, 128.45, 127.21, 122.77, 122.55, 122.37, 119.64, 114.41, 114.20, 110.49, 55.35, 55.27, 47.84. IR (neat): 1602, 1236 cm^{-1} . m/z : [(M+H) $^+$] calcd for (C₂₂H₂₀N₂O₂ $^+$) 345.1603; Found 345.1665. mp 106-110 °C.



1-(4-((1-(4-fluorobenzyl)-1H-benzo[d]imidazol-2-yl)amino)piperidin-1-yl)-2-(4-

methoxyphenyl)ethan-1-one (3-7) Compound **3-2** (0.15 mmol, 50 mg) and triethylamine (0.2 mmol, 0.03 mL) were dissolved in dichloromethane (2 mL), followed by dropwise addition of 4-methoxyphenylacetyl chloride (0.15 mmol, 0.023 mL). The reaction mixture was stirred at room temperature for 4 hours. The crude product was purified by column chromatography (methanol/ethyl acetate 5:95) to afford Compound **3-7** (31.5 mg, 53%) as colorless oil.

^1H NMR (500 MHz, Methanol- d_4) δ 7.32 (d, J = 7.8 Hz, 1H), 7.20 – 7.16 (d, 2H), 7.13 – 7.08 (m, 2H), 7.07 – 6.99 (m, 4H), 6.95 (t, J = 7.6 Hz, 1H), 6.91 – 6.84 (d, 2H), 5.49 (s, 1H), 5.22 (s, 2H), 4.52 (m, 1H), 4.06 – 3.94 (m, 2H), 3.76 (s, 3H), 3.74 (d, J = 4.5 Hz, 1H), 3.68 (d, J = 14.9 Hz, 1H), 3.20 (m, 1H), 2.85 (m, 1H), 2.08 – 2.02 (d, 1H), 1.99 (d, J = 12.9 Hz, 1H), 1.45 – 1.37 (m, 1H), 1.19 (m, 1H). ^{13}C NMR (126 MHz, Methanol- d_4) δ 172.32, 163.57 (d, J = 244.4 Hz), 160.06, 142.58, 142.46, 135.17, 133.67 (d, J = 3.2 Hz), 130.67, 129.58 (d, J = 8.2 Hz), 128.29, 122.60, 121.03, 116.44 (d, J = 21.9 Hz), 115.98, 115.18, 109.25, 55.64, 51.37, 46.46, 45.27, 42.26, 40.64, 33.52, 32.81. IR (neat): 3289, 1682, 1260 cm^{-1} . m/z : $[(\text{M}+\text{H})^+]$ calcd for $(\text{C}_{28}\text{H}_{30}\text{FN}_4\text{O}_2^+)$ 473.2353; Found 473.2353.

3.4.2 Biological Methods

20S proteasome activation activity assay. The activity assay was conducted in 100 μL reaction volume in a black, clear-bottom 96-well plate. Purified human 20S proteasome (1 nM) and stock solutions of the test compound were added to final concentrations ranging from 1.25-80 μM in assay buffer (38 mM Tris-HCl, 100 mM NaCl, pH 7.8) and the plate was incubated at 37 $^\circ\text{C}$ for 15

min. The fluorogenic substrates (Suc-LLVY-AMC, Boc-LRR-AMC, Z-LLE-AMC) were added to a final concentration of 20 μM total. The fluorescence was measured at 37 °C on a SpectraMax M5e spectrometer taking kinetic readings every 5 mins for 1 hour (380/460 nm).

Molecular docking studies. Docking studies were performed using Autodock Vina, supported through computational resources and services provided by the Institute for Cyber-Enabled Research at Michigan State University. The macromolecule for the docking studies was defined using a crystal structure of the human 20S proteasome obtained from the PDB database (PDB ID: 4R3O). Small molecule ligands were generated using Perkin Elmer's Chem3D, minimized using the MM2 force field, and converted to PDB files. These files were then uploaded to PyRx and converted to ligand pdbqt files. Unbiased docking studies were performed by docking against the entire human 20S proteasome (grid box 153.2 Å × 138.0 Å × 189.4 Å) three times with exhaustiveness set to 1000. The top nine docking modes were analyzed using PyMOL. To further analyze each docking mode, BIOVIA Discovery Studio 2020 was used to obtain the 2D predictive ligand-receptor interaction diagrams.

***In vitro* 20S proteasome-mediated degradation of α -synuclein.** Purified 20S proteasome (final concentration of 15 nM) in assay buffer (38 mM Tris-HCl, 100 mM NaCl, pH 7.8) was incubated with varying concentrations of drug (final concentrations ranging from 1 to 10 μM ; 2% DMSO) and incubated at 37°C for 15 min. Purified α -synuclein was added to a final concentration of 0.5 μM , and the samples were incubated at 37 °C for 2 hours. Following incubation, the samples were boiled at 95°C with 5X SDS loading buffer. The samples were resolved on a 4-20% Tris/glycine gel and visualized by silver stain (Thermo Scientific).

***In vitro* 20S proteasome-mediated degradation of Tau441.** Purified 20S proteasome (final concentration of 2 nM) in assay buffer (50 mM Tris-HCl, 0.1% Tween 20, pH 7.5) was incubated with varying concentrations of drug (final concentrations ranging from 1 to 10 μM ; 2% DMSO) and incubated at 37°C for 15 min. Purified Tau441 (rPeptide; cat#T-1001-1) was added to a final concentration of 0.5 μM , and the samples were incubated at 37 °C for 1 hour. Following incubation, the samples were boiled at 95°C with 5X SDS loading buffer, resolved on a 4–20% Tris/glycine gel and transferred to a PVDF membrane that was probed with anti-tau (Cell Signaling; cat#46687) or anti-GAPDH-HRP (Novus; cat#NBP2-27103H) antibodies. After washing

and application of appropriate secondary antibodies, the blots were developed with ECL Western reagent (Radiance Plus, Azure Biosystems; cat#AC2103) and imaged with a chemiluminescent Western blot imager (Azure Biosystems 300Q). Band intensities were acquired using Biorad Image Lab analysis software.

Transfection using X-tremeGENE™ HP DNA Transfection Reagent. Cells were grown to 70-80% confluency in a 37 °C incubator (5% CO₂) in 60 x 15 mm culture dishes in Opti-MEM Reduced-Serum Medium supplemented with 1% penicillin/streptomycin. The plasmid DNA (3.0 µg) was diluted in fresh Opti-MEM medium (500 µL) and gently mixed. The X-tremeGENE™ HP DNA transfection reagent was added to the diluted DNA in a 2:1 ratio (6 µL) and incubated at room temperature for 15 mins. The transfection complex was then added to the cells in a dropwise manner, followed by a gentle swirl for even distribution across the plate. The cells were incubated at 37 °C (5% CO₂) for 48 hours before any drug treatments.

Cellular EGFP-Tau degradation assay. PC12 cells were grown to 70-80% confluency in a 37 °C incubator (5% CO₂) in Opti-MEM Reduced-Serum Medium supplemented with 1% penicillin/streptomycin. The cells were transiently transfected with 3.0 µg of the pRK5-EGFP-Tau plasmid (addgene; plasmid #46904) using the X-tremeGENE™ HP DNA transfection reagent (Sigma-Aldrich) protocol as described above. At 48 hours post-transfection, the cells were treated with DMSO, 10 µM 20S activator, or 50 nM bortezomib (0.1% DMSO). Following an 18-hour drug treatment, the cells/media were transferred to a conical centrifuge tube (15 mL). The cells were pelleted via centrifugation at 1000 rpm for 3 mins and the supernatant was discarded. The cells were washed with ice cold PBS buffer (5 mL) and centrifuged at 1000 rpm for 3 mins to pellet the cells. The cells were resuspended in chilled lysis buffer (PBS buffer supplemented with cComplete™ Mini Protease Inhibitor Cocktail; 1 tablet in 7 mL of PBS; Sigma-Aldrich). The cells were lysed by sonication (two 5 sec pulses at 40% amplitude, with 3 sec pause in between) and the lysate was clarified by centrifugation at 5000 rpm for 15 mins. The total protein concentration of the supernatant was determined using a bicinchoninic acid assay (BCA assay), and the samples were normalized to 2.0 mg/mL total protein concentration. The samples were then boiled at 95 °C with 5X SDS loading buffer, and equal amounts of cell lysate were resolved on a 4-20% Tris/glycine gel and transferred to a PVDF membrane. The membrane was probed with anti-tau

(Cell Signaling; cat#46687) or anti-GAPDH-HRP (Novus; cat#NBP2-27103H) antibodies. After washing and application of appropriate secondary antibodies, the blots were developed with ECL Western reagent (Radiance Plus, Azure Biosystems; cat#AC2103) and imaged with a chemiluminescent Western blot imager (Azure Biosystems 300Q). Band intensities were acquired using Biorad Image Lab analysis software.

Cell viability assay. SH-SY5Y cells (5,000/well) were seeded in a white, opaque 96-well plate in 100 μ L of Dulbecco's Modified Eagle Medium (DMEM) supplemented with 10% fetal bovine serum (FBS) and 1 % penicillin/streptomycin. The cells were then treated with the test compound at concentrations ranging from 1.25-80 μ M (0.5% DMSO) for 72 hours at 37 °C and 5% CO₂. Cells were equilibrated to room temperature and CellTiter-Glo (Promega) solution (100 μ L) was added and incubated with shaking for 2 minutes at room temperature. The assay plate was then allowed to equilibrate for 10 more minutes at room temperature and luminescence readings were taken on a SpectraMax M5e spectrometer.

20S proteasome-mediated degradation of fluorogenic poly-GR DPR protein substrate. Purified 20S proteasome (final concentration of 1 nM) in assay buffer (38 mM Tris-HCl, 100 mM NaCl, pH 7.8) was added to a black, clear-bottom 96-well plate and incubated with various concentrations of drug (1.25–80 μ M; 1%DMSO) at 37°C for 15 min. Fluorogenic poly-GR DPR protein substrate (Suc-GR₃-AMC; aka Suc-GRGRGR-AMC) was added to each well to a final concentration of 20 μ M. Fluorescence was measured at 37°C on a SpectraMax M5e spectrometer taking kinetic readings every 5 min at 380/460nm for 1 hour.

Proteasome inhibitor titration assays. The activity assay was conducted in 100 μ L reaction volume in a black, clear-bottom 96-well plate. **Bortezomib (BTZ):** Purified human 20S proteasome (1 nM) and stock solutions of the BTZ were added to final concentrations ranging from 1.25-80 μ M in assay buffer (38 mM Tris-HCl, 100 mM NaCl, pH 7.8) and the plate was incubated at 37 °C for 15 min. **AEBSF (4-(2-aminoethyl) benzenesulfonyl fluoride):** Purified human 20S proteasome (1 nM) and stock solutions of the AEBSF were added to final concentrations ranging from 100-1000 μ M in assay buffer (38 mM Tris-HCl, 100 mM NaCl, pH 7.8) and the plate was incubated at 37 °C for 30 min. The fluorogenic substrates (Suc-LLVY-AMC, Boc-LRR-AMC, Z-LLE-AMC) were

added to a final concentration of 20 μM total. The fluorescence was measured at 37 °C on a SpectraMax M5e spectrometer taking kinetic readings every 5 mins for 1 hour (380/460 nm).

Selective activation of T-L site. The activity assay was conducted in 100 μL reaction volume in a black, clear-bottom 96-well plate. Purified human 20S proteasome (1 nM) was incubated with bortezomib, BTZ (1.25 μM ; 0.5% DMSO) in assay buffer (38 mM Tris-HCl, 100 mM NaCl, pH 7.8) at 37 °C for 15 min. Two vehicles were included in the assay; one treated with only DMSO, and one treated with BTZ (1.25 μM). This allowed the percent 20S proteasome activity of a fully functioning proteolytic site to be calculated to plot the dose-response curves. Next, stock solutions of 20S proteasome activator were added to final concentrations ranging from 1.25-40 μM (0.5% DMSO) and the plate was incubated at 37 °C for 15 min. The fluorogenic substrates (Suc-LLVY-AMC, Boc-LRR-AMC, Z-LLE-AMC) or (Suc-GR₃-AMC for DPR degradation with only T-L site activity) were added to a final concentration of 20 μM total. The fluorescence was measured at 37 °C on a SpectraMax M5e spectrometer taking kinetic readings every 5 mins for 1 hour (380/460 nm).

Selective activation of CT-L and Casp-L sites. The activity assay was conducted in 100 μL reaction volume in a black, clear-bottom 96-well plate. Purified human 20S proteasome (1 nM) was incubated with AEBSF (500 μM ; 0.5% DMSO) in assay buffer (38 mM Tris-HCl, 100 mM NaCl, pH 7.8) at 37 °C for 30 minutes. Two vehicles were included in the assay; one treated with only DMSO, and one treated with AEBSF (500 μM). This allowed the percent 20S proteasome activity of a fully functioning proteolytic site to be calculated to plot the dose-response curves. Next, stock solutions of 20S proteasome activator were added to final concentrations ranging from 1.25-40 μM (0.5% DMSO) and the plate was incubated at 37 °C for 15 min. The fluorogenic substrates (Suc-LLVY-AMC, Boc-LRR-AMC, Z-LLE-AMC) or (Suc-GR₃-AMC for DPR degradation with only CT-L and Casp-L sites) were added to a final concentration of 20 μM total. The fluorescence was measured at 37 °C on a SpectraMax M5e spectrometer taking kinetic readings every 5 mins for 1 hour (380/460 nm).

REFERENCES

- (1) Dunker, A. K.; Lawson, J. D.; Brown, C. J.; Williams, R. M.; Romero, P.; Oh, J. S.; Oldfield, C. J.; Campen, A. M.; Ratliff, C. M.; Hipps, K. W.; Ausio, J.; Nissen, M. S.; Reeves, R.; Kang, C.; Kissinger, C. R.; Bailey, R. W.; Griswold, M. D.; Chiu, W.; Garner, E. C.; Obradovic, Z. Intrinsically Disordered Protein. *Journal of Molecular Graphics and Modelling* **2001**, *19* (1), 26–59.
- (2) DeForte, S.; Uversky, V. N. Order, Disorder, and Everything in Between. *Molecules* **2016**, *21* (8), 1090–1112.
- (3) Babu, M. M.; van der Lee, R.; de Groot, N. S.; Gsponer, J. Intrinsically Disordered Proteins: Regulation and Disease. *Current Opinion in Structural Biology* **2011**, *21* (3), 432–440.
- (4) Uversky, V. N.; Oldfield, C. J.; Dunker, A. K. Intrinsically Disordered Proteins in Human Diseases: Introducing the D2 Concept. *Annual Review of Biophysics* **2008**, *37*, 215–246.
- (5) Vilchez, D.; Saez, I.; Dillin, A. The Role of Protein Clearance Mechanisms in Organismal Ageing and Age-Related Diseases. *Nature Communications* **2014**, *5* (5659), 1–13.
- (6) Selkoe, D. J. Alzheimer's Disease. *Cold Spring Harbor Perspectives in Biology* **2011**, *3* (7), 1–16.
- (7) Bosco, D. A.; LaVoie, M. J.; Petsko, G. A.; Ringe, D. Proteostasis and Movement Disorders: Parkinson's Disease and Amyotrophic Lateral Sclerosis. *Cold Spring Harbor Perspectives in Biology* **2011**, *3* (10), 1–24.
- (8) Finkbeiner, S. Huntington's Disease. *Cold Spring Harbor Perspectives in Biology* **2011**, *3* (6), 1–23.
- (9) Brettschneider, J.; Del Tredici, K.; Lee, V. M.-Y.; Trojanowski, J. Q. Spreading of Pathology in Neurodegenerative Diseases: A Focus on Human Studies. *Nature Reviews Neuroscience* **2015**, *16* (2), 109–120.
- (10) Rubinsztein, D. C. The Roles of Intracellular Protein-Degradation Pathways in Neurodegeneration. *Nature* **2006**, *443* (7113), 780–786.
- (11) Selkoe, D. J. Folding Proteins in Fatal Ways. *Nature* **2003**, *426* (6968), 900–904.
- (12) Ciechanover, A.; Brundin, P. The Ubiquitin Proteasome System in Neurodegenerative Diseases: Sometimes the Chicken, Sometimes the Egg. *Neuron* **2003**, *40* (2), 427–446.
- (13) Keller, J. N.; Hanni, K. B.; Markesbery, W. R. Impaired Proteasome Function in Alzheimer's Disease. *Journal of Neurochemistry* **2000**, *75* (1), 436–439.
- (14) McNaught, K. S. P.; Olanow, C. W.; Halliwell, B.; Isacson, O.; Jenner, P. Failure of the Ubiquitin-Proteasome System in Parkinson's Disease. *Nature Reviews Neuroscience* **2001**, *2* (8), 589–594.
- (15) Ortega, Z.; Díaz-Hernández, M.; Lucas, J. J. Is the Ubiquitin-Proteasome System Impaired in Huntington's Disease? *Cellular and Molecular Life Sciences* **2007**, *64* (17), 2245–2257.

- (16) Ben-Nissan, G.; Sharon, M. Regulating the 20S Proteasome Ubiquitin-Independent Degradation Pathway. *Biomolecules* **2014**, *4* (3), 862–884.
- (17) Eralles, J.; Coffino, P. Ubiquitin-Independent Proteasomal Degradation. *Biochimica et Biophysica Acta* **2014**, *1843* (1), 216–221.
- (18) Höhn, T. J. A.; Grune, T. The Proteasome and the Degradation of Oxidized Proteins: Part III—Redox Regulation of the Proteasomal System. *Redox Biology* **2014**, *2*, 388–394.
- (19) Jung, T.; Höhn, A.; Grune, T. The Proteasome and the Degradation of Oxidized Proteins: Part II – Protein Oxidation and Proteasomal Degradation. *Redox Biology* **2014**, *2*, 99–104.
- (20) Tanaka, K.; Mizushima, T.; Saeki, Y. The Proteasome: Molecular Machinery and Pathophysiological Roles. *Biological Chemistry* **2012**, *393* (4), 217–234.
- (21) Groll, M.; Ditzel, L.; Lowe, J.; Stock, D.; Bochtler, M.; Bartunik, H. D. Structure of 20S Proteasome from Yeast at 2.4Å Resolution. *Nature* **1997**, *386* (6624), 463–471.
- (22) Finley, D.; Chen, X.; Walters, K. J. Gates, Channels, and Switches: Elements of the Proteasome Machine. *Trends in Biochemical Sciences* **2016**, *41* (1), 77–93.
- (23) Groll, M.; Bajorek, M.; Köhler, A.; Moroder, L.; Rubin, D. M.; Huber, R.; Glickman, M. H.; Finley, D. A Gated Channel into the Proteasome Core Particle. *Nature Structural Biology* **2000**, *7* (11), 1062–1067.
- (24) Smith, D. M.; Chang, S.-C.; Park, S.; Finley, D.; Cheng, Y.; Goldberg, A. Docking of the Proteasomal ATPases' C-Termini in the 20S Proteasomes Alpha Ring Opens the Gate for Substrate Entry. *Molecular Cell* **2007**, *27* (5), 731–744.
- (25) Rabl, J.; Smith, D. M.; Yu, Y.; Chang, S.-C.; Goldberg, A. L.; Cheng, Y. Mechanism of Gate Opening in the 20S Proteasome by the Proteasomal ATPases. *Molecular Cell* **2008**, *30* (3), 360–368.
- (26) Uversky, V. N. Wrecked Regulation of Intrinsically Disordered Proteins in Diseases: Pathogenicity of Deregulated Regulators. *Frontiers in Molecular Biosciences* **2014**, *1* (6), 1–24.
- (27) Thibaudeau, T. A.; Anderson, R. T.; Smith, D. M. A Common Mechanism of Proteasome Impairment by Neurodegenerative Disease-Associated Oligomers. *Nature Communications* **2018**, *9* (1), 1–14.
- (28) Njomen, E.; Osmulski, P. A.; Jones, C. L.; Gaczynska, M.; Tepe, J. J. Small Molecule Modulation of Proteasome Assembly. *Biochemistry* **2018**, *57* (28), 4214–4224.
- (29) Vanecek, A. S.; Mojsilovic-Petrovic, J.; Kalb, R. G.; Tepe, J. J. Enhanced Degradation of Mutant C9ORF72-Derived Toxic Dipeptide Repeat Proteins by 20S Proteasome Activation Results in Restoration of Proteostasis and Neuroprotection. *ACS Chemical Neuroscience* **2023**, *14* (8), 1439–1448.

- (30) Njomen, E.; Vanecek, A.; Lansdell, T. A.; Yang, Y.-T.; Schall, P. Z.; Harris, C. M.; Bernard, M. P.; Isaac, D.; Alkharabsheh, O.; Al-Janadi, A.; Giletto, M. B.; Ellsworth, E.; Taylor, C.; Tang, T.; Lau, S.; Bailie, M.; Bernard, J. J.; Yuzbasiyan-Gurkan, V.; Tepe, J. J. Small Molecule 20S Proteasome Enhancer Regulates MYC Protein Stability and Exhibits Antitumor Activity in Multiple Myeloma. *Biomedicines* **2022**, *10* (5), 938.
- (31) Tanaka, K.; Yoshimura, T.; Kumatori, A.; Ichihara, A.; Ikai, A.; Nishigai, M.; Kameyama, K.; Takagi, T. Proteasomes (Multi-Protease Complexes) as 20S Ring-Shaped Particles in a Variety of Eukaryotic Cells. *The Journal of Biological Chemistry* **1988**, *263* (31), 16209–16217.
- (32) Tanaka, K.; Yoshimura, T.; Ichihara, A. Role of Substrate in Reversible Activation of Proteasomes (Multi-Protease Complexes) by Sodium Dodecyl Sulfate. *Journal of Biochemistry* **1989**, *106* (3), 495–500.
- (33) Ruiz de Mena, I.; Mahillo, E.; Arribas, J.; Castaño, J. G. Kinetic Mechanism of Activation by Cardiolipin (Diphosphatidylglycerol) of the Rat Liver Multicatalytic Proteinase. *The Biochemical Journal* **1993**, *296*, 93–97.
- (34) Watanabe, N.; Yamada, S. Activation of 20S Proteasomes from Spinach Leaves by Fatty Acids. *Plant & Cell Physiology* **1996**, *37* (2), 147–151.
- (35) Katsiki, M.; Chondrogianni, N.; Chinou, I.; Rivett, A. J.; Gonos, E. S. The Olive Constituent Oleuropein Exhibits Proteasome Stimulatory Properties In Vitro and Confers Life Span Extension of Human Embryonic Fibroblasts. *Rejuvenation Research* **2007**, *10* (2), 157–172.
- (36) Huang, L.; Ho, P.; Chen, C.-H. Activation and Inhibition of the Proteasome by Betulinic Acid and Its Derivatives. *FEBS Letters* **2007**, *581* (25), 4955–4959.
- (37) Trader, D. J.; Simanski, S.; Dickson, P.; Kodadek, T. Establishment of a Suite of Assays That Support the Discovery of Proteasome Stimulators. *Biochimica et Biophysica Acta* **2017**, *1861* (4), 892–899.
- (38) Coleman, R. A.; Trader, D. J. Development and Application of a Sensitive Peptide Reporter to Discover 20S Proteasome Stimulators. *ACS Combinatorial Science* **2018**, *20* (5), 269–276.
- (39) Lipinski, C. A.; Lombardo, F.; Dominy, B. W.; Feeney, P. J. Experimental and Computational Approaches to Estimate Solubility and Permeability in Drug Discovery and Development Settings. *Advanced Drug Delivery Reviews* **2001**, *46* (1), 3–26.
- (40) Jones, C.; Njomen, E.; Sjogren, B.; Dexheimer, T.; Tepe, J. Small Molecule Enhancement of 20S Proteasome Activity Targets Intrinsically Disordered Proteins. *ACS Chemical Biology* **2017**, *12* (9), 2240–2247.
- (41) Fiolek, T. J.; Keel, K. L.; Tepe, J. J. Fluspirilene Analogs Activate the 20S Proteasome and Overcome Proteasome Impairment by Intrinsically Disordered Protein Oligomers. *ACS Chemical Neuroscience* **2021**, *12* (8), 1438–1448.
- (42) Staerz, S. D.; Jones, C. L.; Tepe, J. J. Design, Synthesis, and Biological Evaluation of Potent 20S Proteasome Activators for the Potential Treatment of α -Synucleinopathies. *Journal of Medicinal Chemistry* **2022**, *65* (9), 6631–6642.

- (43) Harshbarger, W.; Miller, C.; Diedrich, C.; Sacchettini, J. Crystal Structure of the Human 20S Proteasome in Complex with Carfilzomib. *Structure* **2015**, *23* (2), 418–424.
- (44) Shimamura, T.; Shiroishi, M.; Weyand, S.; Tsujimoto, H.; Winter, G.; Katritch, V.; Abagyan, R.; Cherezov, V.; Liu, W.; Won Han, G.; Kobayashi, T.; Stevens, R.; Iwata, S. Structure of the Human Histamine H1 Receptor Complex with Doxepin. *Nature* **2011**, *475* (7354), 65–70.
- (45) Ohta, K.; Hayashi, H.; Mizuguchi, H.; Kagamiyama, H.; Fujimoto, K.; Fukui, H. Site-Directed Mutagenesis of the Histamine H1 Receptor: Roles of Aspartic Acid107, Asparagine198 and Threonine194. *Biochemical and Biophysical Research Communications* **1994**, *203* (2), 1096–1101.
- (46) Nonaka, H.; Otaki, S.; Ohshima, E.; Kono, M.; Kase, H.; Ohta, K.; Fukui, H.; Ichimura, M. Unique Binding Pocket for KW-4679 in the Histamine H1 Receptor. *European Journal of Pharmacology* **1998**, *345* (1), 111–117.
- (47) Bruysters, M.; Pertz, H. H.; Teunissen, A.; Bakker, R. A.; Gillard, M.; Chatelain, P.; Schunack, W.; Timmerman, H.; Leurs, R. Mutational Analysis of the Histamine H1-Receptor Binding Pocket of Histaprodifens. *European Journal of Pharmacology* **2004**, *487* (1), 55–63.
- (48) Anaya deParrodi, C.; Quinero-Cortes, L.; Sandoval-Ramirez, J. A Short Synthesis of Astemizole. *Synthetic Communications* *26* (17), 3323–3329.
- (49) Chaturvedi, A. K.; Verma, A. K.; Thakur, J. P.; Roy, S.; Bhushan Tripathi, S.; Kumar, B. S.; Khwaja, S.; Sachan, N. K.; Sharma, A.; Chanda, D.; Shanker, K.; Saikia, D.; Negi, A. S. A Novel Synthesis of 2-Arylbenzimidazoles in Molecular Sieves-MeOH System and Their Antitubercular Activity. *Bioorganic & Medicinal Chemistry* **2018**, *26* (15), 4551–4559.
- (50) Stefanis, L. α -Synuclein in Parkinson's Disease. *Cold Spring Harbor Perspectives in Medicine* **2012**, *2* (2), 1–23.
- (51) Zondler, L.; Kostka, M.; Garidel, P.; Heinzemann, U.; Hengerer, B.; Mayer, B.; Weishaupt, J. H.; Gillardon, F.; Danzer, K. M. Proteasome Impairment by α -Synuclein. *PLOS ONE* **2017**, *12* (9), 1–14.
- (52) Lindersson, E.; Beedholm, R.; Højrup, P.; Moos, T.; Gai, W.; Hendil, K. B.; Jensen, P. H. Proteasomal Inhibition by α -Synuclein Filaments and Oligomers. *Journal of Biological Chemistry* **2004**, *279* (13), 12924–12934.
- (53) Tai, H.-C.; Serrano-Pozo, A.; Hashimoto, T.; Frosch, M. P.; Spires-Jones, T. L.; Hyman, B. T. The Synaptic Accumulation of Hyperphosphorylated Tau Oligomers in Alzheimer Disease Is Associated with Dysfunction of the Ubiquitin-Proteasome System. *The American Journal of Pathology* **2012**, *181* (4), 1426–1435.
- (54) Myeku, N.; Clelland, C. L.; Emrani, S.; Kukushkin, N. V.; Yu, W. H.; Goldberg, A. L.; Duff, K. E. Tau-Driven 26S Proteasome Impairment and Cognitive Dysfunction Can Be Prevented Early in Disease by Activating cAMP-PKA Signaling. *Nature Medicine* **2016**, *22* (1), 46–53.
- (55) Njomen, E.; Osmulski, P.; Jones, C.; Gaczynska, M.; Tepe, J. Small Molecule Modulation of Proteasome Assembly. *Biochemistry* **2018**, *57*, 4214–4224.

- (56) Keşmir, C.; Nussbaum, A. K.; Schild, H.; Detours, V.; Brunak, S. Prediction of Proteasome Cleavage Motifs by Neural Networks. *Protein Engineering, Design and Selection* **2002**, *15* (4), 287–296.
- (57) Nielsen, M.; Lundegaard, C.; Lund, O.; Keşmir, C. The Role of the Proteasome in Generating Cytotoxic T-Cell Epitopes: Insights Obtained from Improved Predictions of Proteasomal Cleavage. *Immunogenetics* **2005**, *57* (1), 33–41.

APPENDIX

3.1 *In vitro* α -synuclein Digestion – Astemizole

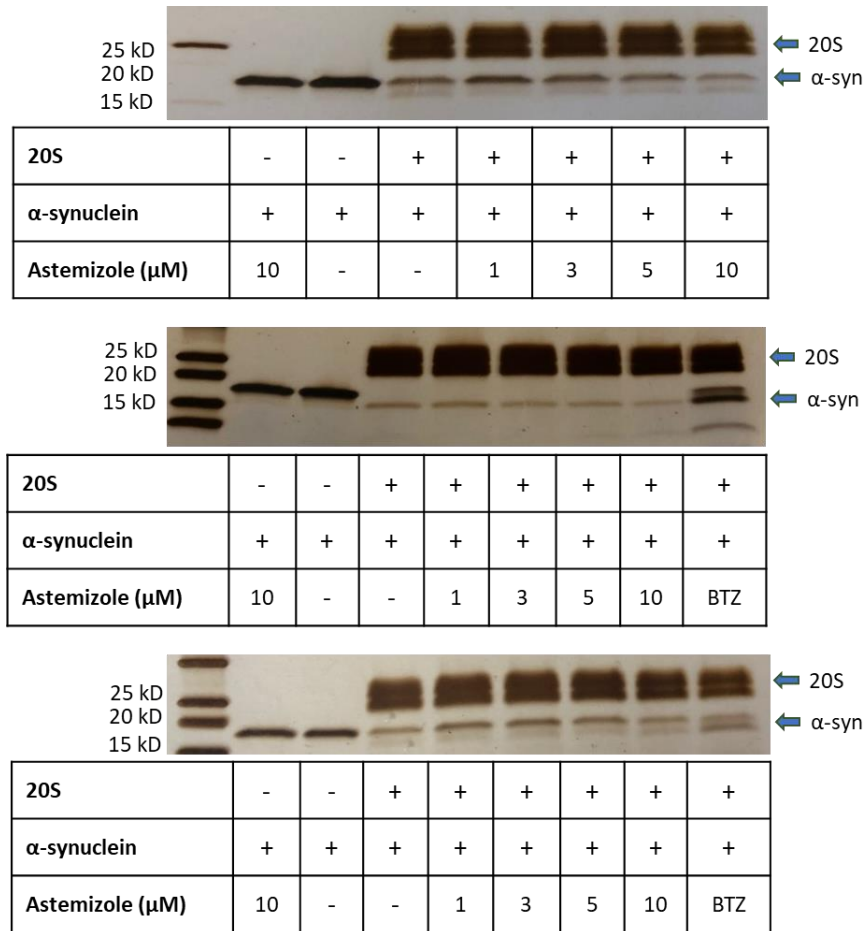


Figure 3.19 Astemizole enhances 20S proteasome-mediated degradation of α -synuclein *in vitro*. Silver stained gels of α -synuclein digestion with the 20S proteasome pretreated with astemizole or proteasome inhibitor bortezomib (BTZ, 5 μ M); (n=3).

3.2 *In vitro* α -synuclein Digestion – Acyl Astemizole

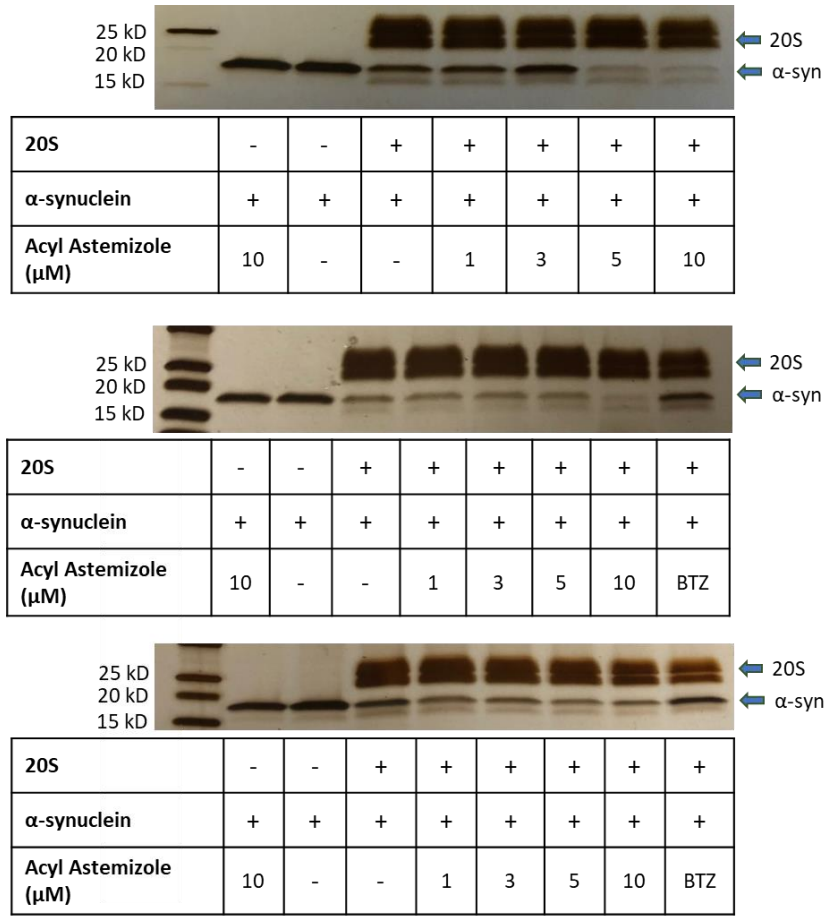


Figure 3.20 Acyl astemizole enhances 20S proteasome-mediated degradation of α -synuclein *in vitro*. Silver stained gels of α -synuclein digestion with the 20S proteasome pretreated with acyl astemizole or proteasome inhibitor bortezomib (BTZ, 5 μ M); (n=3).

3.3 Cellular EGFP-Tau Degradation Assay

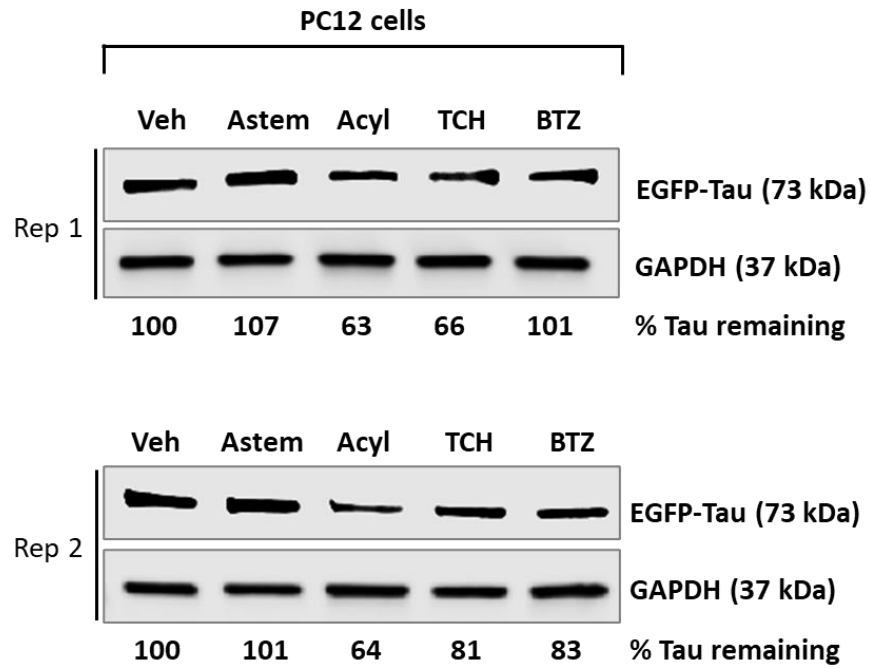


Figure 3.21 Acyl astemizole enhances 20S proteasome-mediated degradation of tau in PC12 cells. Immunoblots of the amount of EGFP-Tau in PC12 cells following an 18-hour treatment with vehicle (DMSO), 20S proteasome activator (10 μ M), or BTZ (50 nM). Immunoblots probed with anti-tau and anti-GAPDH antibodies (n=2).

3.4 Cell Viability Assay in SH-SY5Y Cells

Percent Cell Viability:

	Astemizole	Acyl Astemizole
40.0 μ M	0	19
20.0 μ M	0	76
10.0 μ M	0	92
5.0 μ M	34	95
2.5 μ M	88	104
1.3 μ M	115	105
Vehicle	100	100

Figure 3.22 Cytotoxicity data for astemizole and acyl astemizole in SH-SY5Y cells (n=1).

3.5 Activation of Individual Proteolytic Activities of the 20S Proteasome – TCH-165

Enhancement of 20S Proteolytic Activities

Catalytic Site	Substrate	EC ₂₀₀ (μM)	Max fold increase
CT-L	Suc-LLVY-AMC	2.1 ± 0.3	9.2 ± 0.2
T-L	Boc-LRR-AMC	2.0 ± 0.4	13.9 ± 2.1
Casp-L	Z-LLE-AMC	4.6 ± 1.0	6.6 ± 0.9
All 3 Sites	all	1.3 ± 0.2	10.0 ± 0.4

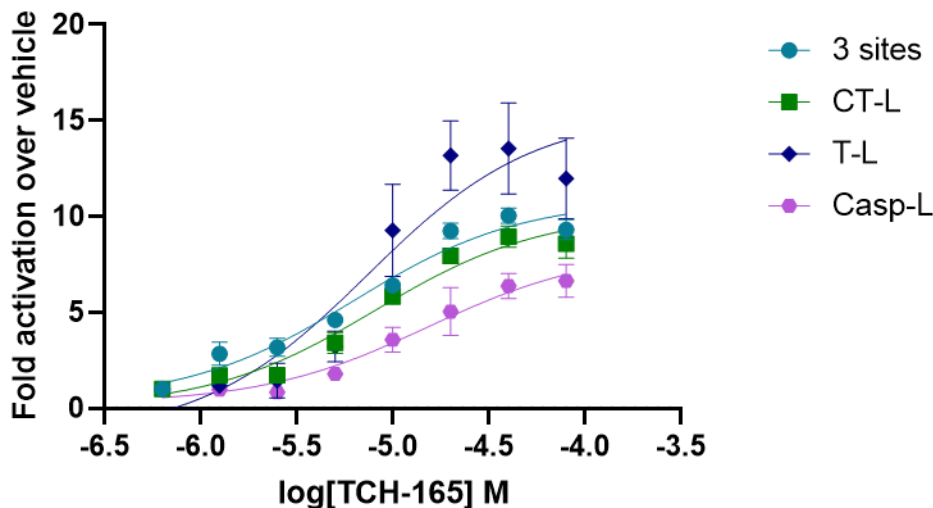


Figure 3.23 Dose-response curve of TCH-165 for 20S proteasome-mediated proteolysis of fluorogenic substrates Suc-LLVY-AMC, Boc-LRR-AMC, and Z-LLE-AMC specific to the 3 proteolytic sites CT-L, T-L, and Casp-L, respectively. All data was collected in triplicate (n=3); error bars denote the standard deviation.

3.6 Activation of Individual Proteolytic Activities of the 20S Proteasome – Acyl Astemizole

Enhancement of 20S Proteolytic Activities

Catalytic Site	Substrate	EC ₂₀₀ (μM)	Max fold increase
CT-L	Suc-LLVY-AMC	14.4 ± 0.3	6.5 ± 1.0
T-L	Boc-LRR-AMC	9.1 ± 2.0	7.7 ± 1.4
Casp-L	Z-LLE-AMC	40.6 ± 13.8	3.2 ± 0.7
All 3 Sites	all	4.6 ± 1.2	8.3 ± 1.0

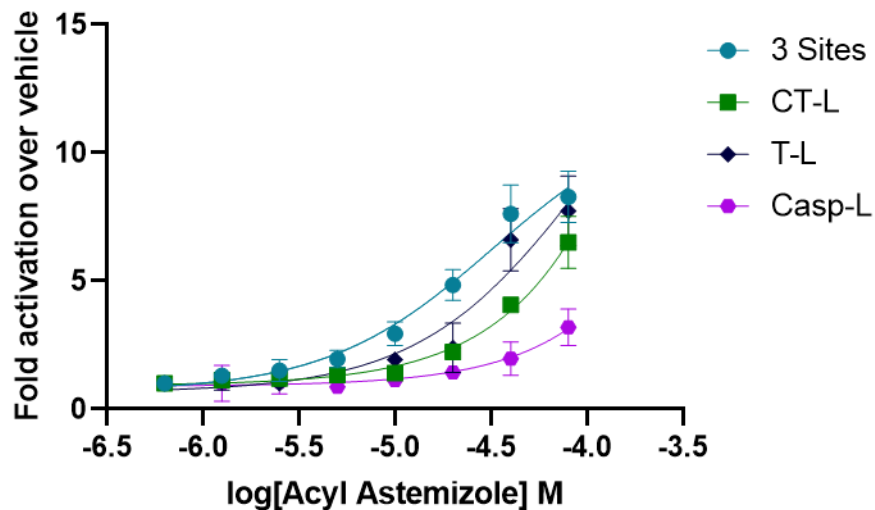


Figure 3.24 Dose-response curve of acyl astemizole for 20S proteasome-mediated proteolysis of fluorogenic substrates Suc-LLVY-AMC, Boc-LRR-AMC, and Z-LLE-AMC specific to the 3 proteolytic sites CT-L, T-L, and Casp-L, respectively. All data was collected in triplicate (n=3); error bars denote the standard deviation.

3.7 Activation of Individual Proteolytic Activities of the 20S Proteasome – Astemizole

Enhancement of 20S Proteolytic Activities

Catalytic Site	Substrate	EC ₂₀₀ (μM)	Max fold increase
CT-L	Suc-LLVY-AMC	2.1 ± 0.5	11.8 ± 0.4
T-L	Boc-LRR-AMC	20.1 ± 6.8	3.9 ± 0.7
Casp-L	Z-LLE-AMC	10.2 ± 3.2	4.5 ± 0.5
All 3 Sites	all	4.0 ± 1.3	7.5 ± 1.3

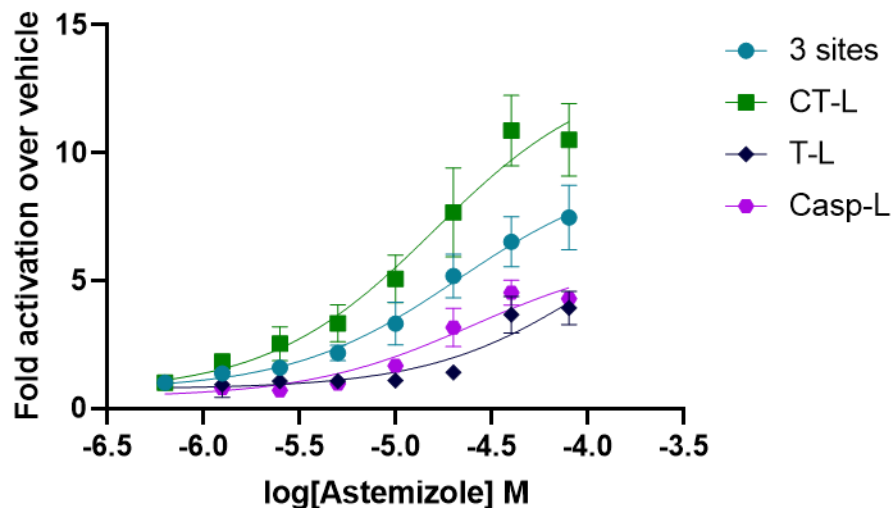


Figure 3.25 Dose-response curve of astemizole for 20S proteasome-mediated proteolysis of fluorogenic substrates Suc-LLVY-AMC, Boc-LRR-AMC, and Z-LLE-AMC specific to the 3 proteolytic sites CT-L, T-L, and Casp-L, respectively. All data was collected in triplicate (n=3); error bars denote the standard deviation.

3.8 Selective Activation of T-L Site with Astemizole and Acyl Astemizole

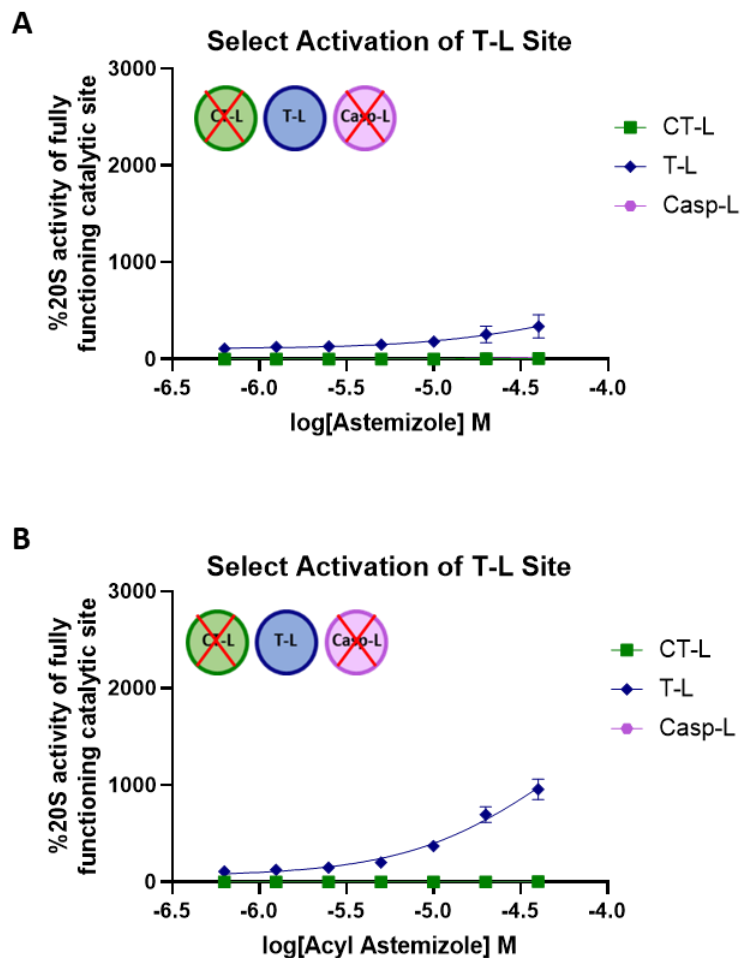


Figure 3.26 Proof-of-concept studies show selective activation of T-L proteolytic site activity is possible. Dose-response curve of astemizole (A) and acyl astemizole (B) for the 20S proteasome-mediated proteolysis of the three unique fluorogenic substrates (Suc-LLVY-AMC, Boc-LRR-AMC, Z-LLE-AMC) with the CT-L and Casp-L sites inhibited with BTZ (1.25 μ M) prior to addition of the 20S activator. All data was collected in triplicate (n=3); error bars denote the standard deviation.

3.9 Selective Activation of CT-L and Casp-L Sites with Astemizole and Acyl Astemizole

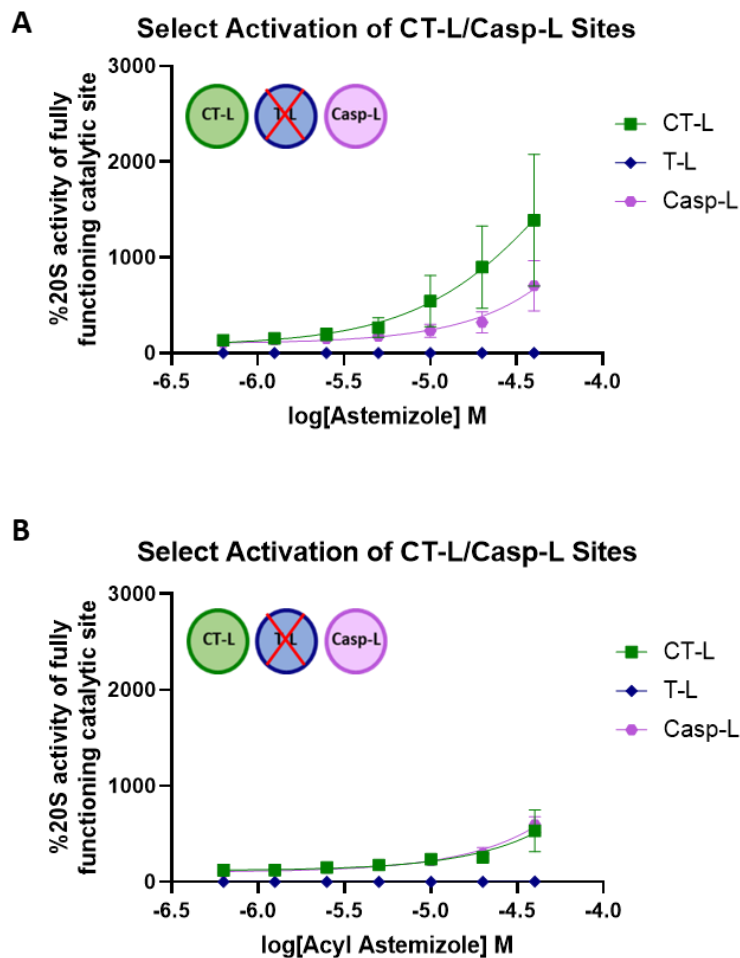


Figure 3.27 Proof-of-concept studies show selective activation of CT-L and Casp-L proteolytic site activities is possible. Dose-response curve of astemizole (A) and acyl astemizole (B) for the 20S proteasome-mediated proteolysis of the three unique fluorogenic substrates (Suc-LLVY-AMC, Boc-LRR-AMC, Z-LLE-AMC) with the T-L site inhibited with AEBSF (500 μ M) prior to addition of the 20S proteasome activator. All data was collected in triplicate (n=3); error bars denote the standard deviation.

3.10 RYE Probe – Sequence and Predicted Proteasomal Cleavage Sites

RYE Probe Sequence: YPYDVPDYAAGGGGGGGGRAGGGAGGGAYAGGAGAGAAEAGGAAGAGGA

NetChop 3.0 predictions using version 20S. Threshold 0.500000

pos	AA	C	score
1	Y	S	0.612655
2	P	.	0.125407
3	Y	.	0.053212
4	D	.	0.248776
5	V	S	0.952255
6	P	.	0.058504
7	D	.	0.039954
8	Y	S	0.533575
9	A	S	0.940885
10	A	.	0.308937
11	G	.	0.115868
12	G	.	0.097154
13	G	.	0.061384
14	G	.	0.074919
15	G	.	0.074919
16	G	.	0.075546
17	G	.	0.037955
18	G	.	0.115678
19	R	S	0.816936
20	A	.	0.282968
21	G	.	0.122136
22	G	.	0.074807
23	G	.	0.166901
24	A	.	0.235630
25	G	.	0.048727
26	G	.	0.155419
27	G	.	0.129376
28	A	.	0.288436
29	Y	S	0.831784
30	A	.	0.410210
31	G	.	0.087039
32	G	.	0.209100
33	A	.	0.093060
34	G	.	0.097779
35	A	.	0.125747
36	G	.	0.065199
37	A	.	0.376120
38	A	.	0.147498
39	E	S	0.785001
40	A	.	0.239735
41	G	.	0.042146
42	G	.	0.087017
43	A	.	0.347850
44	A	.	0.098983
45	G	.	0.323520
46	A	.	0.192325
47	G	.	0.038041
48	G	.	0.248385
49	A	.	0.168065

HA-tag { 1-9

Predicted T-L Cleavage Site → 19

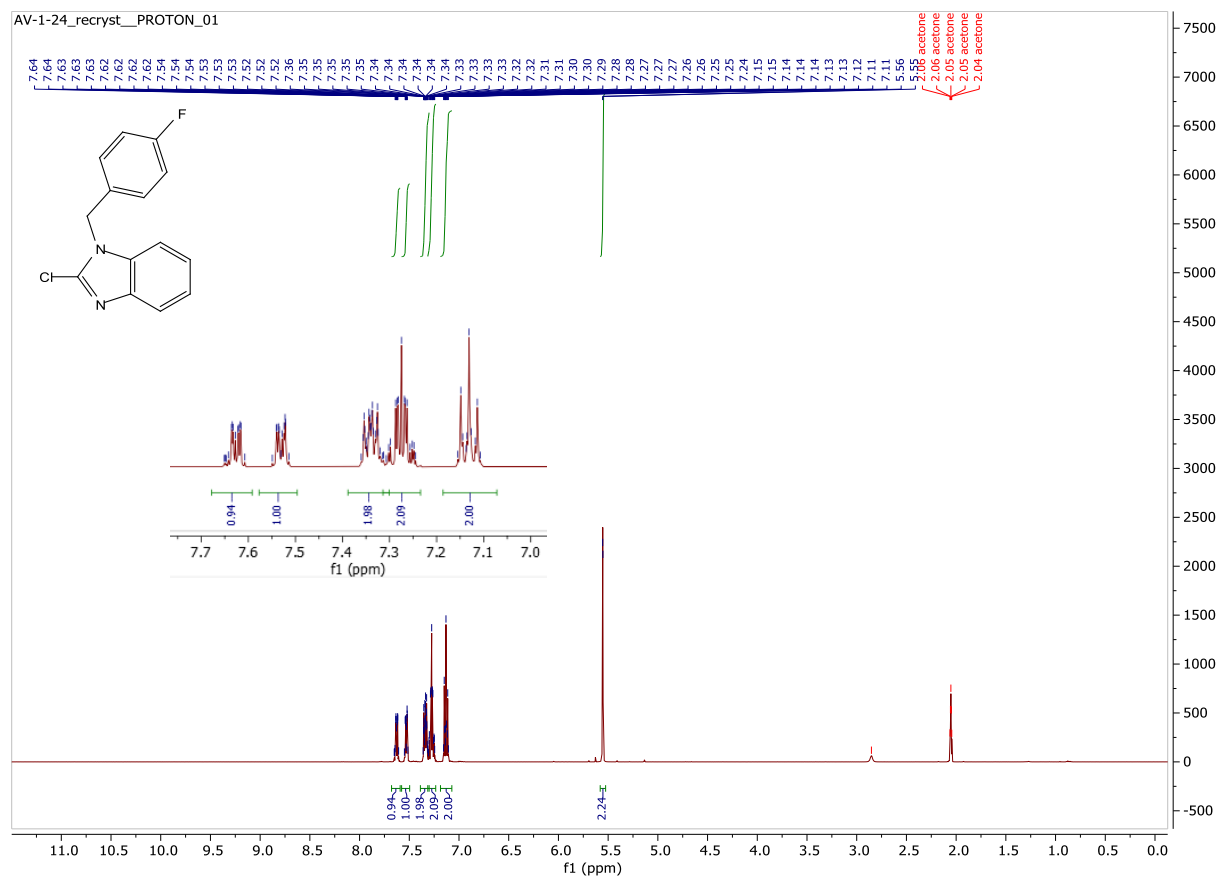
Predicted CT-L Cleavage Site → 29

Predicted Casp-L Cleavage Site → 39

Figure 3.28 Sequence of the RYE probe (synthesized by GenScript) and proteasomal cleavage sites predicted using NetChop 3.0 software using version 20S with the threshold set to 0.5 for a predicted cleavage site. Abbreviations denote the following, AA = amino acid, score = probability score of proteolytic cleavage at indicated amino acid, C = cleavage with S denoting an amino acid with a score of 0.5 or higher and a predicted cleavage site. Note: HA-tag was incorporated for use in immunoblot probing with anti-HA-tag antibody.

3.11 ¹H and ¹³C Spectrum of Compound 3-1i

Compound 3-1i ¹H NMR (500 MHz, Acetone-*d*₆)



Compound 3-1i ¹³C NMR (126 MHz, Methanol-*d*₄)

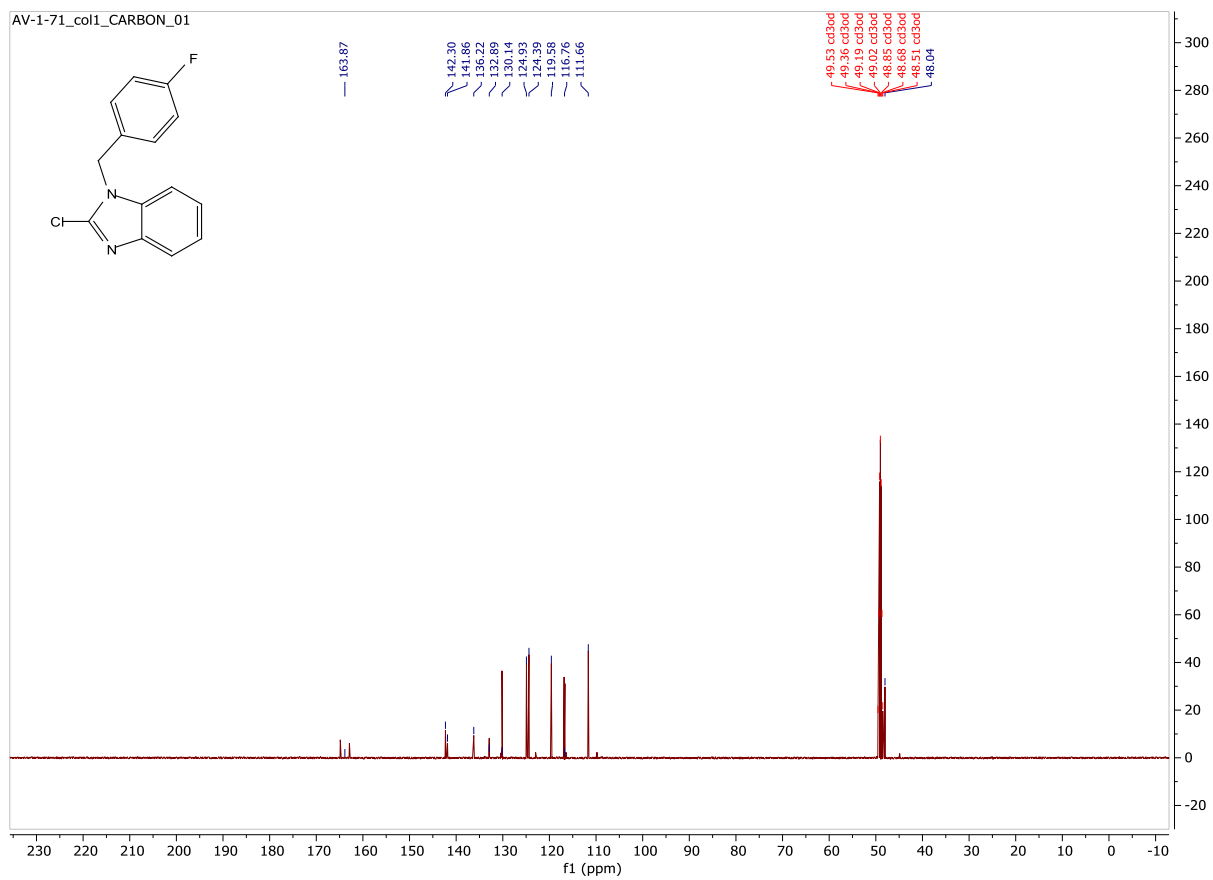


Figure 3.30 Compound 3-1i ¹³C NMR (126 MHz, Methanol-*d*₄).

3.12 ¹H and ¹³C Spectrum of Compound 3-1

Compound 3-1 ¹H NMR (500 MHz, Methanol-*d*₄)

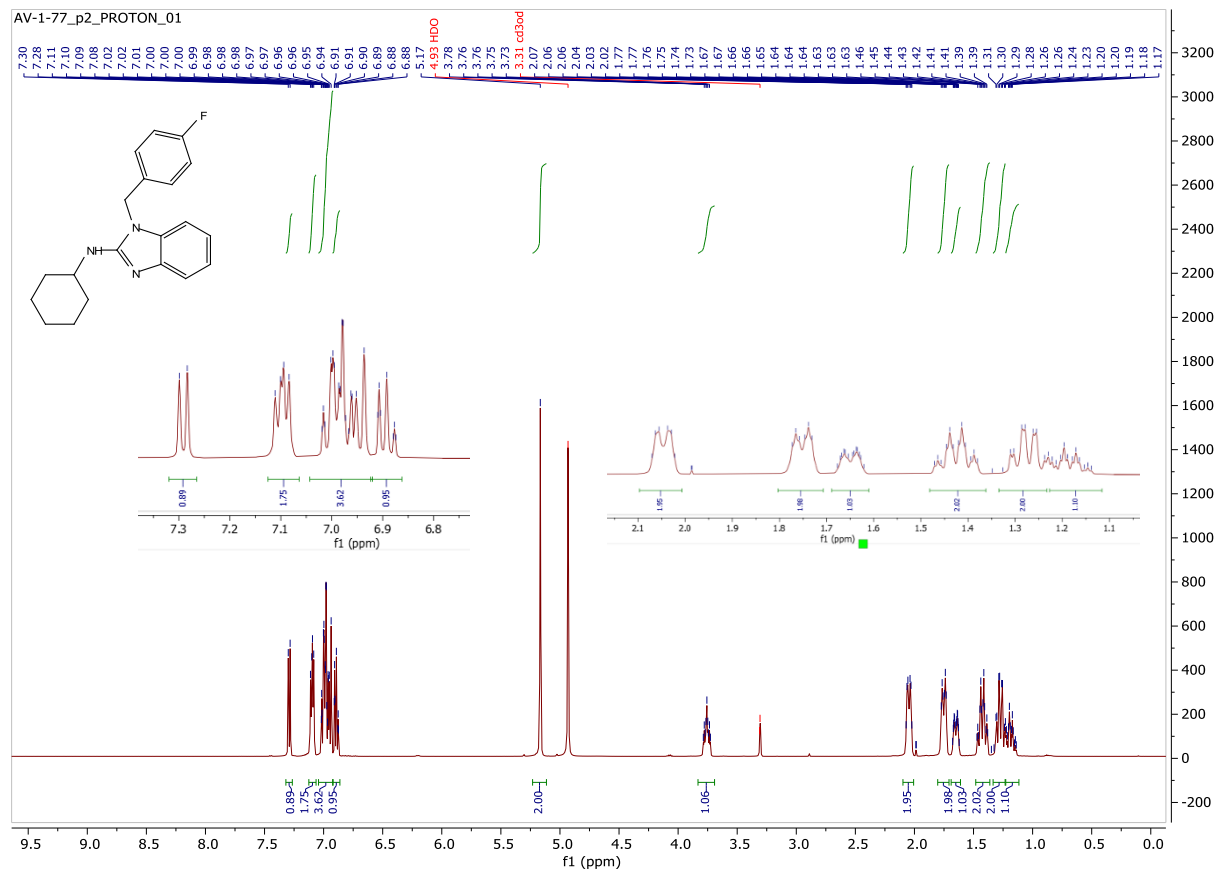


Figure 3.31 Compound 3-1 ¹H NMR (500 MHz, Methanol-*d*₄).

Compound 3-1 ^{13}C NMR (126 MHz, Methanol- d_4)

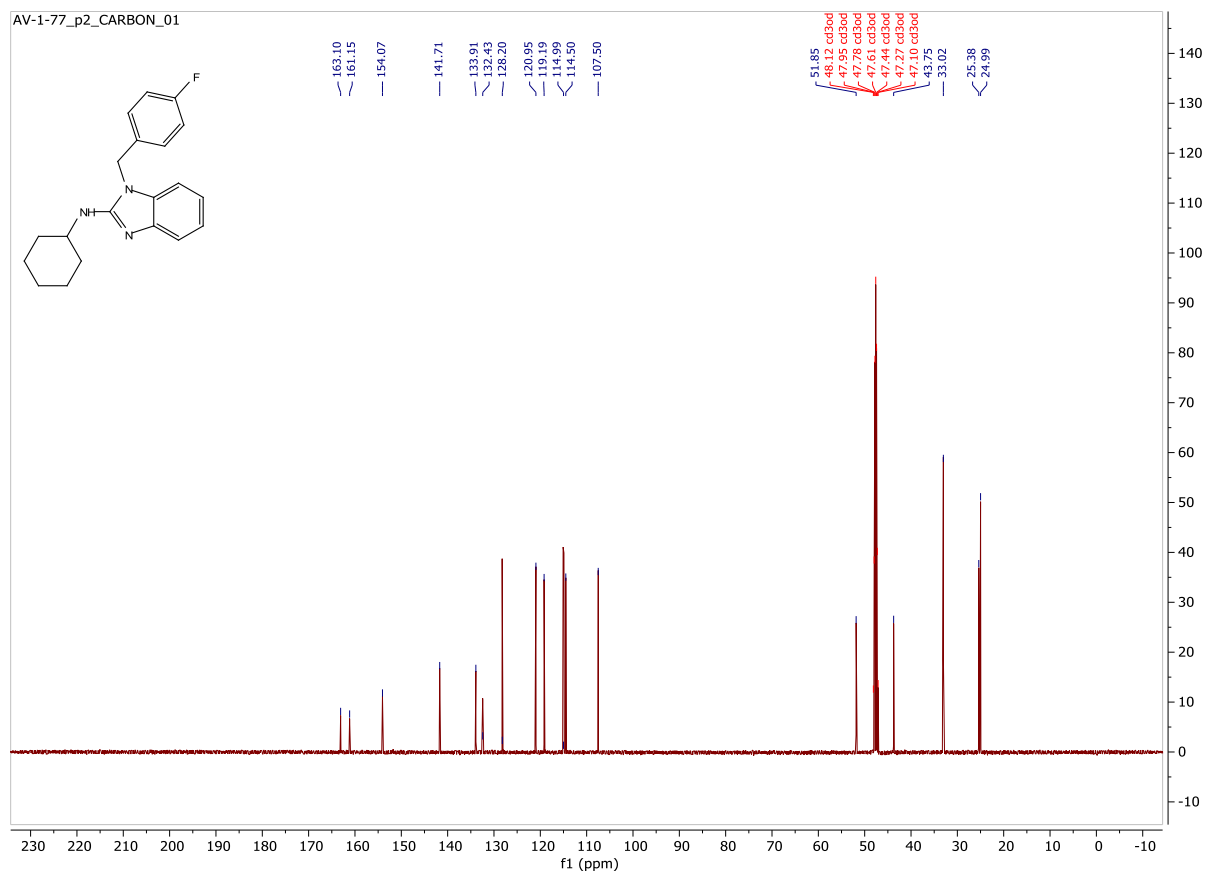


Figure 3.32 Compound 3-1 ^{13}C NMR (126 MHz, Methanol- d_4).

3.13 ¹H and ¹³C Spectrum of Compound 3-2i

Compound 3-2i ¹H NMR (500 MHz, Methanol-*d*₄)

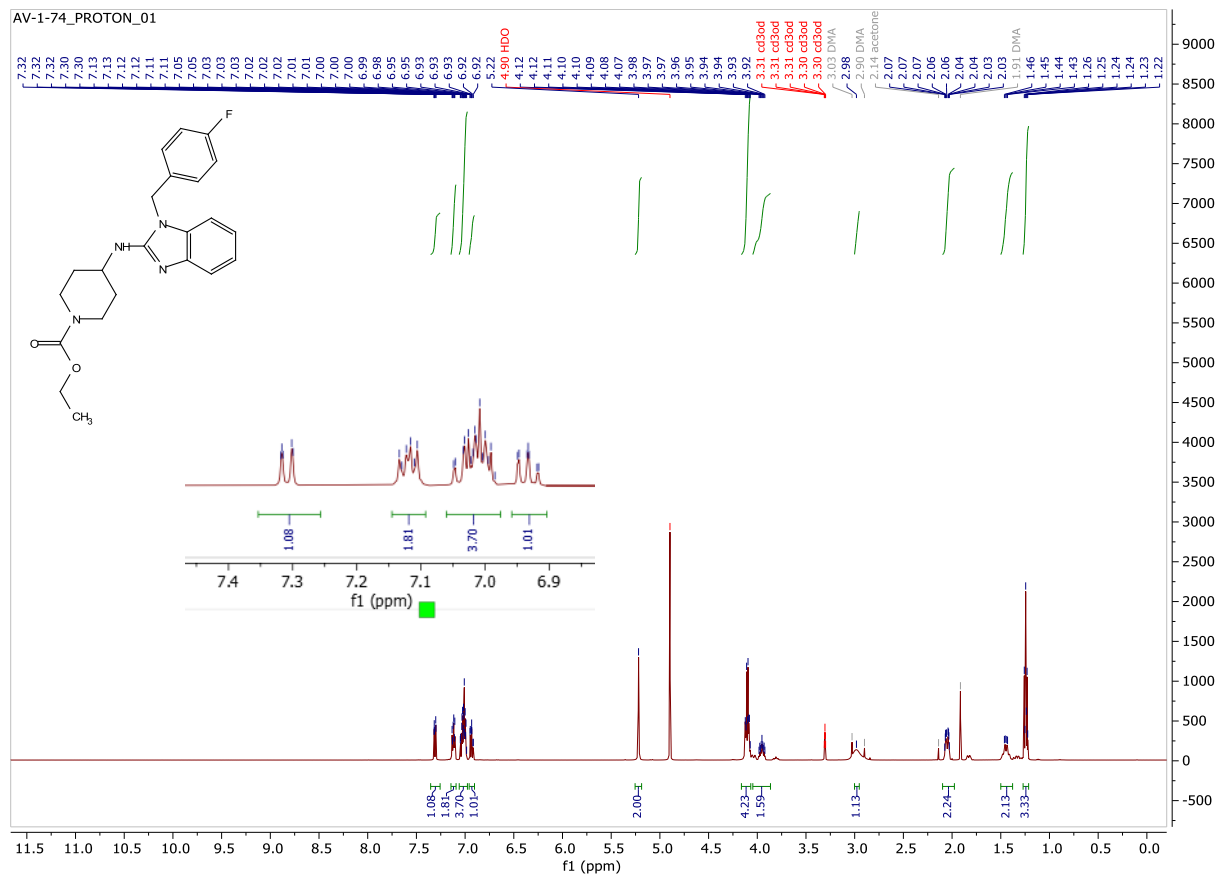


Figure 3.33 Compound 3-2i ¹H NMR (500 MHz, Methanol-*d*₄).

3.14 ¹H and ¹³C Spectrum of Compound 3-2

Compound 3-2 ¹H NMR (500 MHz, Chloroform-d)

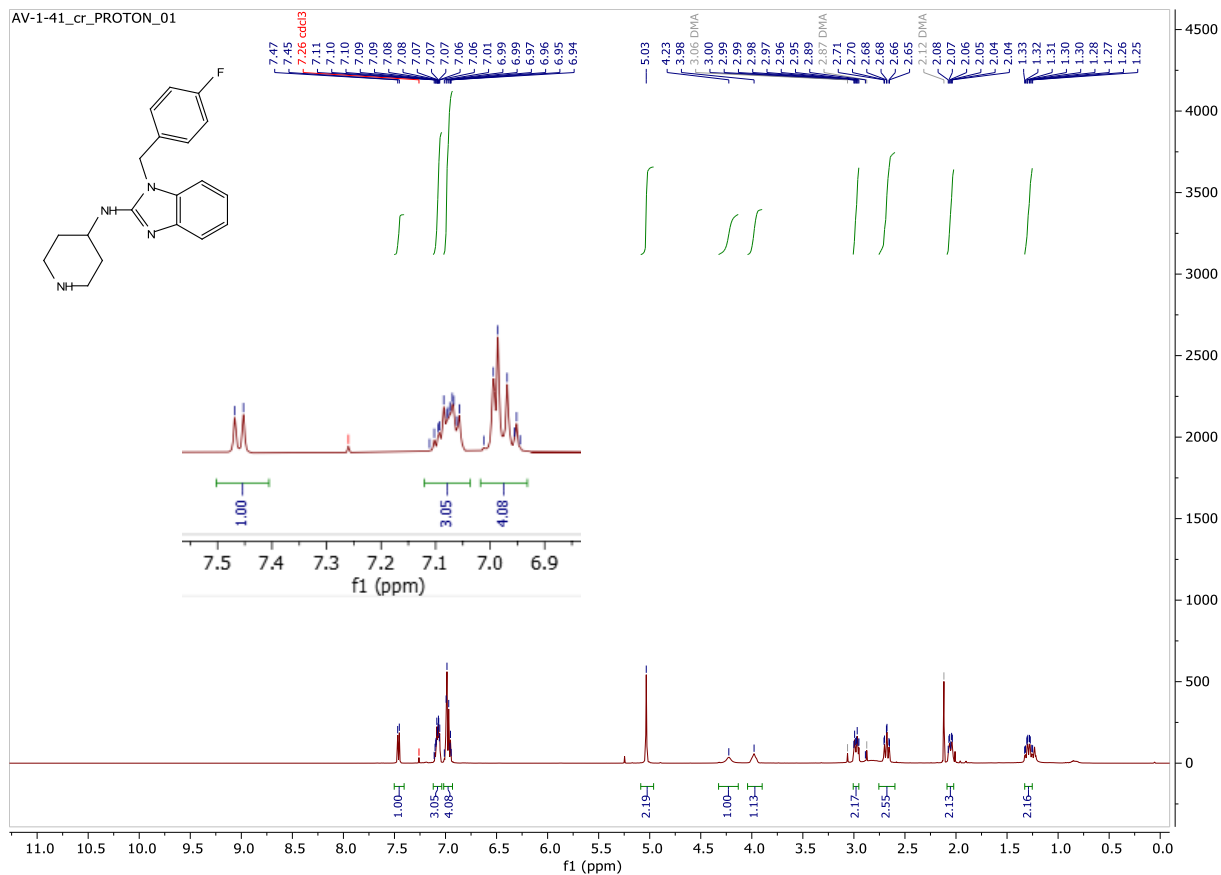


Figure 3.35 Compound 3-2 ¹H NMR (500 MHz, Chloroform-d).

Compound 3-2 ^{13}C NMR (126 MHz, Chloroform-*d*)

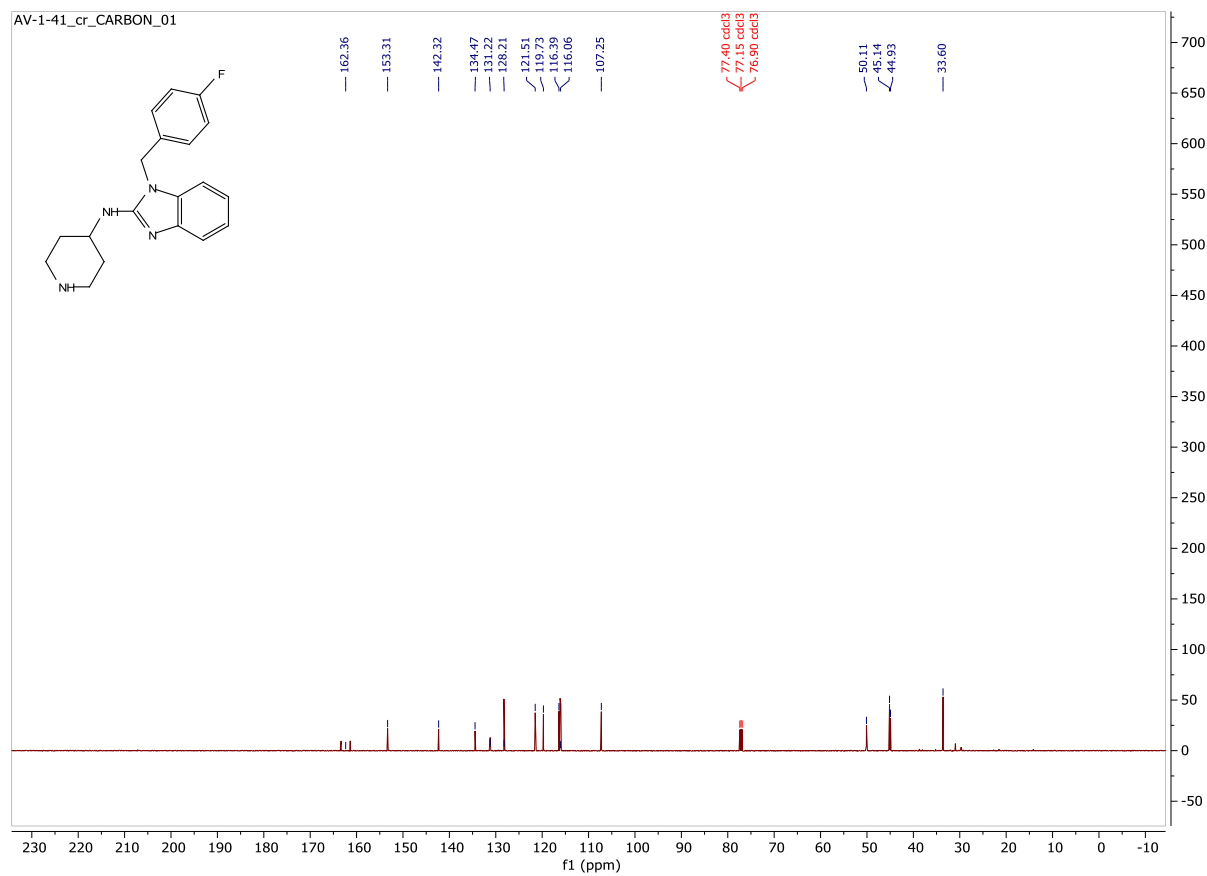


Figure 3.36 Compound 3-2 ^{13}C NMR (126 MHz, Chloroform-*d*).

3.15 ^1H and ^{13}C Spectrum of Compound 3-3

Compound 3-3 ^1H NMR (500 MHz, Methanol- d_4)

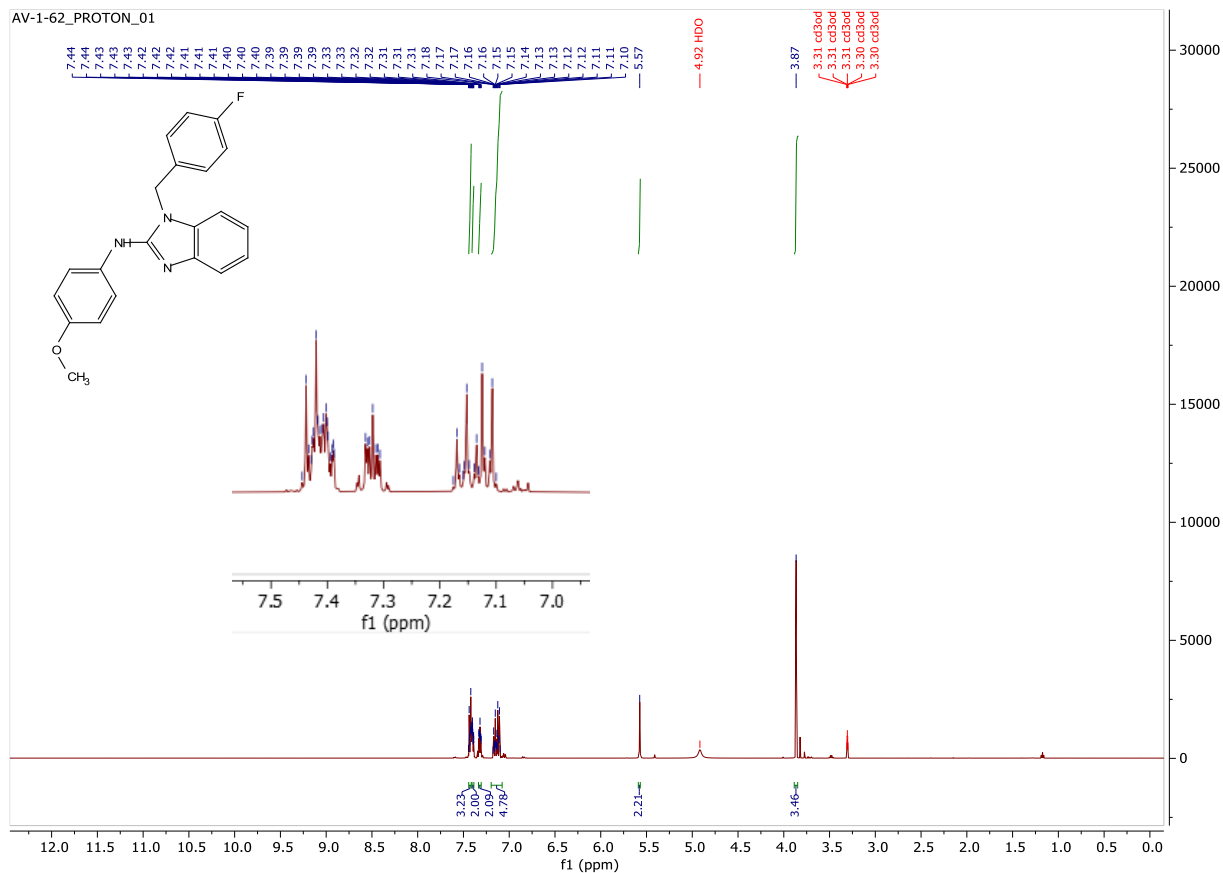


Figure 3.37 Compound 3-3 ^1H NMR (500 MHz, Methanol- d_4).

Compound 3-3 ^{13}C NMR (126 MHz, Methanol- d_4)

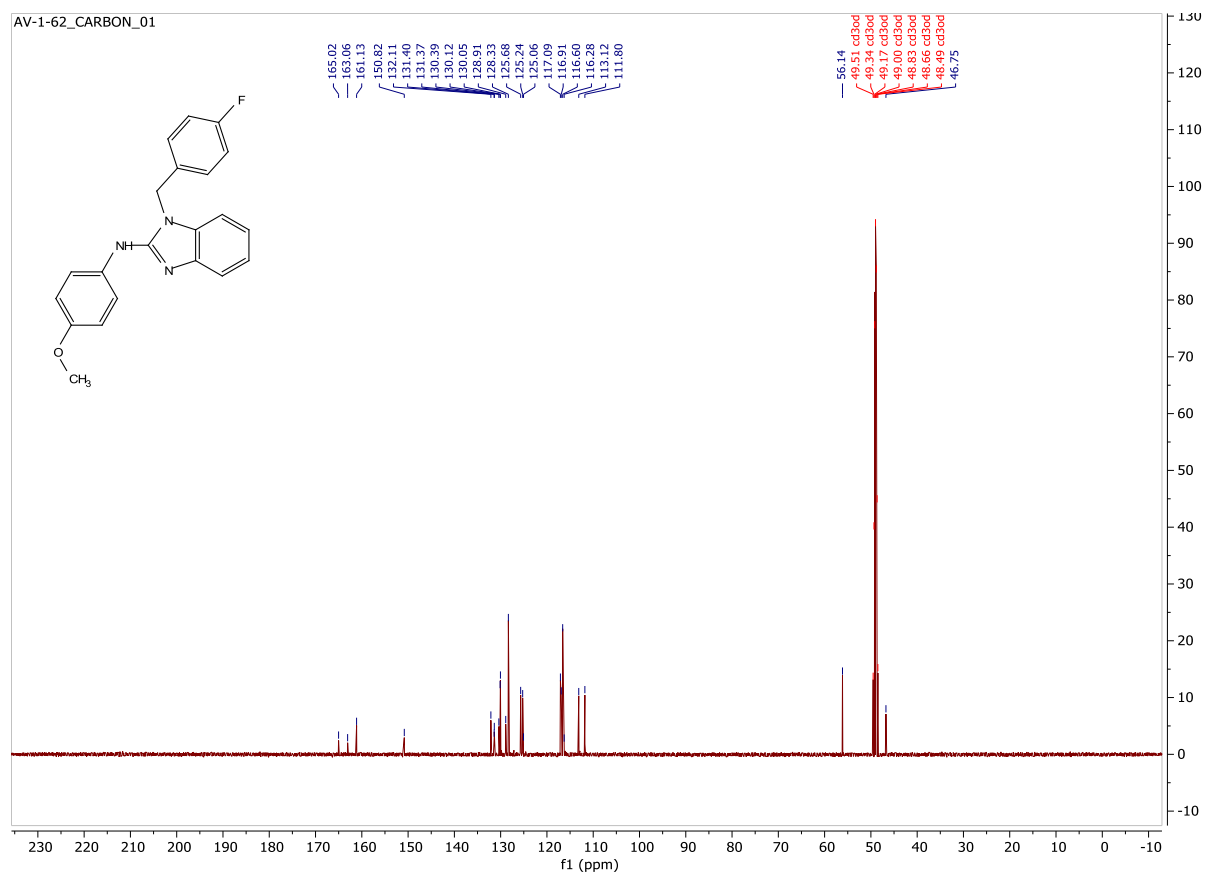


Figure 3.38 Compound 3-3 ^{13}C NMR (126 MHz, Methanol- d_4).

3.16 ^1H and ^{13}C Spectrum of Compound 3-4

Compound 3-4 ^1H NMR (500 MHz, Methanol- d_4)

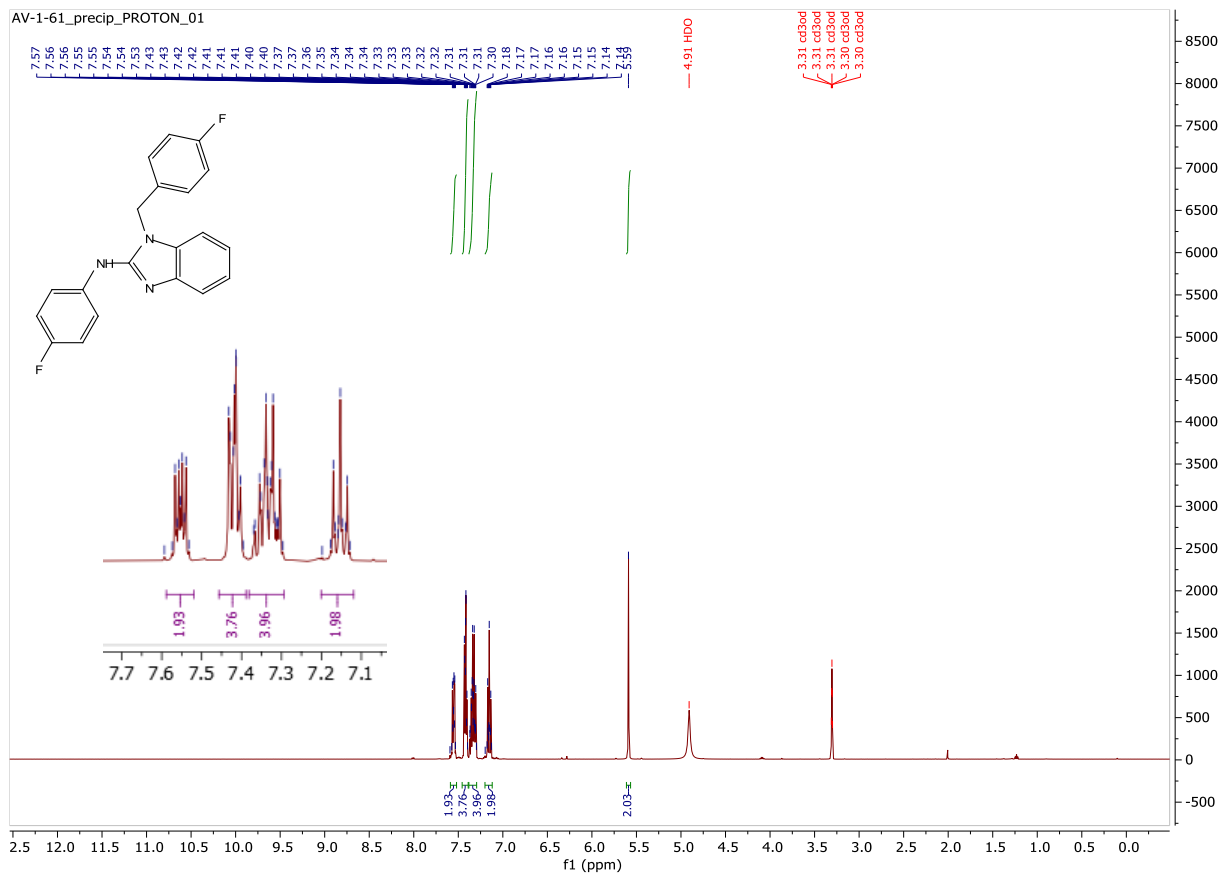


Figure 3.39 Compound 3-4 ^1H NMR (500 MHz, Methanol- d_4).

Compound 3-4 ^{13}C NMR (126 MHz, Methanol- d_4)

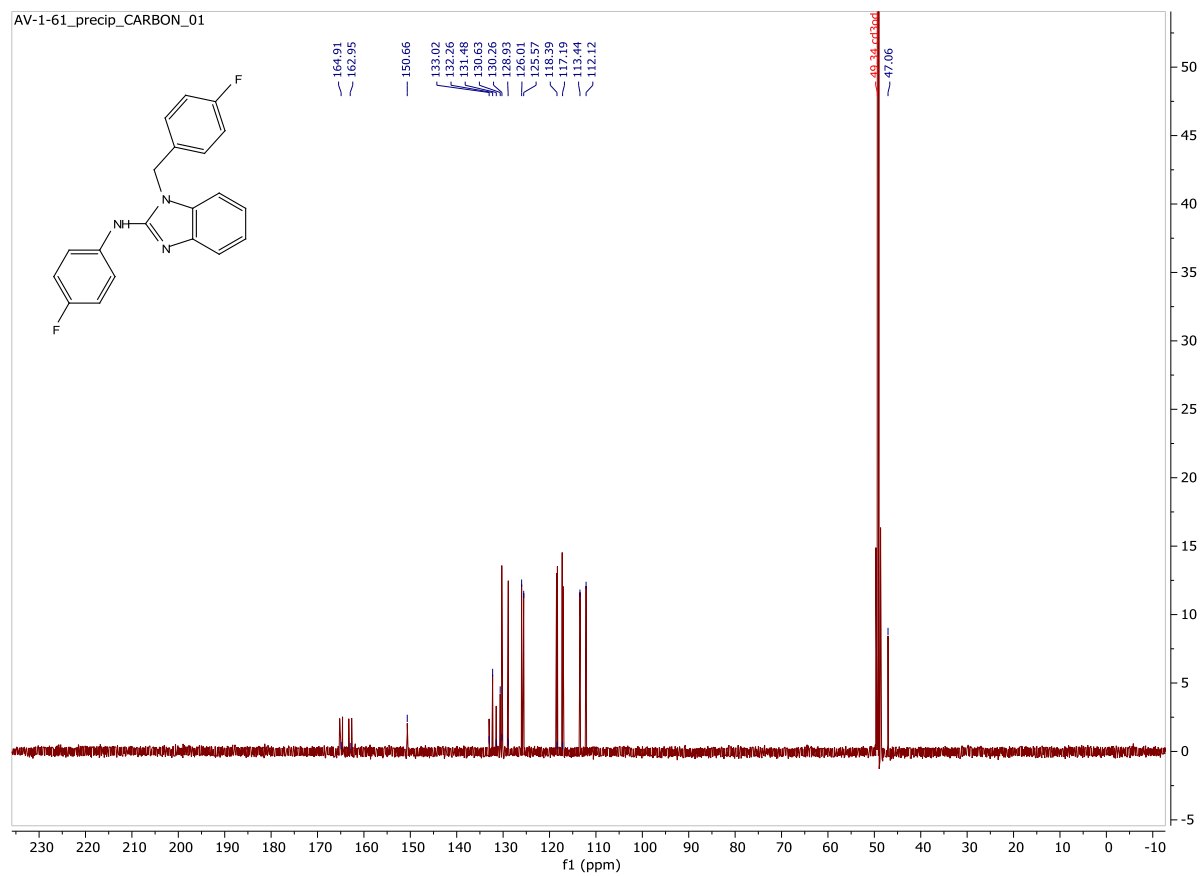


Figure 3.40 Compound 3-4 ^{13}C NMR (126 MHz, Methanol- d_4).

3.17 ^1H and ^{13}C Spectrum of Compound 3-5

Compound 3-5 ^1H NMR (500 MHz, Methanol- d_4)

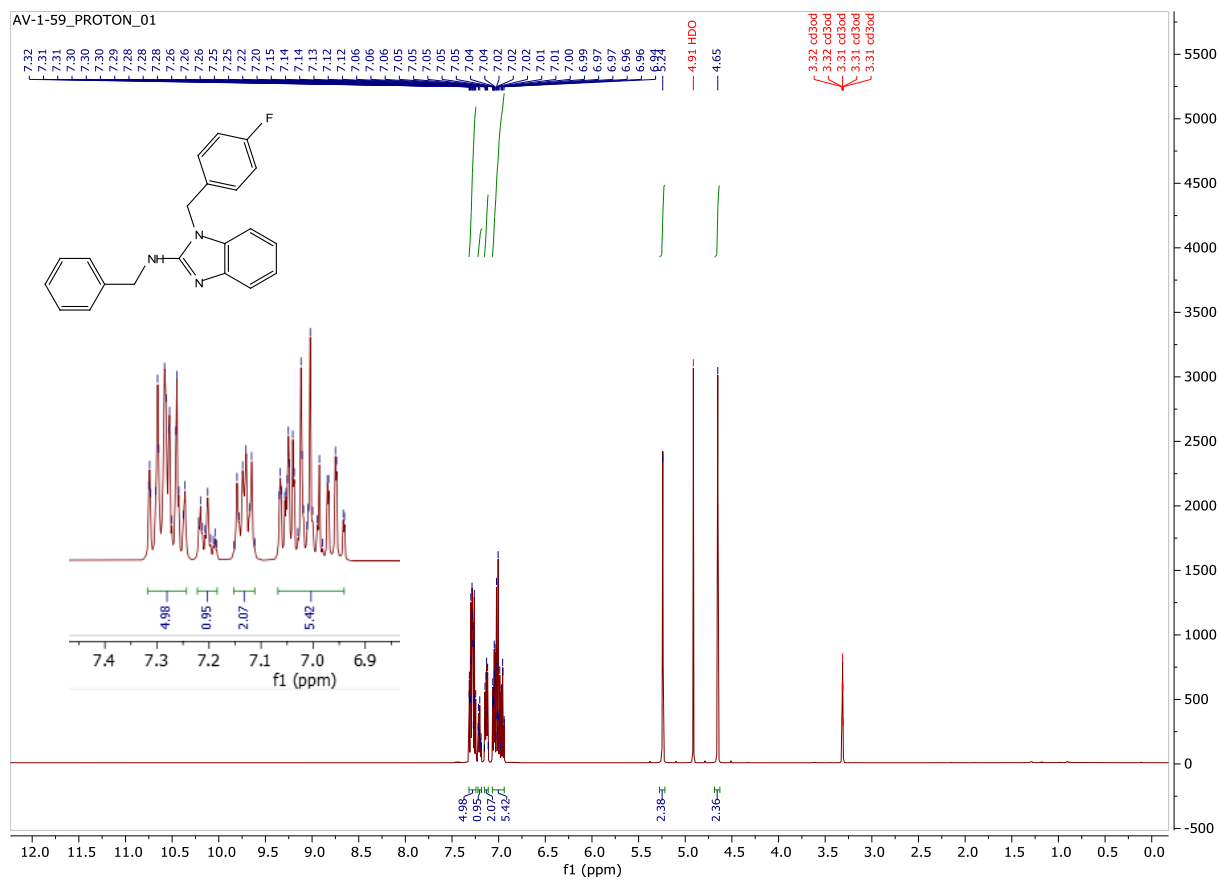


Figure 3.41 Compound 3-5 ^1H NMR (500 MHz, Methanol- d_4).

Compound 3-5 ^{13}C NMR (126 MHz, Methanol- d_4)

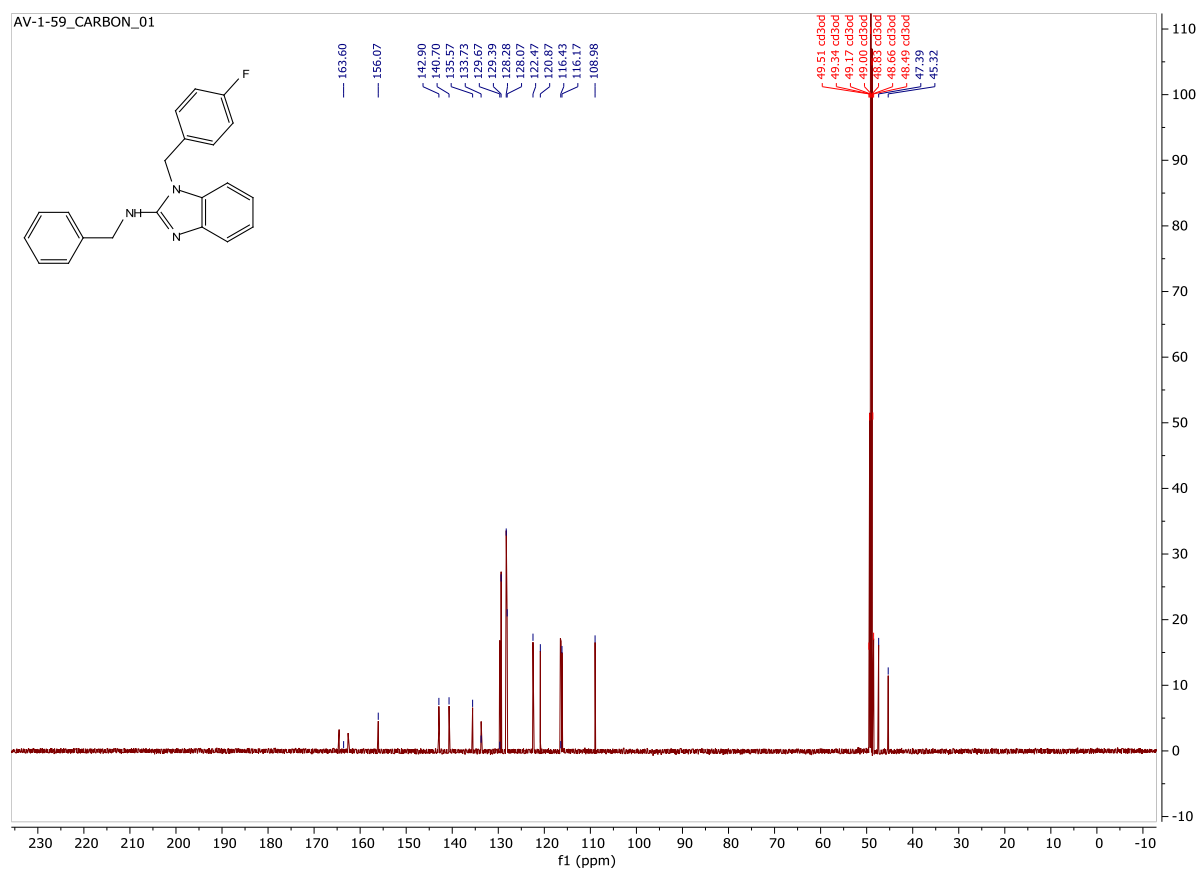


Figure 3.42 Compound 3-5 ^{13}C NMR (126 MHz, Methanol- d_4).

3.18 ¹H and ¹³C Spectrum of Compound 3-6

Compound 3-6 ¹H NMR (500 MHz, Chloroform-*d*)

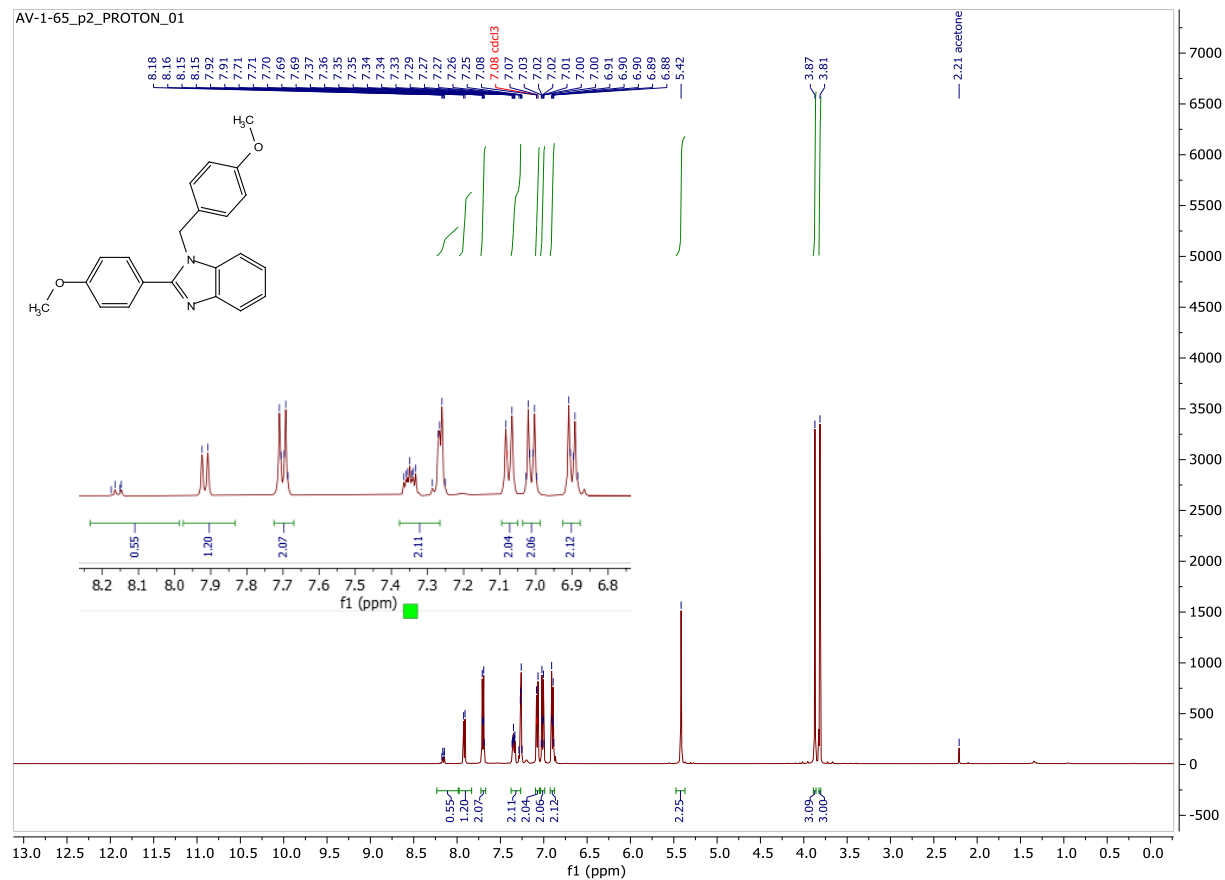


Figure 3.43 Compound 3-6 ¹H NMR (500 MHz, Chloroform-*d*).

Compound 3-6 ^{13}C NMR (126 MHz, Chloroform-*d*)

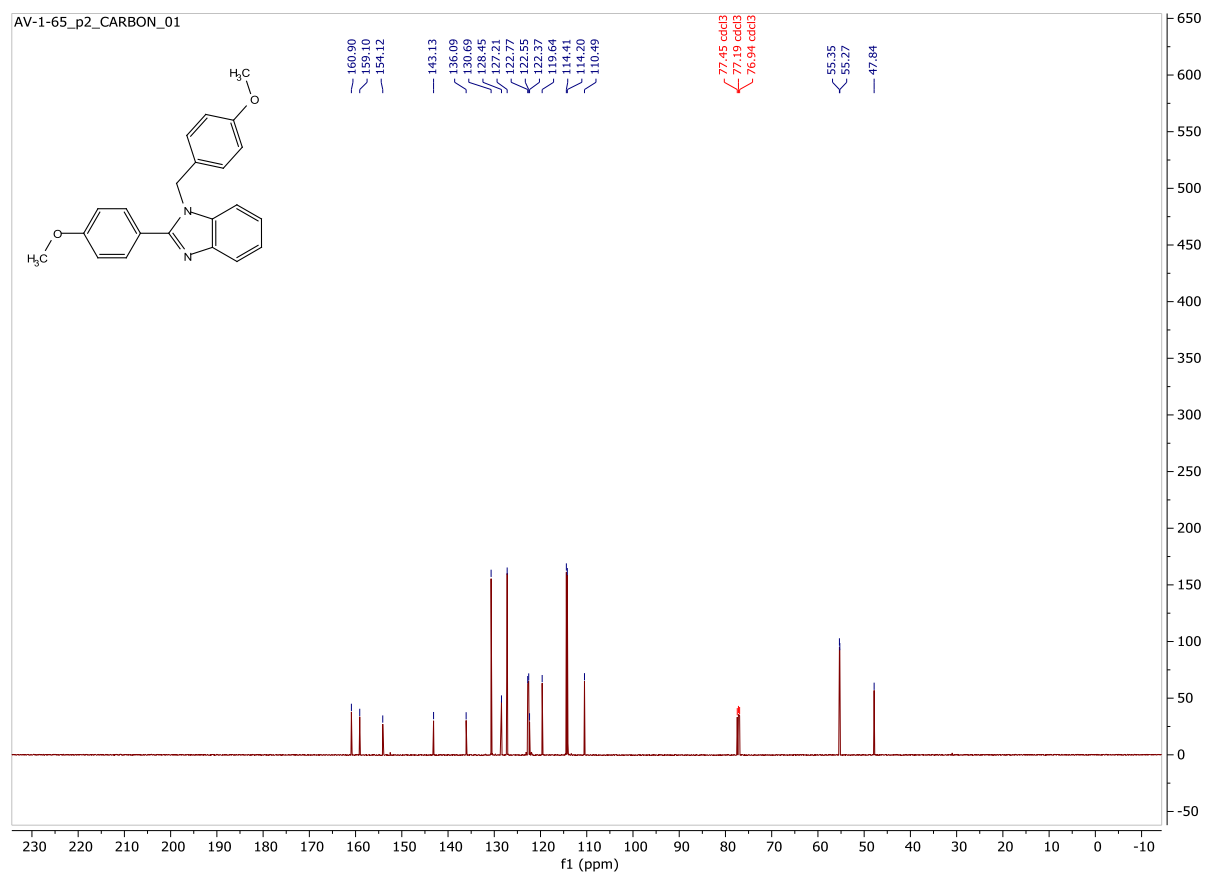


Figure 3.44 Compound 3-6 ^{13}C NMR (126 MHz, Chloroform-*d*).

3.19 ^1H , ^{13}C , gCOSY, HSQC and HMBC Spectrum of Compound 3-7 (Acyl Astemizole)

Compound 3-7 ^1H NMR (500 MHz, Methanol- d_4)

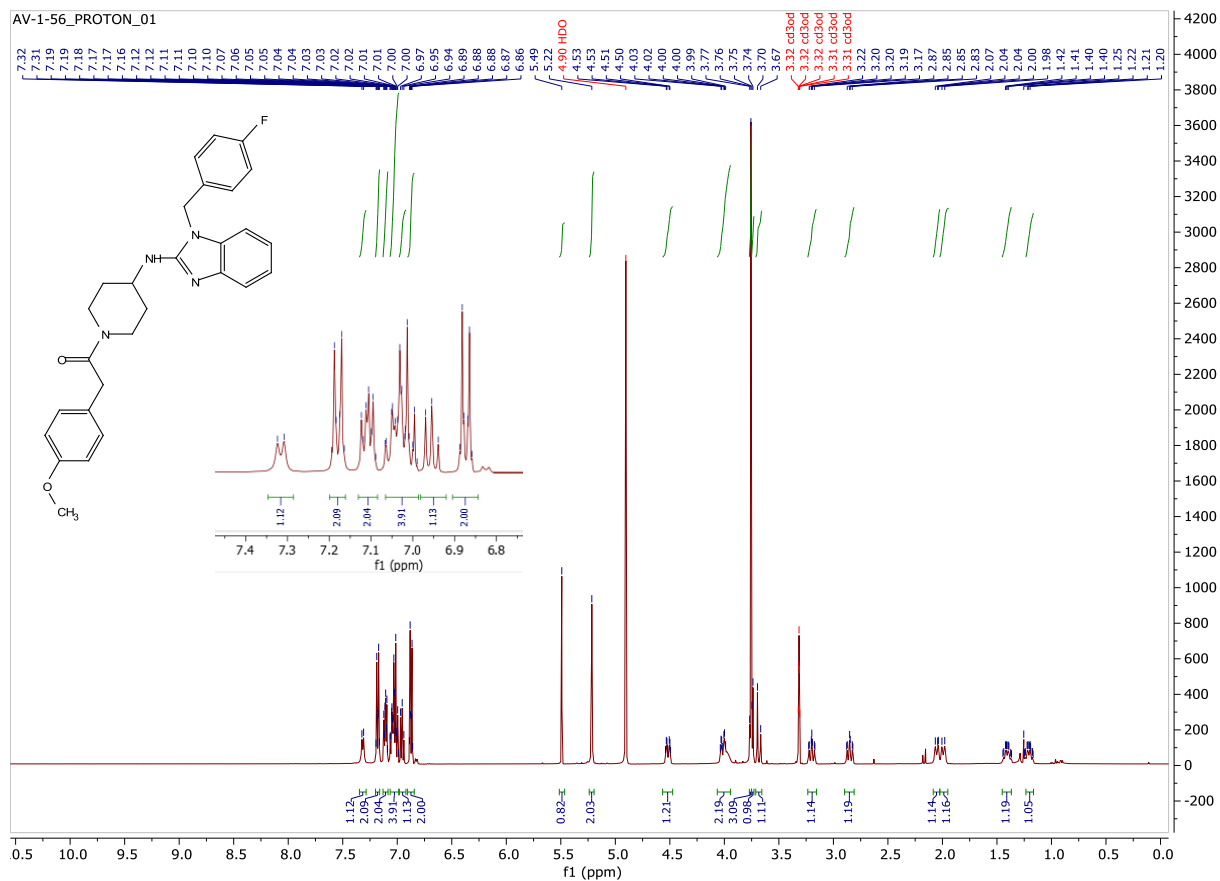


Figure 3.45 Compound 3-7 ^1H NMR (500 MHz, Methanol- d_4).

Compound 3-7 ¹³C NMR (126 MHz, Methanol-d₄)

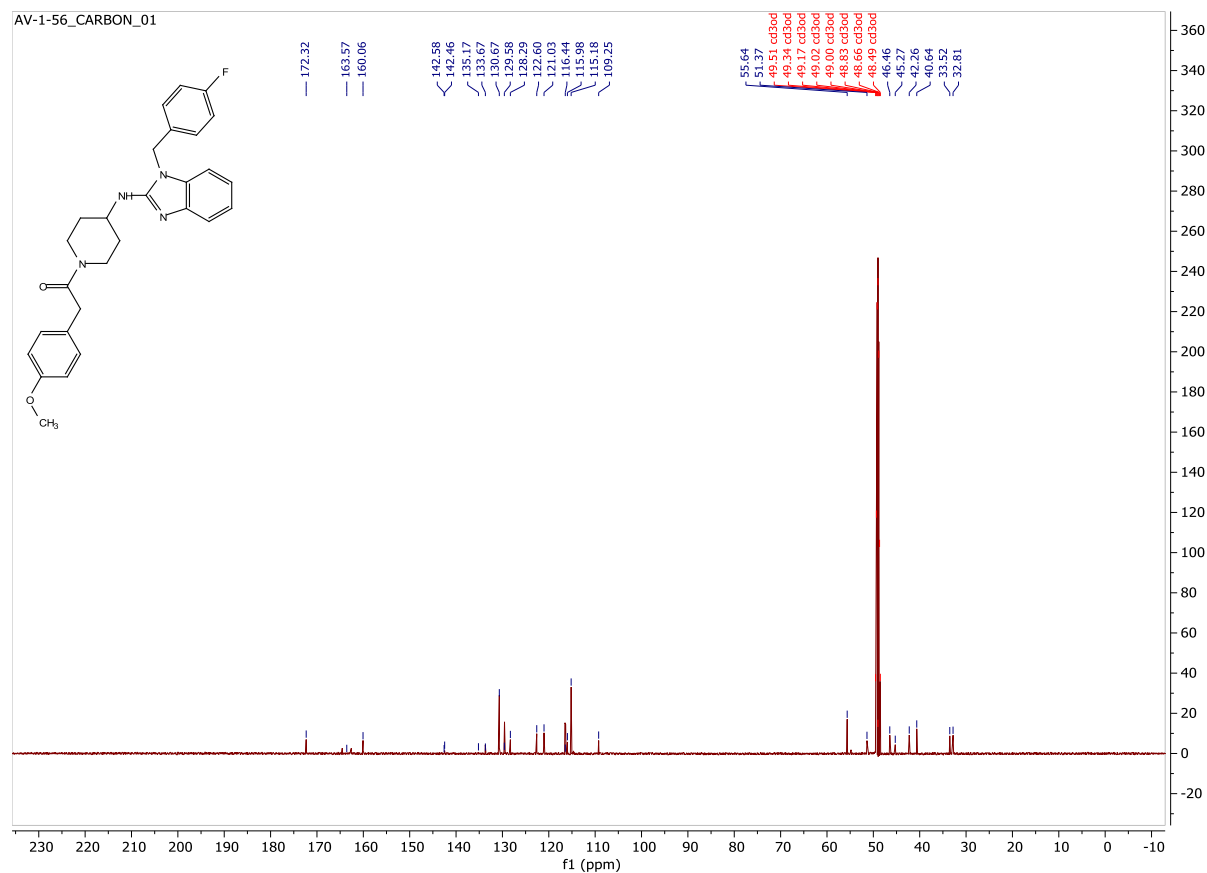


Figure 3.46 Compound 3-7 ¹³C NMR (126 MHz, Methanol-d₄).

Compound 3-7 gCOSY (Methanol-*d*₄)

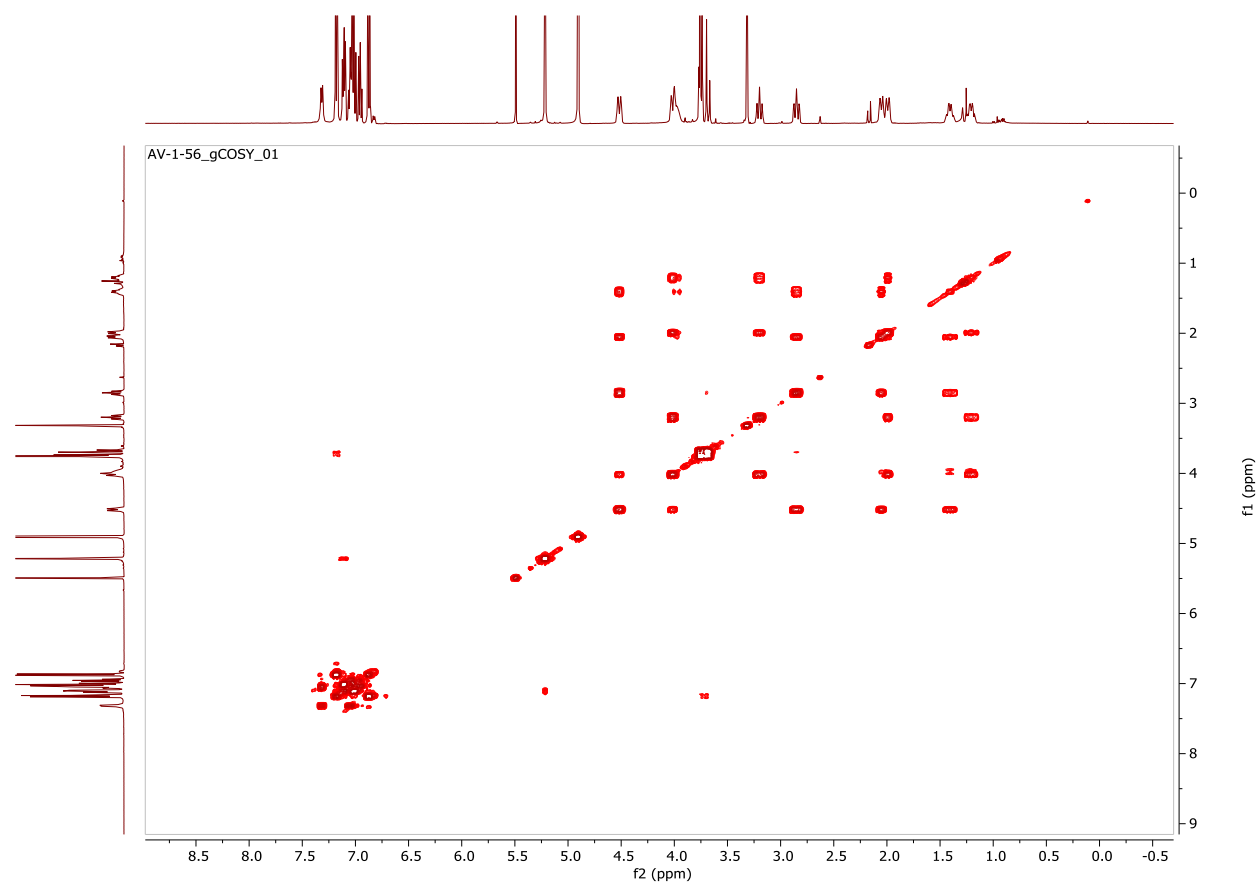


Figure 3.47 Compound 3-7 gCOSY (Methanol-*d*₄).

Compound 3-7 HSQC (Methanol- d_4)

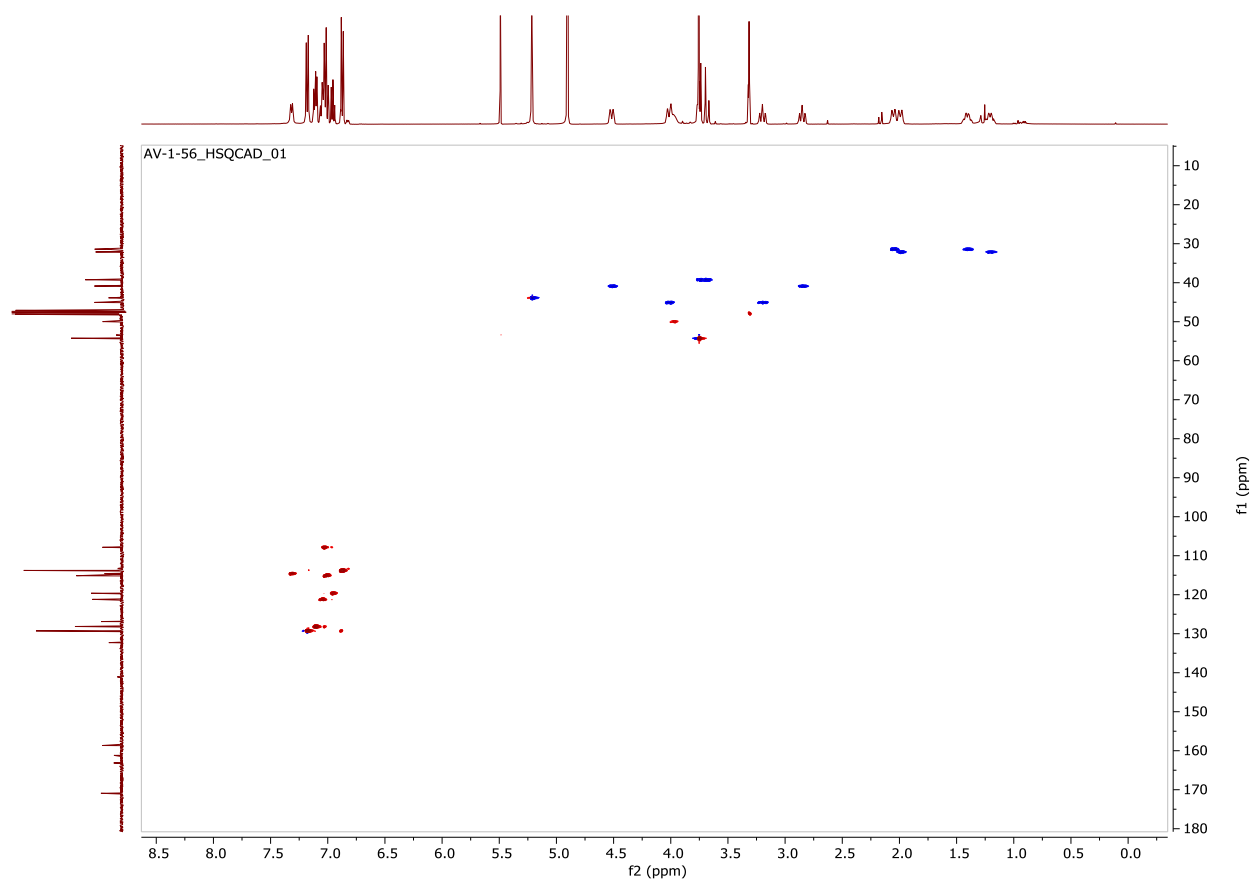


Figure 3.48 Compound 3-7 HSQC (Methanol- d_4).

Compound 3-7 HMBC (Methanol-*d*₄)

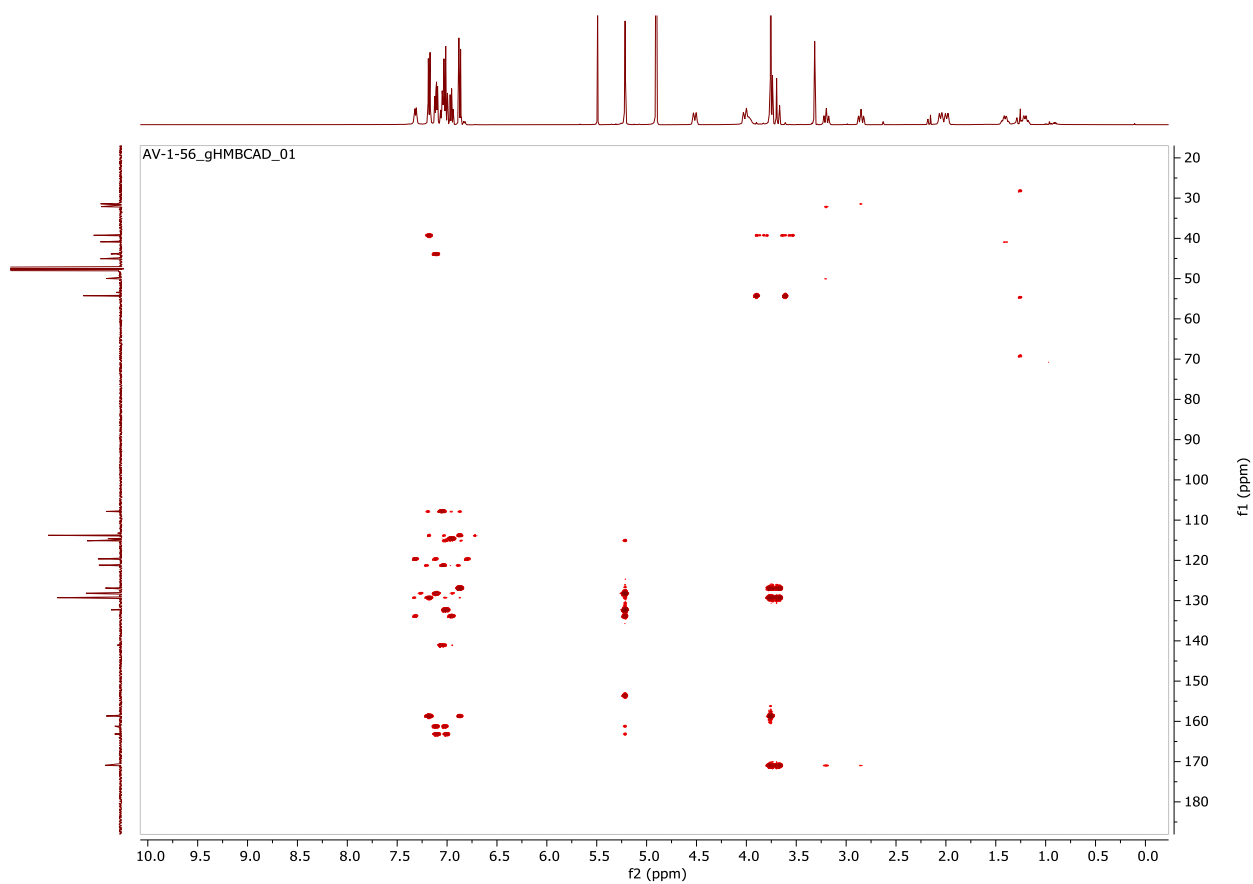


Figure 3.49 Compound 3-7 HMBC (Methanol-*d*₄).

PART II

20S Proteasome Modulation as a Novel Therapeutic for Cancers

CHAPTER FOUR

Identification of a Novel Class of Ruthenium Quinoline Complexes as a Potential Cancer Therapeutic

Reproduced in part from Hou, Z; **Vanecek, A. S.**; Tepe, J. J.; Odom, A. L. Synthesis, Structure, Properties, and Cytotoxicity of a (Quinoline)RuCp⁺ Complex. *Dalton Trans.* **2023**, 52 (3), 721-730 with permission from the Royal Society of Chemistry. <https://doi.org/10.1039/D2DT03484K>.

4.1 Introduction

4.1.1 Transition Metal Complexes as Anticancer Agents

The hallmark discovery of cisplatin by Barnett Rosenberg and coworkers, in the 1960s, revolutionized the anticancer therapeutic landscape.¹ In these studies, it was observed that transition metal complexes, such as platinum and ruthenium complexes, inhibited cell division in bacteria.² Due to the rapid cell division of cancer cells, the application of these compounds toward the treatment of human cancers has been thoroughly investigated.³ The mechanism of cisplatin toxicity has been extensively studied, revealing DNA as a critical target. Cisplatin binds DNA to crosslink DNA strands, thereby inhibiting DNA synthesis, cell division, and resulting in cell death.⁴ While FDA approval of a number of approved anticancer platinum complexes has had a profound effect toward the treatment of many different cancers, cisplatin has shown particular success in the treatment of testicular cancer.^{3,4} Cisplatin-based regimens have shown to result in a cure rate of 90 to 95 percent for testicular cancers.³ While platinum complexes have shown great success as anticancer agents, drug resistance and severe side effects have prompted further cisplatin analogue development and exploration of novel transition metal complexes for use as anticancer agents.^{3,5}

Recently, ruthenium complexes have attracted great attention as anticancer agents.^{6,7} In particular significance to this work, a number of cyclopentadienyl ruthenium (CpRu) and arene ruthenium complexes have shown anticancer activity toward a variety of cancer cells, with some complexes demonstrating toxicity toward cisplatin-resistant cancer cell lines.⁸⁻¹¹ Additionally, some of these compounds have shown increased selectivity toward cancer cells over healthy cells, reducing toxic side effects.^{7,12} Through the investigation and development of a wide range of ruthenium complexes, as one would expect, their cytotoxicity mechanism is highly dependent upon the ligands incorporated. In our own exploration of ruthenium complexes as anticancer agents we chose a quinoline ligand for two reasons, (1) the Tepe and Odom labs have previously identified a novel quinoline scaffold to have activity toward an anticancer target,¹³ and (2) there have been few ruthenium-quinoline complexes reported.

4.1.2 Proteasome Inhibitors as Anticancer Agents

Proteasome inhibitors (i.e. bortezomib, carfilzomib and ixazomib) remain a first-line treatment for certain types of cancers, including multiple myeloma, a hematological malignancy characterized by the abnormal proliferation of plasma cells.^{14,15} Using this treatment strategy, cancer cells die through starvation of resources necessary for cell growth. Extensive alterations in protein expression drive malignant transformation of cancer cells.¹⁶ As cells transform to cancer cells, there are significant upregulations of many proteins, such as those that regulate cell survival and proliferation, cell migration, and metastasis.¹⁶ This altered proteostasis and abnormally high levels of certain proteins found in cancer cells places a high burden on the UPS and other proteostasis machinery. This is to ensure limited resources in the cell, such as amino acids for protein synthesis, are maintained while maintaining cancer cell growth and survival.¹⁷ This oncogenic addition of cancer cells for the UPS has been exemplified in a number of studies, with one study showing that various tumors express high levels of proteasome subunits and have increased proteasome activity.^{18,19} Another study has demonstrated that cancer cells are highly sensitive to proteasome inhibition.¹⁵

The mechanism of action of these proteasome inhibitors is through formation of a covalent bond with an electrophilic moiety of the inhibitor (i.e. boronic acid warhead of bortezomib) and the threonine active residue of the proteasome's proteolytic sites. This induces a staggering halt to protein degradation that leads to the toxic accumulation of proteins and a fatal amino acid shortage which prevents any further protein synthesis, and ultimately leads to cell death.²⁰ While these proteasome inhibitors and other treatments listed above have made great strides to increase patient survival, treatment regimens are challenging and unfortunately a majority of patients experience relapse. Furthermore, after relapse many patients gain a resistance and do not respond to bortezomib treatment a second time.²¹ While the mechanism of bortezomib resistance requires further study, a mutation of the gene which encodes for the $\beta 5$ subunit (i.e. CT-L proteolytic site) has shown to result in its overexpression.²² In addition, mutations to the CT-L proteolytic site of the proteasome have recently been identified in primary cells from a multiple myeloma patient under prolonged bortezomib treatment.^{21,23} A majority of these mutations affected the proteasome inhibitor substrate binding pocket, which could have

significant effects on the ability of the inhibitor to bind and effectively inhibit proteasome activity.²³ As the CT-L site is the binding pocket for bortezomib and the other approved proteasome inhibitors, the modification of the binding site by the mutations may help to explain why the efficacy of the proteasome inhibitors is significantly reduced.²¹ Therefore, it is crucial additional proteasome inhibitors be identified, especially scaffolds with a novel mechanism of action, in the hopes they may be used in the treatment of multiple myeloma in bortezomib resistant patients.

4.1.3 Design of Ruthenium Quinoline Complexes – A Multi-Target Drug?

In 2016, the Odom and Tepe labs, identified a class of quinoline compounds capable of non-covalent inhibition of the 20S proteasome.¹³ Among the compounds, one quinoline (referred to as **Quin1** in this chapter; Figure 4.1) showed a single-digit micromolar potency (half maximal inhibitory concentration, or IC₅₀, of 8.2 ± 1.2 μM) toward inhibition of the 20S proteasome. Incorporation of **Quin1** as a ligand to synthesize a ruthenium complex, therefore offered an intriguing possibility of designing a multi-targeted therapeutic. Multi-targeted drugs are those in which one drug has components that act on multiple biological targets. For example, a ruthenium complex incorporating a P450 enzyme inhibitor was designed for the treatment of breast cancer.²⁴ While further exploration of this therapeutic strategy is needed, these drugs have great potential as anticancer treatments, as combination therapies of multiple individual drugs are widely used in cancer treatment. Of great significance to our work, combination therapies of cisplatin and proteasome inhibitors have shown to have synergistic cytotoxic effects.^{25,26}

To explore whether a multi-targeted drug could be designed to observe this same synergy between a transition metal complex and a proteasome inhibitor, the complex CpRu(Quin1)⁺ PF₆⁻ (**1**; shown in Figure 4.1) was synthesized by Dr. Zhilin Hou of Dr. Aaron Odom's lab.²⁷ A quinoline inactive for proteasome inhibition (**Quin2**) was also used as a ligand to synthesize CpRu(Quin2)⁺ PF₆⁻ (**2**; shown in Figure 4.1) for exploration of the mechanism of action of the ruthenium quinoline complexes. Herein the biological activities and mechanism of action of the complexes are investigated. Through these studies we aimed to explore whether the ruthenium complex would dissociate in the cell to give a ruthenium derivative species and free quinoline which act

in tandem to induce cytotoxicity through a multi-targeted approach, or whether the ruthenium quinoline complex would remain intact within the cell to induce toxicity.

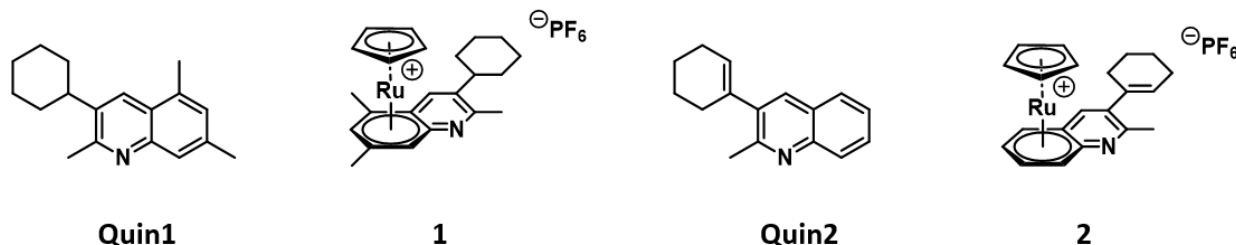


Figure 4.1 Structures of quinolines and CpRu(quinoline)⁺ PF₆⁻ complexes used in the biological studies. Compounds were synthesized by Dr. Zhilin Hou of Dr. Aaron Odom's lab. Synthetic routes and all characterization data can be found in the original manuscript.²⁷

4.2 Results and Discussion

4.2.1 Exploration of 20S Proteasome Inhibitory Activity of Ruthenium Quinoline Complexes

It was previously reported that **Quin1** is a low micromolar noncovalent proteasome inhibitor with a half maximal inhibitory concentration (IC₅₀) equal to $8.2 \pm 1.2 \mu\text{M}$,¹³ therefore we sought to explore how the CpRu quinoline complexes would compare. As previously discussed, the proteasome degrades proteins through the use of three, unique proteolytic sites (β 5, β 2, and β 1) responsible for chymotrypsin-like (CT-L), trypsin-like (T-L), and caspase-like (Casp-L) proteolytic activity, respectively.²⁸ Therefore, the ability of **Quin1** and **Quin2**, along with their respective CpRu⁺ complexes, **1** and **2**, to inhibit each of the proteolytic sites of the proteasome was evaluated using fluorogenic peptide substrates for each site.¹³

Similar to the *in vitro* proteasome activity assay conducted in prior chapters, fluorescent substrate probes conjugated to the fluorophore 7-amino-4-methylcoumarin (AMC), including Suc-LLVY-AMC, Boc-LRR-AMC and Z-LLE-AMC were used. Conversely, to these earlier assays to assess the ability of small molecules to activate 20S proteasome activity, sodium dodecyl sulfate (SDS) is added in this assay to assess the inhibitory activity of small molecules. In these inhibition activity assays, SDS is traditionally added to enhance proteolytic activity of the proteasome prior to treatment with small molecule proteasome inhibitors to ensure the basal activity of the proteasome is great enough to observe inhibition of proteolytic activity.^{29,30} Then as before, the

fluorescence resulting from the release of AMC was then measured over time to quantify 20S proteolytic activity. If an active 20S conformation is present, the fluorescent probe is allowed entry into the proteolytic core of the 20S proteasome where the proteolytic sites degrade the probe, resulting in release of AMC.³¹ Therefore, if the proteasome is inhibited, a decrease in fluorescence compared to the vehicle control is expected.

Consistent with previous results, **Quin1** is inactive for inhibition of T-L site proteolytic activity but inhibited the CT-L and Casp-L site proteolytic activities with single-digit micromolar potencies, or IC₅₀ values (Figures 4.2A and 4.2B; Table 4.1). In addition, the negative control, **Quin2**, was inactive (IC₅₀ > 80.0 μM) and unable to inhibit any of the three proteolytic sites of the 20S proteasome (Figures 4.2C and 4.2D; Table 4.1).

Table 4.1 *In vitro* 20S Proteasome Inhibition Activities.

Compound	CT-L IC ₅₀ (μM)	Casp-L IC ₅₀ (μM)	3 Site IC ₅₀ (μM)
Quin1	8.5 ± 0.3	9.4 ± 0.5	13.7 ± 0.6
Quin2	>80.0	>80.0	>80.0
Ru(Quin1)Cp ⁺ (1)	15.5 ± 1.2	16.0 ± 2.0	29.8 ± 2.0
Ru(Quin2)Cp ⁺ (2)	>80.0	>80.0	>80.0
Ru(NCMe) ₃ Cp ⁺	>80.0	>80.0	>80.0

^a These noncovalent inhibitors are inactive against T-L site.

To compare how complexation with CpRu⁺ would affect activities, ruthenium complexes, **1** and **2**, were tested for their ability to inhibit activity of the proteolytic sites. Ruthenium complex **1** showed approximately a two-fold reduction in the ability to inhibit 20S proteasome activity *in vitro* compared to **Quin1** (Figures 4.2E and 4.2F; Table 4.1). Ruthenium complex **2**, like **Quin2**, was inactive for proteasome inhibition (Figures 4.2G and 4.2H; Table 4.1). A CpRu⁺ control complex, CpRu(NCMe)₃, was also tested for its ability to inhibit 20S proteasome activity. This complex was inactive for proteasome inhibition and demonstrated that the CpRu⁺ portion of these complexes does not impact proteasome activity (Figure 4.6 of Appendix; Table 4.1).

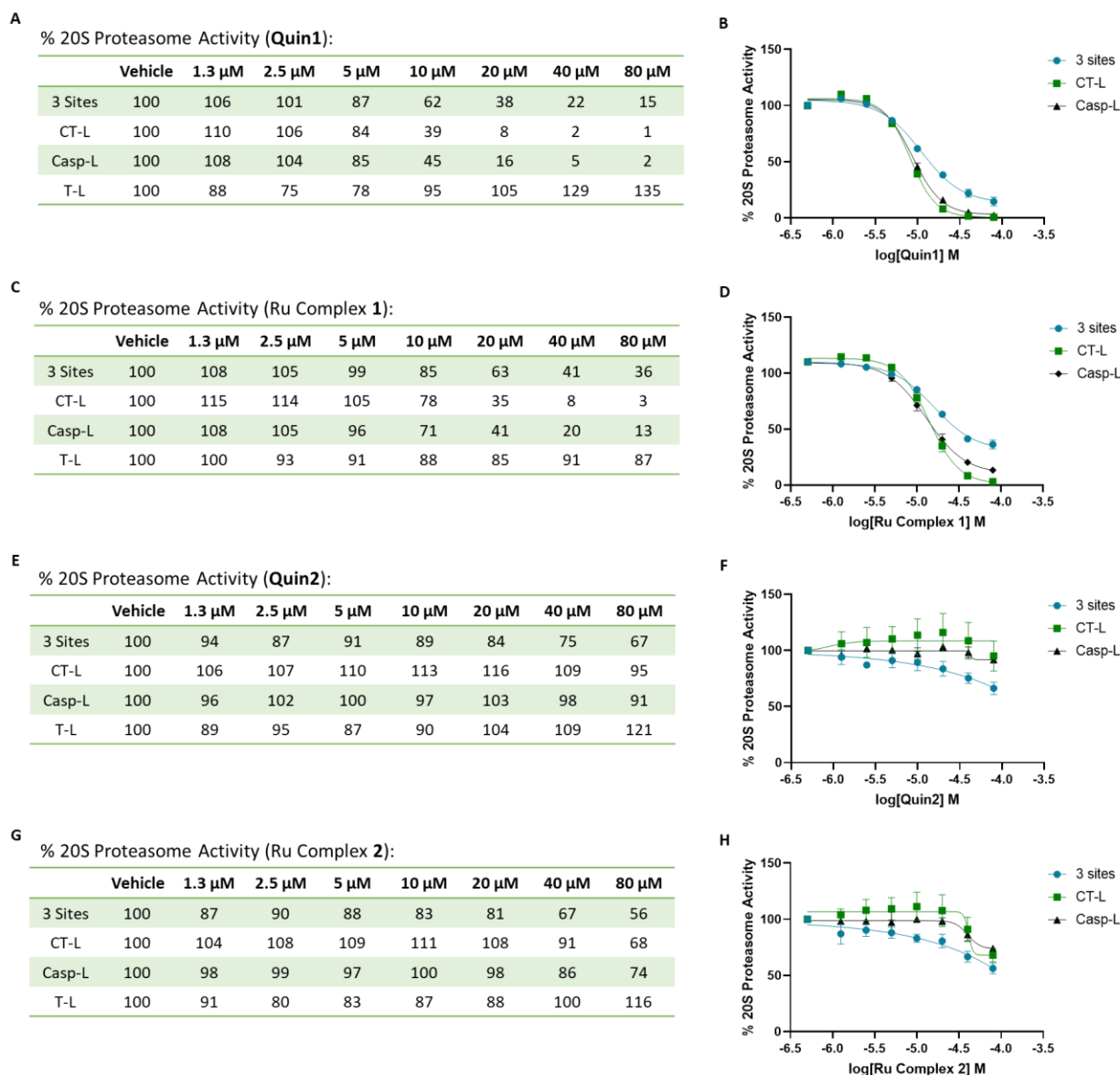
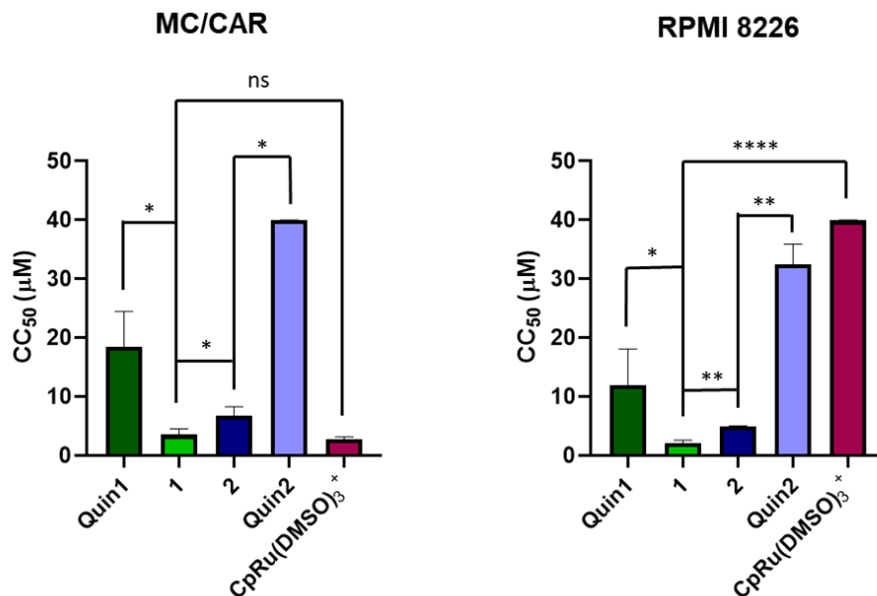


Figure 4.2 *In vitro* 20S proteasome activity assay results. Percent 20S proteasome activity following treatment with **Quin1** (A), Ru complex 1 (C), **Quin2** (E) and Ru complex 2 (G) for each of the three individual proteolytic sites (CT-L, T-L and Casp-L) and the three sites combined (3 sites). Dose-response curve of **Quin1** (B), Ru complex 1 (D), **Quin2** (F) and Ru complex 2 (H) for 20S proteasome-mediated proteolysis of the fluorogenic proteasome substrates. Data for all compounds was collected in triplicate (n=3); error bars denote standard deviation.

4.2.2 Cytotoxicity in Multiple Myeloma Cells

As previously stated, proteasome inhibition is widely used in the treatment of multiple myeloma to induce apoptosis of cancer cells.^{14,15} Additionally, transition metal complexes such as cisplatin, and other ruthenium complexes, are known to inhibit cancer cell growth.^{6,7,32,33} While complexation of the quinoline proteasome inhibitor (**Quin1**) with CpRu⁺ slightly reduced its ability to inhibit proteasome activity *in vitro*, we hypothesized complexation would enhance any cytotoxic effects by the quinoline due to our multi-targeted therapeutic approach.

To test this hypothesis, the cytotoxicity of the quinolines and ruthenium complexes was evaluated in two multiple myeloma cell lines: MC/CAR and RPMI 8226. The cell viability curves for each of the compounds in both cell lines can be found in Figures 4.7 and 4.8 of the Appendix. From these cell viability curves, the concentration of test compound required to reduce cell viability by 50 percent, or CC₅₀ value, was then determined for each compound and is shown in Figure 4.3. The results are generally similar for each of the two distinct cell lines. As expected, the quinoline inactive for proteasome inhibition (**Quin2**) did not show appreciable cytotoxicity. The active proteasome inhibitor **Quin1** demonstrated moderate cytotoxic effects with CC₅₀ values consistent with its IC₅₀ values found in the *in vitro* proteasome activity assays. Both ruthenium complexes **1** and **2** were significantly more cytotoxic than either of the quinoline counterparts, suggesting that their cytotoxicity is not due to the activity of dissociated quinolines.



Compound	MC/CAR CC ₅₀ (μM)	RPMI 8226 CC ₅₀ (μM)
Quin1	19.5 ± 6.0	11.8 ± 6.1
Quin2	>40.0	32.4 ± 3.5
CpRu(DMSO) ₃ ⁺	2.8 ± 0.4	>40.0
Ru(Quin1)Cp ⁺ (1)	3.4 ± 1.0	2.0 ± 0.5
Ru(Quin2)Cp ⁺ (2)	6.8 ± 1.5	5.0 ± 0.1
Bortezomib (BTZ)	<1.3	<1.3

Figure 4.3 Cytotoxicity data (CC₅₀ values) for the quinolines and ruthenium complexes in MC/CAR and RPMI 8226 cells (n=4); Brown-Forsythe and Welch ANOVA with a post hoc Dunnett's T3 test was used to determine statistical significance (ns, not significant, *p ≤ 0.05; **p ≤ 0.01; ***p ≤ 0.001; ****p ≤ 0.0001).

To determine if this enhanced cytotoxicity upon complexation was due to the dissociated CpRu⁺ species, a ruthenium control using DMSO as the ligand, CpRu(DMSO)₃⁺ PF₆⁻, was tested for its cytotoxic effects in both cell lines (Figure 4.3). While CpRu(DMSO)₃⁺ PF₆⁻ was not cytotoxic in the RPMI 8226 cell line at the concentrations tested, its cytotoxicity in MC/CAR cells was comparable to that of both ruthenium complexes **1** and **2**. This suggests that sensitivity to CpRu(DMSO)₃⁺ PF₆⁻ toxicity is cell line specific. In the MC/CAR cell line, all ruthenium complexes had similar cytotoxicity curves with comparable single-digit micromolar CC₅₀ values. However, in the RPMI 8226 cell line, ruthenium toxicity was observed to enhance greatly upon addition of the

quinoline ligands. This supports the notion that ruthenium cytotoxicity is tunable based on the ligand incorporated.

4.2.3 Investigating the Mechanism of Cytotoxicity of the Ruthenium Quinoline Complexes

Further studies to explore the mechanism of cytotoxicity in the RPMI 8226 cell line were conducted. Specifically, we asked whether the complexes remain intact in cell culture to impart their cytotoxic effects. While ruthenium complexes **1** and **2** were significantly more cytotoxic than either of the free quinoline counterparts, a minimal difference in cytotoxicity was observed upon incorporation of the quinoline active or inactive for proteasome inhibition. This suggests that inhibition of the proteasome is likely not the mechanism of cytotoxicity. Furthermore, since both complexes **1** and **2** were significantly more cytotoxic than either of the quinolines or $\text{CpRu}(\text{DMSO})_3^+ \text{PF}_6^-$ we hypothesized that the complexes remain intact in cell culture. As it is expected that the dissociated products of complex **1** would be a derivative of Ru species (shown to be nontoxic in RPMI 8226 cells) and **Quin1**, it is anticipated that the cytotoxicity of **Quin1** and the disassociated products of **1** would be relatively similar. Since this was not what was observed, we sought to explore whether complexes **1** and **2** remained intact in cell culture to elucidate the mechanism of cytotoxicity of the CpRu quinoline complexes.

The incorporation of the quinoline ligands active or inactive for proteasome inhibition presented a novel approach to explore whether ruthenium complexes **1** and **2** remained intact in cell culture. Again, since it is expected that the dissociated products of complex **1** would be $\text{RuCp}(\text{OH}_2)_3^+ \text{PF}_6^-$ and **Quin1**, the cellular proteasome activities of **Quin1** and the dissociated products of **1** should be comparable, as Ru species derivatives, like $\text{CpRu}(\text{DMSO})_3^+ \text{PF}_6^-$, did not inhibit the proteasome *in vitro*.

The ability of **Quin1**, complex **1**, and $\text{CpRu}(\text{DMSO})_3^+$ to inhibit the proteasome in RPMI 8226 cells was investigated using a luminescent peptide substrate of the proteasome. It was observed that **Quin1** (10 μM) resulted in a 43 percent reduction in proteasome activity following a 4-hour treatment, consistent with the *in vitro* IC_{50} value and CC_{50} value in RPMI 8226 cells (Figure 4.4A). Complex **1** and $\text{CpRu}(\text{DMSO})_3^+ \text{PF}_6^-$ did not inhibit the proteasome, ruling out the possibility of proteasome inhibition as the mechanism of cytotoxicity. Furthermore, this suggests that complex **1** remains intact in cell culture at this treatment time, as no proteasome inhibition

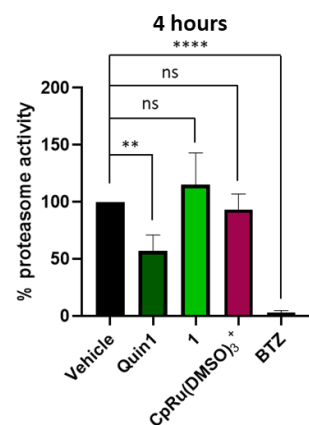
was observed from any liberated **Quin1**. To explore if a longer treatment time would result in decomplexation of **Quin1** from **1**, resulting in proteasome inhibition and cytotoxicity, a lower dose of the test compounds was used to treat the RPMI 8226 cells for 24 hours. In this experiment, **Quin1** (5 μM) resulted in a 36 percent reduction in proteasome activity (Figure 4.4B). As previously observed, treatment with ruthenium complex **1** (3 μM) did not result in proteasome inhibition after correcting for the loss in cell viability over the course of 24 hours. These results provide additional support that cytotoxicity results from the intact $\text{CpRu}(\text{quinoline})^+ \text{PF}_6^-$ complexes in cell culture.

A

Treatment Time – 4 hours

	% Proteasome Activity	% Cell Viability
Vehicle	100	100
Quin1 (10 μ M)	57.0 \pm 14.0	96.7 \pm 3.2
1 (10 μ M)	115.0 \pm 28.1	98.3 \pm 3.5
CpRu(DMSO) ₃ ⁺ (10 μ M)	93.3 \pm 13.7	98.0 \pm 1.7
BTZ (50 nM)	3.0 \pm 1.7	81.0 \pm 11.5

n=3



B

Treatment Time – 24 hours

	% Proteasome Activity	% Cell Viability	% Relative Proteasome Activity per Viable Cells
Vehicle	100	100	100
Quin1 (5 μ M)	56.3 \pm 16.0	87.3 \pm 12.5	64.3 \pm 13.8
1 (3 μ M)	69.3 \pm 17.2	60.3 \pm 12.7	115.0 \pm 20.1
CpRu(DMSO) ₃ ⁺ (3 μ M)	95.7 \pm 13.7	88.7 \pm 10.4	109.0 \pm 22.5
BTZ (3 nM)	22.3 \pm 1.5	94.7 \pm 6.0	23.7 \pm 0.6

n=3

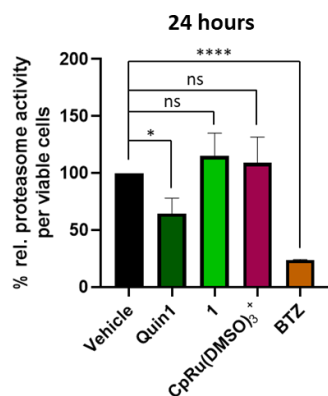


Figure 4.4 Cellular proteasome activity data with corresponding cytotoxicity data in the RPMI 8226 cell line (A) RPMI 8226 cells were treated with vehicle (DMSO), test compound (10 μ M), or proteasome inhibitor, bortezomib (BTZ; 50 nM), for 4 hours. (B) RPMI 8226 cells were treated with vehicle (DMSO), test compound (3 or 5 μ M), or proteasome inhibitor, bortezomib (BTZ; 3 nM), for 24 hours. Proteasome-Glo cell-based (CT-L site) assay was used to measure percent proteasome activity. Cell Titer Glo assay was used to determine the percent cell viability at indicated treatment time. Data for all compounds was collected in triplicate (n=3); error bars denote standard deviation. Relative percent proteasome activity per viable cells was calculated by dividing percent proteasome activity by percent cell viability. One-way ANOVA with a post hoc Sidak test was used to determine statistical significance (ns, not significant, *p \leq 0.05; **p \leq 0.01; ***p \leq 0.001; ****p \leq 0.0001).

After eliminating proteasome inhibition as the mechanism of cytotoxicity, we sought to explore the possible mechanisms by which ruthenium causes toxicity. While the mechanism of anticancer ruthenium complexes varies greatly based on the ligands used, it is generally accepted that their toxicity is related to their ability to bind and modify DNA.^{34,35} Furthermore, it is well known that platinum complexes, like cisplatin, cause toxicity through crosslinking of DNA.^{4,36}

Therefore, as a first look at a ruthenium toxicity mechanism, we investigated the ability of complexes **1**, **2**, and ruthenium derivative species, $\text{CpRu}(\text{NCMe})_3^+ \text{PF}_6^-$ to crosslink DNA in an *in vitro* assay using a denaturing DNA gel (Figure 4.5). In this assay, single stranded DNA was treated with vehicle, ruthenium complex, or cisplatin. Since the vector DNA used was 4361 base pairs in size, if crosslinking resulted upon drug treatment it would be evident by DNA bands greater in size than 4361 base pairs. Compared to the positive control, cisplatin, no DNA crosslinking was observed for the three ruthenium complexes. However, while no crosslinking was observed, the experiment does not rule out other DNA-related toxicity mechanisms, such as DNA damage that does not lead to crosslinking.

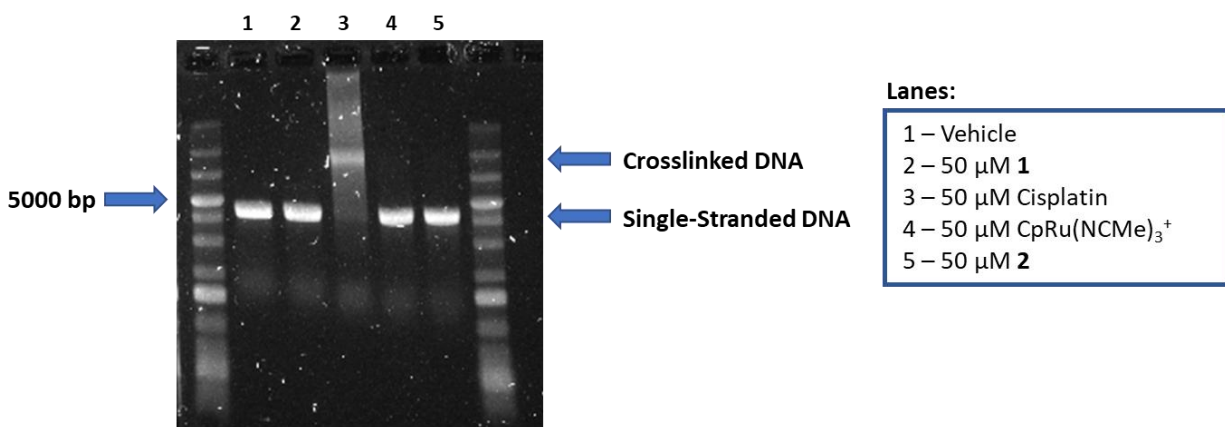


Figure 4.5 DNA crosslinking assay results demonstrate that treatment of single-stranded DNA (4361 bp) with the ruthenium complexes does not result in crosslinking of DNA, as observed for positive control cisplatin.

4.3 Conclusion

Our findings demonstrate that CpRu(quinoline)⁺ PF₆⁻ complexes **1** and **2** were cytotoxic toward two multiple myeloma cell lines with single-digit micromolar potencies. While the CpRu(quinoline)⁺ PF₆⁻ complexes did not inhibit the proteasome in cell culture, addition of the quinoline ligand active for proteasome inhibition did allow for a novel route to explore the mechanism of toxicity by the ruthenium complexes. While the mechanism of cytotoxicity of the quinoline ruthenium complexes is currently unknown, the biological data provides strong support that the intact complex is responsible for the cytotoxic effects in cell culture. Furthermore, our findings suggest that the cytotoxicity is based on the ligand incorporated. While no cytotoxicity was observed in RPMI 8226 cells when DMSO was used as the ligand in the control CpRu(DMSO)₃⁺ PF₆⁻ complex, incorporation of either of the quinolines as the ligand greatly enhanced the cytotoxic effects of the complexes. In all, it was concluded that the CpRu(quinoline)⁺ PF₆⁻ complexes **1** and **2** constitute a novel class of cytotoxic metal complexes and provide an intriguing avenue to explore for anticancer therapeutics.

4.4 Experimental

4.4.1 Methods

Multiple myeloma cell culture. RPMI 8226 and MC/CAR cells were obtained from ATCC (Manassas, VA, USA). RPMI 8226 cells were maintained in RPMI-1640 medium supplemented with 10% fetal bovine serum (FBS) and 1% penicillin/streptomycin at 37 °C and 5% CO₂. MC/CAR cells were maintained in Iscove's Modified Dulbecco's Medium (IMDM) supplemented with 20% FBS and 1% penicillin/streptomycin. DMSO was used as the vehicle control at a 0.5% final concentration for cell culture experiments.

20S proteasome inhibition activity assay. The activity assay was conducted in a 100 μL reaction volume in a black, clear-bottom 96-well plate. Purified human 20S proteasome (1 nM) and stock solutions of the test compound were added to final concentrations ranging from 1.25-80 μM in assay buffer (50 mM Tris-HCl buffer, 0.03% SDS, pH 7.5), and the plate was incubated at 37 °C for 15 min. The fluorogenic substrates (Suc-LLVY-AMC, Boc-LRR-AMC, and Z-LLE-AMC) were added to a final concentration of 50 μM for Suc-LLVY-AMC and Z-LLE-AMC, and a final concentration of

100 μ M for Boc-LRR-AMC. Fluorescence was measured at 37 °C on a SpectraMax M5e spectrometer taking kinetic readings every 1 min for 30 min (380/460 nm).

Cell viability assay. MC/CAR cells (5,000/well) were seeded in a white, opaque 96-well plate in 100 μ L of medium indicated above. RPMI 8226 cells (25,000/well) were seeded in a white, opaque 96-well plate in 100 μ L of medium indicated above. Drug stock solutions were made in 100% DMSO-d₆ or 9:1 water/ DMSO-d₆. The cells were then treated with the test compound at concentrations ranging from 1.25-40 μ M (0.5% DMSO-d₆ final concentration) for 72 hours at 37 °C and 5% CO₂. For samples in 100% DMSO-d₆, a total volume of 0.5 μ L drug stock was added; for samples in 9:1 water/DMSO-d₆, a total volume of 5 μ L drug stock was added. Cells were equilibrated to room temperature and CellTiter-Glo (Promega) solution (100 μ L) was added and incubated with shaking for 2 minutes at room temperature. Assay plate was then allowed to equilibrate for 10 more minutes at room temperature and luminescence readings were taken on a SpectraMax M5e spectrometer. Statistical analyses were performed with GraphPad Prism 8.1; Brown-Forsythe and Welch ANOVA with a post hoc Dunnett's T3 test was used for multiple comparisons of group means (ns, not significant, *p \leq 0.05; **p \leq 0.01; ***p \leq 0.001; ****p \leq 0.0001).

Cellular proteasome activity assay. RPMI 8226 cells (10,000/well) were seeded in a white, clear-bottom 96-well plate in 100 μ L of RPMI-1640 Medium supplemented with 10% FBS and 1% penicillin/streptomycin. **Short (4 hour) treatment time:** The cells were then treated with DMSO, test compound (10 μ M), or BTZ (50 nM); 0.5% final DMSO concentration for 4 hours at 37 °C and 5% CO₂. **Long (24 hour) treatment time:** The cells were treated with DMSO, test compound (3 or 5 μ M), or BTZ (3 nM) for 24 hours. Cells were equilibrated to room temperature and Proteasome-Glo (CT-L site; Promega) solution (100 μ L) was added and incubated with shaking for 12 minutes at room temperature. A Cell Titer Glo viability assay was run in parallel to determine the percent cell viability at this treatment time. To an identical plate, CellTiter-Glo (Promega) solution (100 μ L) was added and incubated with shaking for 2 minutes at room temperature. The assay plate was then allowed to equilibrate for 10 more minutes at room temperature. Luminescence readings were taken on a SpectraMax M5e. Statistical analyses were performed with GraphPad

Prism 8.1; One-way ANOVA with a post hoc Sidak test was used for multiple comparisons of group means (ns, not significant, * $p \leq 0.05$; ** $p \leq 0.01$; *** $p \leq 0.001$; **** $p \leq 0.0001$).

DNA crosslinking assay. Plasmid pBR322 was linearized with *EcoR1* for 1 h at 37 °C. Linearized DNA (250 mg) was incubated with DMSO or drug (50 μ M) for 16 h at 37 °C. An alkaline agarose gel was prepared using 20 mL of buffer (50 mM NaCl, 2 mM EDTA pH 8.0) and 0.2 g of agarose. The suspension was heated in a microwave for 45 seconds to dissolve, then 2 μ L of GelGreen stain was added. The gel was poured and allowed to cool at room temperature and then soaked in alkaline running buffer (25 mL of 2 N NaOH, 2 mL of 0.5 M EDTA in 1 L of H₂O) for 1 h. The samples were then loaded into the wells with loading dye (5 μ L) and the gel was run at 4 °C for 1.5 h. Gel was visualized on an Azure Biosystems Imager (green LED/orange filter).

REFERENCES

- (1) Rosenberg, B.; Van Camp, L.; Krigas, T. Inhibition of Cell Division in Escherichia Coli by Electrolysis Products from a Platinum Electrode. *Nature* **1965**, *205* (4972), 698–699.
- (2) Rosenberg, B.; Renshaw, E.; Vancamp, L.; Hartwick, J.; Drobnik, J. Platinum-Induced Filamentous Growth in Escherichia Coli. *Journal of Bacteriology* **1967**, *93* (2), 716–721.
- (3) Ghosh, S. Cisplatin: The First Metal Based Anticancer Drug. *Bioorganic Chemistry* **2019**, *88*, 102925.
- (4) Dasari, S.; Bernard Tchounwou, P. Cisplatin in Cancer Therapy: Molecular Mechanisms of Action. *European Journal of Pharmacology* **2014**, *740*, 364–378.
- (5) Cvitkovic, E. Cumulative Toxicities from Cisplatin Therapy and Current Cytoprotective Measures. *Cancer Treatment Reviews* **1998**, *24* (4), 265–281.
- (6) Antonarakis, E. S.; Emadi, A. Ruthenium-Based Chemotherapeutics: Are They Ready for Prime Time? *Cancer Chemotherapy and Pharmacology* **2010**, *66* (1), 1–9.
- (7) Lee, S. Y.; Kim, C. Y.; Nam, T.-G. Ruthenium Complexes as Anticancer Agents: A Brief History and Perspectives. *Drug Design, Development and Therapy* **2020**, *14*, 5375–5392.
- (8) Kumar, P.; Mondal, I.; Kulshreshtha, R.; Patra, A. K. Development of Novel Ruthenium(II)–Arene Complexes Displaying Potent Anticancer Effects in Glioblastoma Cells. *Dalton Transactions* **2020**, *49* (38), 13294–13310.
- (9) Wang, H.; Wei, J.; Jiang, H.; Zhang, Y.; Jiang, C.; Ma, X. Design, Synthesis and Pharmacological Evaluation of Three Novel Dehydroabietyl Piperazine Dithiocarbamate Ruthenium (II) Polypyridyl Complexes as Potential Antitumor Agents: DNA Damage, Cell Cycle Arrest and Apoptosis Induction. *Molecules* **2021**, *26* (5), 1453.
- (10) Murray, B. S.; Babak, M. V.; Hartinger, C. G.; Dyson, P. J. The Development of RAPTA Compounds for the Treatment of Tumors. *Coordination Chemistry Reviews* **2016**, *306*, 86–114.
- (11) Teixeira-Guedes, C.; Brás, A. R.; Teixeira, R. G.; Valente, A.; Preto, A. Ruthenium(II)–Cyclopentadienyl-Derived Complexes as New Emerging Anti-Colorectal Cancer Drugs. *Pharmaceutics* **2022**, *14* (6), 1293.
- (12) Tian, M.; Li, J.; Zhang, S.; Guo, L.; He, X.; Kong, D.; Zhang, H.; Liu, Z. Half-Sandwich Ruthenium(II) Complexes Containing N^N-Chelated Imino-Pyridyl Ligands That Are Selectively Toxic to Cancer Cells. *Chemical Communications* **2017**, *53* (95), 12810–12813.
- (13) McDaniel, T.; Lansdell, T.; Dissanayake, A.; Azevedo, L.; Claes, J.; Odom, A.; Tepe, J. Substituted Quinolines as Noncovalent Proteasome Inhibitors. *Bioorganic & Medicinal Chemistry* **2016**, *24* (11), 2441–2450.

- (14) Richardson, P. G.; Xie, W.; Mitsiades, C.; Chanan-Khan, A. A.; Lonial, S.; Hassoun, H.; Avigan, D. E.; Oaklander, A. L.; Kuter, D. J.; Wen, P. Y.; Kesari, S.; Briemberg, H. R.; Schlossman, R. L.; Munshi, N. C.; Heffner, L. T.; Doss, D.; Esseltine, D.-L.; Weller, E.; Anderson, K. C.; Amato, A. A. Single-Agent Bortezomib in Previously Untreated Multiple Myeloma: Efficacy, Characterization of Peripheral Neuropathy, and Molecular Correlations With Response and Neuropathy. *Journal of Clinical Oncology* **2009**, *27* (21), 3518–3525.
- (15) Adams, J.; Kauffman, M. Development of the Proteasome Inhibitor Velcade™ (Bortezomib). *Cancer Investigation* **2004**, *22* (2), 304–311.
- (16) Pessoa, J.; Martins, M.; Casimiro, S.; Pérez-Plasencia, C.; Shoshan-Barmatz, V. Editorial: Altered Expression of Proteins in Cancer: Function and Potential Therapeutic Targets. *Frontiers in Oncology* **2022**, *12*, 1–6.
- (17) Tsvetkov, P.; Adler, J.; Myers, N.; Biran, A.; Reuven, N.; Shaul, Y. Oncogenic Addiction to High 26S Proteasome Level. *Cell Death & Disease* **2018**, *9* (7), 1–14.
- (18) Arlt, A.; Bauer, I.; Schafmayer, C.; Tepel, J.; Mürköster, S. S.; Brosch, M.; Röder, C.; Kalthoff, H.; Hampe, J.; Moyer, M. P.; Fölsch, U. R.; Schäfer, H. Increased Proteasome Subunit Protein Expression and Proteasome Activity in Colon Cancer Relate to an Enhanced Activation of Nuclear Factor E2-Related Factor 2 (Nrf2). *Oncogene* **2009**, *28* (45), 3983–3996.
- (19) Chen, L.; Madura, K. Increased Proteasome Activity, Ubiquitin-Conjugating Enzymes, and EEF1A Translation Factor Detected in Breast Cancer Tissue. *Cancer Research* **2005**, *65* (13), 5599–5606.
- (20) Suraweera, A.; Münch, C.; Hanssum, A.; Bertolotti, A. Failure of Amino Acid Homeostasis Causes Cell Death Following Proteasome Inhibition. *Molecular Cell* **2012**, *48* (2), 242–253.
- (21) Allmeroth, K.; Horn, M.; Kroef, V.; Miethe, S.; Müller, R.-U.; Denzel, M. S. Bortezomib Resistance Mutations in PSMB5 Determine Response to Second-Generation Proteasome Inhibitors in Multiple Myeloma. *Leukemia* **2021**, *35* (3), 887–892.
- (22) Oerlemans, R.; Franke, N. E.; Assaraf, Y. G.; Cloos, J.; van Zantwijk, I.; Berkers, C. R.; Scheffer, G. L.; Debipersad, K.; Vojtekova, K.; Lemos, C.; van der Heijden, J. W.; Ylstra, B.; Peters, G. J.; Kaspers, G. L.; Dijkmans, B. A. C.; Scheper, R. J.; Jansen, G. Molecular Basis of Bortezomib Resistance: Proteasome Subunit B5 (PSMB5) Gene Mutation and Overexpression of PSMB5 Protein. *Blood* **2008**, *112* (6), 2489–2499.
- (23) Barrio, S.; Stühmer, T.; Da-Viá, M.; Barrio-Garcia, C.; Lehnert, N.; Besse, A.; Cuenca, I.; Garitano-Trojaola, A.; Fink, S.; Leich, E.; Chatterjee, M.; Driessen, C.; Martinez-Lopez, J.; Rosenwald, A.; Beckmann, R.; Bargou, R. C.; Braggio, E.; Stewart, A. K.; Raab, M. S.; Einsele, H.; Kortüm, K. M. Spectrum and Functional Validation of PSMB5 Mutations in Multiple Myeloma. *Leukemia* **2019**, *33* (2), 447–456.
- (24) Golbaghi, G.; Castonguay, A. Rationally Designed Ruthenium Complexes for Breast Cancer Therapy. *Molecules* **2020**, *25* (2), 265.

- (25) Konac, E.; Varol, N.; Kiliccioğlu, I.; Bilen, C. Y. Synergistic Effects of Cisplatin and Proteasome Inhibitor Bortezomib on Human Bladder Cancer Cells. *Oncology Letters* **2015**, *10* (1), 560–564.
- (26) Zhang, Z.; Zhang, S.; Lin, B.; Wang, Q.; Nie, X.; Shi, Y. Combined Treatment of Marizomib and Cisplatin Modulates Cervical Cancer Growth and Invasion and Enhances Antitumor Potential in Vitro and in Vivo. *Frontiers in Oncology* **2022**, *12*, 974573.
- (27) Hou, Z.; Vanecek, A. S.; Tepe, J. J.; Odom, A. L. Synthesis, Structure, Properties, and Cytotoxicity of a (Quinoline)RuCp⁺ Complex. *Dalton Transactions* **2023**, *52* (3), 721–730.
- (28) Finley, D.; Chen, X.; Walters, K. J. Gates, Channels, and Switches: Elements of the Proteasome Machine. *Trends in Biochemical Sciences* **2016**, *41* (1), 77–93.
- (29) Tanaka, K.; Yoshimura, T.; Kumatori, A.; Ichihara, A.; Ikai, A.; Nishigai, M.; Kameyama, K.; Takagi, T. Proteasomes (Multi-Protease Complexes) as 20S Ring-Shaped Particles in a Variety of Eukaryotic Cells. *The Journal of Biological Chemistry* **1988**, *263* (31), 16209–16217.
- (30) Tanaka, K.; Yoshimura, T.; Ichihara, A. Role of Substrate in Reversible Activation of Proteasomes (Multi-Protease Complexes) by Sodium Dodecyl Sulfate. *Journal of Biochemistry* **1989**, *106* (3), 495–500.
- (31) Gaczynska, M.; Osmulski, P. A. Characterization of Noncompetitive Regulators of Proteasome Activity. In *Methods in Enzymology; Ubiquitin and Protein Degradation, Part A*; Academic Press, 2005; Vol. 398, pp 425–438.
- (32) Rosenberg, B.; Vancamp, L.; Trosko, J. E.; Mansour, V. H. Platinum Compounds: A New Class of Potent Antitumor Agents. *Nature* **1969**, *222* (5191), 385–386.
- (33) Ndagi, U.; Mhlongo, N.; Soliman, M. E. Metal Complexes in Cancer Therapy – an Update from Drug Design Perspective. *Drug Design, Development and Therapy* **2017**, *11*, 599–616.
- (34) Frühauf, S.; Zeller, W. J. New Platinum, Titanium, and Ruthenium Complexes with Different Patterns of DNA Damage in Rat Ovarian Tumor Cells. *Cancer Research* **1991**, *51* (11), 2943–2948.
- (35) Gallori, E.; Vettori, C.; Alessio, E.; Vilchez, F. G.; Vilaplana, R.; Orioli, P.; Casini, A.; Messori, L. DNA as a Possible Target for Antitumor Ruthenium(III) Complexes: A Spectroscopic and Molecular Biology Study of the Interactions of Two Representative Antineoplastic Ruthenium(III) Complexes with DNA. *Archives of Biochemistry and Biophysics* **2000**, *376* (1), 156–162.
- (36) Johnstone, T. C.; Suntharalingam, K.; Lippard, S. J. The Next Generation of Platinum Drugs: Targeted Pt(II) Agents, Nanoparticle Delivery, and Pt(IV) Prodrugs. *Chemical Reviews* **2016**, *116* (5), 3436–3486.

APPENDIX

4.1 *In vitro* 20S Proteasome Inhibition Activity Data for CpRu(NCMe)₃⁺

% 20S Proteasome Activity:

	Vehicle	1.3 μM	2.5 μM	5 μM	10 μM	20 μM	40 μM	80 μM
3 Sites	100	97	97	99	98	99	96	93
CT-L	100	98	99	98	100	100	99	87
Casp-L	100	98	98	96	100	98	100	93
T-L	100	92	87	117	102	92	88	74

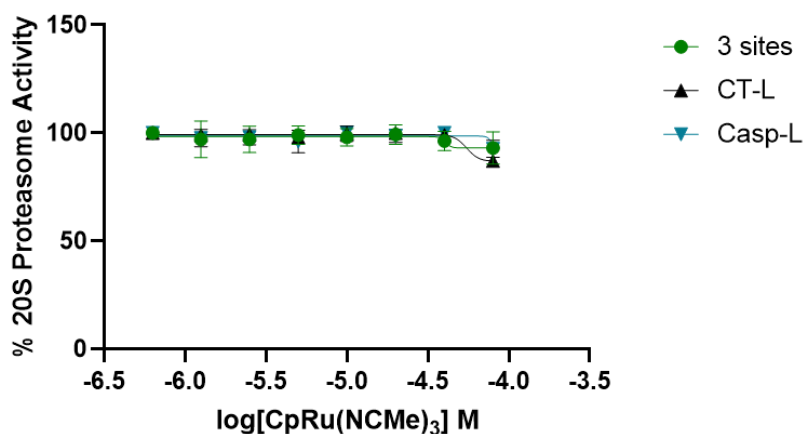


Figure 4.6 *In vitro* 20S proteasome activity assay results. Percent 20S proteasome activity following treatment with CpRu(NCMe)₃⁺ (1.3-80 μM) for each of the three individual proteolytic sites (CT-L, T-L and Casp-L) and the three sites combined (3 sites). Dose-response curve of CpRu(NCMe)₃⁺ for 20S proteasome-mediated proteolysis of the fluorogenic proteasome substrates (n=3); error bars denote standard deviation.

4.2 Cell Viability Curves - MC/CAR Cells

Percent Viable Cells – MC/CAR

	Vehicle	1.3 μM	2.5 μM	5 μM	10 μM	20 μM	40 μM	CC ₅₀ (μM)
Quin1	100	102	95	94	72	51	23	19.5
Ru(Quin1)Cp ⁺ (1)	100	80	61	41	20	6	1	3.4
Ru(Quin2)Cp ⁺ (2)	100	90	75	67	37	5	1	6.8
Quin2	100	124	125	114	98	85	61	>40.0
CpRu(DMSO) ₃ ⁺	100	63	55	41	31	15	4	2.8

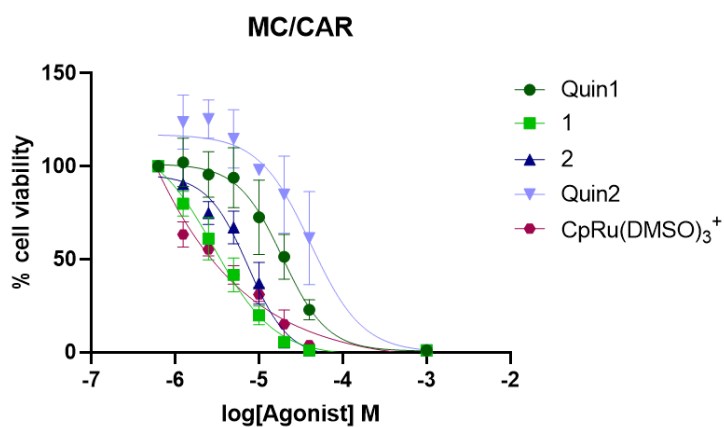


Figure 4.7 Cell viability curves for the quinolines and ruthenium complexes in MC/CAR cells. Data for all compounds was collected in quadruplicate (n=4); error bars denote standard deviation.

4.3 Cell Viability Curves - RPMI 8226 Cells

Percent Viable Cells – RPMI 8226

	Vehicle	1.25 μ M	2.5 μ M	5 μ M	10 μ M	20 μ M	40 μ M	CC ₅₀ (μ M)
Quin1	100	91	88	80	56	33	11	11.8
Ru(Quin1)Cp ⁺ (1)	100	77	38	16	7	3	1	2.0
Ru(Quin2)Cp ⁺ (2)	100	105	96	50	5	1	1	5.0
Quin2	100	121	116	115	107	72	43	32.4
CpRu(DMSO) ₃ ⁺	100	97	103	109	110	106	92	>40.0

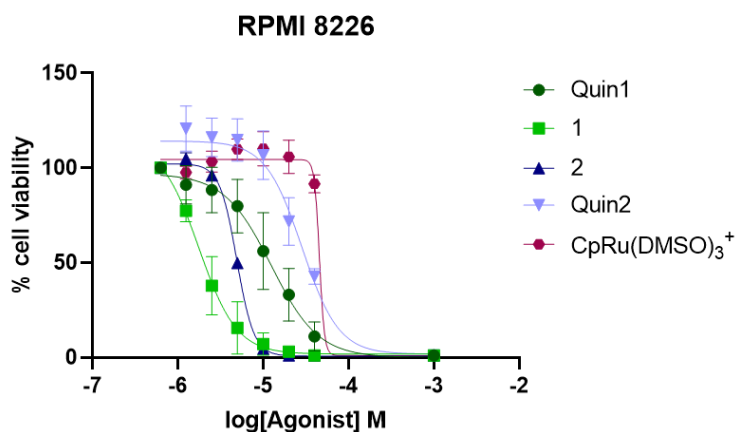


Figure 4.8 Cell viability curves for the quinolines and ruthenium complexes in RPMI 8226 cells. Data for all compounds was collected in quadruplicate (n=4); error bars denote standard deviation.

CHAPTER FIVE

Exploring the Potential of 20S Proteasome Activation as a Novel Cancer Therapeutic Strategy

Reproduced in part with permission from Njomen, E.*; **Vanecek, A.***; Lansdell, T. A.; Yang, Y.-T.; Schall, P. Z.; Harris, C. M.; Bernard, M. P.; Isaac, D.; Alkharabsheh, O.; Al-Janadi, A.; Giletto, M. B.; Ellsworth, E.; Taylor, C.; Tang, T.; Lau, S.; Bailie, M.; Bernard, J. J.; Yuzbasiyan-Gurkan, V.; Tepe, J. J. Small Molecule 20S Proteasome Enhancer Regulates MYC Protein Stability and Exhibits Antitumor Activity in Multiple Myeloma. *Biomedicines* **2022**, *10* (5), 938.

<https://doi.org/10.3390/biomedicines10050938>.

5.1 Introduction

5.1.1 Typical Regulation of Transcription Factor, c-MYC

A transcription factor is a protein that regulates the transcription of genes by producing RNA sequences from DNA. The RNA sequences are then translated into proteins that perform specific functions throughout the cell. The transcription factor, c-MYC, is an important factor responsible for the regulation of many genes involved in cell growth and proliferation, but is believed to regulate almost 15 percent of all genes.¹ c-MYC functions as a transcription factor through binding with MYC Associated Factor X (MAX) to form a heterodimer, which then binds a DNA target sequence to initiate transcription of a number of genes.^{2,3}

Due to the strong growth-promoting and cell proliferative activities, it is essential that c-MYC protein levels are tightly controlled to maintain normal cellular function. Degradation of c-MYC protein through ubiquitin-dependent degradation by the ubiquitin-proteasome system (UPS) has shown to be the most prominent mechanism by which proper c-MYC protein levels are maintained.^{4,5} As previously discussed, ubiquitin-dependent degradation relies on a three-step process involving three different enzymes (E1, E2 and E3 ligases) that results in attachment of a poly-ubiquitin chain to the protein targeted for degradation.⁶ The poly-ubiquitin chain on the protein is then recognized by the 19S cap of the 26S proteasome, which subsequently deubiquitinates, unfolds, and sends the protein into the proteolytic core where it is degraded into small peptide fragments by the 26S proteasome. Furthermore, it has been shown that ubiquitin-dependent degradation of c-MYC relies on a number of post-translational modifications to render it more susceptible to degradation by the UPS. For example, phosphorylation of certain amino acid residues has shown to be required for E3 ligase recognition of c-MYC and subsequent attachment of the poly-ubiquitin chain.^{4,7} This nuanced process allows proper c-MYC protein levels to be maintained in order to prevent uncontrolled cell proliferation as well as other c-MYC-mediated functions.

5.1.2 Dysregulation of c-MYC in Cancer

Dysregulation of c-MYC protein levels has been shown to result from gene mutations of the MYC gene, such as gene amplification.⁸ Additionally, factors that impact c-MYC protein stability can result in an increase in c-MYC protein levels. For example, mutations of E3 ligases

known to be responsible for the ubiquitination of c-MYC protein have been found in a number of cancers.^{4,9} These mutations inactivate their ability to ubiquitinate c-MYC protein, thereby preventing its ubiquitin-dependent degradation by the 26S proteasome.⁹ Furthermore, alteration of cell signaling pathways are known to impact c-MYC protein stability through alteration of its post-translational modifications. For example, phosphorylation of certain amino acid residues of c-MYC renders the protein more susceptible to ubiquitin-dependent degradation by the UPS, and modifications to its phosphorylation state has shown to affect its stability.^{4,10,11}

Dysregulation of c-MYC protein levels and its accumulation can induce its oncogenic transcriptional activity, resulting in the transcription of a number of genes that promote tumor growth and cancer cell proliferation.^{8,12} In fact, overexpression of c-MYC has been found in more than 70 percent of all human cancers, with a high prevalence in hematological cancers, such as acute lymphoblastic leukemia and multiple myeloma.^{13,14} Multiple myeloma is a hematological malignancy characterized by the abnormal proliferation of plasma cells. Current treatments available include immunomodulatory drugs, monoclonal antibodies, chimeric antigen receptor (CAR)T cell therapy, and proteasome inhibitors.¹⁵

Proteasome inhibitors, such as bortezomib, carfilzomib and ixazomib, remain a first-line treatment for many multiple myeloma patients.¹⁶ This strategy aims to kill cancer cells through starvation of resources necessary for cell growth. Extensive alterations in protein expression drive malignant transformation of cancer cells.¹⁷ As cells transform to cancer cells, there are significant upregulations of many proteins, such as those that regulate cell survival and proliferation, cell migration, and metastasis.¹⁷ This altered proteostasis and abnormally high levels of certain proteins found in cancer cells places a high burden on the UPS and other proteostasis machinery. This is to ensure limited resources in the cell, such as amino acids for protein synthesis, are maintained while maintaining cancer cell growth and survival.¹⁸ This oncogenic addition of cancer cells for the UPS has been exemplified in a number of studies, with one study showing that various tumors express high levels of proteasome subunits and have increased proteasome activity.^{19,20} Another study has demonstrated that cancer cells are highly sensitive to proteasome inhibition.²¹

The proteasome inhibitors work through formation of a covalent bond with an electrophilic moiety of the ligand and the threonine active residue of the proteasome's proteolytic sites. This induces a staggering halt to protein degradation that leads to the toxic accumulation of proteins and a fatal amino acid shortage which prevents any further protein synthesis, and ultimately leads to cell death.²² While these proteasome inhibitors and other treatments listed above have made great strides to increase patient survival, treatment regimens are challenging and unfortunately a majority of patients experience relapse. Furthermore, after relapse many patients gain a resistance and do not respond to bortezomib treatment a second time.^{23–25} Due to these reasons, novel approaches to treat this disease are needed.

5.1.3 Pharmacological Targeting of c-MYC

As c-MYC has shown to be dysregulated in around 50 percent of multiple myeloma patients,¹ as well as many other cancers, it is a very highly sought after anticancer target. However, due to its highly disordered 3-D conformation and lack of typical drug binding pockets, it has evaded pharmacological targeting and been deemed an “undruggable” target.²⁶ A variety of strategies to target c-MYC are currently being explored. Strategies to target MYC transcription through the use of small molecule inhibitors of bromodomain and extra-terminal (BET) proteins to suppress MYC expression has been explored.²⁷ Additionally, small molecules to inhibit translation initiation have been studied to target MYC translation.²⁸ Other strategies targeting c-MYC focus on modification of protein-protein interactions necessary for its ability to promote transcription. One method is through the direct inhibition of the MYC-MAX heterodimer using small molecules.^{29–31} By preventing heterodimerization, c-MYC is unable to bind to DNA target sequences and this abrogates c-MYC-mediated transcription.³⁰ Similarly, small molecules that induce MAX-MAX homodimers have been used to indirectly prevent c-MYC-mediated transcription.^{29,32,33} By sequestering MAX from binding to MYC, the MYC-MAX heterodimerization is decreased, which reduces MYC-mediated transcription and oncogenic signaling.^{32,33} Additional strategies to target c-MYC include manipulation of post-translational modifications or alteration of cell signaling pathways to render the protein more vulnerable to proteasome-mediated degradation.^{29,34,35} However, these approaches are still under

development and not yet approved for clinical use. In this chapter, our efforts to develop a novel approach to target c-MYC-driven cancers will be discussed.

5.1.4 Small Molecule Enhancement of 20S Proteasome Activity May Provide Novel Route for Targeting c-MYC

While the UPS is currently being targeted for multiple myeloma treatment, our lab is exploring a novel strategy to target the UPS, which may provide an additional therapeutic approach for the treatment of multiple myeloma. Conversely, to the proteasome inhibition strategy discussed above, activation of the 20S proteasome offers an alternative route to kill cancer cells through enhancement of proteasomal degradation. In this treatment strategy, disordered proteins that are upregulated in malignant transformation, such as c-MYC, which promotes cell proliferation, can be targeted for degradation. It is hypothesized that enhanced degradation of c-MYC could prevent its heterodimerization with MAX, thereby preventing c-MYC-promoted gene transcription and its oncogenic effects (Figure 5.1).

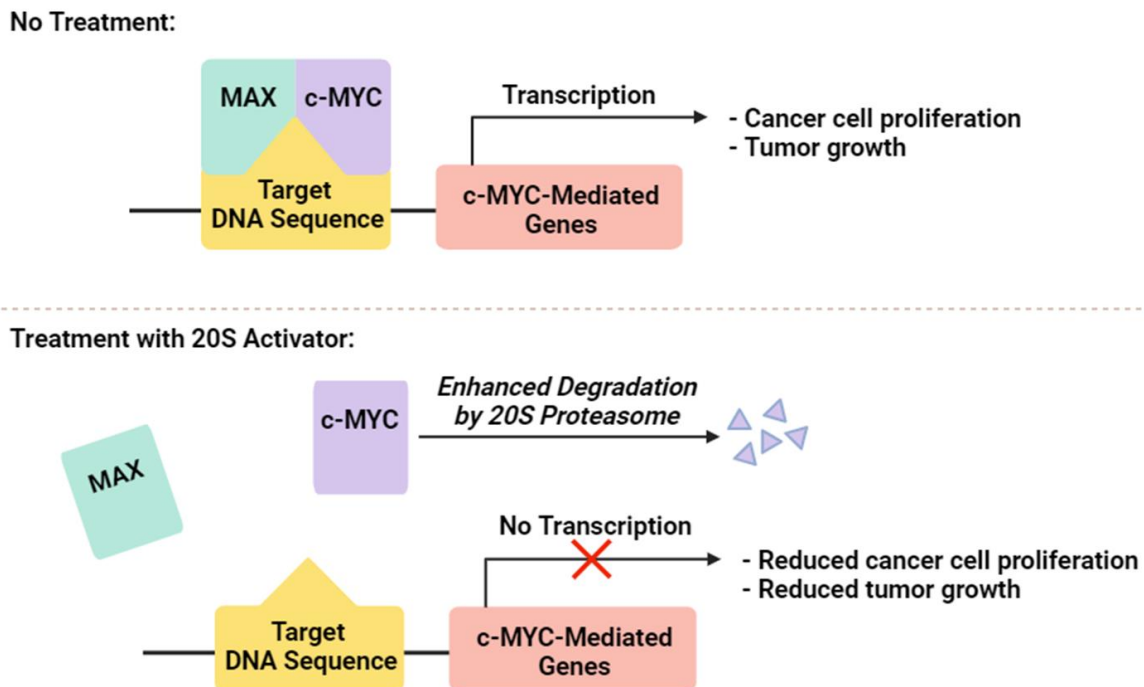


Figure 5.1 Schematic illustration of initial hypothesis that enhanced degradation of c-MYC by the 20S proteasome may inhibit the transcription of c-MYC-mediated genes and reduce cancer cell proliferation and tumor growth.

It is well known that c-MYC protein levels are highly regulated through ubiquitin-dependent protein degradation by the 26S proteasome.^{4,5} However, due to its highly disordered nature, recent studies have shown that c-MYC can be degraded by the 20S proteasome through a ubiquitin-independent pathway.³⁶ In this work, it was demonstrated that c-MYC was degraded by the 20S proteasome in complex with its endogenous protein activator complex, REGy. Furthermore, overexpression of 20S proteasome activator protein, REGy, enhanced c-MYC protein degradation.³⁶ The enhanced degradation of c-MYC subsequently inhibited c-MYC-mediated gene expression and cell proliferation. While these are encouraging results, therapeutic delivery of the activator protein, REGy, would be difficult. As an alternative, we aimed to explore whether a small molecule 20S proteasome activator could reproduce the same anticancer effects as the endogenous protein activator. Herein, we evaluate the therapeutic potential and efficacy of 20S proteasome activator, TCH-165, to reduce cellular c-MYC protein levels and reduce oncogenic signaling events caused by its overexpression and accumulation.

5.2 Results and Discussion

5.2.1 20S Proteasome Activation by TCH-165 Regulates c-MYC Degradation

To begin, the ability of TCH-165 to reduce c-MYC protein levels was evaluated in a number of multiple myeloma cell lines including, RPMI 8226, L363, NCI-H929, MC/CAR, and leukemia cell line, CCRF-CEM. In the experiments analyzed by Western Blot (Figure 5.2A), RPMI 8226 cells were treated with TCH-165 (5 μ M) with or without treatment with proteasome inhibitor, bortezomib (BTZ), for 4 hours. In comparison to the vehicle control, TCH-165 reduced c-MYC protein levels, while BTZ prevented its clearance. Importantly, the effect of TCH-165 was nearly completely abrogated by inhibition of the proteasome's proteolytic activities using BTZ. Similar results were observed in the leukemia cell line, CCRF-CEM. These observations implicate the proteasome as the likely target for the effect of TCH-165 on c-MYC. Although, whether this is due to the direct enhancement of proteasome-mediated degradation of c-MYC, cannot be concluded by these studies. It is possible c-MYC protein levels are reduced by TCH-165 through enhanced proteasome-mediated degradation of another protein involved in regulating c-MYC protein stability; this will be explored later in the chapter.

The efficacy of TCH-165 to reduce c-MYC protein levels in additional multiple myeloma cell lines was also evaluated to ensure the results discussed above were not a unique effect observed for one specific multiple myeloma cell line. Furthermore, it was of interest to determine whether TCH-165 could reduce c-MYC protein levels in a dose-dependent manner. In these experiments, the cells were treated with varying concentrations of TCH-165 or BTZ (5 μ M) for 4 hours. As shown in Figure 5.2B, TCH-165 significantly reduced c-MYC protein levels in a dose-dependent manner in the MC/CAR, L363 and NCI-H929 cell lines. Therefore, it was concluded that TCH-165 has a ubiquitous effect on reducing c-MYC protein levels in multiple myeloma cells.

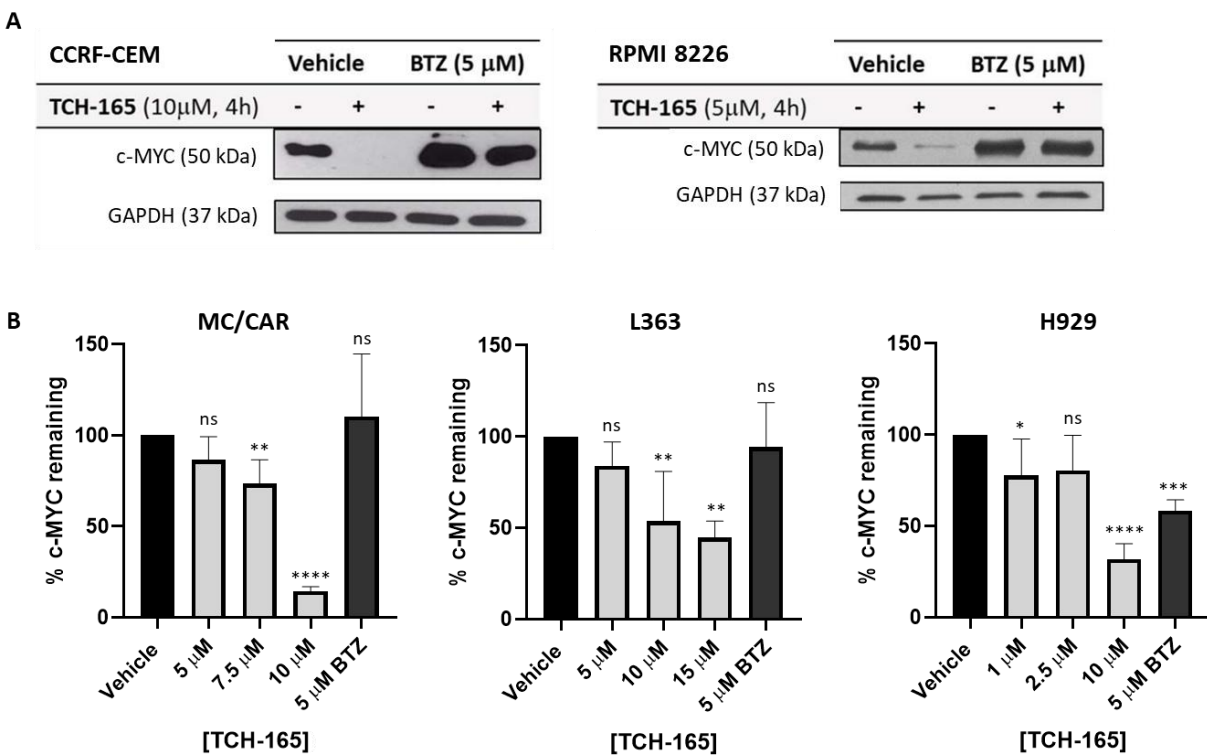


Figure 5.2 TCH-165 reduces c-MYC protein levels in multiple myeloma and leukemia cells. (A) Western blot analysis of the amount of c-MYC in multiple myeloma (RPMI 8226) or leukemia (CCRF-CEM) cells treated with vehicle (DMSO) or TCH-165 (5 or 10 μ M, 4 h) in the presence and absence of proteasome inhibitor BTZ (5 μ M). Western blot analysis by Dr. Evert Njomen. (B) ELISA analysis of the amount of c-MYC in multiple myeloma (MC/CAR, L363, H929) cells treated with vehicle (DMSO), TCH-165 (1-15 μ M, 4 h), or proteasome inhibitor BTZ (5 μ M, 4 h) (n=4); one-way ANOVA (ns, not significant, * $p \leq 0.05$; ** $p \leq 0.01$; *** $p \leq 0.001$; **** $p \leq 0.0001$).

5.2.2 Exploration of the Mechanism of TCH-165-induced Reduction of c-MYC Protein Levels

While treatment with TCH-165 significantly reduced c-MYC protein levels, further work was necessary to determine whether this decrease was due to direct enhancement of proteasome-mediated degradation of c-MYC. To explore this, cellular experiments to determine the half-life of c-MYC with and without TCH-165 treatment were developed. Protein levels are controlled in the cell by regulating the synthesis and degradation of proteins. Since I was interested in whether TCH-165 affects the rate of degradation of c-MYC, an experimental tool to halt protein synthesis was utilized. This would ensure levels of c-MYC are not affected by continued c-MYC synthesis, and that any changes in c-MYC protein levels are due to its degradation. Treatment of cells with cycloheximide stops all protein synthesis in the cell and allows the half-life of a protein to be determined.³⁷ A protein half-life is defined as the time it takes for the concentration of the protein of interest to be reduced by 50 percent. The half-life of c-MYC is known to be a very short (20 to 30 minutes),¹¹ but we aimed to evaluate whether TCH-165 decreased or modified this half-life further. If the mechanism by which TCH-165 reduces c-MYC protein levels is through direct enhancement of 20S proteasome-mediated degradation, it is anticipated that the half-life of c-MYC in the presence of TCH-165 would be decreased.

Initial experiments conducted involved treatment of MC/CAR cells with vehicle or TCH-165 (5 μ M) and then cycloheximide (50 μ g/mL) was immediately added to stop all protein synthesis. Various time points were collected by lysing the cells and the amount of c-MYC remaining at each time point was determined. As shown in Figure 5.3A, there were only very minimal differences in c-MYC protein concentration at any of the time points collected. A time response curve was then constructed (Figure 5.3C) and the half-life for both the vehicle and TCH-165 treated cells was between 10 and 12 minutes. Similar results were observed in an additional cell line (Figure 5.5 of the Appendix). Since c-MYC was degraded so quickly, I hypothesized that a possible explanation for no differences in half-life between the vehicle and TCH-165 could be due to a lack of target engagement by TCH-165 in such a short time. Perhaps TCH-165 had not yet reached the proteasome target in the cells prior to the addition of cycloheximide. Due to the short half-life of c-MYC, a large majority of c-MYC protein was likely degraded before TCH-165

was able to bind to the proteasome and enhance activity, and therefore its effect may not be observed in this assay.

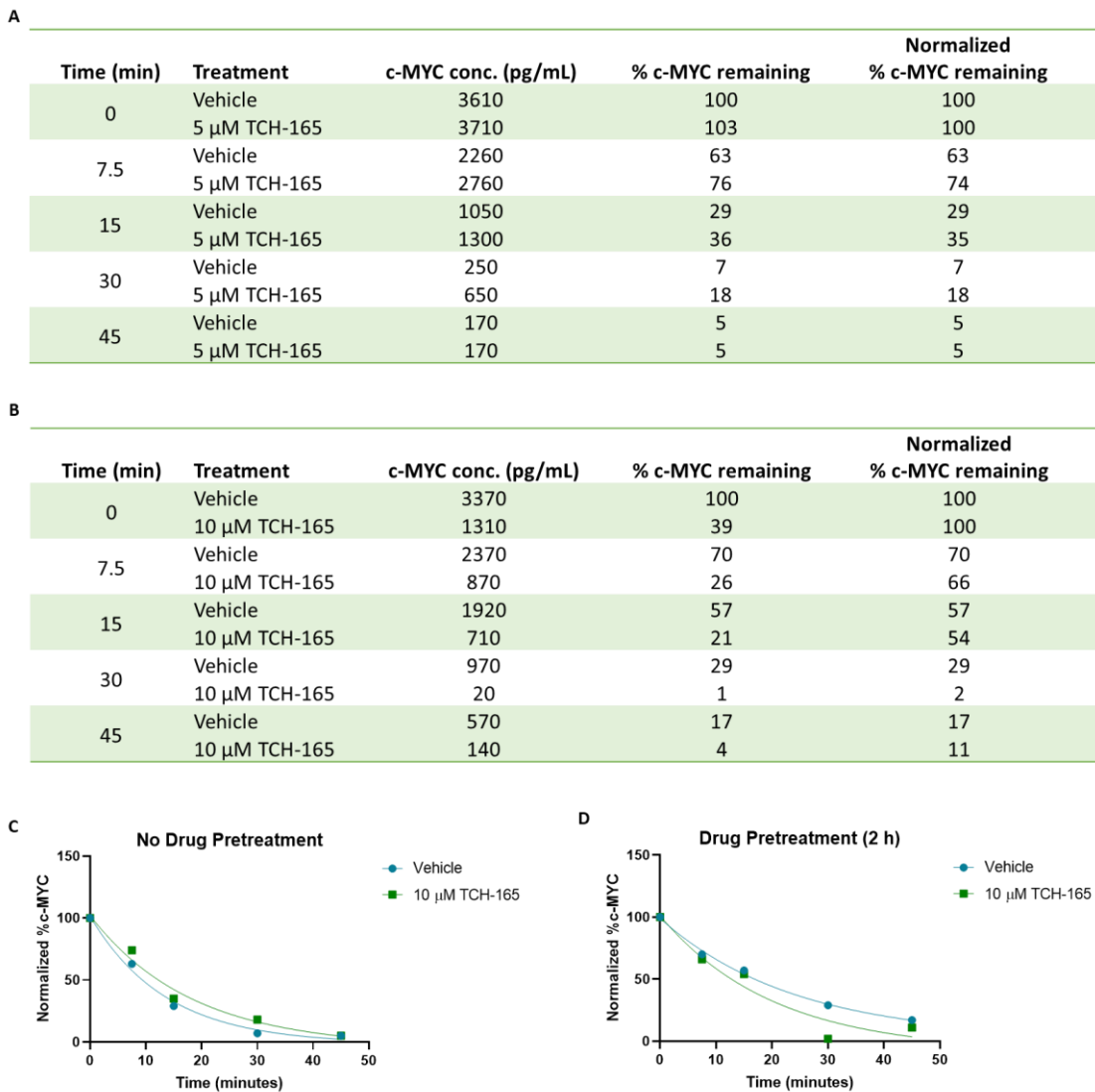


Figure 5.3 TCH-165 does not enhance the rate of degradation of c-MYC in MC/CAR cells compared to vehicle control (A) Concentrations of c-MYC remaining in MC/CAR cells following treatment with DMSO or TCH-165 (5 μ M; without drug pretreatment), followed by addition of cycloheximide (50 μ g/mL) determined by ELISA. (B) Concentrations of c-MYC remaining in MC/CAR cells following treatment with DMSO or TCH-165 (10 μ M; with 2 h drug pretreatment), followed by addition of cycloheximide (50 μ g/mL) determined by ELISA. (C) Percent c-MYC remaining over time without drug pretreatment; T=0 time point for vehicle and TCH-165 treatment each normalized to 100 percent. (D) Percent c-MYC remaining over time with 2 h drug pretreatment; T=0 time point for vehicle and TCH-165 treatment each normalized to 100 percent, as T=0 c-MYC concentration is significantly reduced with TCH-165 treatment.

To test this hypothesis, cells were pretreated with TCH-165 (10 μ M) for two hours prior to the addition of cycloheximide to allow for target engagement. Interestingly, following the 2-hour drug pretreatment, the T=0 time point of the TCH-165 treated cells had a greatly reduced concentration of c-MYC (1310 pg/mL, 39%) compared to the T=0 time point of the vehicle treated cells (3370 pg/mL, 100%) (Figure 5.3B). Therefore, to determine the half-life of c-MYC for both the vehicle and TCH-165 treated cells, the percent c-MYC remaining was normalized so that each of their T=0 concentrations were set to 100 percent. This allowed for the amount of c-MYC degradation to be determined between 0 and 45 minutes regardless of the starting c-MYC protein concentration. Following this normalization, minimal differences in the amount of c-MYC degraded was observed between the vehicle and TCH-165 treated cells. A time response curve (Figure 5.3D) was plotted and resulted in a c-MYC half-life between 13 and 17 minutes for both the vehicle and TCH-165 treated cells. Similar results were observed in the leukemia cell line, CCRF-CEM (Figure 5.6 of the Appendix).

While further investigation is required, these experiments suggest that the mechanism by which TCH-165 reduces c-MYC protein levels is something other than directly enhancing the 20S proteasome-mediated degradation of c-MYC protein itself. However, as previously discussed above, proteasome inhibitor, bortezomib, completely abrogated the ability of TCH-165 to reduce c-MYC protein levels. This suggests that TCH-165 induced c-MYC clearance is likely a 20S proteasome-mediated event. Although, it is possible that the reduction of c-MYC by TCH-165 is indirectly regulated by 20S proteasome-mediated degradation of another protein which regulates c-MYC protein stability. For example, the proteolytic stability of c-MYC is highly regulated by multiple E3 ligases, many of which are intrinsically disordered proteins.^{4,38} Enhancing 20S proteasome-mediated degradation of these regulatory proteins could therefore have an impact on c-MYC protein stability. The enhancement of 20S proteasome activity could also indirectly impact c-MYC clearance by affecting the many post-translational modifications that regulate its proteolytic stability.³⁹ Another possibility could be due to affecting its heterodimeric interaction with its intrinsically disordered binding partner MAX.²⁹ It is possible that enhancement of 20S proteasome-mediated degradation of MAX could result in more free c-MYC, rendering it more susceptible to 20S proteasome-mediated degradation. While further

work is needed to determine the mechanism by which TCH-165 reduces c-MYC protein levels, it is evident the compound was quite effective in reducing c-MYC protein accumulation. As a result, we next aimed to explore whether reduction of c-MYC protein levels would inhibit oncogenic c-MYC-mediated processes, such as cancer cell proliferation and promotion of tumor growth.

5.2.3 Collaborative Efficacy Studies Demonstrate 20S Proteasome Activation by TCH-165 Results in Anticancer Properties

In collaboration with a number of individuals at Michigan State University and the University of Waterloo, the efficacy of TCH-165 to regulate additional c-MYC-mediated processes was evaluated. It is well known that c-MYC is essential for promoting cell proliferation, and that its dysregulated accumulation contributes to uncontrolled cell proliferation in many cancers.^{8,12} Therefore, we aimed to explore whether reduction of c-MYC protein levels by TCH-165 would inhibit c-MYC promoted cancer cell proliferation. Assessment of cell viability following TCH-165 treatment demonstrated that the drug inhibited cancer cell proliferation in the RPMI 8226, L363, and NCI-H929 cell lines at low single-digit micromolar potencies.⁴⁰ While bortezomib remains a first-line therapy for multiple myeloma treatment, after relapse many patients gain a resistance and do not respond to bortezomib treatment a second time.²³ Remarkably, TCH-165 treatment was also effectively able to kill primary cells from both a newly diagnosed and bortezomib unresponsive multiple myeloma patient.⁴⁰

The translational efficacy to further assess the therapeutic potential of TCH-165 was also evaluated in an RPMI 8226 multiple myeloma xenograft tumor model. In this experiment, TCH-165 was administered to mice at 100 mg/kg twice per day, resulting in a 76 percent reduction in tumor growth compared to the untreated control mice.⁴⁰ This reduction in tumor growth by TCH-165 was significantly greater than the 38 percent reduction in tumor growth observed with BTZ treatment. A tolerance study was conducted in parallel with the tumor model and showed TCH-165 treatment was well tolerated by the mice, with less than a 10 percent loss in body weight. A more detailed tolerance study was also conducted in beagles with TCH-165 treatment for five consecutive days (oral capsule, 50 mg/kg twice per day).⁴⁰ Clinical observation, body weight (less than 1 percent change), standard complete blood count, and clinical chemistry panel following

the five-day tolerance study identified no significant changes compared to the pre-treatment evaluations.

5.2.4 Development of a Target Engagement Assay

In parallel to the canine tolerance study, I developed a target engagement assay to determine whether TCH-165 was reaching the desired proteasome target using oral delivery of the drug to the beagles. In this experiment, peripheral blood mononuclear cells (PBMCs) were isolated from the canine blood samples prior to TCH-165 treatment and following day five of TCH-165 treatment. The PBMCs were then lysed, and the proteasome activity of the lysate was evaluated using a small peptide proteasome substrate conjugated to the fluorophore, 7-amino-4-methylcoumarin (AMC) (i.e. Suc-LLVY-AMC). Proteolytic cleavage of the peptide results in the release of AMC, and this fluorescence was measured over time to quantify 20S proteolytic activity. If the target was engaged, it is anticipated an increase in proteasome activity would be observed. After a five-day treatment with TCH-165, the proteasome activity of Canine 1 increased to 488 percent and Canine 2 increased to 233 percent compared to their respective pre-treatment vehicle/baseline proteasome activities (Figure 5.4). This enhancement of proteasome activity in the PBMC lysate confirms target engagement. In combination with the tolerance data, these studies show that TCH-165 is well tolerated *in vivo* at concentrations in which it significantly enhanced activity of the proteasome.

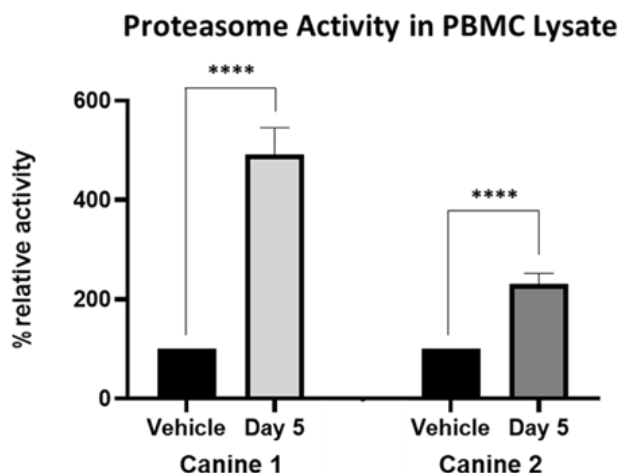


Figure 5.4 Enhanced proteasome activity in canine PBMCs confirms target engagement of 20S proteasome activator TCH-165 (n=3); one-way ANOVA (ns, not significant, *p ≤0.05; **p≤0.01; ***p≤0.001; ****p≤0.0001).

5.3 Conclusion

In all, our findings demonstrate that TCH-165 reduces c-MYC protein levels in cell culture, inhibits cancer cell proliferation, and inhibits tumor growth *in vivo*. While the mechanism by which TCH-165 reduces c-MYC protein levels requires further investigation, evidence suggests c-MYC induced clearance by TCH-165 is a 20S proteasome-mediated event. Furthermore, the compound is well tolerated *in vivo* at therapeutic concentrations. These data suggests that further exploration of this therapeutic strategy is warranted, as it may provide a novel treatment for c-MYC-driven cancers and other diseases in which intrinsically disordered protein accumulation plays a significant role in disease progression.

5.4 Experimental

5.4.1 Methods

Multiple myeloma cell culture. RPMI 8226, MC/CAR, L363 and NCI-H929 cells were obtained from ATCC (Manassas, VA, USA). RPMI 8226 cells were maintained in RPMI-1640 medium supplemented with 10% fetal bovine serum (FBS) and 1% penicillin/streptomycin at 37 °C and 5% CO₂. MC/CAR cells were maintained in Iscove's Modified Dulbecco's Medium (IMDM) supplemented with 20% FBS and 1% penicillin/streptomycin. L363 cells were maintained in RPMI-1640 medium supplemented with 15% heat-inactivated FBS and 1% penicillin/streptomycin. NCI-H929 cells were maintained in RPMI-1640 medium supplemented with 10% FBS, 0.05 mM 2-mercaptoethanol, and 1% penicillin/streptomycin. DMSO was used as the vehicle control at a 0.1% final concentration for cell culture experiments.

Degradation of c-MYC in multiple myeloma cells (with ELISA analysis). MC/CAR, L363, or H929 cells were grown in T25 flasks in medium indicated above. Cells were treated with DMSO, TCH-165, or bortezomib (BTZ) at the indicated concentrations for 4 h (0.1% final DMSO concentration). Following the 4-hour treatment, cells were pelleted, washed with chilled PBS buffer, and resuspended in chilled lysis buffer (10 mM Tris, 100 mM NaCl, 1 mM EDTA, 1 mM EGTA, 1 mM NaF, 20 mM Na₄P₂O₇, 2 mM Na₃VO₄, 1% Triton X-100, 10% glycerol, 0.1% SDS, and 0.5% deoxycholate; pH 7.4) supplemented with Complete Mini Protease Inhibitor Cocktail (Sigma Aldrich). The lysate was clarified by centrifugation at 5000 rpm (4 °C) for 15 min. Total protein of the lysate was quantified by bicinchoninic acid assay (BCA assay, Thermofisher Scientific;

Waltham, MA, USA). and normalized to 1.5 mg/mL total protein. The supplied protocol for the human c-MYC (Total) ELISA Kit (Invitrogen; Waltham, MA, USA) was used to determine the total c-MYC concentration of the lysates. Prior to loading lysate into ELISA plate wells, lysate (5 μ L) was diluted into 45 μ L of supplied standard diluent buffer.

Cellular c-MYC half-life assay. *No drug pretreatment:* MC/CAR cells were grown in T25 flasks in medium indicated above. Cells were treated with DMSO or TCH-165 (5 μ M) and cycloheximide (50 μ g/mL) was immediately added. Various time points were collected by harvesting cells at (0, 7.5, 15, 30 and 45 min) following cycloheximide addition. ***With drug pretreatment:*** MC/CAR cells were grown in T25 flasks in medium indicated above. Cells were pretreated with DMSO or TCH-165 (10 μ M) for 2 h, and then cycloheximide (50 μ g/mL) was added post two-hour incubation. Various time points were collected by harvesting cells at (0, 7.5, 15, 30 and 45 min) following cycloheximide addition. To harvest cells, cells were pelleted, washed with chilled PBS buffer, and resuspended in chilled lysis buffer (10 mM Tris, 100 mM NaCl, 1 mM EDTA, 1 mM EGTA, 1 mM NaF, 20 mM $\text{Na}_4\text{P}_2\text{O}_7$, 2 mM Na_3VO_4 , 1% Triton X-100, 10% glycerol, 0.1% SDS, and 0.5% deoxycholate; pH 7.4) supplemented with Complete Mini Protease Inhibitor Cocktail (Sigma Aldrich). The lysate was clarified by centrifugation at 5000 rpm (4 $^\circ$ C) for 15 min. Total protein of the lysate was quantified by bicinchoninic acid assay (BCA assay, Thermofisher Scientific; Waltham, MA, USA). and normalized to 1.5 mg/mL total protein. The supplied protocol for the human c-MYC (Total) ELISA Kit (Invitrogen; Waltham, MA, USA) was used to determine the total c-MYC concentration of the lysates. Prior to loading lysate into ELISA plate wells, lysate (5 μ L) was diluted into 45 μ L of supplied standard diluent buffer.

Target engagement assay in canine PBMC lysate. Canine blood samples obtained in BD Vacutainer CPT mononuclear cell preparation tubes containing sodium citrate were used to isolate PBMCs. For PBMC isolation, sample tubes were inverted five times and equilibrated for the centrifuge with sterile PBS buffer. Tubes were centrifuged at 1800 \times g with the acceleration set at 5 and a break set to 0 at room temperature for 30 min. Half of the plasma layer was discarded. Using a sterile Pasteur pipette, the buffy coat was collected and put into a 15 mL conical tube and sterile PBS buffer was added to 10 mL. The conical tubes were centrifuged at 300 \times g for 10 min and the supernatant was removed. Cells were resuspended in 150 μ L of lysis

buffer (50 mM Tris-HCl, 2 mM Na₂ATP, 5 mM MgCl₂, 0.5 mM EDTA, 10% glycerol) and lysed by vortex. Samples were centrifuged for 20 min at 14,000 × g. The total protein concentration of the supernatant was determined using bicinchoninic acid assay (BCA assay), and the samples were normalized to 1 mg/mL. Samples were diluted to 0.036 µg/µL in assay buffer (38 mM Tris, 100 mM NaCl, pH 7.8) and 140 µL of the diluted sample was added to three wells of a black, clear-bottom 96-well plate. Substrate stock solution (10 µL of 375 µM Suc-LLVY-AMC in assay buffer) was added to each well. Fluorescence was measured and kinetic readings were taken every 5 min at 37 °C, at 380/460 nm for 1 h.

REFERENCES

- (1) Kumar, S. K.; Rajkumar, V.; Kyle, R. A.; van Duin, M.; Sonneveld, P.; Mateos, M.-V.; Gay, F.; Anderson, K. C. Multiple Myeloma. *Nature Reviews Disease Primers* **2017**, *3* (1), 1–20.
- (2) Carroll, P. A.; Freie, B. W.; Mathsyaraja, H.; Eisenman, R. N. The MYC Transcription Factor Network: Balancing Metabolism, Proliferation and Oncogenesis. *Frontiers of Medicine* **2018**, *12* (4), 412–425.
- (3) Fisher, F.; Crouch, D. H.; Jayaraman, P. S.; Clark, W.; Gillespie, D. A.; Goding, C. R. Transcription Activation by Myc and Max: Flanking Sequences Target Activation to a Subset of CACGTG Motifs in Vivo. *The EMBO Journal* **1993**, *12* (13), 5075–5082.
- (4) Farrell, A. S.; Sears, R. C. MYC Degradation. *Cold Spring Harbor Perspectives in Medicine* **2014**, *4* (3), 1–15.
- (5) Thomas, L. R.; Tansey, W. P. Proteolytic Control of the Oncoprotein Transcription Factor Myc. In *Advances in Cancer Research*; Klein, G., Ed.; Academic Press, 2011; Vol. 110, pp 77–106.
- (6) Ciechanover, A.; Schwartz, A. L. The Ubiquitin-Proteasome Pathway: The Complexity and Myriad Functions of Proteins Death. *Proceedings of the National Academy of Sciences of the United States of America* **1998**, *95* (6), 2727–2730.
- (7) Vervoorts, J.; Lüscher-Firzlaff, J.; Lüscher, B. The Ins and Outs of MYC Regulation by Posttranslational Mechanisms. *Journal of Biological Chemistry* **2006**, *281* (46), 34725–34729.
- (8) Kalkat, M.; De Melo, J.; Hickman, K. A.; Lourenco, C.; Redel, C.; Resetca, D.; Tamachi, A.; Tu, W. B.; Penn, L. Z. MYC Deregulation in Primary Human Cancers. *Genes* **2017**, *8* (6), 151.
- (9) O’Neil, J.; Grim, J.; Strack, P.; Rao, S.; Tibbitts, D.; Winter, C.; Hardwick, J.; Welcker, M.; Meijerink, J. P.; Pieters, R.; Draetta, G.; Sears, R.; Clurman, B. E.; Look, A. T. FBW7 Mutations in Leukemic Cells Mediate NOTCH Pathway Activation and Resistance to γ -Secretase Inhibitors. *Journal of Experimental Medicine* **2007**, *204* (8), 1813–1824.
- (10) Bahram, F.; von der Lehr, N.; Cetinkaya, C.; Larsson, L. G. C-Myc Hot Spot Mutations in Lymphomas Result in Inefficient Ubiquitination and Decreased Proteasome-Mediated Turnover. *Blood* **2000**, *95* (6), 2104–2110.
- (11) Gregory, M. A.; Hann, S. R. C-Myc Proteolysis by the Ubiquitin-Proteasome Pathway: Stabilization of c-Myc in Burkitt’s Lymphoma Cells. *Molecular and Cellular Biology* **2000**, *20* (7), 2423–2435.
- (12) Miller, D. M.; Thomas, S. D.; Islam, A.; Muench, D.; Sedoris, K. C-Myc and Cancer Metabolism. *Clinical Cancer Research* **2012**, *18* (20), 5546–5553.
- (13) Schick, M.; Habringer, S.; Nilsson, J. A.; Keller, U. Pathogenesis and Therapeutic Targeting of Aberrant MYC Expression in Haematological Cancers. *British Journal of Haematology* **2017**, *179* (5), 724–738.
- (14) Dang, C. V. MYC on the Path to Cancer. *Cell* **2012**, *149* (1), 22–35.

- (15) Podar, K.; Leleu, X. Relapsed/Refractory Multiple Myeloma in 2020/2021 and Beyond. *Cancers* **2021**, *13* (20), 5154.
- (16) Richardson, P. G.; Xie, W.; Mitsiades, C.; Chanan-Khan, A. A.; Lonial, S.; Hassoun, H.; Avigan, D. E.; Oaklander, A. L.; Kuter, D. J.; Wen, P. Y.; Kesari, S.; Briemberg, H. R.; Schlossman, R. L.; Munshi, N. C.; Heffner, L. T.; Doss, D.; Esseltine, D.-L.; Weller, E.; Anderson, K. C.; Amato, A. A. Single-Agent Bortezomib in Previously Untreated Multiple Myeloma: Efficacy, Characterization of Peripheral Neuropathy, and Molecular Correlations With Response and Neuropathy. *Journal of Clinical Oncology* **2009**, *27* (21), 3518–3525.
- (17) Pessoa, J.; Martins, M.; Casimiro, S.; Pérez-Plasencia, C.; Shoshan-Barmatz, V. Editorial: Altered Expression of Proteins in Cancer: Function and Potential Therapeutic Targets. *Frontiers in Oncology* **2022**, *12*, 1–6.
- (18) Tsvetkov, P.; Adler, J.; Myers, N.; Biran, A.; Reuven, N.; Shaul, Y. Oncogenic Addiction to High 26S Proteasome Level. *Cell Death & Disease* **2018**, *9* (7), 1–14.
- (19) Arlt, A.; Bauer, I.; Schafmayer, C.; Tepel, J.; Mürköster, S. S.; Brosch, M.; Röder, C.; Kalthoff, H.; Hampe, J.; Moyer, M. P.; Fölsch, U. R.; Schäfer, H. Increased Proteasome Subunit Protein Expression and Proteasome Activity in Colon Cancer Relate to an Enhanced Activation of Nuclear Factor E2-Related Factor 2 (Nrf2). *Oncogene* **2009**, *28* (45), 3983–3996.
- (20) Chen, L.; Madura, K. Increased Proteasome Activity, Ubiquitin-Conjugating Enzymes, and EEF1A Translation Factor Detected in Breast Cancer Tissue. *Cancer Research* **2005**, *65* (13), 5599–5606.
- (21) Adams, J.; Kauffman, M. Development of the Proteasome Inhibitor Velcade™ (Bortezomib). *Cancer Investigation* **2004**, *22* (2), 304–311.
- (22) Suraweera, A.; Münch, C.; Hanssum, A.; Bertolotti, A. Failure of Amino Acid Homeostasis Causes Cell Death Following Proteasome Inhibition. *Molecular Cell* **2012**, *48* (2), 242–253.
- (23) Allmeroth, K.; Horn, M.; Kroef, V.; Miethe, S.; Müller, R.-U.; Denzel, M. S. Bortezomib Resistance Mutations in PSMB5 Determine Response to Second-Generation Proteasome Inhibitors in Multiple Myeloma. *Leukemia* **2021**, *35* (3), 887–892.
- (24) Barrio, S.; Stühmer, T.; Da-Viá, M.; Barrio-Garcia, C.; Lehnert, N.; Besse, A.; Cuenca, I.; Garitano-Trojaola, A.; Fink, S.; Leich, E.; Chatterjee, M.; Driessen, C.; Martinez-Lopez, J.; Rosenwald, A.; Beckmann, R.; Bargou, R. C.; Braggio, E.; Stewart, A. K.; Raab, M. S.; Einsele, H.; Kortüm, K. M. Spectrum and Functional Validation of PSMB5 Mutations in Multiple Myeloma. *Leukemia* **2019**, *33* (2), 447–456.
- (25) Oerlemans, R.; Franke, N. E.; Assaraf, Y. G.; Cloos, J.; van Zantwijk, I.; Berkers, C. R.; Scheffer, G. L.; Debipersad, K.; Vojtekova, K.; Lemos, C.; van der Heijden, J. W.; Ylstra, B.; Peters, G. J.; Kaspers, G. L.; Dijkmans, B. A. C.; Scheper, R. J.; Jansen, G. Molecular Basis of Bortezomib Resistance: Proteasome Subunit B5 (PSMB5) Gene Mutation and Overexpression of PSMB5 Protein. *Blood* **2008**, *112* (6), 2489–2499.

- (26) Dang, C. V.; Reddy, E. P.; Shokat, K. M.; Soucek, L. Drugging the “undruggable” Cancer Targets. *Nature Reviews Cancer* **2017**, *17* (8), 502–508.
- (27) Delmore, J. E.; Issa, G. C.; Lemieux, M. E.; Rahl, P. B.; Shi, J.; Jacobs, H. M.; Kastiris, E.; Gilpatrick, T.; Paranal, R. M.; Qi, J.; Chesi, M.; Schinzel, A. C.; McKeown, M. R.; Heffernan, T. P.; Vakoc, C. R.; Bergsagel, P. L.; Ghobrial, I. M.; Richardson, P. G.; Young, R. A.; Hahn, W. C.; Anderson, K. C.; Kung, A. L.; Bradner, J. E.; Mitsiades, C. S. BET Bromodomain Inhibition as a Therapeutic Strategy to Target C-Myc. *Cell* **2011**, *146* (6), 904–917.
- (28) Manier, S.; Huynh, D.; Shen, Y. J.; Zhou, J.; Yusufzai, T.; Salem, K. Z.; Ebright, R. Y.; Shi, J.; Park, J.; Glavey, S. V.; Devine, W. G.; Liu, C.-J.; Leleu, X.; Quesnel, B.; Roche-Lestienne, C.; Snyder, J. K.; Brown, L. E.; Gray, N.; Bradner, J.; Whitesell, L.; Porco, J. A.; Ghobrial, I. M. Inhibiting the Oncogenic Translation Program Is an Effective Therapeutic Strategy in Multiple Myeloma. *Science Translational Medicine* **2017**, *9* (389), 1–13.
- (29) Llombart, V.; Mansour, M. R. Therapeutic Targeting of “Undruggable” MYC. *eBioMedicine* **2022**, *75*, 1–17.
- (30) Castell, A.; Yan, Q.; Fawcner, K.; Hydbring, P.; Zhang, F.; Verschut, V.; Franco, M.; Zakaria, S. M.; Bazzar, W.; Goodwin, J.; Zinzalla, G.; Larsson, L.-G. A Selective High Affinity MYC-Binding Compound Inhibits MYC:MAX Interaction and MYC-Dependent Tumor Cell Proliferation. *Scientific Reports* **2018**, *8* (1), 1–17.
- (31) Choi, S. H.; Mahankali, M.; Lee, S. J.; Hull, M.; Petrassi, H. M.; Chatterjee, A. K.; Schultz, P. G.; Jones, K. A.; Shen, W. Targeted Disruption of Myc–Max Oncoprotein Complex by a Small Molecule. *ACS Chemical Biology* **2017**, *12* (11), 2715–2719.
- (32) Jiang, H.; Bower, K. E.; Beuscher, A. E.; Zhou, B.; Bobkov, A. A.; Olson, A. J.; Vogt, P. K. Stabilizers of the Max Homodimer Identified in Virtual Ligand Screening Inhibit Myc Function. *Molecular Pharmacology* **2009**, *76* (3), 491–502.
- (33) Struntz, N. B.; Chen, A.; Deutzmann, A.; Wilson, R. M.; Stefan, E.; Evans, H. L.; Ramirez, M. A.; Liang, T.; Caballero, F.; Wildschut, M. H. E.; Neel, D. V.; Freeman, D. B.; Pop, M. S.; McConkey, M.; Muller, S.; Curtin, B. H.; Tseng, H.; Frombach, K. R.; Butty, V. L.; Levine, S. S.; Feau, C.; Elmiligy, S.; Hong, J. A.; Lewis, T. A.; Vetere, A.; Clemons, P. A.; Malstrom, S. E.; Ebert, B. L.; Lin, C. Y.; Felsher, D. W.; Koehler, A. N. Stabilization of the Max Homodimer with a Small Molecule Attenuates Myc-Driven Transcription. *Cell Chemical Biology* **2019**, *26* (5), 711–723.
- (34) Huang, H.-L.; Weng, H.-Y.; Wang, L.-Q.; Yu, C.-H.; Huang, Q.-J.; Zhao, P.-P.; Wen, J.-Z.; Zhou, H.; Qu, L.-H. Triggering Fbw7-Mediated Proteasomal Degradation of c-Myc by Oridonin Induces Cell Growth Inhibition and Apoptosis. *Molecular Cancer Therapeutics* **2012**, *11* (5), 1155–1165.
- (35) Campaner, E.; Rustighi, A.; Zannini, A.; Cristiani, A.; Piazza, S.; Ciani, Y.; Kalid, O.; Golan, G.; Baloglu, E.; Shacham, S.; Valsasina, B.; Cucchi, U.; Pippione, A. C.; Lolli, M. L.; Giabbai, B.; Storici, P.; Carloni, P.; Rossetti, G.; Benvenuti, F.; Bello, E.; D’Incalci, M.; Cappuzzello, E.; Rosato, A.; Del Sal, G. A Covalent PIN1 Inhibitor Selectively Targets Cancer Cells by a Dual Mechanism of Action. *Nature Communications* **2017**, *8* (1), 1–15.

- (36) Li, S.; Jiang, C.; Pan, J.; Wang, X.; Jin, J.; Zhao, L.; Pan, W.; Liao, G.; Cai, X.; Li, X.; Xiao, J.; Jiang, J.; Wang, P. Regulation of C-Myc Protein Stability by Proteasome Activator REGγ. *Cell Death & Differentiation* **2015**, *22* (6), 1000–1011.
- (37) Miao, Y.; Du, Q.; Zhang, H.-G.; Yuan, Y.; Zuo, Y.; Zheng, H. Cycloheximide (CHX) Chase Assay to Examine Protein Half-Life. *Bio-protocol* **2023**, *13* (11), 1–11.
- (38) Bhowmick, P.; Pancsa, R.; Guharoy, M.; Tompa, P. Functional Diversity and Structural Disorder in the Human Ubiquitination Pathway. *PLOS ONE* **2013**, *8* (5), 1–18.
- (39) Sun, X.-X.; Li, Y.; Sears, R. C.; Dai, M.-S. Targeting the MYC Ubiquitination-Proteasome Degradation Pathway for Cancer Therapy. *Frontiers in Oncology* **2021**, *11*, 1–9.
- (40) Njomen, E.; Vanecek, A.; Lansdell, T. A.; Yang, Y.-T.; Schall, P. Z.; Harris, C. M.; Bernard, M. P.; Isaac, D.; Alkharabsheh, O.; Al-Janadi, A.; Giletto, M. B.; Ellsworth, E.; Taylor, C.; Tang, T.; Lau, S.; Bailie, M.; Bernard, J. J.; Yuzbasiyan-Gurkan, V.; Tepe, J. J. Small Molecule 20S Proteasome Enhancer Regulates MYC Protein Stability and Exhibits Antitumor Activity in Multiple Myeloma. *Biomedicines* **2022**, *10* (5), 938.

APPENDIX

5.1 c-MYC Half-Life Determination Assay in Jeko-1 Cells

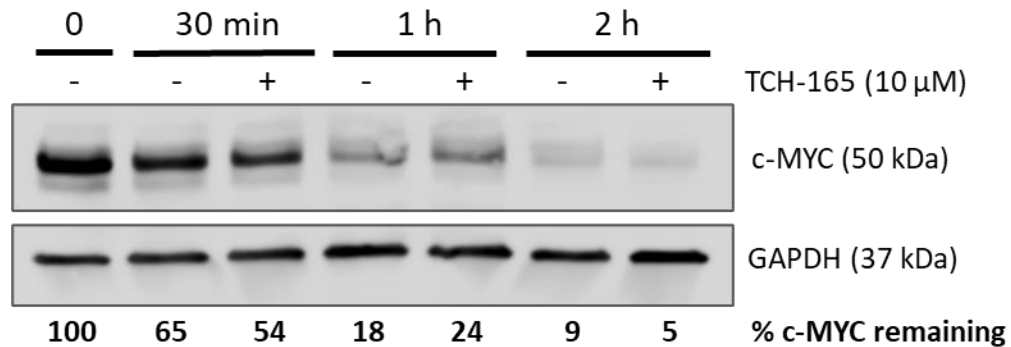
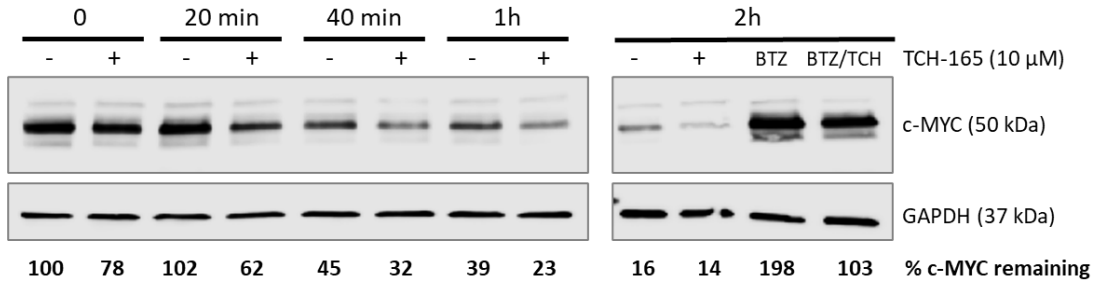


Figure 5.5 TCH-165 does not enhance the rate of degradation of c-MYC compared to vehicle control in Jeko-1 cells. Concentrations of c-MYC remaining in Jeko-1 cells following treatment with DMSO or TCH-165 (10 μ M; without drug pretreatment), followed by addition of cycloheximide (50 μ g/mL) determined by Western Blot. Percent c-MYC remaining over time was calculated by dividing amount of c-MYC at each time point by c-MYC concentration at T=0 time point (n=1).

5.2 c-MYC Half-Life Determination Assay in CCRF-CEM Cells



Time (min)	Treatment	% c-MYC remaining	Normalized % c-MYC remaining
0	Vehicle	100	100
	10 μ M TCH-165	78	100
20	Vehicle	102	102
	10 μ M TCH-165	62	79
40	Vehicle	45	45
	10 μ M TCH-165	32	40
60	Vehicle	39	39
	10 μ M TCH-165	23	29
120	Vehicle	16	16
	10 μ M TCH-165	14	18
	5 μ M BTZ	198	198
	BTZ/TCH-165	103	103

Figure 5.6 TCH-165 does not enhance the rate of degradation of c-MYC compared to vehicle control in CCRF-CEM cells. Concentrations of c-MYC remaining in CCRF-CEM cells following treatment with DMSO or TCH-165 (10 μ M; with 1 h drug pretreatment), followed by addition of cycloheximide (50 μ g/mL) determined by Western Blot. Percent c-MYC remaining over time was calculated by dividing amount of c-MYC at each time point by c-MYC concentration at T=0 time point (n=1). To calculate normalized percent c-MYC remaining, T=0 time point for vehicle and TCH-165 treatment were each normalized to 100 percent, as T=0 c-MYC concentration is slightly reduced with TCH-165 treatment (n=1).